3D INVERSION MODELLING OF THE NECHAKO BASIN, BRITISH COLUMBIA, MAGNETOTELLURIC DATA SET

MATTHEW DREW

3D Inversion Modelling of the Nechako Basin, British Columbia, Magnetotelluric Data Set

by

© *Matthew Drew*

A thesis submitted to the

School of Graduate Studies

in partial fulfilment of the

requirements for the degree of

Master of Science

Department of Earth Sciences

Memorial University of Newfoundland

March 2012

St. John's Newfoundland and Labrador

Abstract

The Nechako Basin is an intermontane basin situated in south central British Columbia, Canada. Due to a desire for an alternative source of employment stemming from the impact of the mountain pine beetle on the forestry industry, the government of British Columbia has commissioned several geophysical and geological surveys of the area in order to assess its hydrocarbon potential. This sedimentary basin is covered with a layer of volcanic extrusive rocks which renders seismic methods nearly ineffective. As an alternative, a magnetotelluric (MT) survey was performed in order to determine subsurface conductivity and structure. Data from this survey were used in this thesis to produce a 3D conductivity model of the subsurface, by running multiple inversions with varied parameters. Data from four profiles as well as additional sites filling in gaps between profiles were used: Profile A ran west of Nazko, Profile B ran south of Nazko, Profile C ran north-west of Nazko, and Profile D ran east from Nazko toward Quesnel. Models from inversion of this MT survey show sensitivity to thicker surface volcanic rock and show where these bodies may thin or pinch out (e.g. conductivity at the west end of profile A and south end of Profile B). Additionally potential faulting and partial melt is seen in the subsurface, in profile D and at depth between profiles A and C respectively. 3D inversion models have provided information in addition to previous 2D results, giving a different placement of features out of the restricted plane of 2D inversion and showing lateral extent of conductivity anomalies, thus contributing to hydrocarbon exploration in the Nechako Basin.

Acknowledgements

I am forever endebted to David Hornidge who gave me my start in physics, showed me how to do research, and instilled a passion for international travel in me. His contributions are not directly contained within this document but have nevertheless been essential in the writing of it. I am also grateful to Ralph Bruening and the rest of the Mount Allison University Physics Department faculty for the excellent education and opportunities provided to me.

I would like to thank Colin Farquharson, my supervisor and mentor for these last years. His encouragement and patience have not only taught me about geophysical methods and enabled the undertaking of this degree, but have inspired and spurred me to pursue my curiosity. I want as well to thank Colin for his understanding and enthusiasm, even, for time taken away from thesis work for globe trotting and side projects. He is a rare supervisor that works to develop every facet of his students.

I am grateful to Colin Hogg and Duygu Kiyan for bringing me to Morocco to get a taste of magnetotelluric field work. An understanding of the practicalities of data acquisition expedited an understanding of this method. I am also thankful to the other members of the 2009 Morocco team for good conversations on MT and geology and the great times had in North Africa. The Dublin Institute for Advanced Studies also deserves thanks here for their financial contributions and making this trip possible.

Members of the Memorial University of Newfoundland Earth Science Department have been ever helpful. I would like to thank Jeremy Hall and Michael Slawinski in particular for enlightening chats about geology and math. I appreciate my of-

fice mates Masoud Ansari and Hormoz Jahandari for friendship and collaboration all those long nights on the fourth floor. Jessica Spratt and Jim Craven have also facilitated this project: from recommendations to strengthen this document to suggestions on research avenues and support with new queries. The financial support of Geoscience BC, the INCO Innovation Centre, and the Geological Survey of Canada, is acknowledged for making this project possible.

Most importantly of all, I would like to thank my loving parents. Their support in my academic career has always pushed me ahead. I am grateful to have folks who are so good at what they do.

Contents

List of Tables

List of Figures

Chapter 1

Introduction

1.1 Motivation

The British Columbia forestry industry has been hit in some areas by an infestation of the mountain pine beetle. A provincial government (BC Government, 2006) report estimated potential damages to the industry could claim 80% of viable pine growth by 2013. While the government attempts to slow the epidemic and mitigate effects on industry and unemployment, the British Columbians are also looking for ways to create jobs in other sectors.

One prospective area for job creation is the oil and gas industry. The Nechako Basin, an intermontane basin in south central BC, has had very little exploration done by industry, thus the onus has fallen to academic government institutions like the GSC and Geoscience BC to assess the potential of the region and promote its resources. The Nechako Basin is covered in most part by glacial overburden and extrusive volcanics, namely, basalt (Calvert et al., 2008). Seismic imaging of the area

is rendered difficult by the covering of basalt and so other methods have been required to image the sub-surface (Spratt and Craven, 2010; Best, 2004). Originally these other methods involved potential field measurements (e.g. magnetic and gravity). In addition to the challenges posed to the seismic methods by the volcanics, limited borehole information is available and geological information is lacking due to the sparsity of outcrops in this basin (Calvert et al., 2008). This thesis presents the results of 3D inversion of a magnetotelluric (MT) data-set acquired for Geoscience BC. 2D modelling and interpretation of the MT data has previously been done by Spratt and Craven (2011). The work of this thesis also contributes to the growing number of examples of the use of magnetotelluric data modelling in hydrocarbon exploration.

1.2 Geology

1.2.1 Regional Setting

The boundaries of the Nechako Basin (Fig. 1.1) are poorly defined (Riddell, 2011). It lies in the Intermontane Belt of the Canadian Cordillera, bordered by the Coastal Mountains to the west, the Omineca Crystalline belt/Quesnel trough to the east, the Skeena arch to the north, and the Fraser fault to the south-east. Basaltic lava extrusion occuring circa Eocene and Miocene was contemporaneous with transcurrent faulting and the resulting east-west faulting (Spratt and Craven, 2008). Sedimentation in the basin is primarily Upper Cretaceous to Oligocene with a basement of Stikine and Quesnel volcanic arcterranes (Riddell and Ferri, 2008). Geology in this

area is complex as a result of deformation during the Cretaceous to Eocene (Riddell, 2011) and poorly understood due to widespread volcanic and glacial covering of the basin and sparse mapping (the most recent results of detailed mapping are seen in Fig. 1.10).

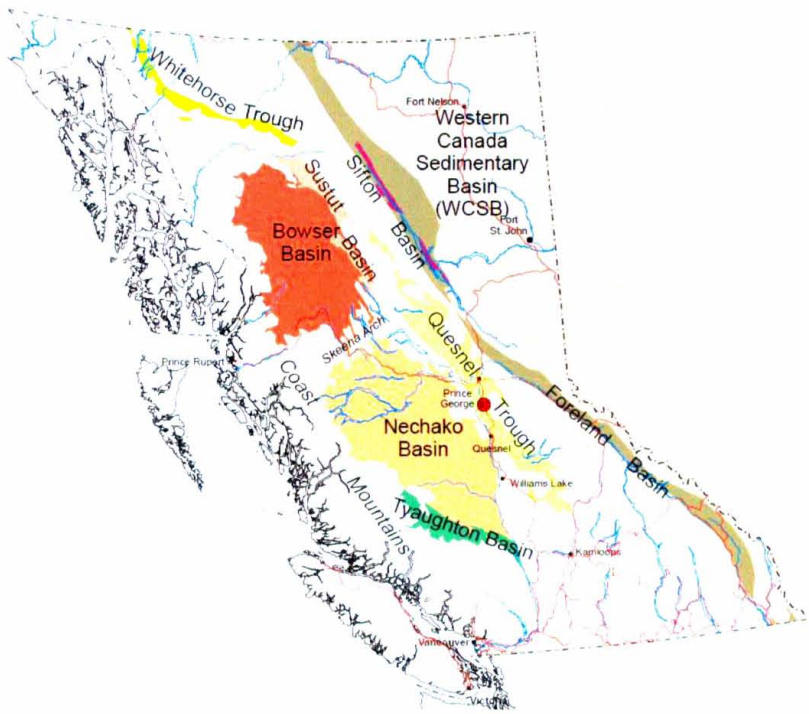

Figure 1.1: Map showing the Nechako Basin (magenta), the MT measurement sites (yellow), and some surrounding geological features in British Columbia (Ferri and Riddell, 2008).

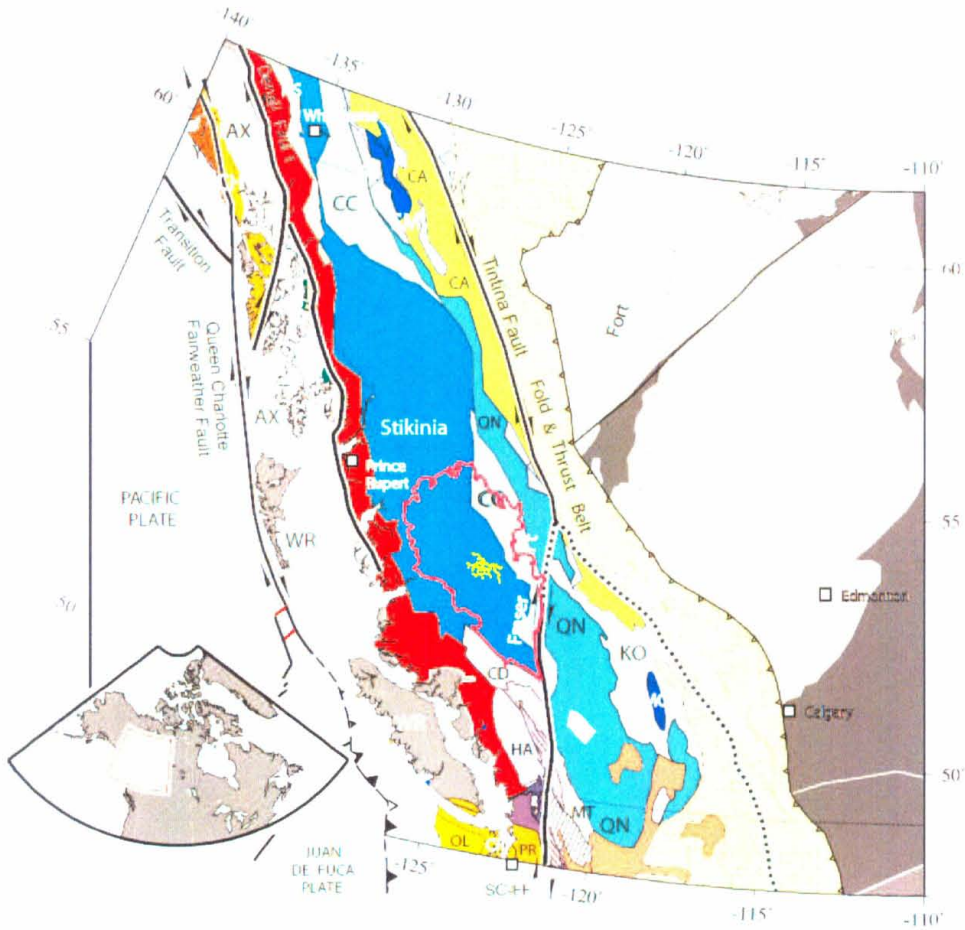

Figure 1.2: Map displaying layout of the geological terranes in the Canadian Cordillera (Hammer and Clowes, 2007). See Fig. 1.1 for location of Nechako Basin. The Intermontane belt overlies parts of Stikinia, Cache Creek (CC) and Quesnellia (QN).

1.2.2 Canadian Cordillera

The formation of the tectonic structure of western Canada is characterized by episodes of subduction, oblique convergence, and transcurrent faulting (Hammer and Clowes, 2007). The resulting orogeny along this margin has produced a series of mountain ranges and basin complexes. One such basin complex lies in the Intermontane Belt, which contains the Nechako Basin seen in Fig. 1.2.

The terranes in the Intermontane Belt represent the accretion of multiple island arcs and oceanic plate materials, as well as igneous extrusion during several volcanic episodes. This makes for an interesting assortment of geological assemblages and structures.

1.2.2.1 History of West Coast of Laurentia

By the late Proterozoic the Precambrian mountain range comprising the Canadian shield had been flattened by erosion and Laurentia was part of Rodinia. The Foreland Belt – made of the foreland basin and the Rocky Mountains in the Canadian Cordillera – contains limestone, sandstone, and shale sediment which was deposited during the Cambrian rifting of Rodinia. This rifting is shown in Fig. 1.3.

In Late Proterozoic to Devonian marine deposition occurs on the new continental margin (Fig. 1.4). Then in the Devonian a volcanic island arc forms at what is now western Laurentia. The passive margin also becomes convergent, shown in Fig. 1.5.

From Devonian to middle Jurassic Pangea reconnects (Fig. 1.6). A succession of Mesozoic island arcs form offshore Laurentia, separated from the craton by a back arc basin, composed of oceanic lithosphere with deep water deposition. This island

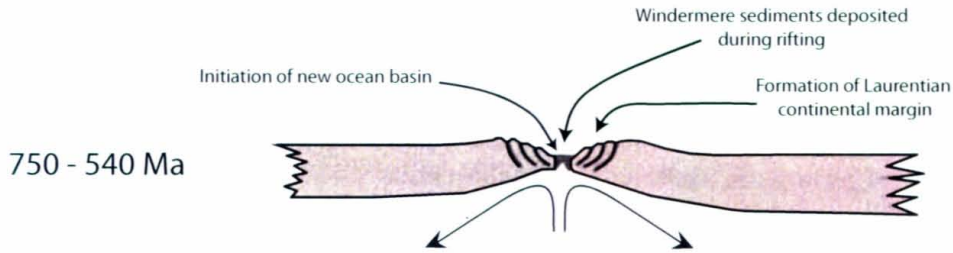

Figure 1.3: Rifting of Rodinia and formation of a new ocean along off present day western Laurentia (Mathews and Monger, 2005).

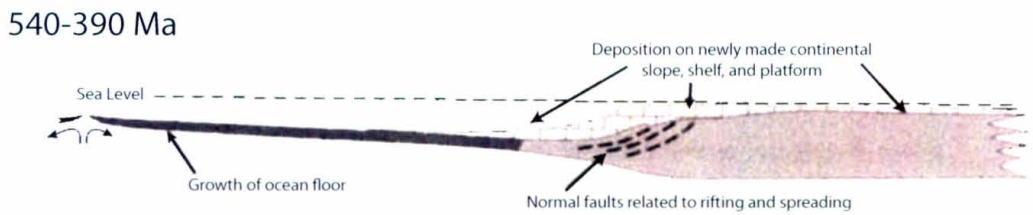

Figure 1.4: Deposition on new continental margin during late Proterozoic to Devonian (Mathews and Monger, 2005).

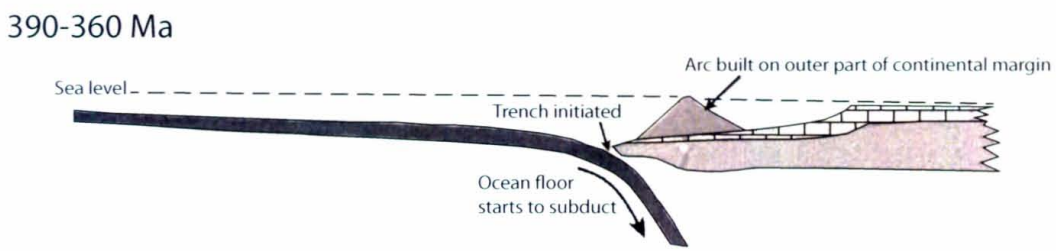

Figure 1.5: Convergence begins in Devonian and magmatic arc appears (Mathews and Monger, 2005).

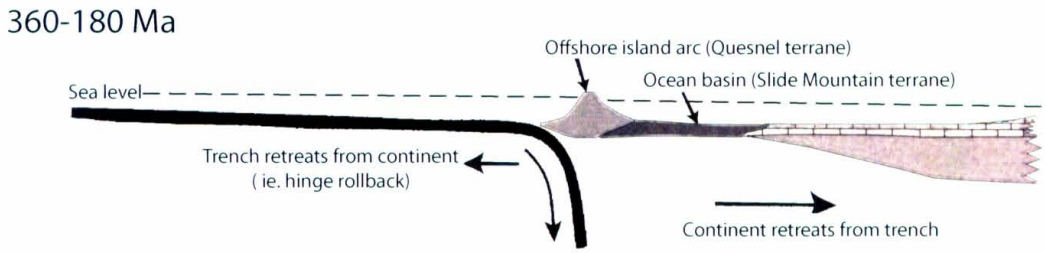

Figure 1.6: Extension creates ocean basin between island arc and continent. Continent converges with Pangea (Mathews and Monger, 2005).

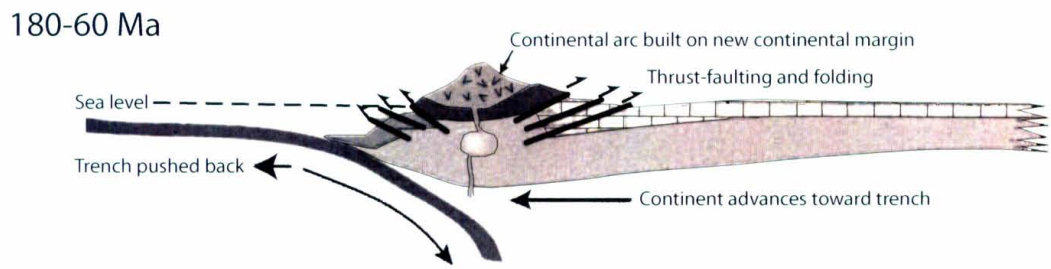

Figure 1.7: Convergence reinitiated, accretion and orogeny shape western Laurentia (Mathews and Monger, 2005).

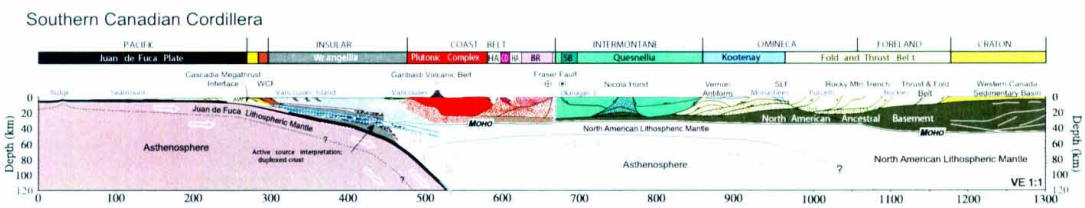

Figure 1.8: Present day margin of western Laurentia (Hammer and Clowes, 2007).

arc and back arc basin will later be accreted to Laurentia forming the Quesnel and Slide Mountain terranes respectively (Mathews and Monger, 2005). The Cache Creek terrane originated from an oceanic platform in the forearc, on the western side of the passive margin with Quesnellia (western Laurentia). Stikinia is even further west of these terranes in the ancient ocean, Panthalassa (Hannigan et al., 1994).

In the Cretaceous the convergent margin is reactivated, continuing accretion and orogeny (Fig. 1.7). During the Eocene the Fraser Fault was activated (Jones et al., 1992) in the east of the Nechako Basin. The Fraser Fault resulted from a split of the Tintina Fault (a major fault system givingway with 425 km of dextral slip since the Paleocene) into this fault and the Rocky Mountain Trench (Hammer and Clowes, 2007). To the west of the Nechako Basin, the Yalakom Fault accomodates 115 km of dextral slip motion between Late Cretaceous to Late Eocene (Umhoefer and Kleinspehn, 1995).

1.2.2.2 The Beginning of the Foreland Belt

The Foreland Belt is a fold and thrust belt in the east of the Canadian Cordillera overlying ancestral North America. Obduction of the Quesnellia and Slide Mountain terranes onto the west coast began in 187 Ma (Fig. 1.7), spawning uplift in the Omineca Belt (Evenchick et al., 2007). The Omineca Belt is the suture zone between the terranes of the Intermontane Belt and those of the Foreland Belt (Hammer and Clowes, 2007). Middle Jurassic subsidence in the foreland basin began shortly after uplift in Omineca with sediment infill from the western metamorphosed highlands. In mid-Cretaceous real deformation begins with fold/thrust belt structure appearing still accompanied by sedimentation from Omineca and the rising Rocky Mountains.

The major period of deformation took place during late Campanian to early Eocene along with fast, coarse clastic sediment deposition into the foreland basin.

1.2.2.3 Formation of the Intermontane Belt

In late Triassic the margin is reactivated and the island arc comprising Cache Creek begins to subduct under the continent of Laurentia. The convergence drives the amalgamation of Slide Mountain, Quesnellia, Cache Creek, and Stikinia onto west coast Laurentia. The Skeena and Stikine Arches which divide the Bowser Basin from the Nechako Basin rose in Lower to middle Jurassic. The accretion of the terranes in the Intermontane Belt ended in middle Jurassic (Mathews and Monger, 2005).

In late Jurassic, uplift occured in western Quesnellia due to accretion of the terranes currently in the Insular Belt, which also caused uplift on the Slide Mountain Terrane. This episode was accompanied by widespread erosion and a major Early Cretaceous unconformity along the cordillera. A subsequent mid-Cretaceous uplift provided sedimentary material for the deposition of the Aptian to Cenomanian Skeena Group in the cordillera and the western-most part of the Nechako Basin (Mathews and Monger, 2005).

In Late Cretaceous, after cessation of accretion, westerly derived marine and non-marine deposition is recorded by Paleocene sediments of the Nechako Basin. Then in Mid-Eocene extension took place with sedimentation in extensional basins overlain by the extrusive volcanics of the mid-Eocene volcanic episode. Extensional tectonics have persisted until recent time, causing block-faulting with non-marine deposition in the graben valleys (Mathews and Monger, 2005).

1.2.3 Volcanism in the Intermontane Belt

Two main volcanic excitations have dominated the geology in the Intermontane Superterrane since the end of the Paleozoic – one in the Eocene, the other during the Neogene. Eocene volcanism in the Nechako Basin is represented by the Endako and Ootsa Lake formations while the Neogene is recorded by the Chilcotin formation.

The Eocene volcanic Princeton group was deposited in fault bounded valleys and grabens, indicating that volcanism during this time likely reflects the historical topography (Ickert et al., 2009). It has been suggested by Engebretson et al. (1985) that this massive volcanism during early Tertiary was due to a subcontinental breakage in the subducting plate, or a 'slab window' as described by Dostal et al. (2003) and shown in Fig. 1.9

1.2.4 Formations and Groups

Following is a listing of geological divisions which have been made by various geoscientist working in the area.

1.2.4.1 Smithers Formation

Deposited in a shallow marine setting, this formation consists of feldspar greywacke, arkosic arenite, and siltstone. This sequence has low amounts of organic carbon and therefore low hydrocarbon source rock potential (Riddell and Ferri, 2008).

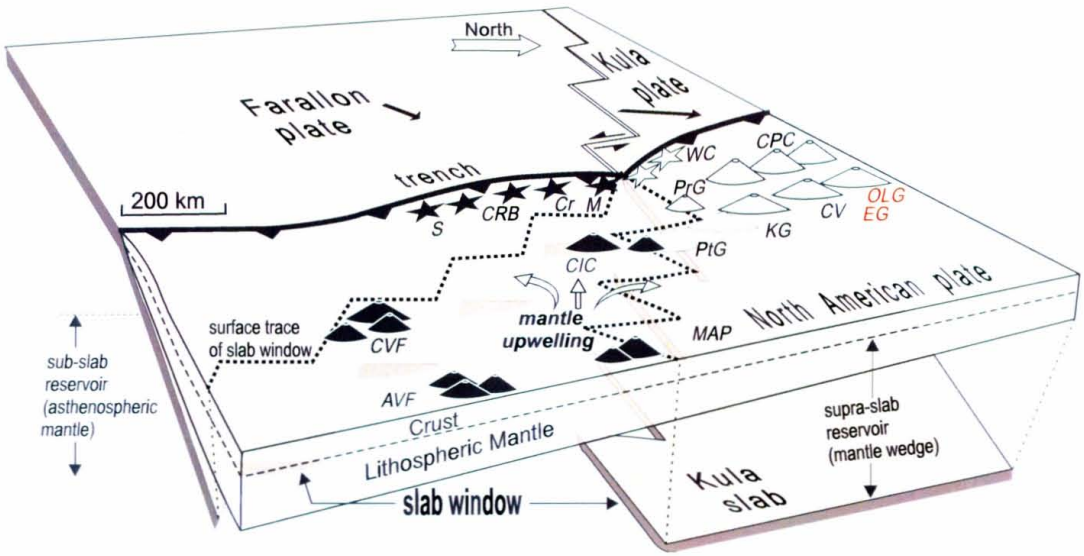

Figure 1.9: Breakage between the Kula and Farallon plates takes place at the approximate location of the Canada-USA border (Engebretson et al., 1985). A slab window is one explanation for elevated levels of volcanism in early Tertiary. After Dostal et al. (2003): Endako and Ootsa Lake groups shown in red lettering.

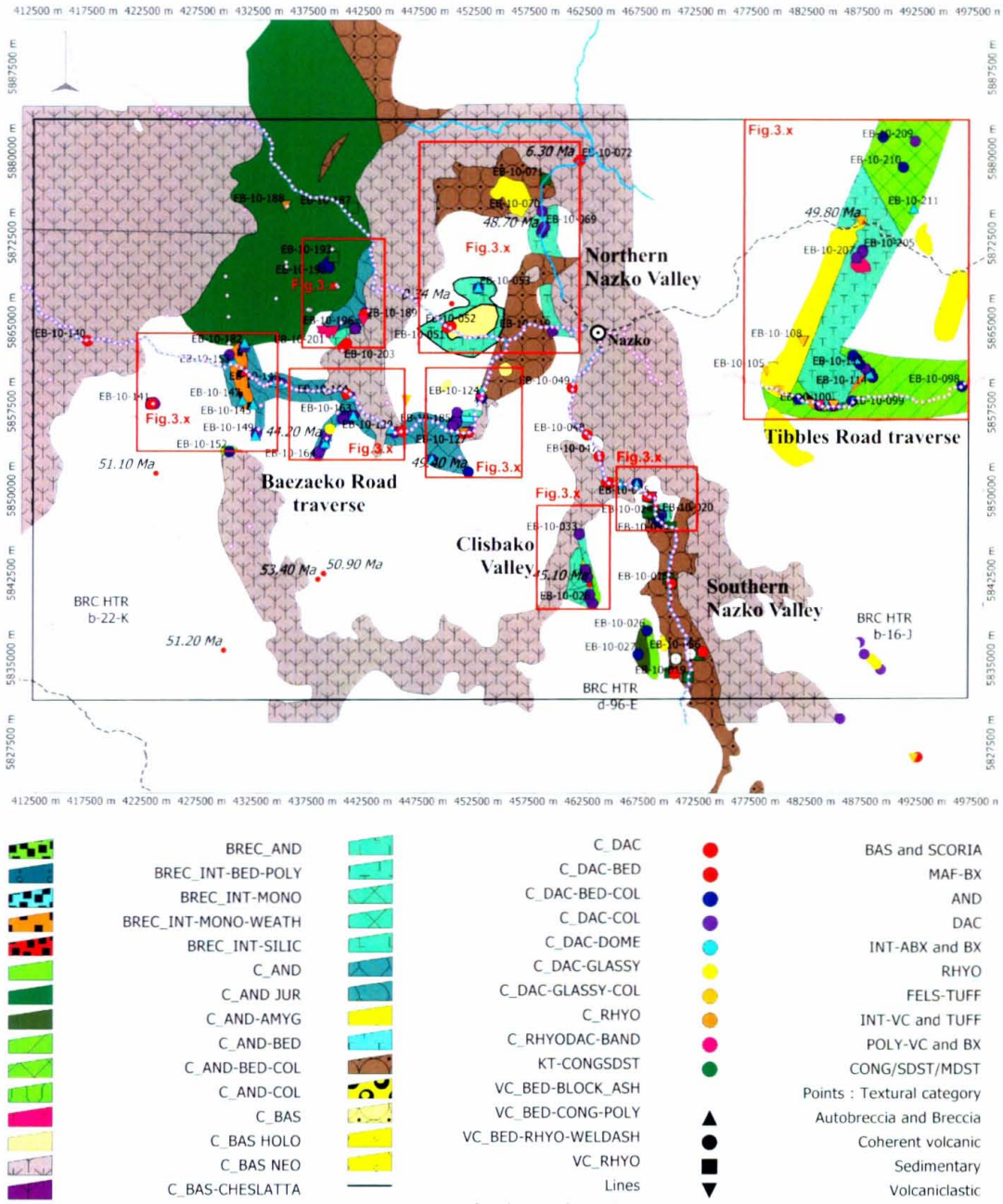

Figure 1.10: Geology map of Eocene volcanics from Bordet et al. (2011). For comparison with surface conductivities in Fig. 7.11.

1.2.4.2 Ashman Formation

This mid to late Jurassic formation is mostly dark grey to black shale with some lesser coarse clastics. Ashman shales have good carbon content with maturation in the oil to gas window. Beds seen as good source rock in the Bowser basin are thinner in the Nechako Basin with poorer quality of organic material. All in all, Ashman rocks are in the "fair" range for hydrocarbon potential (Riddell and Ferri, 2008).

1.2.4.3 Skeena Group

The Skeena Group is comprised of marine sedimentary, non-marine sedimentary, and volcanic rock. It is dominated by a basaltic volcanic sequence overlain by interbedded fine-grained sanstone and shale. The sandstones have low reservoir potential but the shales have good amounts of organic carbon (Riddell and Ferri, 2008).

The Skeena group was desposited in early Cretaceous, after uplift and erosion of the Skeena Arch. Lower portions of this group typically contain a lot of detrital muscovite and have been a known producer of coal (Palsgrove and Bustin, 1990). During interpretation of 2D inversion models Spratt and Craven (2010) assigned a resistivity to this unit lying mostly in the range of 10-100 Ω m.

1.2.4.4 Princeton Group

This group in the Intermontane Superterrane resulted from an intense early magmatic event. The Princeton group basement is mostly Mesozoic arc and Paleozoic oceanic rock. Volcanics in this assemblage are tuff, breccia, and lava of basaltic andesite to rhyolite composition. Meanwhile sedimentary portions consist of conglomerate,

sandstone, siltstone, and coal (Ickert et al., 2009).

1.2.4.5 Kamloops Group

Lying north and east of the Princeton group, this assemblage is made of mafic, intermediate, and felsic arc-like material and non-marine sedimentary rock (Ickert et al., 2009).

1.2.4.6 Chilcotin Group

The Chilcotin group is made of basaltic flows with some hyaloclastite tephra and pillow basalt. In the Nechako Basin this group overlies Cretaceous to Eocene sedimentary rock. Large volumes of basalt flooded over the area with break periods between volcanic events indicated by zones of oxidations and soil formation in the layering (Ickert et al., 2009). This group is Neogene in age and was formed as a series of extensive plateaus etched with deep river channels. The estimated coverage area of Chilcotin basalt is 36 500 km^2 (Farrell et al., 2007).

The Chilcotin Group is underlain by Paleozoic-Mesozoic basement. In the Quesnel trough this basement is the Nicola group volcanic and Copper Mountain suite plutonic rock. In the Nechako Basin this is Cretaceous-Eocene sedimentary rocks. This Neogene group is overlain by Pleistocene glacial deposit, exposed in valleys and canyon walls. Canadian Hunter logs in the Nechako Basin show this basalt to have a resistivity of >1000 Ω m (Spratt and Craven, 2010) and Hayward and Calvert (2009) estimate the group's P-wave velocity between 1500 and 2500 m/s. This group is labelled as C_BAS_NEO in Fig. 1.10.

1.2.4.7 Endako Formation

The Endako group is comprized of andesitic basalts and basalt flows, also pyroclastic rocks, lava flows and sedimentary rocks in some regions, all Eocene in age (Bordet et al., 2011). Interpretation of resistivity models in Spratt and Craven (2010) show this formation have resistivity of 20-2000 Ω m. Hayward and Calvert (2009) estimate the P-wave velocity of these rocks to be between 2400-3400 m/s.

1.2.4.8 Ootsa Lake Formation

The Ootsa group is 54-48 Ma in age (Ickert et al., 2009), and is composed of rhyolite flows, lesser volumes of basalt, andesite, pyroclastic, and sedimentary rock (Diakow and Mihalynuk, 1986). Spratt and Craven (2010) interpret 2D resistivity subsections to show around 20-2000 Ω m for these volcanics.

1.2.4.9 Bowser Lake Group

The Bowser Lake Group consists of basaltic to rhyolitic composition. It was deposited in Stikinia during Early to Mid-Jurassic from volcanic chains to the east and the west. These chains were separated by a marine and non-marine basin created during extension in Stikinia. After cooling of the region, the Cache Creek oceanic plate subducted under eastern Stikinia and was accreted to it (Evenchick and Thorkelson, 2005).

This group is composed of both marine and non-marine shale, siltstone, sandstone, congelomerate, and some chert clasts from the Cache Creek terrane. The Bowser basin was the depocenter during amalgamation of Stikinia and Cache Creek. The group

is distinguished from older and younger strata by a lack of metamorphic detritus (Evenchick and Thorkelson, 2005). Lowe et al. (2006) measured a mean density of 2611 kg/m^3 and a mean magnetic susceptibility of 0.265 $\times 10^{-3}$ SI in the Bowser basin.

1.2.4.10 Hazelton Group

These volcanic and sedimentary rocks are dated Triassic to Early-Middle Jurassic (Best, 2004), with the island arc material at the upper end (Riddell et al., 2007). Lowe et al. (2006) determined that Hazelton group rocks have a mean density of 2611 kg/m^3 and mean magnetic susceptibility of 0.1590 $\times 10^{-3}$ SI in the Bowser basin. Spratt and Craven (2010) interpret these rocks to have a resistivity of $>1500\Omega$ m.

1.2.4.11 Taylor Group

This Albian group contains conglomerate, black shale, siltstone, and sandstone (Ferri and Riddell, 2008). These rocks can be found in the study area around the Nazko River and were deposited during the uplift of oceanic and arc rock resulting from the accretion of the Insular Superterrane. Shale from this group has source rock potential, and its sandy units have reservoir potential. Spratt and Craven (2010) used borehole measurements and 2D inversion models to estimate resistivities in the range of 10-100 Ω m

1.2.4.12 Quaternary

The Nechako Quaternary deposits are till, lacustrine clay, and gravel, with some volcanics (Riddell et al., 2007). Lowe et al. (2006) measured the mean density of

the Quaternary drift in the Bowser basin to be 2785 kg/m^3 and mean magnetic susceptibility at 6.231 $\times 10^{-3}$ SI. Hayward and Calvert (2009) estimate the P-wave velocity of Quaternary drift in the Nechako Basin at around 2500 m/s.

1.3 Geophysics in the Area

Geophysical surveys and drilling have been done in the Nechako Basin since the 1930's but with no petroleum production to date (see Calvert et al. (2008)). One well in 1931, several in the 1950's, and one in 1981 all reached a depth of 500-600m with no oil. Honolulu Oil Co. began exploration in the area in 1959 and drilled in 1960. Hudson's Bay Oil and Gas Company drilled a 1300m hole in the same year. The last hole drilled before Canadian Hunter entered the scene was done by Texalta in 1972. Amoco Canada did a magnetic susceptibility survey in 1969 but Canadian Hunter performed the most exploration in the basin area: two years of seismic and gravity from 1979 to 1980 and 5 wells drilled by 1985. None of these companies were able to locate significant amounts of oil and most oil and gas exploration was abandoned in 1986 when Hunter did not find any economic deposits (Calvert et al., 2008).

The Geoscience BC-funded Nechako Project has reviewed these data and has carried out new geophysical surveys. The surveys began in 2004 and included new gravity and magnetic data in 2004, a heat flow study, a passive seismic survey in 2006, and a MT survey in 2007 (Ferri and Riddell, 2008), the data from which are studied in this thesis (specifics of this survey discussed next in § 1.3.1). The gravity survey was done along Big Creek across the Nechako Basin (Best, 2004). A drop in Bouguer gravity toward the center of the basin has a width of 800 m and measures 3-4 mGal.

This could be a paleochannel, perhaps a fault related graben filled with sedimentary rock. This gravity anomaly could, however, be explained with a change in volcanic rock. The magnetic survey was also presented by Best (2004). Magnetic variations were interpreted as deeper features, and lined up with the gravity low. This could indicate a magnetic basement below sedimentary rock. After a preliminary review of these data a vibroseis survey was done in 2008 (Calvert et al., 2008).

Previously, regional 2D modelling was done on MT data by Ledo and Jones (2001). They found a generally resistive (1 000 - 30 000 Ωm) upper crust (10 km depth) with a conductive (1 - 200 Ωm) lower crust (10 - 40 km depth). Site density was insufficient to determine small scale local variations on the order of features in the Nechako basin, their targets were crustal scale and tectonic features.

1.3.1 The Nechako Basin MT Data-Set

Data were collected at 734 sites (see Fig. 1.11) along different lines within the Nechako Basin with a 500 - 1000m spacing (Geosystem-Canada, 2007). AMT, MT, and telluric sites were set up with AMTC-30 Phoenix induction coils (bandwidth 10000 - 1 Hz), MTC-50 Phoenix coils (bandwidth 400 - 0.00002 Hz) (Phoenix-Geophysics, 2008), and telluric dipole length of 50m (Geosystem-Canada, 2007). Recording location and time were measured by a GPS antenna attached to the MTU5a unit which collects and stores signals from all acquisition hardware. Man-made noise was almost non existent with the occasional passing vehicle as the only source. Data were processed within 48 hours of collection by Geosystem using remote referenced robust techniques implemented in Phoenix Geophysics' MT2000 software package (Spratt and Craven,

2008). These data were planned along pre-existing seismic lines around the town of Nazko (see Fig. 1.11). Sites were organized in 8 profiles for 2D inversion, with infill in the northern group for a 3D inversion.

1.3.2 2D Inversion of Nechako MT Data

Sites concentrated along the roads and seismic lines for profiles A (137 sites included), B (80 sites included), C (101 sites included), D (162 sites included), E (25 sites included), F (58 sites included), and G (69 sites included), were inverted for 2D conductivity sections, omitting line H and the other 62 infill sites (Geosystem-Canada, 2007; Spratt and Craven, 2010). Both the TE and TM modes were used in the inversion process with models produced after 100 iterations for each profile (Spratt and Craven, 2010). The profiles have a general structure of a surface resistor (>500 Ω m), underlain by a shallow conductor (<100 Ω m), with a resistive basement (>300 Ω m). In general these inversion models are interpreted to show resistive surficial volcanic rock, underlain by Cretaceous sediment (Spratt and Craven, 2011). In profile A (Fig. 1.12), sedimentary rock is seen across the section (indicated by 2a/b). Surface Chilcotin Basalt, labelled by 1, overlies the Cretaceous sedimentary package. A mid-crustal conductor rises lower in the section in the same location as previous micro-seismic activity, and is interpreted as possible partial melt. Similar structure is seen in profiles B and C, with thicker sedimentary rock in B (see Fig. 1.13 and 1.14). MT was able to distinguish between the Cretaceous sedimentary and Eocene volcaniclastic lithologies and may therefore be able to point out targets of interest for hydrocarbon exploration (Spratt and Craven, 2011).

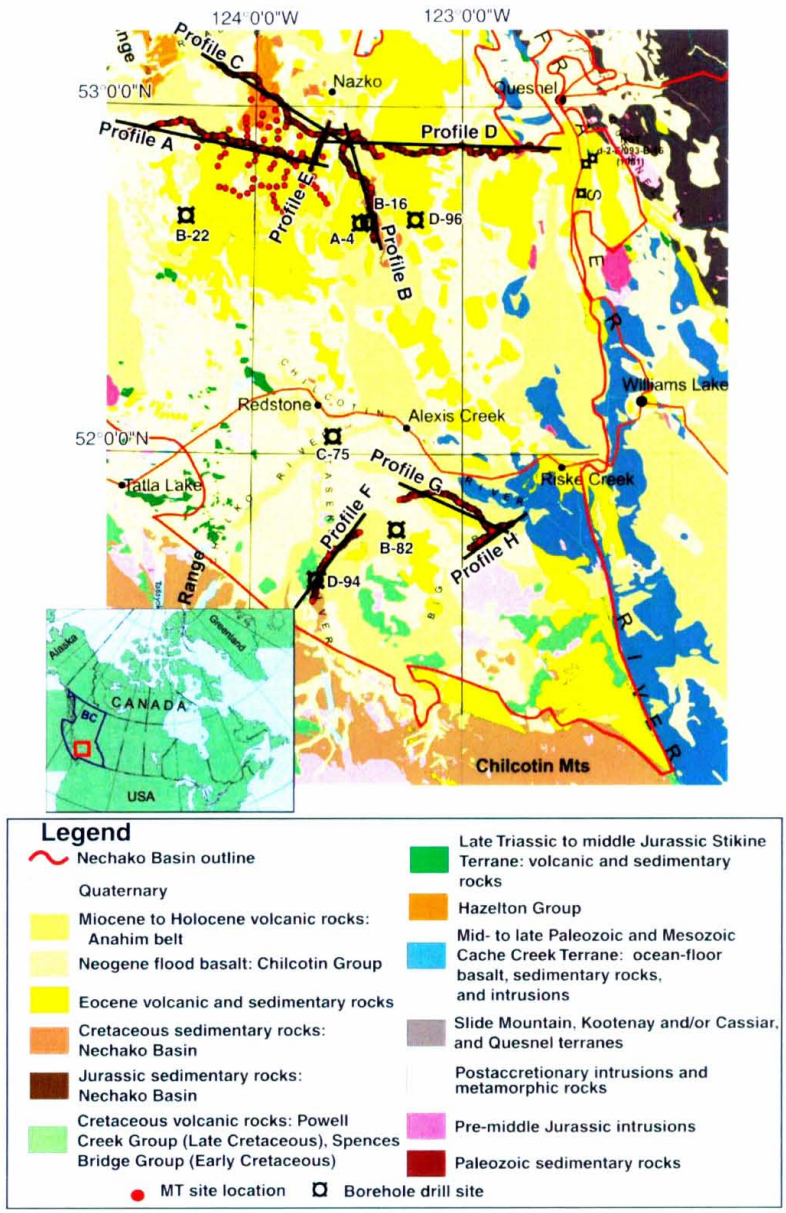

Figure 1.11: Location of MT sites in survey studied in this thesis superimposed on a geology map of the area, after Spratt and Craven (2010).

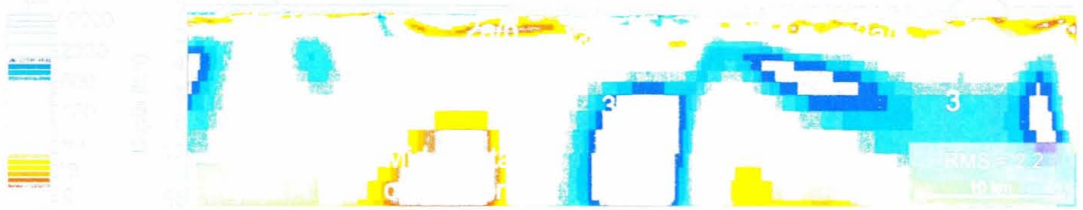
3
3
RMS = 2.2
10 km

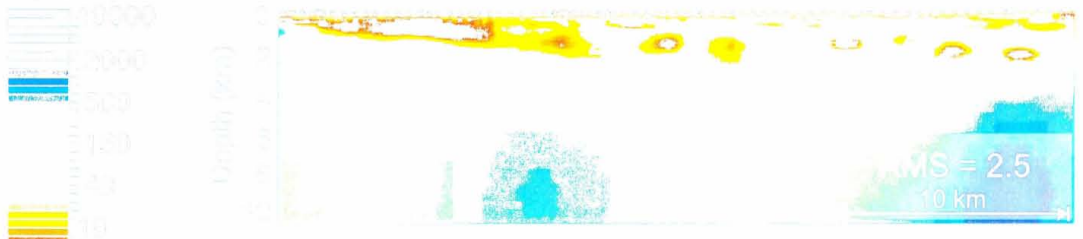
RMS = 2.5
10 km


Profile C
RMS = 1.8
10 km

1.4 Preview of Layout

In the coming chapters of this thesis, MT and geophysical inversion methods will be used to develop a 3D conductivity structure for interpretation. Following this chapter the MT method will be described starting with the source energy used for measurement, theoretical background, and data acquisition techniques. After this description two previous examples of the use of MT in hydrocarbon exploration will be presented.

In Chapter 3 the forward modelling portion of the inversion process will be presented, starting with the one dimensional case. The finite difference method will then be applied to the 1D Maxwell Equations before moving into the three dimensional case. In Chapter 4 the inversion process will be explained starting with an analogy with curve fitting, then an outline of the Marquardt-Levenberg and minimum structure inversion methods. Continuing the modelling theme, Chapter 5 will examine the Particle Swarm Optimization method: how it works, using it to find a point, then modelling MT responses with both synthetic and real data.

Chapter 6 provides a detailed walkthrough of the steps required for data selection and formatting in order to start an inversion. Chapter 7 presents the resulting inversion models and the interpretation of them via comparison with other types of data and models. Finally, Chapter 8 summarizes the findings of the thesis and draws conclusions from the modelling results.

At the end of this thesis several appendices explain the impedance rotation that was used (Appendix A), a source code directory on cd-rom (Appendix B), present a comparison of observed and predicted data for the main model (Appendix C), and

present a listing of results for other models (Appendix D).

Chapter 2

Magnetotellurics

The magnetotelluric method (MT) uses natural sources of electromagnetic radiation to excite responses in the Earth and estimate its physical properties. This method has a broad range of exploration depths, from hundreds of metres to hundreds of kilometres (Simpson and Bahr, 2005). MT can work well in places which cannot be explored by seismology because of high acoustic impedance contrast and acoustic scattering in overlying horizons. These include areas characterized by salt, carbonate, and volcanic layers (Constable et al., 1998). It is also good for geothermal exploration, detecting mineral concentrations, porosity, and fluid properties in rocks (Simpson and Bahr, 2005).

In the following sections several concepts necessary for understanding the MT method will be described. Beginning with the naturally sourced energy, its characteristics will be laid out as well as a list of assumptions and approximations necessary for the mathematical analysis used in this method. In order to understand the physics behind MT, the response in a "homogeneous half-space" (an earth with uniform con-

ductivity) will be examined, then for a layered or one dimensional case, followed by the two and three dimensional cases. Once the underlying concepts have been presented, data acquisition and the basics of processing into the frequency domain will be described. Finally previous uses of MT for hydrocarbon exploration will be examined along with a couple of cases comparable to the topic of this thesis.

2.1 Sources

Part of the attractiveness of MT is its source, which is the omnipresent (with some dependence on latitude) and naturally varying geomagnetic field (Vozoff, 1987). The quality of the collected data depends on the frequency band being examined and the amount of ambient electromagnetic noise resulting from man made sources. Typically frequencies from electrical storms, which occur regularly, fall in the 1-10^5 Hz range. Frequencies below 1 Hz stem from hydromagnetic waves in the magnetosphere and ionosphere (Simpson and Bahr, 2005). At the overlap of these two frequency ranges there is a band of low natural electromagnetic activity called the "dead zone" at 0.1 to 2.0 Hz (Orange, 1989). There is also another zone of low power from 1000-2000 Hz (Vozoff, 1987). The ionosphere is a highly conductive layer which exists because pressures are low enough that ions do not recombine as in the lower atmosphere and ion number densities are high enough to maintain a sufficient amount of free charges (Simpson and Bahr, 2005). The magnetosphere lies outside the ionosphere where the Earth's magnetic field and its interaction with the solar wind govern the behaviour of matter present in this outer atmospheric layer (Siingh et al., 2004). Due to the inclination of the Earth's rotational axis toward the sun and variation in frequency of

electrical storms throughout the year, there is a seasonal dependence on natural source strength which is generally taken into consideration when planning MT surveys.

The source in the upper atmosphere is a complex system of flowing plasmas and fluctuating input of solar winds (Simpson and Bahr, 2005) composed mostly of neutral hydrogen and protons (Siingh et al., 2004) as depicted in Fig. 2.1. Solar winds fluctuate with the periodicity of sunspots, which follow an 11-year cycle (Labitzke, 2001). Energy is put into the system in the magnetopause (10-12 Earth radii out) on the sun-ward side (Siingh et al., 2004). This creates a combination of chaotic behaviour and some localized periodic behaviour. Fields reaching Earth from the upper atmosphere have travelled through both the ionosphere and the insulatory lower atmosphere, attenuating the vertical components of electric and magnetic fields, leaving their horizontal components (Simpson and Bahr, 2005).

A spheric is an electromagnetic impulse originating from a flash of lightning, which consists of three to four discharges called strokes in a period of 200 to 300 ms (Vozoff, 1987). Signals from spherics travel the whole distance around the globe from their start point (Simpson and Bahr, 2005), and occur 100-1000 times every second world-wide (Vozoff, 1987). Their trajectory is controlled by the interfaces of high conductivity contrast between the Earth, lower atmosphere and ionosphere, which provide a waveguide. This is the same principle of refraction as in fiber optics except that much more energy is absorbed at the interface and transmitted to the Earth. Snell's law shows the angle of propagation into the Earth (Simpson and Bahr, 2005) (see Fig. 2.2 for explanation):

$$\sin\theta_1 / \sin\theta_2 = v_1 / v_2 >> 1 \tag{2.1}$$

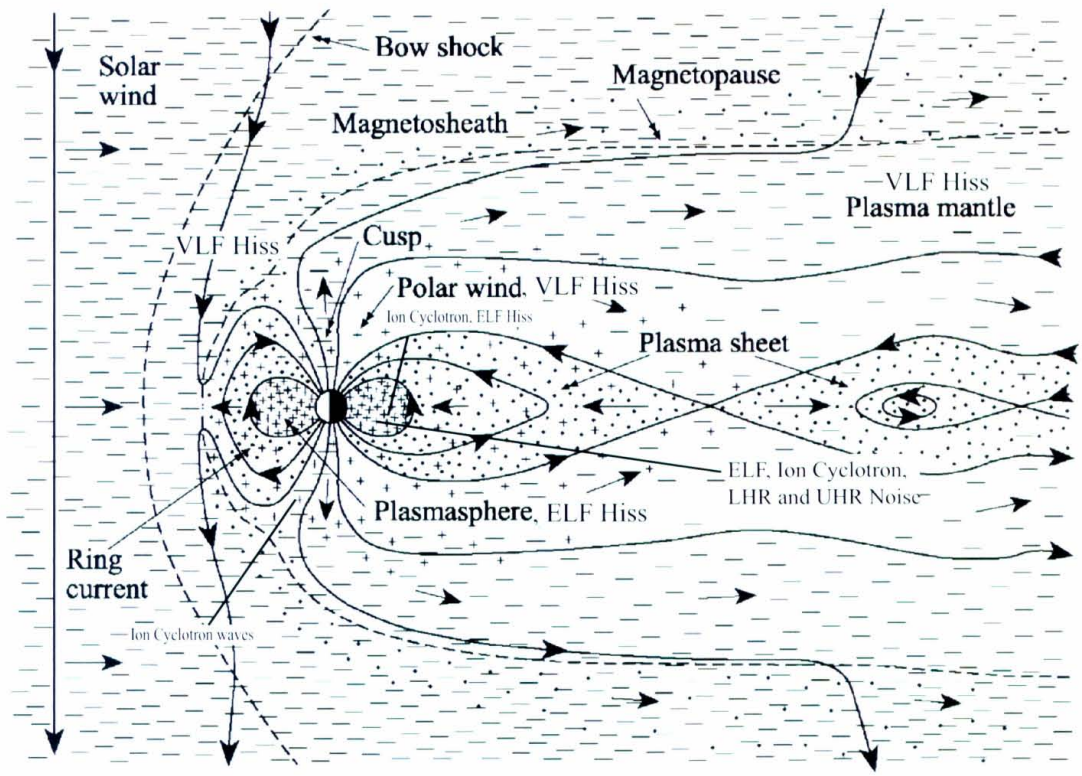

Figure 2.1: Illustration of interactions of solar wind/radiation with the Earth's magnetic field. These interactions produce electromagnetic waves which in large part are chaotic but have some localized periodic behaviour. Frequency ranges are: MF – 0.3-3 MHz, LF – 30-300 kHz, VLF – 3-30 kHz, ELF – 3-3000 Hz, ULF – <3 Hz, LHR and UHR stand for "lower hybrid resonance" and "upper hybrid resonance" respectively and both reside within the VLF band (Vozoff, 1987). After Vozoff (1987) and Cowley (2007).

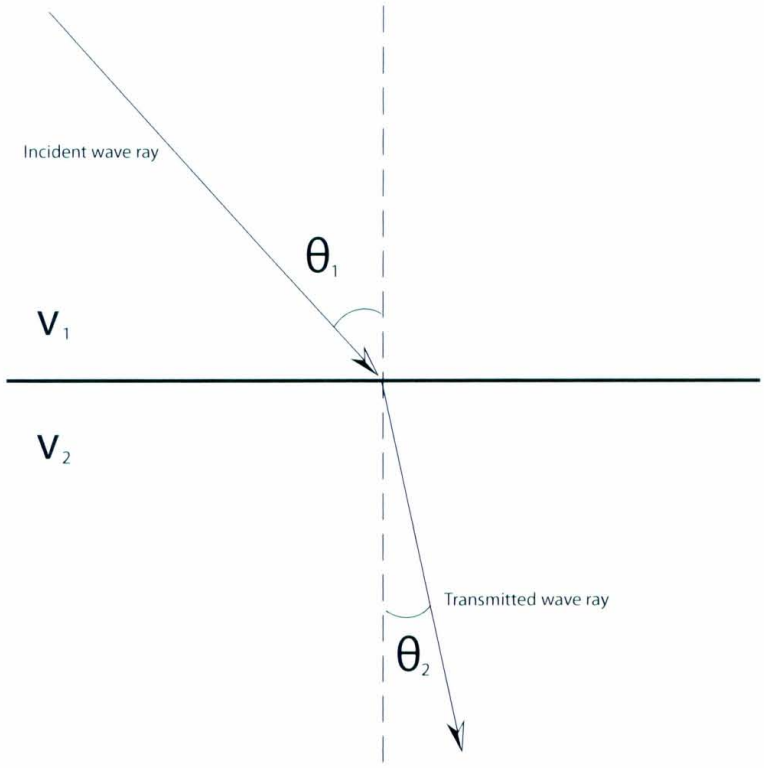

Figure 2.2: Depiction of Snell's law in accordance with eq. 2.1.

The component of the Poynting vector ($\mathbf{S} = 1/\mu_0 \mathbf{E} \times \mathbf{B}$ (Griffiths, 1999)) associated with signals passing through the interface is nearly vertical. Since $\mathbf{E}$ and $\mathbf{H}$ are perpendicular to this vector, the electric and magnetic fields fluctuate in the horizontal plane (given no lateral variation in conductivity). In this way waves at the surface and in the Earth behave approximately the same as the plane waves originating in the magnetosphere. The EM waves from both of these sources have a direction of propagation which deviates from the vertical by at most 1 or 2° (Simpson and Bahr, 2005).

2.2 Theory Behind MT

2.2.1 Assumptions and Fundamental Equations

For the study of MT a set of assumptions is presented in Simpson and Bahr (2005):

- It is assumed that the Earth is not a source for EM energy and only attenuates it.
- Sources may be treated as uniform sheets of current generating plane polarized waves meeting the Earth's surface with normal incidence. Snell's law, eq. 2.1, shows how this is mostly true. This assumption may deteriorate at the equator and poles.
- There is no accumulation of charge in a one dimensional Earth. Charges build up at 2D and 3D inhomogeneities.
- The quasi-static approximation may be used for frequencies characteristic of MT.

In the quasi-static limit: $\sigma >> \epsilon\omega$ (σ is conductivity, ϵ is permittivity, ω is angular frequency), which is opposite the dielectric limit (Vozoff, 1987). For MT measurement frequencies the velocity of the EM wave appears infinite and the fields follow a diffusive behaviour. Another consequence of the quasi-static limit is that magnetic fields from displacement currents become negligible (Berdichevsky and Dmitriev, 2002). The physics of the MT method is governed by Maxwell's equations.

Maxwell's equations in the time domain with the quasi static approximation are as follows:

$$\nabla \cdot \mathbf{D} = \rho_f \tag{2.2}$$

$$\nabla \times \mathbf{E} = -\frac{\partial \mathbf{B}}{\partial t} \tag{2.3}$$

$$\nabla \cdot \mathbf{B} = 0 \tag{2.4}$$

$$\nabla \times \mathbf{H} = \mathbf{J} \tag{2.5}$$

where $\mathbf{E}$ is the electric field, $\mathbf{B}$ is the magnetic field, $\mathbf{D}$ is the electric displacement, ρ_f is the free charge density, $\mathbf{H}$ is the magnetic intensity, and $\mathbf{J}$ is the current density. To convert these equations into the frequency domain perform a Fourier transform:

$$\tilde{\mathbf{F}}(\omega) = \int_{-\infty}^{\infty} \mathbf{F}(t) e^{-i\omega t} dt \tag{2.6}$$

where $\mathbf{F}$ is a given vector function, $i = \sqrt{-1}$. The Fourier transforms for the electric and magnetic Gauss's laws (eq. 2.2 and 2.4 resp.) are trivial. However those for Ampère's and Faraday's laws look a bit different. The following derivations can also be seen in *Electromagnetics* by Rothwell and Cloud (2009). Frequency domain Faraday's law:

$$\int_{-\infty}^{\infty} (\nabla \times \mathbf{E}) e^{-i\omega t} dt = \int_{-\infty}^{\infty} -\frac{\partial \mathbf{B}}{\partial t} e^{-i\omega t} dt$$

Integrating the right-hand side by parts we get:

$$\nabla \times \int_{-\infty}^{\infty} (\mathbf{E}) e^{-i\omega t} dt = \left[\mathbf{B} e^{-i\omega t} \right|_{-\infty}^{\infty} - \int_{-\infty}^{\infty} (i\omega) \mathbf{B} e^{-i\omega t} dt$$

$$\nabla \times \tilde{\mathbf{E}} = -i\omega \tilde{\mathbf{B}} \tag{2.7}$$

Performing a Fourier transform on the general form of Ampère's law for linear media ($\mathbf{D} = \epsilon\mathbf{E}$) (Griffiths, 1999) gives the following:

$$\int_{-\infty}^{\infty} (\nabla \times \mathbf{H}) e^{-i\omega t} dt = \int_{-\infty}^{\infty} \mathbf{J} e^{-i\omega t} dt + \int_{-\infty}^{\infty} \epsilon \frac{\partial \mathbf{E}}{\partial t} e^{-i\omega t} dt$$

$$\nabla \times \int_{-\infty}^{\infty} (\mathbf{H}) e^{-i\omega t} dt = \tilde{\mathbf{J}} + \epsilon \frac{\partial \tilde{\mathbf{E}}}{\partial t}$$

The substitution for current density is made with Ohm's law,

$$\mathbf{J} = \sigma\mathbf{E}, \tag{2.8}$$

and given that $\epsilon \frac{\partial \tilde{\mathbf{E}}}{\partial t} = -i\omega\epsilon\tilde{\mathbf{E}}$, we can write

$$\nabla \times \tilde{\mathbf{H}} = (\sigma - i\omega\epsilon)\tilde{\mathbf{E}} \tag{2.9}$$

The two Gauss equations look similar in both time and frequency domain, unaffected in form by the Fourier transform, with charge density ρ which is the sum of the free charge (ρ_f in eq. 2.2) and the bound charge (ρ_b):

$$\nabla \cdot \tilde{\mathbf{E}} = \rho \tag{2.10}$$

$$\nabla \cdot \tilde{\mathbf{B}} = 0 \tag{2.11}$$

The complex ratio between the horizontal components of $\mathbf{E}$ and $\mathbf{H}$ is defined as the impedance: $\mathbf{E} = \mathbf{Z}\mathbf{H}$. The impedance depends on the resistivity/conductivity structure and the frequency of the incident wave. This tensor is a 2×2 complex valued matrix varying spatially and in frequency.

2.2.2 Homogeneous Half-Space

In a homogeneous half-space, the impedance is given by (Simpson and Bahr, 2005):

$$Z_{xy} = \frac{E_x}{H_y} = (1+i)(\omega\mu_0/2\sigma)^{1/2} \tag{2.12}$$

μ_0 is the permeability (assumed to be that of free space), and σ is the conductivity of the half-space with $Z_{xx} = Z_{yy} = 0$ and $Z_{yx} = -Z_{xy}$. z is positive vertically downwards, y is positive to the east, and positive x is $\pi/2$ radians counter-clockwise (towards the north) as shown in the first step of Fig. **??**. The ratio depends on the resistivity as follows:

$$\frac{1}{\omega\mu}\left|\frac{E_x}{H_y}\right|^2 = \rho \tag{2.13}$$

where ρ is the resistivity of the half-space, depicted in Fig. 2.3. The phase, ϕ, is

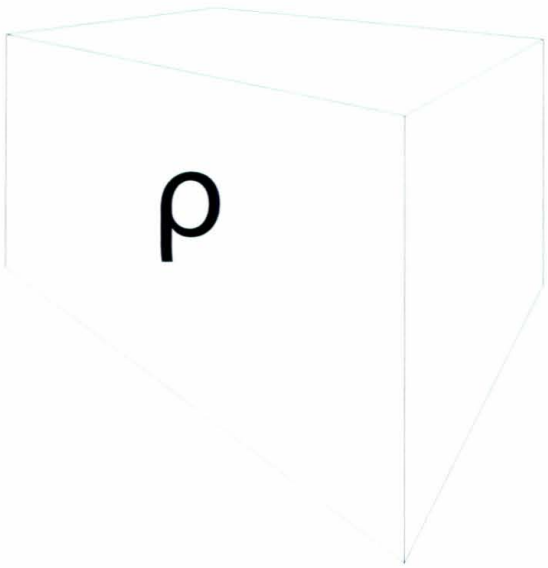

Figure 2.3: Depiction of resistivity, ρ, in a homogeneous half-space. Consistent with Fig. 2.4, 2.6, 2.7.

the phase difference between the undulating components of the electric and magnetic

fields. $\Im(Z_{xy})$ and $\Re(Z_{xy})$ are the imaginary and real components of the xy element of the impedance tensor respectively. The phase in a half space of uniform resistivity is $\phi = \pi/4$.

The relation between the electric field, magnetic field, and frequency is:

$$\mathbf{H} = \frac{k}{\mu_0 \omega} \hat{n} \times \mathbf{E} \tag{2.14}$$

for a plane wave where $k = \sqrt{\frac{\omega\mu\sigma}{2}}(i+1)$ is the complex wave number (Berdichevsky and Dmitriev, 2002), $\hat{n}$ is a unit vector in the direction of $\mathbf{H}$. The imaginary portion of k gives the plane wave a decaying behaviour with depth into the Earth. The skin depth is defined as the depth at which the amplitude of a wave will have attenuated to $1/e$ of its value at the surface. This is achieved when the depth is:

$$\delta = \sqrt{\frac{2}{\omega\mu_0\sigma}}. \tag{2.15}$$

This expression shows that the depth of penetration drops with increasing frequency. As conductivity increases the electric field moves particles around more and more, thus the EM fields lose strength from energy loss moving the charges. Higher frequencies move these particles around more quickly, also causing increasing amount of energy loss.

2.2.3 1D Earth

The logical progression in complexity from a homogeneous halfspace is a one dimensional, i.e. a layered, Earth (see Fig. 2.4). In the one dimensional case the impedance tensor has only one unique component, $Z_{xy} = -Z_{yx}$ (Marti et al., 2009).

The Hertz vector is a vector potential used to describe both the $\mathbf{E}$ and $\mathbf{H}$ fields

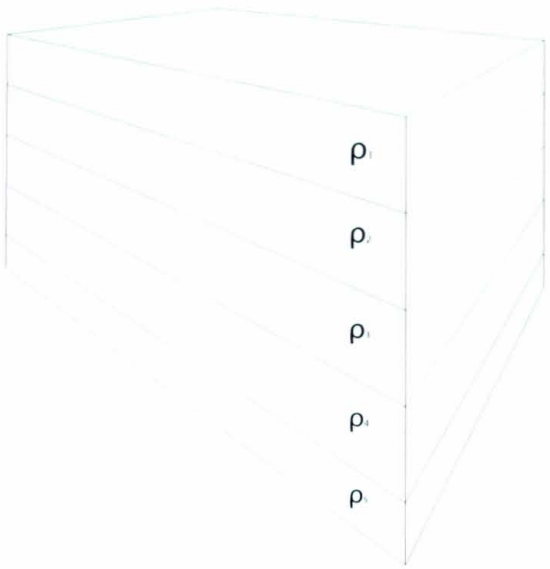

Figure 2.4: Depiction of resistivity, ρ, in a 1D horizontally layered Earth

in a stratified one dimensional Earth, as seen in Cagniard (1952):

$$\mathbf{H} = 4\pi\nabla \times \mathbf{\Pi} \tag{2.16}$$

$$\mathbf{E} = 4\pi\nabla(\nabla \cdot \mathbf{\Pi}) - \nabla^2\mathbf{\Pi} \tag{2.17}$$

Since, in one dimension, $\mathbf{\Pi}$ is proportional to $\mathbf{E}$, the field relationships within a given layer become (Cagniard, 1952):

$$\frac{\partial^2 E_x}{\partial z^2} + i\sigma\omega\mu_0 E_x = 0 \tag{2.18}$$

$$\frac{-i}{\omega}\frac{\partial E_x}{\partial z} = H_y \tag{2.19}$$

In the atmosphere conductivity is assumed to be effectively zero. This results in the second spatial derivative of E_x being null, limiting the change in electric field in the air to a linear one with the magnetic field constant. In the very bottom layer we have a boundary condition that the fields disappear at ∞. This makes sense since we have

already assumed that the Earth itself is not generating waves, only dissipating them. A second boundary condition of a continuous magnetic field tagential to material (layer or body) boundaries also applies.

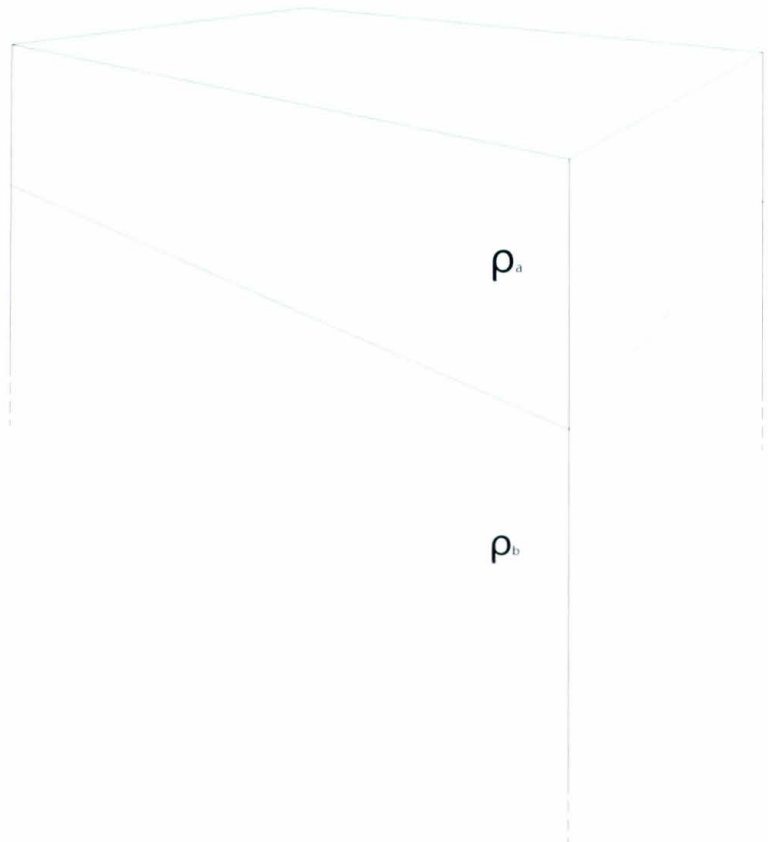

Figure 2.5: Cartoon of a two layered Earth with resistivities ρ_1 and ρ_2 for the upper and lower layers respectively.

In a two layered Earth (depicted in Fig. 2.5), these fields, oscillating into different layers, now see two different resistivities. This changes how the resistivity looks from above from that for a homogeneous half-space which is shown in eq. 2.13. We will not detect ρ_1 or ρ_2, but will obtain some intermediate value, ρ_a. This quantity is called

the apparent resistivity, given in Vozoff (1987) as

$$\rho_{xy} = \frac{1}{\mu\omega}\left|\frac{E_x}{H_y}\right|^2 \tag{2.20}$$

where E_x and H_y are the componenets of the electric and magnectic fields observed on the Earth's surface. The value of apparent resistivity is a measure of how much of each layer the incident fluctuation sees. In one limit where the skin depth decreases to less than the thickness of the top later, the apparent resistivity will tend toward ρ_1. In the other limit where ω drops and the penetration depth reaches far beyond that thickness, $\lim_{\delta\to\infty}\rho_a = \rho_2$.

2.2.4 2D and 3D Earth

In the two dimensional case (see Fig. 2.6) the impedance tensor has two unique components, $Z_{xy} \neq Z_{yx}$, and, when the coordinate system is aligned with geoelectric strike, $Z_{xx} = Z_{yy} = 0$ (Marti et al., 2009). In the three dimensional case (see Fig. 2.7), all complex impedance components are non-zero (Marti et al., 2009). 3D modelling of magnetotelluric data can have several advantages over 2D modelling of data (Siripunvaraporn). Firstly, the Earth is three dimensional so that 3D modelling represents the truest form. Secondly, there is no requirement to make an assumption about strike direction in 3D modelling as opposed to 2D modelling where the response must be separated into TM and TE modes along strike. Higher degrees of freedom in 3D modelling allow three dimensional features to be placed where they belong, instead of 2D modelling needing to place features on profile, skewing their true character and location. Additionally, measurement sites do not need to be projected onto a straight line but can be modelled in place. 3D modelling is, however, more computationally

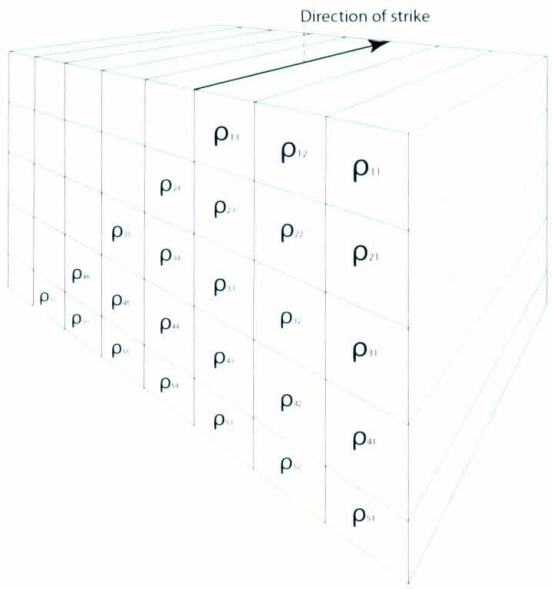

Figure 2.6: Depiction of resistivity, ρ, in a 2D Earth with strike

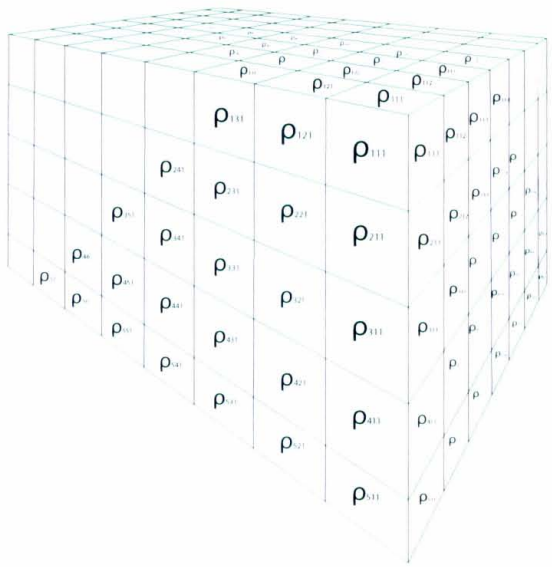

Figure 2.7: Depiction of resistivity, ρ, in a 3D heterogeneous earth

taxing.

2.3 Data Acquisition

The layout of an MT site usually has a north-south aligned electric dipole and an east-west electric dipole to measure the two horizontal components of the electric field. Site layout also includes fluxgate magnetometer or induction coils to measure all three components of the magnetic field (see Fig. 2.8 and 2.9). In the Nechako Basin survey broadband induction coils were used as discussed in §1.3.1. The varying components of the fields are measured as time series and stored on location until measurement is finished. Once the measurement window is done, the data are collected for processing. Processing involves using Fourier transforms to bring the data from a time series into the frequency domain and solving for the impedance tensor elements. Robust processing and remote referencing techniques are used in order to limit noise from sources other than those used in MT (Simpson and Bahr, 2005; Vozoff, 1987).

2.4 MT in Hydrocarbon Exploration

MT has been increasingly used in recent decades for hydrocarbon exploration. The method has been used as a reconnaissance method to plan seismic surveys and as an aid to process seismic data more effectively (Unsworth, 2005). MT has been employed in rough topography due to the portability of the equipment and its low cost when compared with seismic acquisition (Christopherson, 1991). This versatile survey can also provide complimentary information to mitigate ambiguities during geophysical

Figure 2.8: Field work in Morocco with the Dublin Institute for Advanced Studies in 2009. Data were collected to measure depth of water and the surface seismic velocity aspects of MASW measurement. Acquisition and processing time (~2000) was 3 days of struggle from the group as shown.

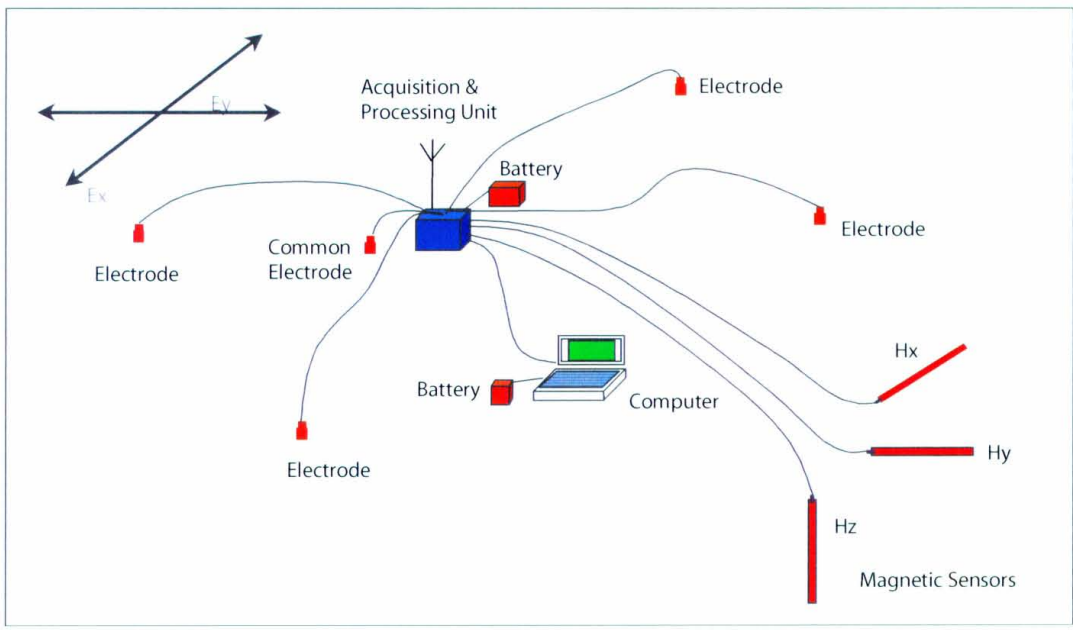

Figure 2.9: Cartoon depiction of a typical site layout when collecting MT data (Geosystem-Canada, 2007).

interpretation. Its primary application in hydrocarbon exploration has been in areas where seismic data is of poor quality (Unsworth, 2005). Marine MT has also been recently increasingly used in hydrocarbon exploration, particularly in the last decade.

2.4.1 MT for Hydrocarbon Exploration in Russia

Russia has been at the forefront in the use and development of MT for hydrocarbon exploration with 100 MT crews actively exploring the great expanse of the USSR during the 1970's. Much of this progress is not openly available, but Spies (1983) has released several case studies in Russian oil fields where EM methods have proved to be useful. These include a first with a layer of sand and clay under limestone, marl, and clay, a second of a salt dome, and a third with an anticline made of clay, siltstone, quartz, and limestone (Spies, 1983). Spies (1983) concludes that EM methods such as MT are useful in identifying structures of interest to oil and gas companies, but also states the induced polarization method may be the most effective of this family.

2.4.2 Case Studies for MT in Hydrocarbon Exploration

Orange (1989) also details several exemplary situations where MT has been paramount in hydrocarbon exploration. These examples, which have been stripped of geographical information, use MT as a reconnaissance tool, where it is used to obtain a preliminary description of features suggested by gravity and magnetic anomalies. Seismic surveys were then planned based on the MT results. The second case in Orange (1989) involves an area with volcanic cover which was blinding the seismic reflection method. MT was used to trace known reservoir units under a mountain range follow-

ing indicators from gravity and magnetic data. The interpretation of the inversion models produced from the MT data showed a faulted sedimentary unit continuing under the mountain and this interpretation was successfully substantiated by drilling. The third example is a thrust fault problem in which drilling encountered an unconformity which could either be explained by a thrust fault or a lack of the Mesozoic, potentially hydrocarbon bearing, rocks. MT was used to clarify the subsurface structure and make the decision whether or not to continue drilling. The MT results suggested a thrust fault situation, confirmed in the subsequent drilling, in which the Paleozoic sequences had been thrust over the Mesozoic rocks (Orange, 1989).

2.4.3 MT in Papua New Guinea

In Papua New Guinea a large MT survey was used by Christopherson (1991) to find the depth and thickness of Darai limestone in the Papuan fold belt (see Fig. 2.10). In addition to the seismic impediment of carbonates and folding, the topography of the area varied from 0 to 5000 metres above sea level. The island was blanketed in 500 MT stations on 32 profiles with a site spacings of between 400 and 2500 m.

The Darai limestone is Eocene to Miocene in age and extensively folded and thrusted. Underlying the up to 1000 m of limestone is a mid-Mesozoic clastic deposit which is up to 10 000 m thick. Hydrocarbon traps are provided by the complex folding in the area.

The data were interpreted with a 2D finite element solver which included topography in order to find the base of the Darai limestone. The conductivity model that was produced for one of the survey lines is shown in Fig. 2.11. The approximate

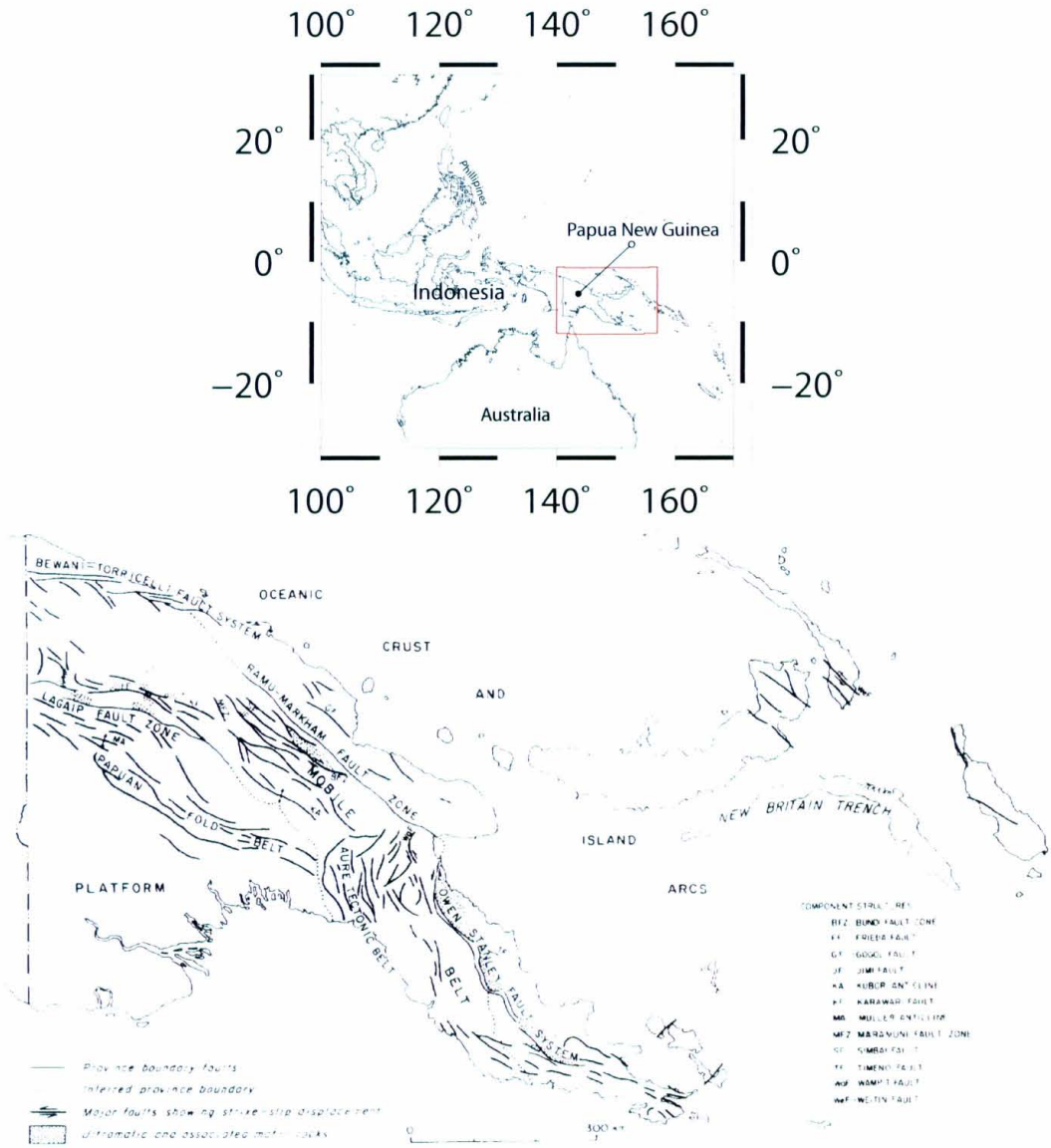

Figure 2.10: Tectonic map of Papua New Guinea with inset shown in red, after Christopherson (1991).

location of the anticline below the Darai limestone was seen during modelling of the MT data, a prime target for hydrocarbon exploration.

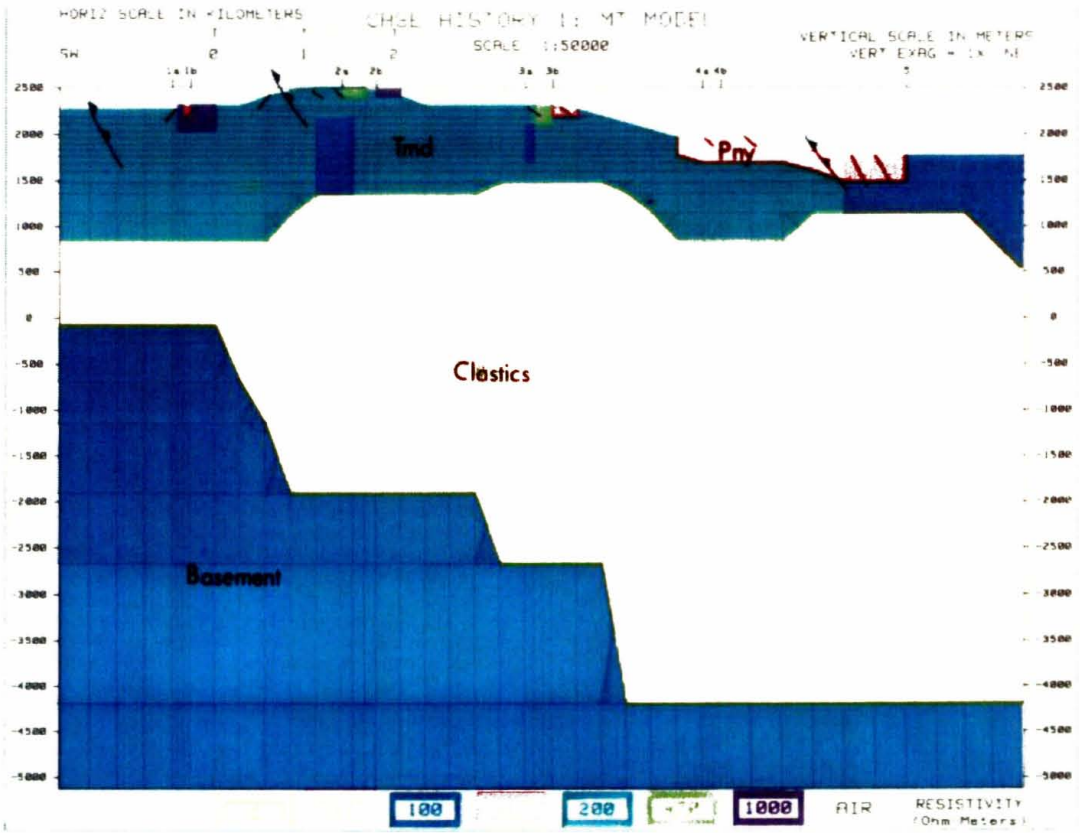

Figure 2.11: Inversion results and interpretation of one profile of MT survey in Papua New Guinea, from Christopherson (1991). Average resistivity of Darai limestone is 200-250 Ω m, anticline peaks beneath station 2, base of Darai highest below station 3.

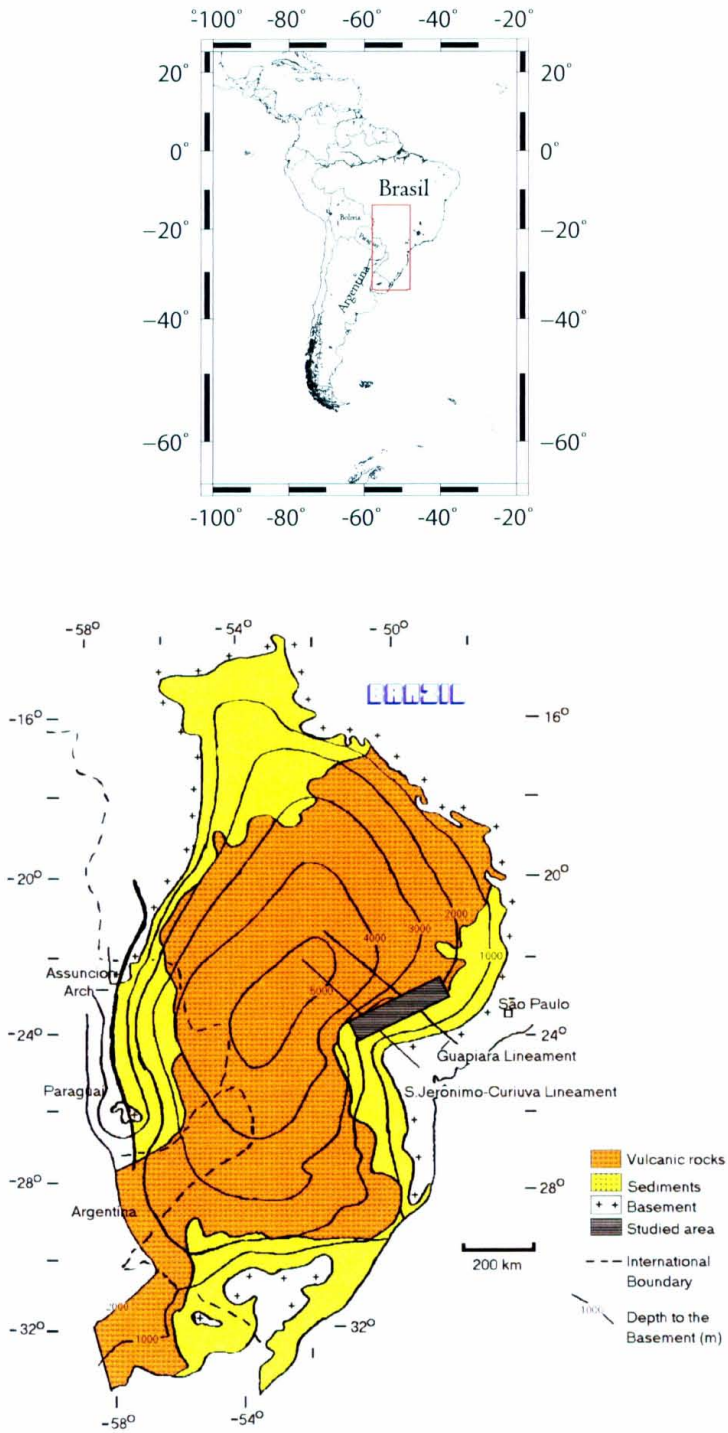

Figure 2.12: Map positioning the Paraná basin in South America. Study area map is outlined in red. After Menezes and Travassos (2010).

2.4.4 MT in the Paraná Basin, Brazil

The hydrocarbon exploration situation in the Paraná basin is very similar to that of the Nechako basin. Deposition occured from the Triassic/Jurassic to the Early Cretaceous and the basin is overlain by massive flood basalts (second largest in the world) (Menezes and Travassos, 2010). This volcanic covering and the added difficulties resulting from environmental issues in the delicate rainforest ecosystem make seismic exploration problematic (Filho et al., 2008). The area is contains abundent diabase dikes and sills which provide migration and trapping mechanisms in the area, and thus are important exploration targets. Drilling in the Sãu Paulo State, slightly north east of the study area, showed oil associated with these dike systems and their structural highs. Hydrocarbons in the reservoir rock are sourced from the Permian Irati formation with heat from magmatism occuring ca. 138-127 Ma (Menezes and Travassos, 2010). Study of the basin is made even more difficult by the lack of previous exploration: it comprises half of the unexplored onshore sedimentary rock volume in Brazil.

Menezes and Travassos (2010) carried out an MT survey across the Paraná Basin (see Fig. 2.12). The MT data consisted of 16 remote referenced MT sites, cutting across 170 km SW-NE over the Ponta Grossa Arch, and perpendicular to the geoelectric strike which is parallel to the magnetic trend of the dike swarms. These data were then processed using 2D tensor decompositions and modelled with a finite element forward modeller and a 2D smooth inversion. The inversion and forward modeller used 20 frequencies in the range 100-0.001 Hz with a 100 Ω m half space as the starting model. Fig. 2.13 shows the model constructed by the inversion. The

forward modeller was used to test the model as well as check the effect on model fitness of adding certain known geological features. Interpretation of the data was constrained with a well log and airborne magnetic data (see Fig. 2.14). The diabase dikes are essential to the petroleum system of the Paraná basin (Filho et al., 2008), and, while Menezes and Travassos (2010) estimate that the area is 3D in nature, the authors believe the 2D models accurately describe the first order structure in the subsurface.

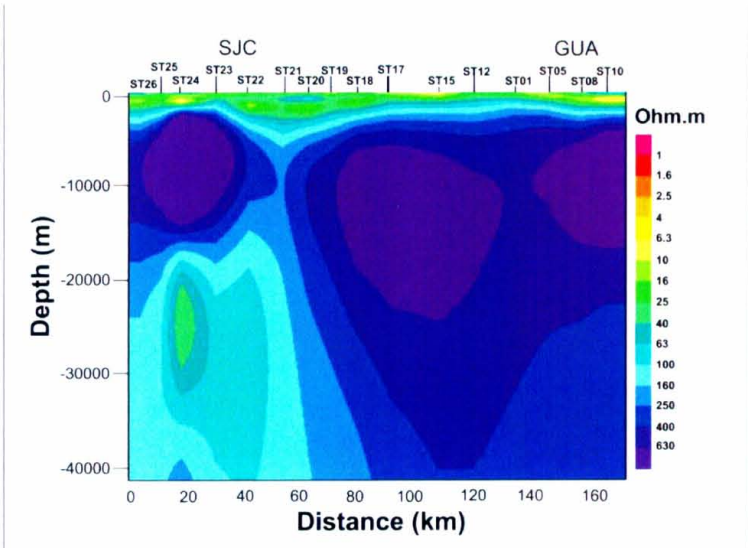

Figure 2.13: Inversion results for the upper 40 km of MT survey in Paraná Basin, Brazil (Menezes and Travassos, 2010)

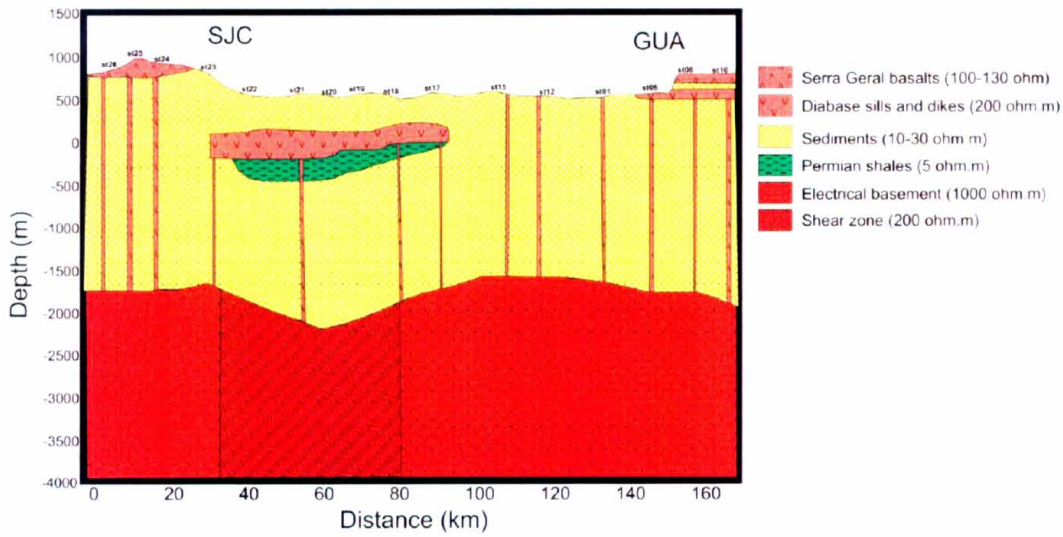

Figure 2.14: Interpretation (of upper 4 km) of MT inversion results in Paraná Basin, Brazil (Menezes and Travassos, 2010). Known basalt outcrops interpreted at the south, west and north east ends of the profile, thin Creatceous sediment overlies a central body of Serra Geral flood basalt.

Chapter 3

Forward Modelling

The basis of foward modelling is synthesizing data by computing the numerical solution of physical laws as they apply to specific circumstances. In MT this means solving Maxwell's equations in a given conductivity structure to obtain values of electric and magnetic fields. These fields can be used to yield synthetic impedance estimates. Various techniques can be used for the numerical computation of these fields. The method used by the software used in this thesis, however, is that of Haber et al. (2000a), modified for MT by Farquharson et al. (2002).

Synthesizing responses for MT has been done in a variety of ways assuming either a 1D, 2D, or 3D nature of the Earth. In 1D layered models, analytical results are possible, but with increasing complexity at higher dimensionality, these calculations become less feasible. In two and three dimensions, the finite difference, finite element, and integral equation techniques have been used (Avdeev, 2005). This author has programmed the 1D analytical results for a layered Earth, presented in § 3.1, and used software employing a 3D finite difference method by Farquharson et al. (2002)

for inversion modelling.

3.1 1D MT Forward Modelling

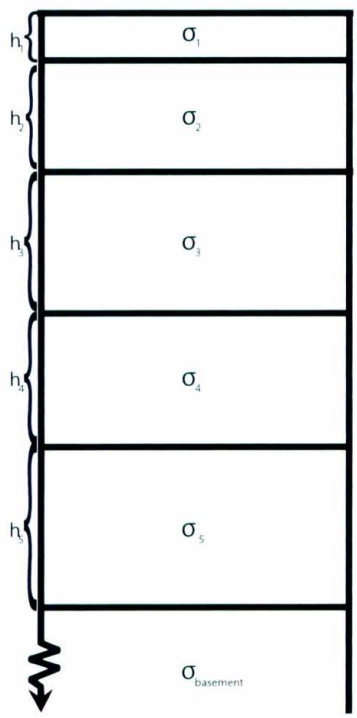

Figure 3.1: Typical layering of a 1D Earth model

1D frequency domain behaviour for an n-layered isotropic Earth (see Fig. 3.1) is described by Ward and Hohmann (1987). The intrinsic impedance (the impedance that would be seen if this were the only layer in the subsurface, i.e. a uniform Earth) of the j^{th} layer is given by:

$$Z_j = \frac{\omega \mu_0}{k_j} \tag{3.1}$$

where ω is the angular frequency, μ_0 is the permeability of free space, and k_j is the

complex wave number of the j^{th} layer given by

$$k_j = \sqrt{\frac{\omega \mu_0 \sigma_j}{2}}(1+i) \tag{3.2}$$

with σ_j as the layer conductivity. The impedance in the bottom layer is then propagated up to the layer above in the following way:

$$\hat{Z}_j = Z_j \left[\frac{\hat{Z}_{j+1} + Z_j \tanh(ik_j h_j)}{Z_j + \hat{Z}_{j+1} \tanh(ik_j h_j)} \right], \tag{3.3}$$

where h_j is the thickness for that layer and $\hat{Z}_j$ is the apparent impedance (the impedance of that finite layer, with the influence of underlying layers), $\hat{Z}_n = Z_n$ for the bottom, infinite layer. This recursive definition is used to find the propagated impedance at the top layer. One important caveat to note is the sign in front of the imaginary number in eq. 3.2. The sign used here comes from the positive sign in the exponent of the inverse Fourier Transform used in the processing.

3.2 Finite Difference Method

The finite difference method is a numerical computation method which uses finite differences to approximate derivatives in a discretized medium. Applying the curl operator to each side of eq. 2.7, we get:

$$\nabla \times \nabla \times \mathbf{E} = i\omega \nabla \times \mathbf{B}.$$

A substitution of magnetic field for magnetic intensity $\mathbf{B} = \mu_0 \mathbf{H}$ in the last step gives:

$$\nabla \times \nabla \times \mathbf{E} = i\omega \mu_0 \nabla \times \mathbf{H}.$$

Substituting Ampère's law (eq. 2.5):

$$\nabla \times \nabla \times \mathbf{E} = i\omega \mu_0 \mathbf{J}$$

Substituting Ohm's law (eq. 2.8):

$$\nabla \times \nabla \times \mathbf{E} = i\omega\mu_0\sigma\mathbf{E}$$

For the purposes of the analysis, it is sufficient to have a 1D Earth in which the electric and magnetic fields vary in the z-direction and point in the x and y directions, i.e. $\mathbf{E}(z) = E_x(z)\hat{\mathbf{x}}$ and $\mathbf{H} = H_y(z)\hat{\mathbf{y}}$. In this layered world the governing equations from § 2.2 the electric field curl terms are:

$$\nabla \times \mathbf{E} = \frac{\partial E_x}{\partial z}\hat{y}$$

and

$$\nabla \times \nabla \times \mathbf{E} = -\frac{\partial^2 E_x}{\partial z^2}\hat{x}$$

So the 1D governing equation becomes:

$$\frac{\partial^2 E_x}{\partial z^2} + i\omega\mu_0\sigma(z)E_x = 0 \tag{3.4}$$

Taylor series can be used to approximate the derivatives with finite differences. The following is one example of how to derive a finite-difference approximation for eq. 3.4 with nodes at z_j and z_{j+1} on either side of layer j and $z_{j+1/2}$ indicating the center of that layer as shown in Fig. 3.2:

$$E(z) = E_j + \left.\frac{\partial E}{\partial z}\right|_z (z_{j+1/2} - z_j) + \mathcal{O}(\Delta^2) \tag{3.5}$$

$$E_{j+1/2} - E_{j-1/2} = \left.\frac{\partial E}{\partial z}\right|_{z_j} (z_{j+1/2} - z_j) - (z_{j-1/2} - z_j) + \mathcal{O}(\Delta^2)$$

So the first derivative is approximated as:

$$\frac{E_{j+1/2} - E_{j-1/2}}{z_{j+1/2} - z_{j-1/2}} = \frac{\partial E}{\partial z}|_z + \mathcal{O}(\Delta) \tag{3.6}$$

The second derivative is approximated as:

$$\frac{1}{z_{j+1/2} - z_{j-1/2}} \left\{ \left. \frac{\partial E}{\partial z} \right|_{z_{j+1}} - \left. \frac{\partial E}{\partial z} \right|_{z_j} \right\} = \left. \frac{\partial^2 E}{\partial z^2} \right|_{z_{j+1/2}} + \mathcal{O}(1)$$

$$\frac{\partial^2 E}{\partial z^2} = \left\{ E_{j+3/2} - 2E_{j+1/2} + E_{j-1/2} \right\} + \mathcal{O}(1) \tag{3.7}$$

Now that we have finite difference approximations for the first and second derivatives of the electric field, we need a finite difference expression for the conductivity term in eq. 3.4. We can do this with an Amperian loop around one of the layers (see Fig. 3.2):

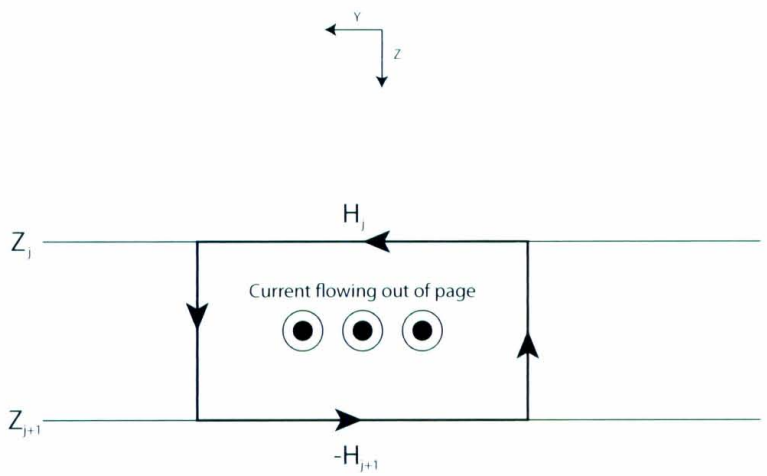

Figure 3.2: Formulation of an Amperian loop after Farquharson (2009).

$$\int_c \mathbf{H} \cdot \hat{t} dl = \int_s \mathbf{J} \cdot \hat{n} ds \tag{3.8}$$

where $\hat{t}$ is a vector pointing around the closure of the loop, and $\hat{n}$ is the normal vector of the area enclosed by that loop. In the 1D case, the vertical component of

the magnetic field is 0, and the horizontal components are constant along the layer interface, so the path integral becomes easy to calculate.

$$\begin{aligned} \int_c \mathbf{H} \cdot \hat{t} dl &= H_j \Delta y - H_{j+1} \Delta y \\ &= (H_j - H_{j+1}) \Delta y \end{aligned}$$

Integrating eq. 2.8 over a surface gives a relationship for electric field which applies to the right hand side of eq. 3.8, $\int_s \mathbf{J} \cdot \hat{n} ds = \sigma_j \int_s \mathbf{E} \cdot \hat{n} ds$. The Taylor series approximation for the integral of $E(z)$ over layer j is:

$$\begin{aligned} \int_{z_j}^{z_{j+1}} E(z) dz &= \int_{z_j}^{z_{j+1}} \left(E_{j+1/2} + \frac{\partial E}{\partial z}\Big|_{z_{j+1/2}} (z - z_{j+1/2}) + \mathcal{O}(\Delta^2) \right) dz \\ &= E_{j+1/2} + \int_{z_j}^{z_{j+1}} dz + \frac{\partial E}{\partial z} \int_{z_j}^{z_{j+1}} (z - z_{j+1/2}) dz + \mathcal{O}(\Delta^2) \int_{z_j}^{z_{j+1}} dz \\ &= E_{j+1/2} \Delta z + \mathcal{O}(\Delta z^3) \end{aligned} \tag{3.9}$$

Using our result from Ohm's law:

$$(H_j - H_{j+1}) \Delta y = \sigma_j E_{j+1/2} \Delta y \Delta z + \mathcal{O}(z^3)$$

Dividing through by Δy and Δz:

$$\frac{H_j - H_{j+1}}{\Delta z} = \sigma_j E_{j+1/2} + \mathcal{O}(\Delta z^2) \tag{3.10}$$

Boundary conditions of $\mathbf{H}(0) = 1$ and $\mathbf{H}(\infty) = 0$ can be used to calculate impedances measured at the surface.

3.3 3D MT Forward Modelling

In order to improve solution accuracy and efficiency, potentials are employed in the software used in this thesis instead of actual $\mathbf{E}$ and $\mathbf{H}$ fields. The electric field is

decomposed into a vector and scalar potential, $\mathbf{A}$ and ϕ:

$$\mathbf{E} = \mathbf{A} + \nabla\phi. \tag{3.11}$$

The Coulomb gauge enforces uniqueness:

$$\nabla \cdot \mathbf{A} = 0. \tag{3.12}$$

Using Ampère's law (eq. 2.9) and Faraday's law (eq. 2.7) with these potentials, we obtain the following equation (Haber et al., 2000a; Farquharson et al., 2002):

$$\nabla^2\mathbf{A} + i\omega\mu_0\sigma(\mathbf{A} + \nabla\phi) = \mathbf{J}^s = 0 \tag{3.13}$$

$\mathbf{J}^s$ is zero because the source for MT is outside our "computational world." Instead the electromagnetic system is driven by boundary conditions. A lack of current sources means that the current density is divergence free:

$$\nabla \cdot \mathbf{J} = 0, \tag{3.14}$$

and when combined with eq. 2.8 in potential form, $\mathbf{J} = \sigma(\mathbf{A} + \nabla\phi)$, this gives:

$$\nabla \cdot (\sigma\mathbf{A} + \sigma\nabla\phi) = 0 \tag{3.15}$$

The system (eq. 3.13, 3.15) is discretized into a grid of cells indexed i, j, k, each with conductivity σ_{ijk} (see Fig. 2.7) and the finite-difference approximation of eq. 3.13 and 3.15 is done in a similar manner to that described in § 3.2. The conductivity is constant within one cell, but may change freely between cells. Here we can see an advantage of using potentials: the normal component of $\mathbf{E}$ is discontinuous at cell faces because σ may vary (Haber et al., 2000a). Splitting the electric field into two potentials allows for the two main contributions to electric variations to be expressed

in greater detail: the galvanic contribution and the inductive contribution (Aruliah et al., 2001). The galvanic effect is seen when lower frequencies setup large scale currents similar to those of the DC resistivity method, increasing the contribution of $\nabla\phi$. The inductive effect sets up eddy currents and is captured in the contribution of $\mathbf{A}$.

The components of the vector potential are caculated at the centers of the cell faces, with the scalar potential harmonically averaged over the cell and placed at the center (Haber et al., 2000a; Farquharson et al., 2002). Boundary conditions imposed in this method are that the tangential and normal components of $\nabla \times \mathbf{A}$ and $\mathbf{A}$ vanish on the mesh boundary. These equations are summed up in a block matrix form from eq. 3.13 and 3.15:

$$\begin{pmatrix} L + j\omega\mu_0 S & j\omega\mu_0 SG \\ DS & DSG \end{pmatrix} \begin{pmatrix} \mathbf{A} \\ \phi \end{pmatrix} = 0 \tag{3.16}$$

L, D, and G are the discrete versions of the Laplacian, divergence and gradient operators respectively, and S is the diagonal matrix of cell conductivities. This matrix equation is solved for $\mathbf{A}$ and ϕ using the BICGStab algorithm with incomplete LU decomposition preprocessing (Haber et al., 2000a).

Chapter 4

Inversion

4.1 Inversion – Curve Fitting

Newton's method is used for finding zeros and minima of functions. It is an iterative procedure which uses the first terms of the Taylor series to approximate the minimum over and over until the method converges (Burden and Faires, 2005), this method is a classical descent method which tends toward a local minimum. More modern methods, such as particle swarm optimization (discussed in Chapter. 5), work to locate the global minimum. Formulation of Newton's method at each iteration shown below starts with the last approximation for the location of the local minimum of $f(x)$, x_i, and finds a better approximation, x_{i+1}:

$$x_{i+1} - x_i = -f'(x_i)/f''(x_i) \tag{4.1}$$

In multiple dimensions the Newton method used for finding local minima becomes:

$$\mathbf{H}_i \mathbf{p}_i = -\mathbf{g}_i \tag{4.2}$$

where $\mathbf{H}_i$ is the Hessian of the multivariate function, $\mathbf{f}$, being minimized, $\mathbf{p}_i$ is a vector pointing to the next approximation of the minimum (shown in eq. 4.4), and $\mathbf{g}_i$ is the product of the transposed jacobian, $\mathbf{J}^T$ and the multivariate function, or the gradient of that function (shown in eq. 4.6). The Newton method effectively uses an n dimensional Taylor series to approximate a function with a parabolic bowl, finding the bowl's minimum, moving to that point, and starting all over. The Newton method becomes the Gauss-Newton method when the function being minimized is a sum of squares:

$$F = \sum_i [f_i(\mathbf{x})]^2 \tag{4.3}$$

where the f_i terms are the elements of $\mathbf{f}$, and the Hessian is appoximated by:

$$\mathbf{H} \approx \mathbf{J^T J}. \tag{4.4}$$

Elements of the Jacobian are defined as:

$$J_{ij}(\mathbf{f}) = \frac{\partial f_i}{\partial x_j}. \tag{4.5}$$

The Jacobian is a matrix of derivatives of the elements in the function vector with respect to the model parameters.

$$\mathbf{g} = \nabla F = \mathbf{J^T f} \tag{4.6}$$

A comparison of the Gauss-Newton method to Newton's method can be seen in the following rearrangement: $\mathbf{p}_i = -\mathbf{H}_i^{-1}\mathbf{g}_i$. Substituting the Gauss-Newton approximation for the Hessian in eq. 4.4, the following is obtained:

$$\mathbf{p} = (\mathbf{J}^T\mathbf{J})^{-1}\mathbf{J}^T\mathbf{f} \tag{4.7}$$

The first thing needed when performing data fitting is an organized, methodical way of adjusting a function to approximate data. In a polynomial fitting scenario, we could adjust the coefficients of each term, i.e. $f(x) = \sum_i a_i x^i$. For exponential fitting we could adjust the amplitude and base, i.e. $f(x) = Ab^x$. In a sinusoidal regression we could adjust the amplitude and frequency, i.e. $f(x) = A \sin \omega x$. The things which are being adjusted are called the "function" or "model" parameters.

The second thing required is a measure of the distance (i.e. metric) between values of a function and the data points. This measure should include all points in an appropriately equivalent (weighted) way, and should generally be indifferent to the sign or sense of the distance between a function value and a data point. One such measure is the aggregate squared distances between each data point and its function value:

$$\phi_d = ||\mathbf{d}^{obs} - \mathbf{d}^{prd}||^2 = \sum_i (d_i^{obs} - d_i^{prd}(\mathbf{m}))^2, \tag{4.8}$$

$\mathbf{d}^{obs}$ is the vector filled with observed data points, $\mathbf{d}^{prd}$ is the vector filled with function values or produced data, i.e. $\mathbf{d}_i^{pred}(\mathbf{m}) = f(\mathbf{m})$, and $\mathbf{m}$ is the vector of our model parameters. This misfit measure is a sum of squares function, for which Gauss-Newton minimization is effective. The algorithm requires a start point, so a guess is made. The Jacobian is then calculated and difference in data vectors obtained.

$$\mathbf{J}^{\mathbf{T}}\mathbf{J}\mathbf{p} = -\mathbf{J}^{\mathbf{T}}\delta\mathbf{d}(\mathbf{m}), \tag{4.9}$$

where $\delta\mathbf{d} = \mathbf{d}^{obs} - \mathbf{d}^{prd}$, and $\mathbf{p}$ is the update to the model parameters, i.e. a vector from the current approximation of the minimum to the next in "model parameter space." $\mathbf{p}$ will be called the change in model parameters, $\delta\mathbf{m}$, from now on. It is

given by:

$$\delta \mathbf{m} = -(\mathbf{J}^{\mathrm{T}}\mathbf{J})^{-1}\mathbf{J}^{\mathrm{T}}\delta \mathbf{d}(\mathbf{m}) \tag{4.10}$$

Gauss-Newton minimization works well for many well-posed optimization problems. The geophysical inversion problem does not in general, however, have a unique solution and so presents a challenge.

4.2 Inverse Problem

Geophysical inversion is more complex than curve fitting: it is often ill-posed, poorly-constrained, and non-unique. Mathematically, this means that the Hessian is not invertible. This problem can also present itself in data fitting: What kind of function should be used to fit the data? If a high degree polynomial is chosen then it will go through all the points but may not make physical sense. It will also fit all the noise in the data as well as signal. On the other hand, if we use a low degree polynomial we get a bad fit but it gives a better idea of the underlying physical relationship and it will ignore much of the noise. The right fit is somewhere in between. This is a trade off, and solving the geophysical inverse problem presents a similar dilemma.

The Hessian can be augmented (to solve eq. 4.10) using two methods common to geophysical inversion (Gill et al., 1981):

- Marquardt-Levenberg
- Minimum Structure.

4.2.1 Marquardt-Levenberg

In the Marquardt-Levenberg approach, a constant value is added along the diagonal of the Hessian to ensure that its determinant is non-zero and the Hessian is invertible:

$$(\mathbf{J^T J} + \lambda \mathbf{I})\delta \mathbf{m} = -\mathbf{J}^T(\mathbf{d^{obs}} - \mathbf{d^{prd}}) \tag{4.11}$$

This approach has the effect of tending toward a steepest-descent (taking the steepest path to the minimum or maximum) solution as the trade off parameter, λ in eq. 4.11, gets bigger and the identity takes over from the Jacobian term. As λ drops to zero the solution approaches the Gauss-Newton method (Gill et al., 1981).

4.2.2 Minimum Structure

The minimum structure approach augments the function being minimized (Gill et al., 1981):

$$\Phi = \phi_d + \lambda \phi_m, \tag{4.12}$$

where ϕ_d is the measure of misfit (see eq. 4.8) and ϕ_m is a measure of model structure. The misfit, including estimates of the uncertainties in the data, is:

$$\phi_d = \sum_i \left(\frac{d_i^{obs} - d_i^{prd}}{\sigma_i} \right)^2 \tag{4.13}$$

Dividing by the measurement uncertainty puts less emphasis on data with more uncertainty. This is put into matrix form:

$$W_d = \begin{pmatrix} \frac{1}{\sigma_{11}} & \frac{1}{\sigma_{12}} & \cdots & \frac{1}{\sigma_{1N}} \\ \frac{1}{\sigma_{21}} & \frac{1}{\sigma_{22}} & \cdots & \frac{1}{\sigma_{2N}} \\ \vdots & \vdots & \ddots & \vdots \\ \frac{1}{\sigma_{N1}} & \frac{1}{\sigma_{N2}} & \cdots & \frac{1}{\sigma_{NN}} \end{pmatrix} \tag{4.14}$$

The $\mathbf{W_d}$ matrix is diagonal for uncorrelated noise, i.e. $\sigma_{ij} = 0,\ \forall i \neq j$, which is usually assumed to be the case. This means noise in one measurement does not depend on or is unaffected by noise in another. The component of the Gauss-Newton Hessian matrix from ϕ_d is therefore:

$$\mathbf{H} = \mathbf{J}^T {\mathbf{W_d}}^T \mathbf{W_d} \mathbf{J}. \tag{4.15}$$

The measure of model structure, ϕ_m, can be written as:

$$\phi_m = ||\mathbf{W_z m}||^2 + ||\mathbf{W_y m}||^2 + ||\mathbf{W_x m}||^2, \tag{4.16}$$

where $\mathbf{W_x}$ is the matrix:

$$\mathbf{W_x} = \begin{pmatrix} \frac{1}{\Delta x_1} & \frac{-1}{\Delta x_1} & 0 & 0 & \cdots \\ 0 & \frac{1}{\Delta x_1} & \frac{-1}{\Delta x_1} & 0 & \cdots \\ \vdots & \vdots & \vdots & \vdots & \ddots \end{pmatrix} \tag{4.17}$$

This term quantifies the difference in model parameter between adjacent cells in the x-direction. This has the effect of minimizing the variation of the model parameter in the x-direction when included in eq. 4.12. Similarly $\mathbf{W_y}$ and $\mathbf{W_z}$ minimize variation between cells in the y- and z-directions respectively. Incoporating ϕ_m into the minimization problem results in the following Gauss-Newton system of equations:

$$\begin{aligned} &\left(\mathbf{J}_i^T {\mathbf{W_d}}^T \mathbf{W_d} \mathbf{J}_i + \lambda \left(\sum_{i=x,y,z} \mathbf{W}_i^T \mathbf{W}_i \right) \right) \delta \mathbf{m}_i \\ &\qquad = \mathbf{J}_i^T {\mathbf{W_d}}^T \mathbf{W_d} \mathbf{J}_i (\mathbf{d^{obs}} - \mathbf{d^{prd}}) - \lambda \left(\sum_{j=x,y,z} \mathbf{W}_j^T \mathbf{W}_j \right) \mathbf{m}_i \end{aligned} \tag{4.18}$$

This equation is the essence of the inversion process. It will be used to obtain succession of Earth models, given by $\mathbf{m} + \delta \mathbf{m}_i$ (iteration indicated by i), providing generally better data fits while remaining as simple as called for by the trade off parameter, λ.

4.2.3 Straight Ray Travel Time Inversion Example

Travel times for seismic rays travelling from transmitters in a left hand borehole, through a medium, on a straight ray path to recievers in a right hand borehole were inverted to reproduce a model from synthetic data with Gaussian noise. The difference between this noisy synthetic (observed) data and predicted data from the model was used to calculate the value of the objective function, ϕ_d in eq. 4.13 for the measurement of error. The medium between the boreholes consisted of a high velocity block in a low velocity background. Five transmitters on the left shoots rays to each of the 26 recievers on the right (see Fig. 4.1) with gaussian noise added to the travel times. The travel times for these rays are shown in Fig. 4.2 Rays travelling

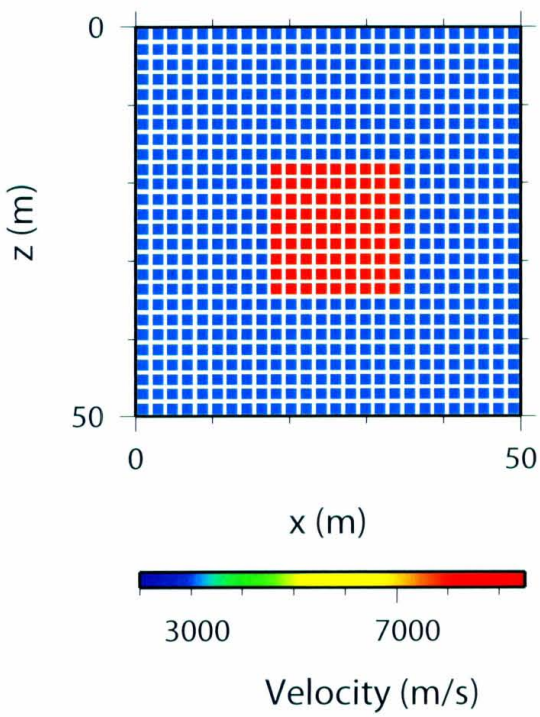

Figure 4.1: Original model used for producing synthetic data in straight ray travel time inversion.

through the center saw more of the high velocity structure and so have lower values of travel time, indicated by data in the central portions of in Fig. 4.2. Rays at the ends of this graph saw more of the low velocity background and so have higher values of travel time.

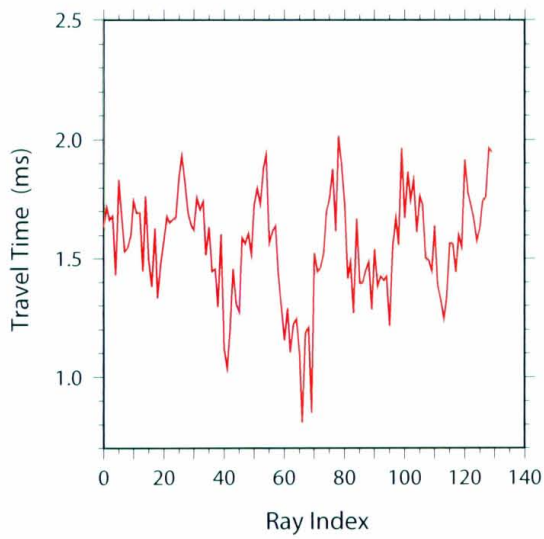

Figure 4.2: The data (shown as points) generated for the model and rays in Fig. 4.1. A tight fitting curve fits the data closely but fits a lot of noise as well. Measured (observed) travel times are shown as points, travel times produced (predicted) from the model are in red line. Rays are indexed according to transmitter and receiver from top to bottom, i.e. the ray travelling from the second transmitter from the top on the left to the third receiver from the top on the right, the ray index is $i_{ray} = 26 \times i_{transmitter} + i_{receiver} = 26 \times 1 + 2 = 28$, such that the top transmitter has an index of $i_{transmitter} = 0$, and the top receiver has an index of $i_{receiver} = 0$.

Model parameters were indexed according to the cell in the lattice from left to right, top to bottom and travel times where calculated through those cells. Fig. 4.3 shows a noisy model which overfits the data (see Fig. 4.2) while Fig. 4.4 shows a model with very little structure and a fit which ignores much of the character of the observed data (see Fig. 4.5). Fig. 4.6 shows an accomodation of both ends, containing

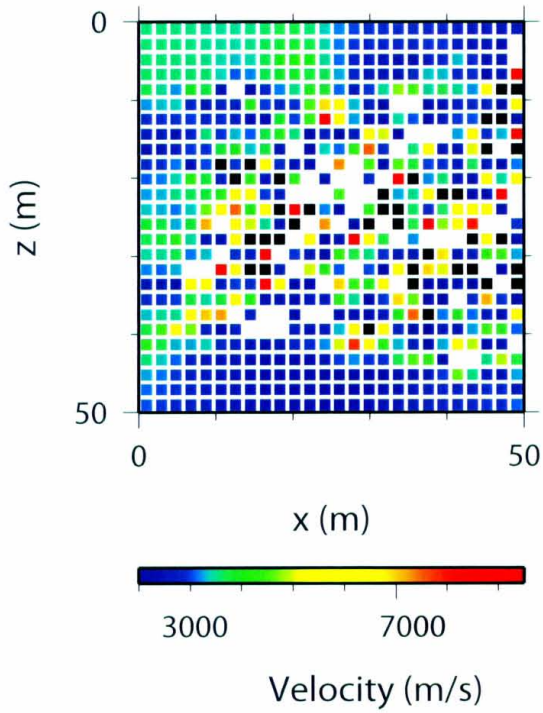

Figure 4.3: Model resulting from tightly fitting observed travel times.

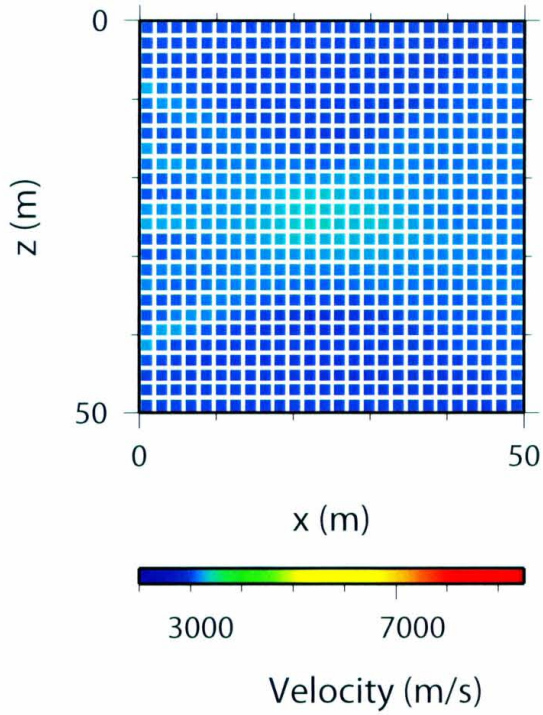

Figure 4.4: Model resulting from loosely fitting observed travel times.

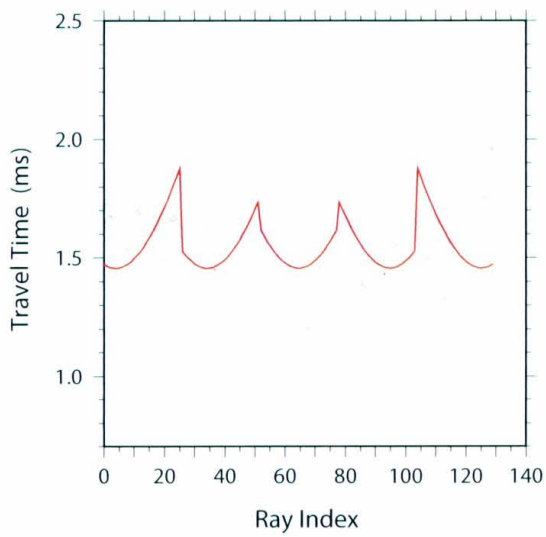

Figure 4.5: A loose fitting curve models less of the noise but does not fit the data as closely. Travel times become a reflection of ray path length through a flat medium, structure is lost. Compare with Fig. 4.2.

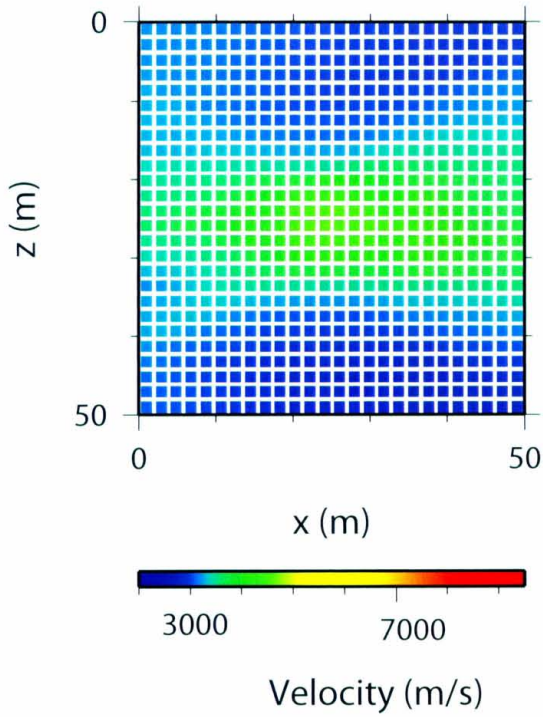

Figure 4.6: Model resulting from a compromise between tightly fitting and loosely fitting straight ray travel times.

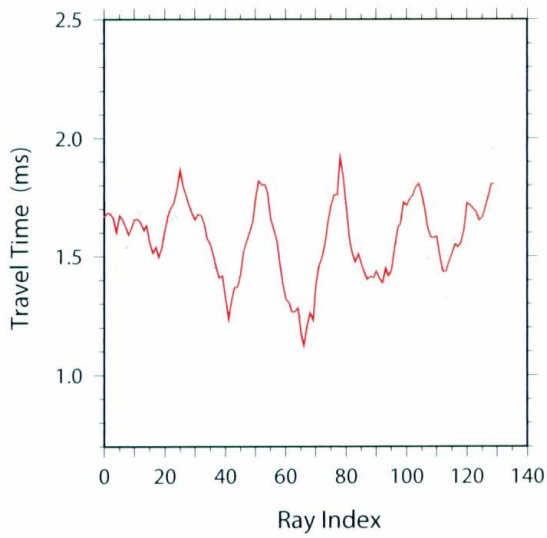

Figure 4.7: A compromise between tight fit and loose fit gives a good picture of the underlying physical process. Noise is not overfitted, but model still retains structure. Compare with Fig. 4.2 and 4.5.

a moderate amount of structure (established by visual inspection) which does not fit much noise but does not underfit the data (see Fig. 4.7).

4.2.4 3D MT Inversion – Program MT3Dinv

MT3Dinv uses a Gauss-Newton algorithm as described by Haber et al. (2000b) (Farquharson et al., 2002). This method solves eq. 4.18 with a conjugate gradient algorithm (Farquharson et al., 2002), preconditioned with partial LU decomposition of the matrix $\mathbf{W}^T\mathbf{W} + 0.1\mathbf{I}$, where $\mathbf{I}$ is the identity matrix. MT3Dinv combines the forward and inversion modelling processes to produce conductivities in a rectilinear mesh. The forward modelling process was briefly described in § 3.3. Structure weighting parameters may be adjusted differently in the x, y, and z directions, however in this thesis these parameters have all been set equal so that structure is minimized equally in all directions.

Chapter 5

Particle Swarm Optimization

5.1 The Paradigm of Particle Swarm Optimization

Particle Swarm Optimization (PSO) has one foot in artificial intelligence (in social systems), and the other in evolutionary or genetic algorithms (Kennedy and Eberhart, 1995). This is a more modern optimization technique which works to find the global minimum of a function, as opposed to the more classical methods which find local minima (e.g. those of Chapter. 4). It takes its cue from groups of individuals in nature which use information sharing to find resources and thus are able to find new sources quickly. In these systems, the advantages of information sharing seem to outweigh its disadvantages, i.e. granting public access to a personal stash, and the ensuing resource thinning. For example, schools of fish looking for food all swarm to the same sources whose locations are shared by the first to find them, and, even though a limited good is being shared across the collective, the good of the group seems to benefit the individual. Kennedy and Eberhart (1995) began development of

the PSO algorithm in an attempt to mimic social behaviour in nature. This development of social mimickery grew into an exploitation of the ability of these collectives to "optimize environmental parameters" (Kennedy and Eberhart, 1995) and apply this ability to mathematical optimization problems. These authors summarized the paradigm of PSO in a few poignant lines: "Why is social behavior so ubiquitous in the animal kingdom? Because it optimizes. What is a good way to solve engineering optimization problems? Modeling social behavior" (Kennedy and Eberhart, 1995).

A typical PSO algorithm tries to express the tendency of individuals in a group to do the following (Pedersen and Chipperfield, 2009):

1. Obey inertia. They travel in the same direction unless influenced to do otherwise

2. Be drawn toward their best known position. Kennedy and Eberhart (1995) call this "simple nostalgia", returning to places known to host resources.

3. Follow the leader. Kennedy and Eberhart (1995) call this responding to "publicized knowledge," or moving to the best location the group has recently found.

These three points specify how each particle will search for local minima in an effort to select the best candidate for a global minimum.

Because geophysical inversion is so computationally taxing, inversionists are always looking for new methods for model construction which might expedite or enhance the process. The work done in applying PSO to a particular geophysical problem that was undertaken here was motivated by a desire to test the method's potential to help with geophysical inversion. The test performed here is for the 1D MT inverse problem. Shaw and Srivastava (2007) found PSO to be a simple tool for use with 1D

DC resistivity, IP, and MT data, acheiving results comparable with other inversion software. When producing conductivity models for a three layered Earth, Shaw and Srivastava (2007) reproduced conductivity values generally a 50% margin of error of the original synthetic model, imposing a search space of about one power of 10. Models produced in that instance closely matched those produced by rigid regression and genetic algorithms and observed and predicted data for trials of each type of inversion modelling agreed closely.

5.2 The Algorithm

The main quantities in a PSO algorithm are the positions in model space of the particles, velocities of the particles, and some optimal positions. An individual's velocity is represented as $\mathbf{v}$ and its position as $\mathbf{x}$. There are two optimal positions remembered by each particle: the personal best, $\mathbf{p}$, which pertains to point two in the previous section, and the overall or collective best, $\mathbf{g}$, which is relevant to point three above. The behaviour of the optimization can be modified by adjusting weighting parameters. These weighting parameters decide how important each of the points listed in the preceding section will be to individuals in the swarm. ω, ϕ_p, ϕ_g, represent the weighting of points 1, 2, and 3 respectively.

The general components of a PSO algorithm are as such (Pedersen and Chipperfield, 2009):

- Initialize the positions of all particles using a uniform distribution in search space, i.e. uniformly over the total range for each model parameter.

- Initialize the velocities of all particles using a uniform distribution in velocity space. The range for the velocities at startup determines how fast the particles are to fly around search space initially.

- Calculate values of the function being minimized for each particle to determine the most fit particle (i.e. the particle with the smallest value of the function), then assign the position of that particle to $\mathbf{g}$.

- Update all velocities with:

$$\mathbf{v}_i \leftarrow \omega \mathbf{v}_i + \phi_p \mathbf{r}_p \times (\mathbf{p}_i - \mathbf{x}_i) + \phi_g \mathbf{r}_g \times (\mathbf{g}_i - \mathbf{x}_i), \tag{5.1}$$

  $\mathbf{r}_p$ and $\mathbf{r}_g$ are random vectors whose elements have the uniform distribution, i.e., $r_{x_i} \epsilon [0, 1]$. The velocities are used to update the particles' positions. The idea is that each particle is forced in a direction toward a place that the collective has found favourable. ω controls the "inertia" of the particle, i.e. how much it stays on course. ϕ_p controls the "nostalgia" of a particle, i.e. how much it tends to revisit its personal best, which is updated as the particle searches model space. ϕ_g controls "mob mentality," i.e. how much each particle tends to move toward the collective's best known position. The product in Eq. 5.1, $\times$, is a component-wise vector multiplication so that particles do not move directly for either $\mathbf{p}$ or $\mathbf{g}$, they instead pick a path along n-dimensional cones pointed at each of those positions.

- Update positions, effecting a time step of one unit per iteration, with:

$$\mathbf{x}_i \leftarrow \mathbf{x}_i + \mathbf{v}_i \tag{5.2}$$

- Calculate function values with forward modeller and reset $\mathbf{g}$ again. With each particle's position updated, it is necessary to recalculate the function value for all particles in order to find the new personal best of each particle and check if a new particle has been found with a lower function value than the collective best.

- Repeat until the desired tolerance of misfit is reached

5.3 Example 1: Finding a Point

Code was written implementing PSO to search a 2D space for a given point, which was hidden from the particles. 170 particles were distributed uniformly across a space of $(x, y)\epsilon[-50, 50] \times [-50, 50]$ to look for the point $(x, y) = (10, -30)$. The PSO search parameters were $\omega = \phi_p = \phi_g = 0.8$ so that each component of "particle behaviour" was equally weighted. The function being minimized was the simple Cartesian metric or distance, $misfit = +\sqrt{(x-10)^2 + (y+30)^2}$. The tolerance was $tol = 2.0 \times 10^{-2}$, so that when the global best particle came within this distance ($misfit < tol$) of the sought after point, the algorithm finished. The results (see Fig. 5.1) show the point was found with a misfit (distance from the real value) of 0.0125 in 57 iterations. Fig. 5.1 shows six pairs of scatterplots showing the state of the algorithm at six iterations. The scatterplot in each pair labelled "P's" gives the personal best of that particle up to that point in the algorithm so that the spread of these points should get consistently closer to the sought after point. The scatterplot in each pair labelled "X's" gives the current position of each particle at that iteration in the algorithm, which should generally get closer to the sought after point but can

move away from it in one specific iteration. Fig. 5.2 shows the distances away from the sought after point. The algorithm updates the overall closest particle (point) 9 times before finishing. The algorithm is quick to get close to the solution point (see iteration 17 results in Fig. 5.1), but the majority of the iterations are spent concentrating the swarm as evidenced in the slow drop in misfit after iteration 17. Since the distance is calculated once for each particle at each iteration, this means the inversion required 9690 function evaluations in total. See Appendix B for source code.

5.4 1D MT Modelling with PSO

The implementation of PSO in the previous section was used on the 1D MT inverse problem. The function being minimized in this case is the typical data misfit function, i.e. the sum of squares of the difference between observed and predicted data, (see 4.8). The observed data were synthsized using the forward modeller without noise. The method of § 3.1 was used to build the forward modeller. The code for this PSO solution to the 1D MT problem is given in Appendix B. The variable model parameters for both examples considered below are the thicknesses of the top two layers in a triple-layered Earth model and the three layer logarithmic conductivities.

5.4.1 PSO for Synthetic 1D MT Example

The results, shown in Fig. 5.3 and 5.4, show the development of a model through 100 iterations (the global best fitting model is displayed in each step) and the decrease in misfit. The real and imaginary components of impedance were produced using the forward modeller with a set of conductivities and thicknesses for 16 frequencies.

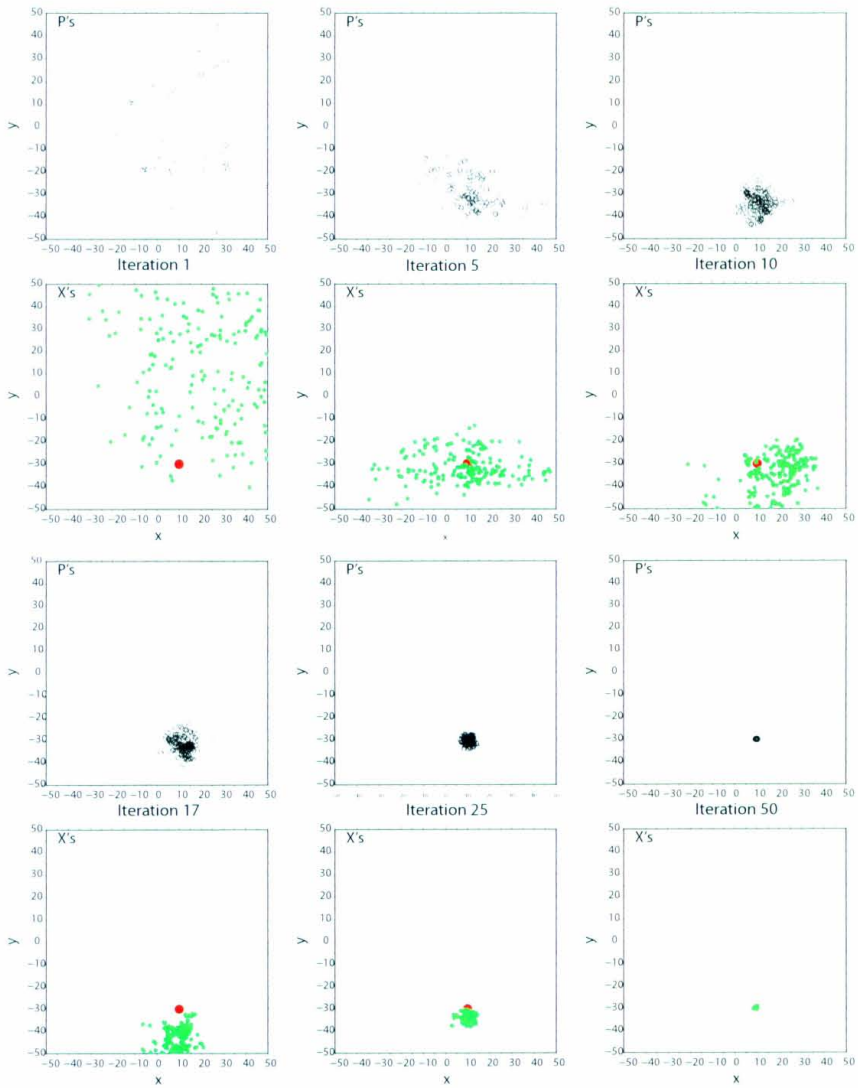

Figure 5.1: Each pair of plots (P's and X's) show a snap shot of swarm position as the optimization code runs, searching for the red dot. P's represent the personal best (closest to red) known position, while X's represent the current position of each particle for that iteration.

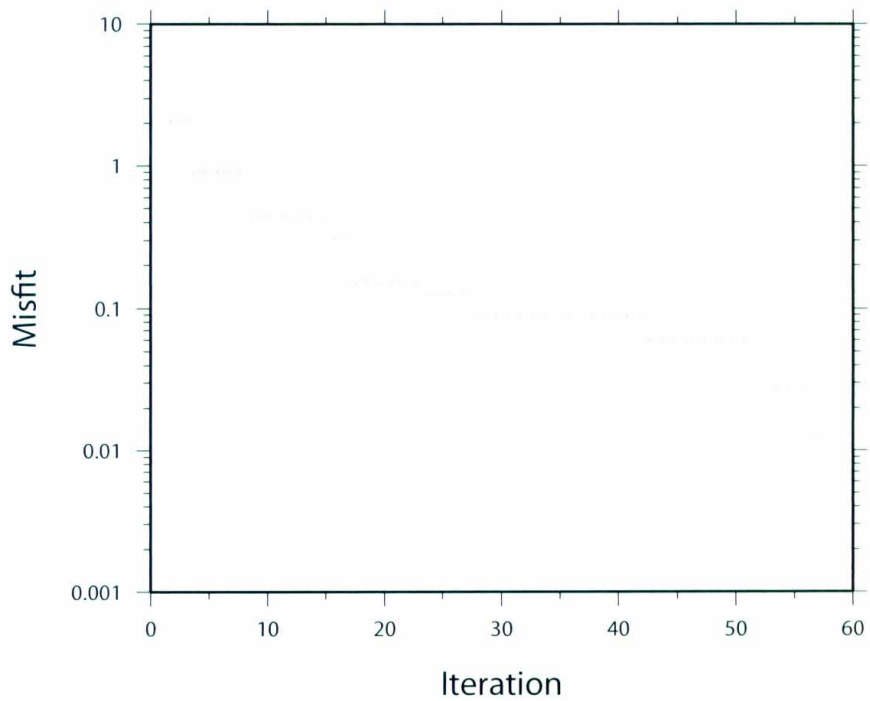

Figure 5.2: Distance of the particle closest to the solution point (collective best) in a PSO trial versus iteration number.

The code was run testing multiple values for PSO parameters until convergence was acheived and a sensible conductivity structure produced. The tolerance for the sum of squares difference between the 16 components of the observed and predicted data was 0.01. The number of particles was set 10000, an upper limit due to memory constraints, in order to see as much of the search space as possible before converging on one model. Particles were intialized over a resistivity search space of 1-1 000 000 Ωm and a layer thickness space (for the top two layers) of 10 - 10 000 m. Synthetic data (apparent resistivity and phase) are shown in Fig. 5.3 and 5.4 for the original model in blue (observed synthetic data) and the PSO model in green (predicted synthetic data). The PSO parameters which gave the best convergence were $\omega = 0.5$, $\phi_p = 0.4$, and $\phi_g = 0.3$, based on speed of convergence to satisfactory results of multiple trials. The algorithm was run with various PSO parameters to find values which combinations seemed to work, a large ω seemed to maintain some of the randomized particle behaviour of the beginning so that more of the search space was explored before converging on a specific model. More particles were needed for the MT example than the point finding example due to the decrease in particle density in MT's five dimensional search space from the point finding example's two dimensional search space. If the parameters have poor values or there are not enough particles to search the space, the algorithm has difficulty finding a good minimum.

5.4.2 Modelling Nechako Basin Data

The 1D MT PSO routine was applied to the Nechako Basin data along lines A, B, and C (the same routine used in § 5.4.1). Line A was made of 59 sites picked at

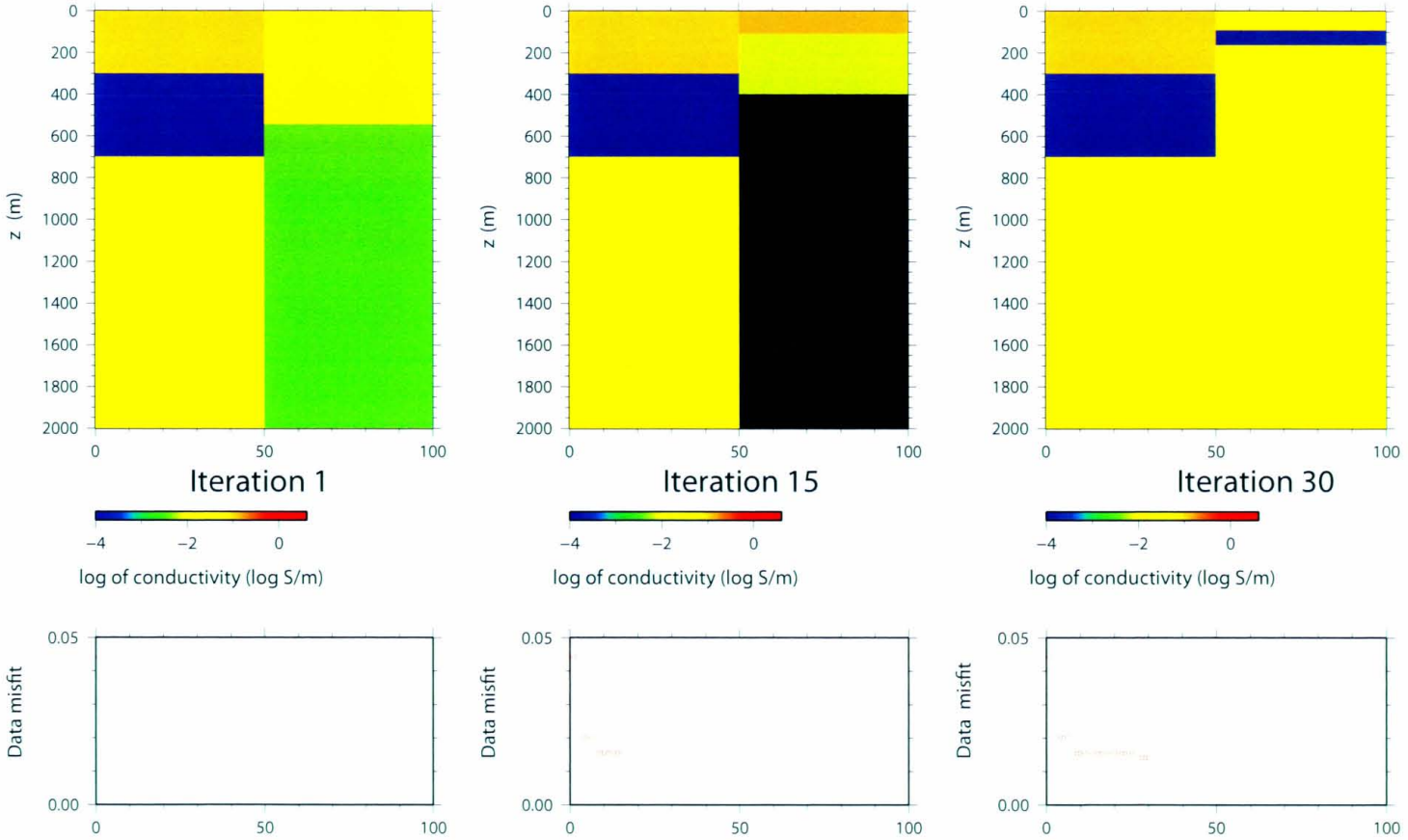

Figure 5.3: Comparison of true Earth layers (left) and the model with lowest misfit (right) at iterations 1, 15, and 30. Progression of collective misfit is in the lower panels.

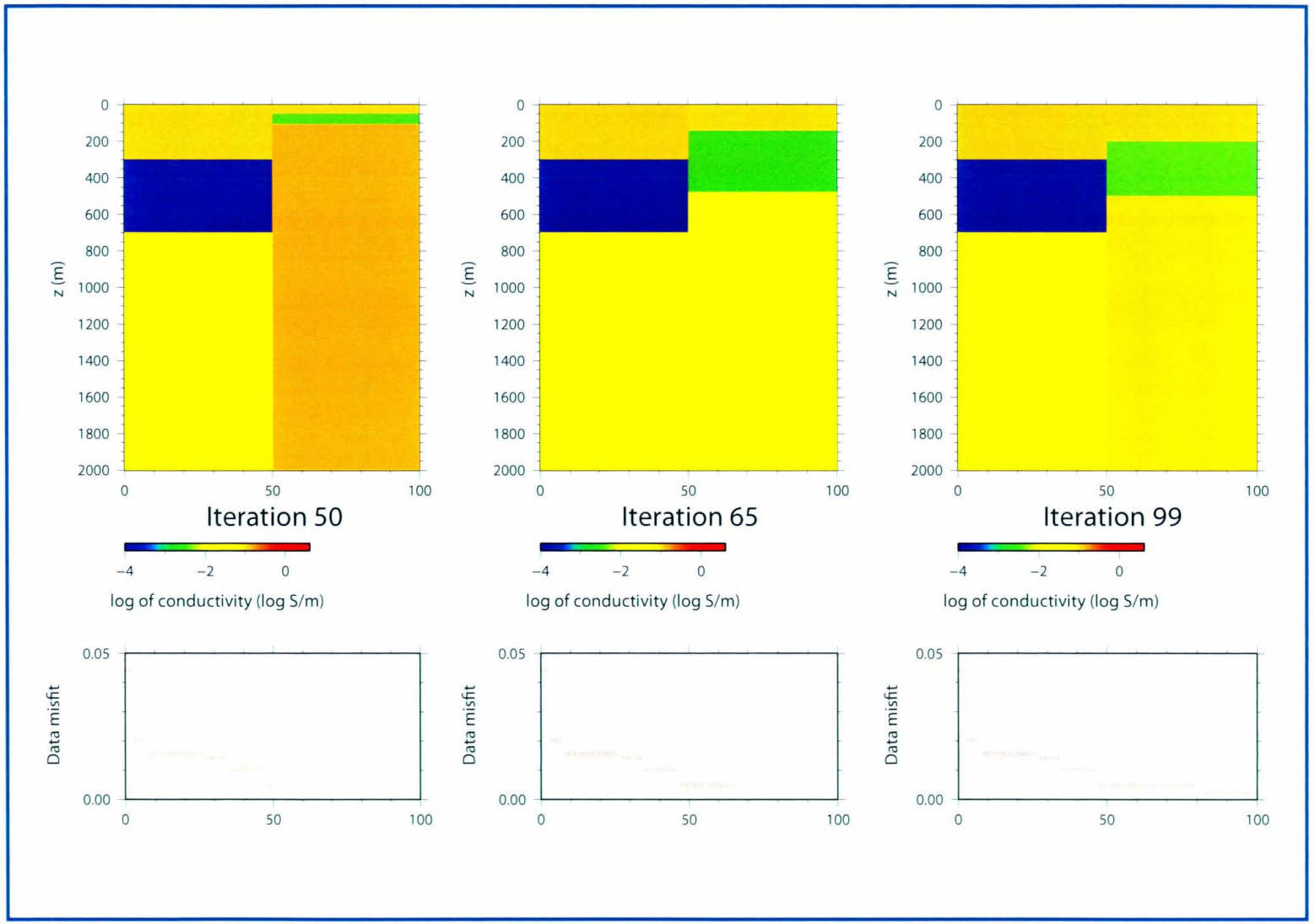

Figure 5.4: Comparison of true Earth layers (left) and the model with lowest misfit (right) at iterations 50, 65, and 99. Progression of collective misfit is shown in the lower panels.

regular intervals along the length of the profile, line B used 42, and line C used 56. 18 frequencies were used with a logarithmic distribution in the range $[5.4\times10^{-2}, 8.8\times10^{3}]$ Hz. In order to do this separate data files were compiled for each line. The data inverted were the unrotated real and imaginary xy components of the impedance tensor at each site and frequency, as were used by Spratt and Craven (2008). These results are shown in Fig. 5.5 to 5.7. It seems that along line A (Fig. 5.5) the PSO algorithm may try and deal with as few dimensions as possible so that the surface layer remains almost uniformly thin in each line, and of uniform condutivity. However a more likely reason for thinner layer generation in the PSO model lies in the unnormalized error term, $\phi_d = \sum_i (d_i^{obs} - d_i^{prd})^2$, which would effectively weight errors in larger-high frequency terms more heavily than lower frequency terms. This behaviour is repeated for lines B (Fig. 5.6) and C (Fig. 5.7). The 1D inversion in Fig. 5.5 was done by Spratt and Craven (2008) using the WinGlink^{TM} commercial inversion tool. The comparison for line A in this figure reveals that the thin surface conductor is likely an artifact of the PSO algorithm. PSO does reproduce a resistor (>1000 Ω m) toward the surface about 100 m thick shown by the WinGlink^{TM} software. Below this the PSO model's basement drops in resistivity to 100 Ω m as does the WinGlink^{TM} inversion. Line B shows a less continuous shallow (150 m) resistor, which is consistent with the WinGlink^{TM} inversion for line A. Line C shows a few stronger resistors at surface as well as further down into basement (500 m) roughly consistent with the WinGlink^{TM} inversion results.

All runs were done in under 100 iterations with 10000 particles and acheived a drop in misfit of 3 orders of magnitude, showing convergence of the algorithm.

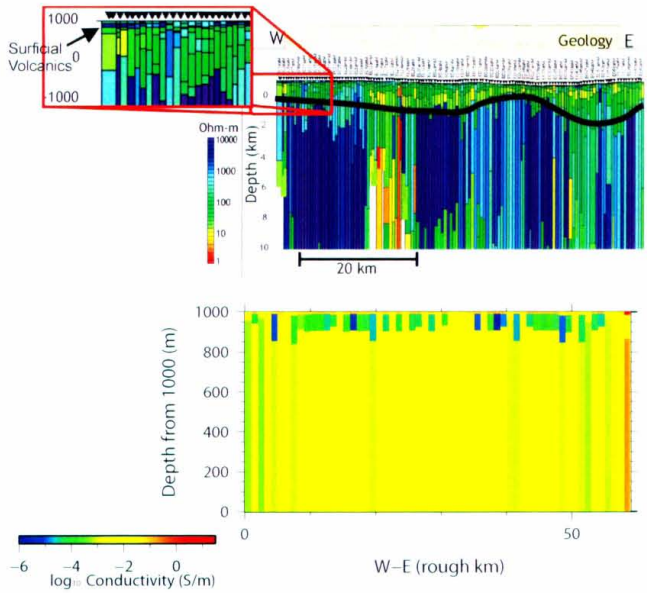

Figure 5.5: Comparison of PSO 1D model of line A of the Nechako basin data set (lower panel) with the modelproduced by Spratt and Craven (2011). PSO model shows high conductivity in red to orange, moderate conductivity in yellow to green, and low conductivity in green to blue. Reader should note vertical scale fo top inset similar to total scale of bottom model.

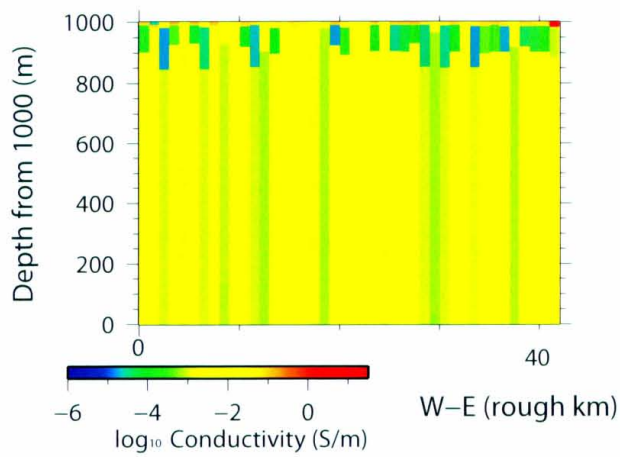

Figure 5.6: 1D conductivity model from PSO for line B. Conductivity shown on the colour bar as log(S/m).

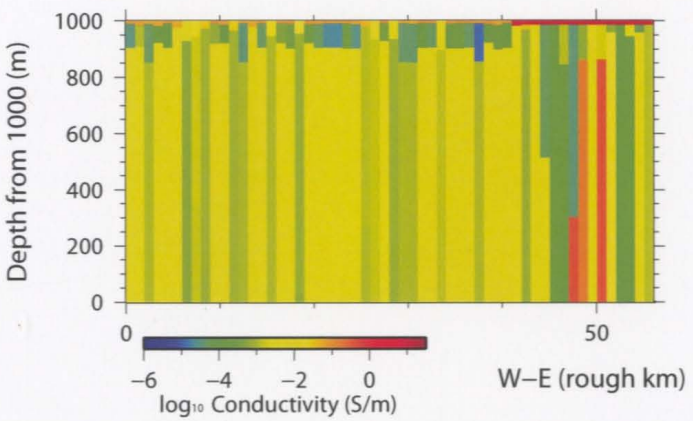

Figure 5.7: 1D conductivity model from PSO for line C. Conductivity shown on the colour bar as log(S/m).

Chapter 6

Data and Model Preparation

The following chapter is an account of the work done to prepare and organize the data for inversion, and to create the model mesh. Various pieces of code that were written by the author to aid in these processes will be explained, along with their inputs and outputs. The results of the inversion runs will be analyzed and interpreted for geological features and structure in Chapter 7.

The program MT3Dinv (discussed in § 4.2.2) was used to produce 3D conductivity models from the Nechako Basin data set. Being that this code cannot directly read data in EDI format (that in which the data were provided), there was a significant amount of reorganization and reformatting of data files and setup that needed to be done before starting the inversions. The inversion process was described in general in § 4.2.2, and more specifically for the case of MT3Dinv in Farquharson et al. (2002). Setting up an inversion required extracting the relevant impedances from the EDI files and shaping them into a single data file as required by MT3Dinv. These data then had to be manipulated into the proper coordinate system, which required a matrix

rotation. In order to check for "handedness" of the coordinate axes in MT3Dinv versus the measurement orientation, two sets of inversions were also performed for each parameter configuration with and without a sign change. The files for the inversion parameters, observed data, and the mesh needed to be packed in a bundle with a job control file and shipped to the ACEnet cluster for extended calculations on a parallel computing setup. Tipper data was not used during the course of this thesis. All C code and shell scripts described in the following sections were written by the author and are included in Appendix B. The process for setting up an inversion will be summarized in Fig. 6.9.

6.1 Spatial Data Selection

The MT data are stored in EDI format (Wight, 1987). Each EDI file contains the impedance data with respect to frequency for one site as well as site coordinates and acquisition parameters. An initial, preliminary exercise in data manipulation was undertaken. The exercise involved reading latitude/longitude site positions from each EDI file and plotting them using Generic Mapping Tools (GMT) (Wessel and Smith, 2011) as seen in Fig. 6.1. Not all sites from the Geoscience BC survey were used; only those lying inside the box used in the 3D inversion were included in the final data file. The exercise of mapping the data also served as a checking mechanism to ensure that coordinates in the data files matched up with those plotted up in the literature (Geosystem-Canada, 2007). Latitude-longitude plots were also used to check the UTM site coordinates in order to check lists containing site coordinates in both conventions for consistency. The UTM coordinates were used in the inversions.

The C program `pointChecker.c`, listed in Appendix B, is used to obtain a list of all sites that lie within a specified rectangle. This area, which is meant to eliminate portions of the survey space which do not have adequate cover for 3D inversion, lies between eastings UTM 10 410000-475000 m and northings 5827500-5887500 m. The output file contains three columns with each site's file name and x-y coordinates.

Site density was concentrated along the 2D lines, about five times more sites on these lines than in the rest of the study area. This increased concentration causes the inversion to focus most of the model structure along the 2D lines where it has the greatest effect on model misfit. To alleviate this problem the sites along these lines were thinned out.

Site thinning required separating sites into each of the lines A, B, C, and D, setting the others aside. The second step is to go through through each cell face at the top of the mesh, finding all sites with coordinates lying in that cell. The progression through cells went from west to east, working its way from north to south. The impedance components from all sites within the same cell in the inversion mesh were averaged and a new site was made with the averaged measurements at the mean of the site locations, e.g.,

$$Z_{jk}^{ave} = \sum_{i=0}^{K} Z_{jk}^{i}/K, \tag{6.1}$$

where K is the number of sites in that cell being averaged. Once the sites were averaged, every third site could be chosen and written into the data file. In this way, a more uniform lateral distribution was achieved between the stations along the primary profiles and the fill-in stations.

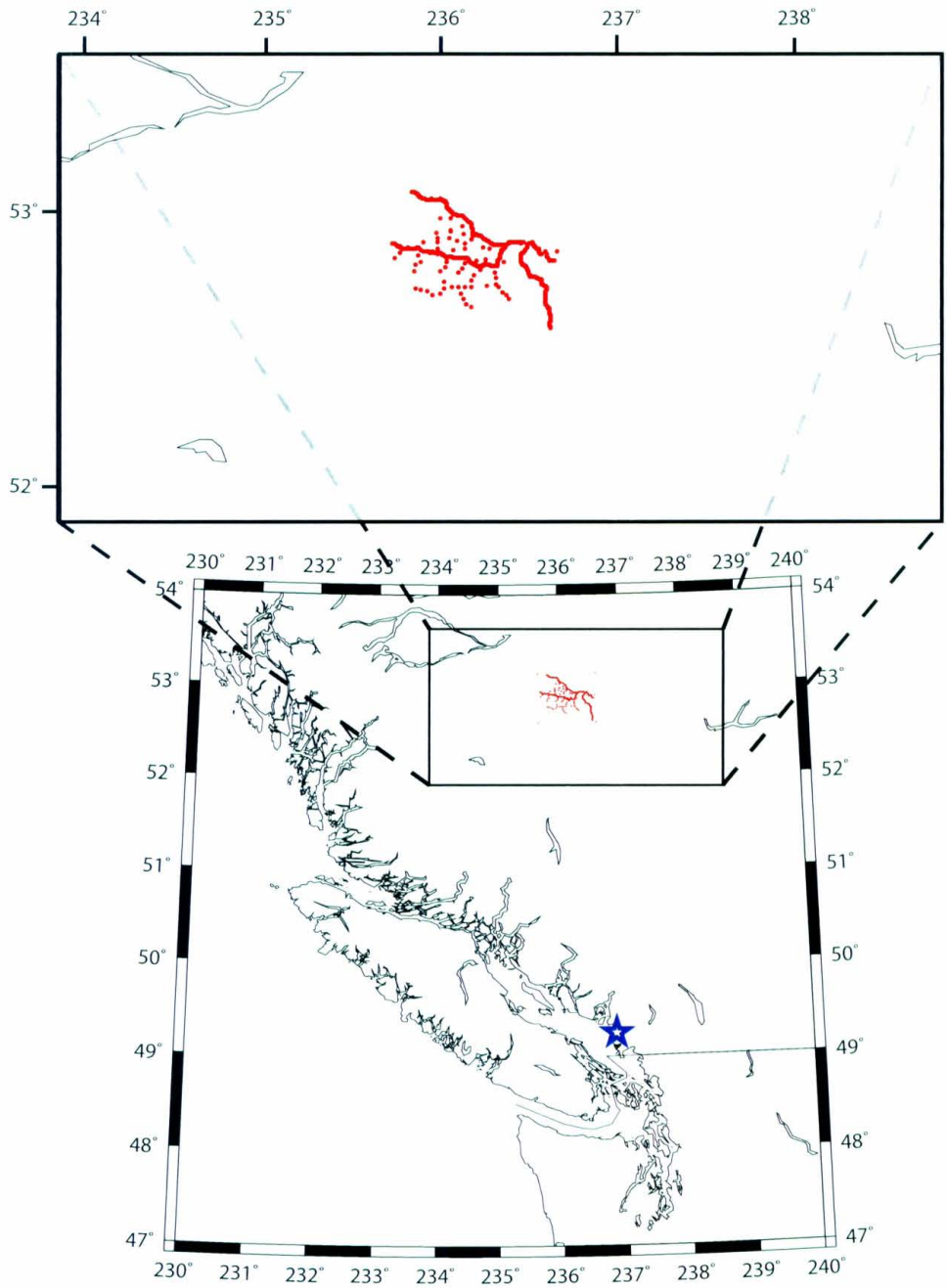

Figure 6.1: A map of survey sites used for 3D inversion. Survey sites are shown in red, the blue star is Vancouver and the black line is the British Columbian border with Washington State, U.S.A.

6.2 Frequency-Based Data Selection

In preparation for an inversion run a subset of frequencies needed to be selected because using all of them was computationally infeasible. The frequencies to be used in the inversions were chosen based on a histogram which displayed the number of sites with measured frequencies lying in the range of each bin seen in Fig. 6.2. For this data-set, all sites were shown in the histogram to have data at the same frequencies. This meant that binning a selection was not an issue. Inversions using different numbers of frequencies chose a subset of frequencies distributed uniformly between 0.00042 to 7200 Hz.

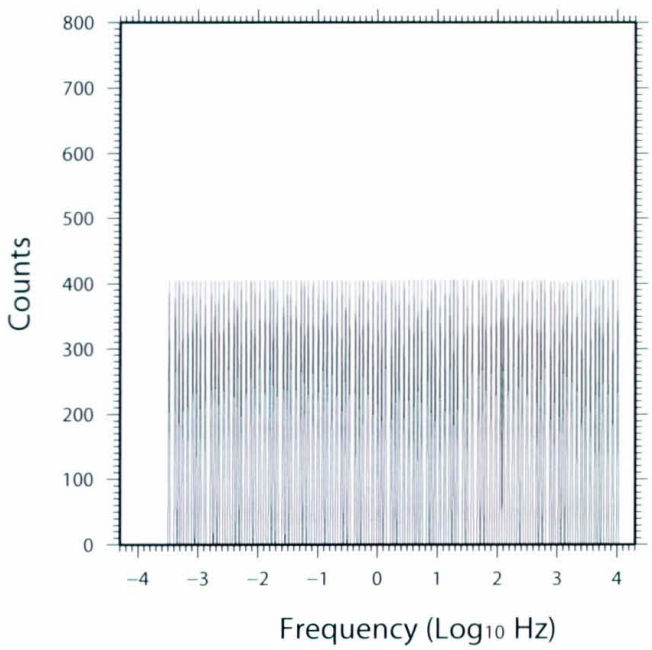

Figure 6.2: Histogram displaying the number of sites within the selection rectangle which have measurements within each frequency bin. This shows a good amount of sites measuring at each frequency. All frequencies are measured for each site so that all are useful for the inversion.

6.3 Data Plotting

Once sites were picked, a C-macro (`impPlotter.c` in Appendix B) was written to read in impedance information from the EDI files for the sites used and plot them using GMT. A C-shell script plotted these impedances versus frequency, with the square root of the variances from the EDI files drawn as error bars (Fig. 6.3). Another C-shell script plotted up apparent resistivity and phase against frequency (Fig. 6.4).

Once the impedances were read from the EDI files, they could be written into data files formatted by this author for MT3Dinv. However, the EDI format coordinate axes (z-axis into Earth, y-axis due east, x-axis due north (Wight, 1987)) differ from the axes used in the inversion software (z-axis out of Earth y-axis due north, x-axis due east (UBC-GIF, 2003)), and so a tensor rotation was required before the data files were useful. Here a second stage data processing C-macro (`impRot.c` in Appendix B) performed the change of coordinates, described in Appendix A. A sign change to the on-diagonal elements was potentially required, although unclear in the documentation so that models with and without the sign change were run. This gave an additional measure of dimensionality: were the models with and without sign change were similar, the Earth produced a 2D response, where they were dissimilar, it produced a 3D response.

Impedance maps of the observed and predicted data were plotted using GMT to compare observations with inversion results. Examples of maps of observed data are shown in Figs. 6.5 and 6.6.

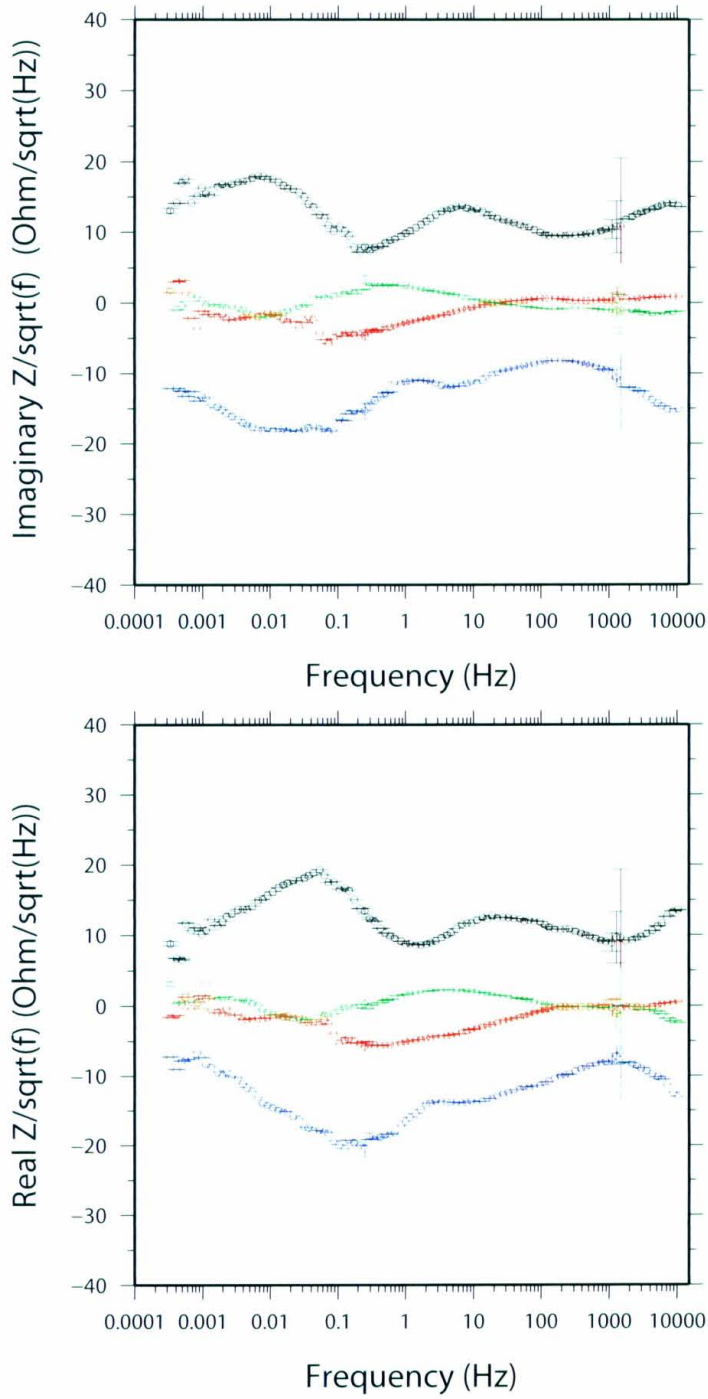

Figure 6.3: Components of impedance with error bars taken from pre-existing uncertainties estimated in the EDI files for site DD20amM. Z_{xx} in red, Z_{xy} in black, Z_{yx} in blue, Z_{yy} in green.

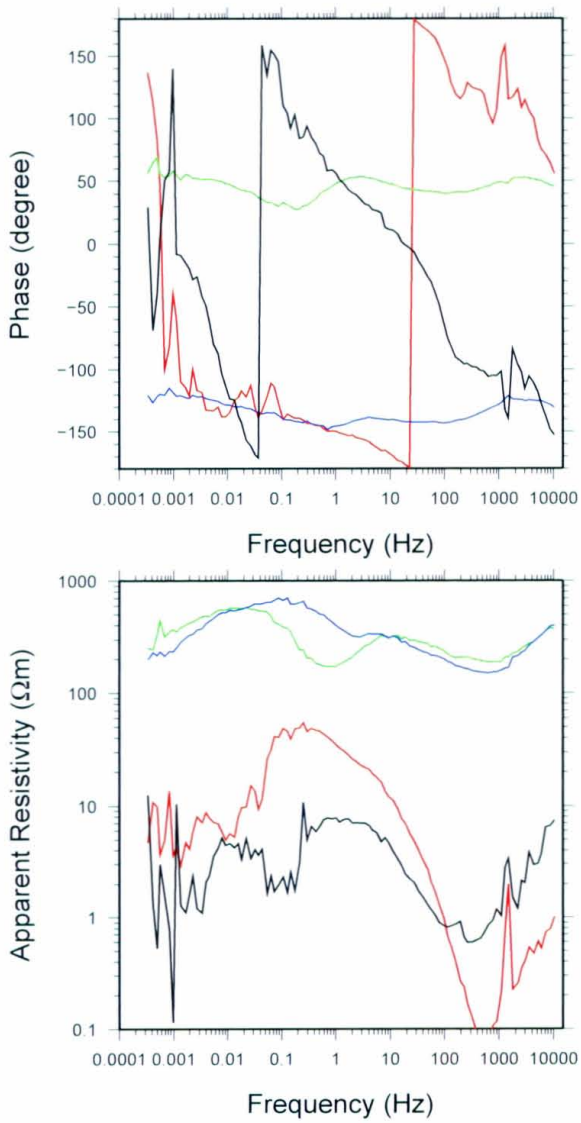

Figure 6.4: Apparent Resistivity and phase versus frequency for site DD20amM. XX components in red, YX in black, YX in blue, and YY in green.

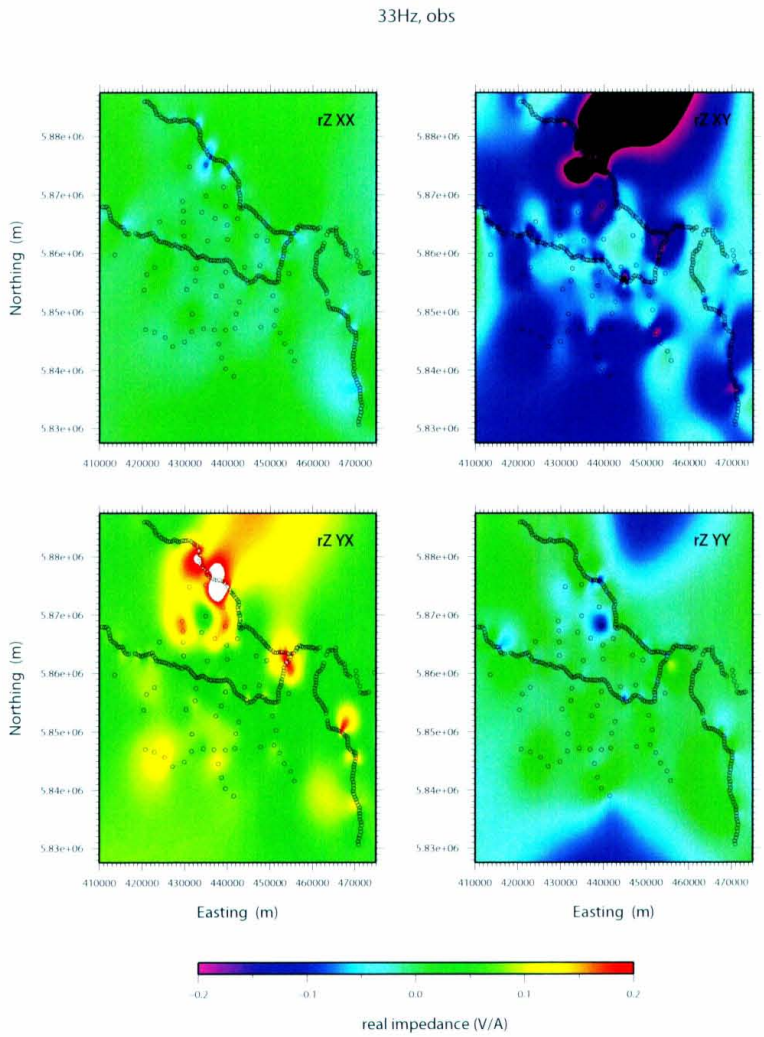

Figure 6.5: Real part of observed impedance for 33 Hz. Site locations indicated (not thinned) by circles.

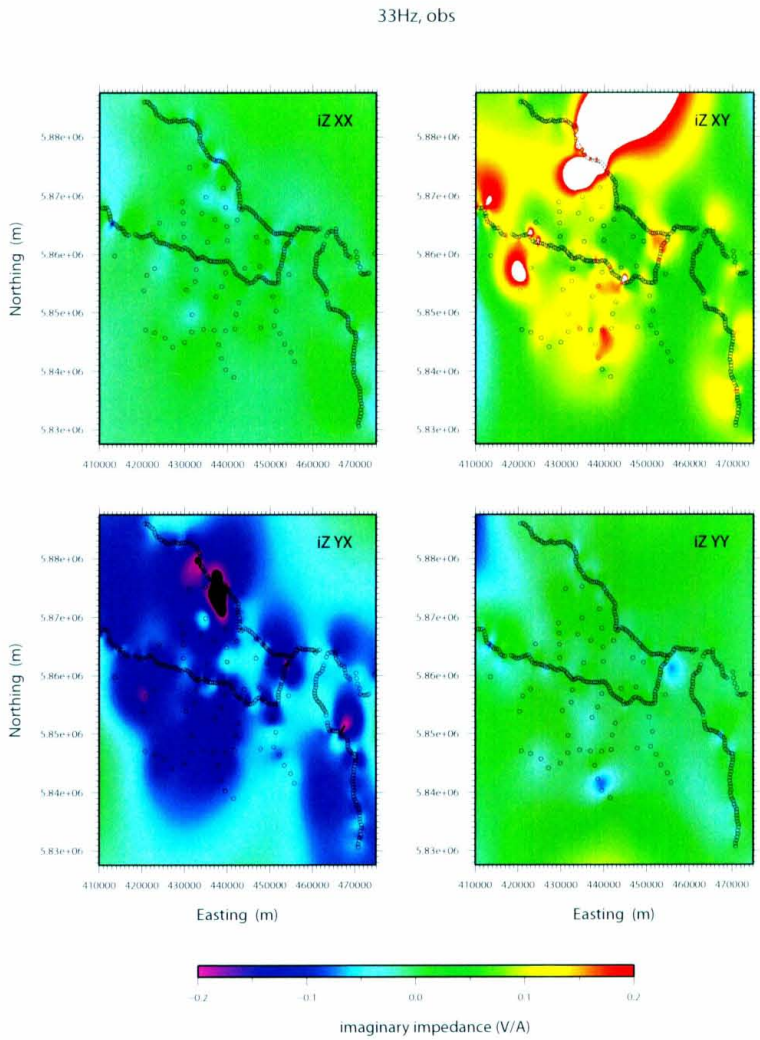

Figure 6.6: Imaginary part of observed impedance for 33 Hz. Site locations (not thinned) indicated by circles.

6.4 Mesh Making

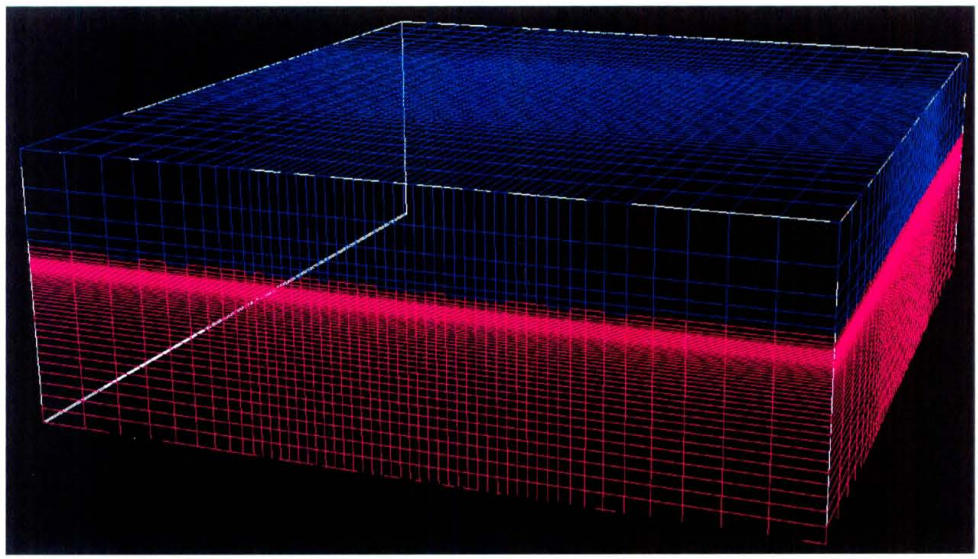

Figure 6.7: An example 3D inversion mesh, colouring indicates conductivity structure of homogeneous half space. Mesh dimensions are 50, 50, and 50 in the x,y, and z directions.

In order for the boundary conditions used by MT3Dinv (described in § 3.3) to hold, meshes must have enough padding cells so that the boundary of the mesh is sufficiently far from the central zone of interest that the secondary field is close enough to zero. At the same time the mesh is required to have higher resolution cells in the region of interest in order to be smaller than the skin depth at the highest frequency used in order for the finite-difference solution not to deteriorate (as seen in Fig. 6.7). Using eq. 2.15 for skin depth with $f = 1Hz$ and $\sigma = 0.01S/m$, a typical skin depth in the Nechako Basin is 12.6 km, however this varies considerably with surface conductivity. Full maps of skin depth at each frequency for the main model presented in this thesis are included in Fig. C.1-C.12.

The C code `meshWriter.c` (see Appendix B) reads in the amount of desired padding to be produced in the mesh, the coordinates of the study area limits, the resolution in the study area, and the number of cells in each direction and generates the mesh parameters in the format required by MT3Dinv. A geometric series is solved for an exponential rate of increase in cell size from the study area out through the padding cells:

$$a\left(\frac{1-r^{n'}}{1-r}\right) = \Sigma, \tag{6.2}$$

$$n' = \frac{n - \Delta y/a}{2}, \tag{6.3}$$

where r is the exponential rate of increase, a is the cell resolution in the area of interest, Δy is the width of the area of interest, Σ is the total mesh width, n the total number of cells, and n' is the number of padding cells to the left and right of the study area as portrayed in Fig. 6.8. These equations are solved with a brute force algorithm which simply loops through values for the exponential increase, r, until these constraints are satisfied within the desired tolerance.

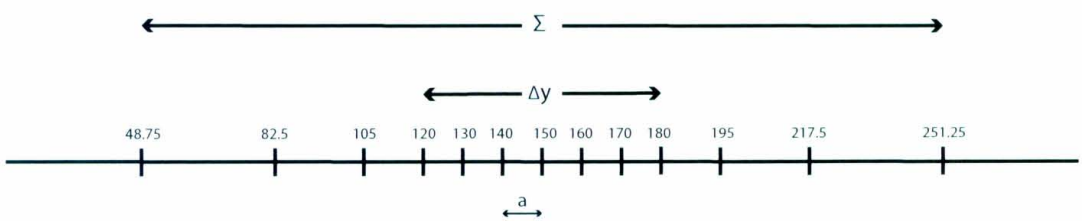

Figure 6.8: Cell resolution here is $a = 10$, with an exponential increase factor of $r = 1.5$ which would normally be solved for. Σ is the total mesh width, Δy the study area width, n the total number of cells, and n' the number of padding cells to the left and right of the study area.

6.5 Data Formatting for Inversion

Given that the inversion code was run on High Performance Computing Clusters, (Computing, Simulation and Landmark Visualization cluster located in the MUN Earth Sciences Department and the ACEnet machines located around Atlantic Canada) the bundle of inversion files and commands had to be arranged for parallel computing. The job scheduler on both the CSLV and the ACEnet machines is N1 Grid Engine written Sun Microsystems. This provided the means of job submission, deletion, monitoring, and manipulation. This information bundle was produced from MT data processed into EDI files and a parameter file in XML format. These files were read by various C programs performing math and file I/O, which were in turn compiled and run by the control shell. The flow of information used to format the input data, create the input bundle, and start an inversion run is laid out in Fig. 6.9.

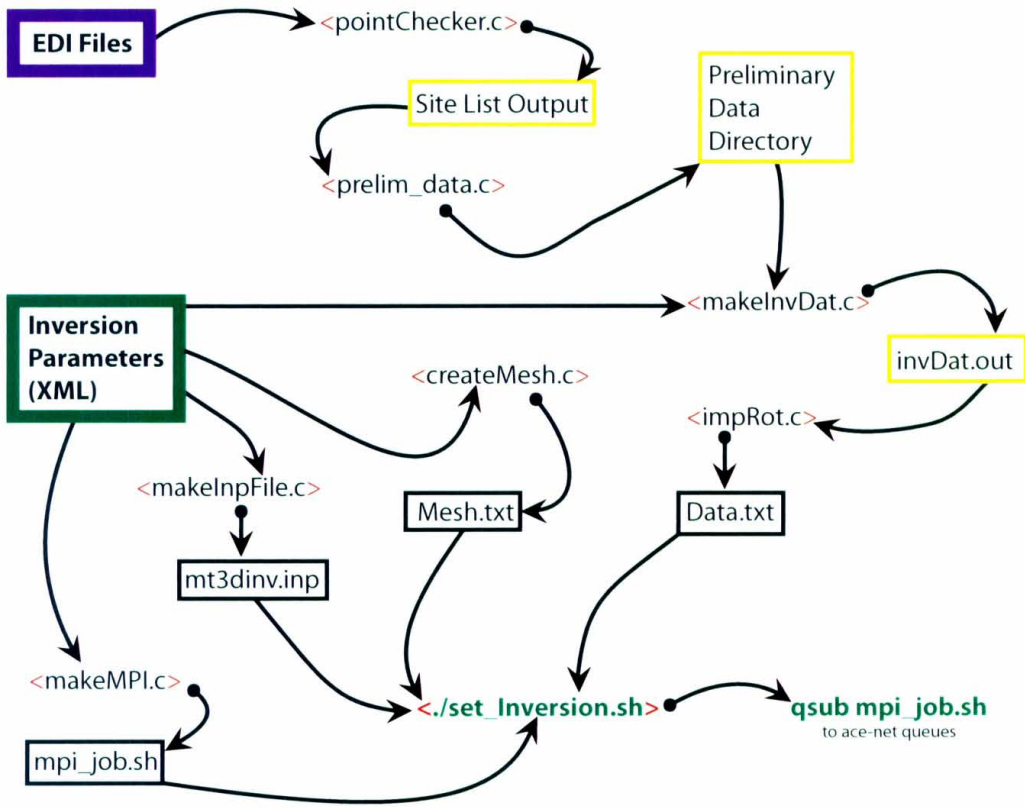

Figure 6.9: Flowchart of information flow during the setup for an inversion. Starting information is seen in purple and green, C code in red angled brackets, temporary files in yellow boxes, output files in black boxes, and relevant commands/files for initiating an inversion in green. Code is included in Appendix B.

Chapter 7

Results

7.1 Introduction

In this chapter the 3D inversion results for the Nechako Basin data-set will be summarized, identifying key features of the inversion models and comparing them with the 2D MT inversion results for the profiles and information from other sources. A suite of models was developed which is listed in Table 7.1. All results are included in Appendices C and D. The various models were run so as to see the results of the increase in model resolution, sign change, and site thinning on the conductivity structure. These results were not far enough along, however, at the time of writing for an in depth examination.

Table 7.1: Summary of inversions that were run

No.	No. Cells	No. Freqs	Freq Range (Hz)	Comments
1	50x50x50	8	$[6.9 \times 10^{-4}, 6.0 \times 10^{3}]$	with sign
2	50x50x50	8	$[6.9 \times 10^{-4}, 6.0 \times 10^{3}]$	no sign
3	62x62x62	8	$[6.9 \times 10^{-4}, 6.0 \times 10^{3}]$	with sign
4	62x62x62	8	$[6.9 \times 10^{-4}, 6.0 \times 10^{3}]$	no sign
5	75x75x75	8	$[6.9 \times 10^{-4}, 6.0 \times 10^{3}]$	with sign
6	75x75x75	8	$[6.9 \times 10^{-4}, 6.0 \times 10^{3}]$	no sign
7	50x50x50	16	$[4.2 \times 10^{-4}, 7.2 \times 10^{3}]$	with sign
8	50x50x50	16	$[4.2 \times 10^{-4}, 7.2 \times 10^{3}]$	no sign
9	62x62x62	16	$[4.2 \times 10^{-4}, 7.2 \times 10^{3}]$	with sign
10	62x62x62	16	$[4.2 \times 10^{-4}, 7.2 \times 10^{3}]$	no sign
11	75x75x75	16	$[4.2 \times 10^{-4}, 7.2 \times 10^{3}]$	with sign
12	75x75x75	16	$[4.2 \times 10^{-4}, 7.2 \times 10^{3}]$	no sign
13	50x50x50	34	$[3.4 \times 10^{-4}, 8.8 \times 10^{3}]$	with sign
14	50x50x50	34	$[3.4 \times 10^{-4}, 8.8 \times 10^{3}]$	no sign
15	62x62x62	34	$[3.4 \times 10^{-4}, 8.8 \times 10^{3}]$	with sign
16	62x62x62	34	$[3.4 \times 10^{-4}, 8.8 \times 10^{3}]$	no sign
17	75x75x75	34	$[3.4 \times 10^{-4}, 8.8 \times 10^{3}]$	with sign
18	75x75x75	34	$[3.4 \times 10^{-4}, 8.8 \times 10^{3}]$	sign
19	75x69x70	16	$[4.2 \times 10^{-4}, 7.2 \times 10^{3}]$	with sign
20	75x69x70	16	$[4.2 \times 10^{-4}, 7.2 \times 10^{3}]$	no sign
21	75x69x70	16	$[4.2 \times 10^{-4}, 7.2 \times 10^{3}]$	with sign, thinning
22	75x69x70	16	$[4.2 \times 10^{-4}, 7.2 \times 10^{3}]$	no sign, thinning

7.2 Low Resolution Model with 16 Frequencies

7.2.1 Inversion Parameters

16 frequencies were incorporated evenly in log space over the range $[4.2 \times 10^{-4}, 7.2 \times 10^{+3}]$. The mesh dimensions (number of cells in the x, y, and z directions) are $n_x = 50$, $n_y = 50$, and $n_z = 50$ (the mesh is shown in Fig. 6.7). Cell width in the area of interest is 2167 m EW, 2000 m NS, and 200m vertically. The area of interest is 65 000 m east-west and 60 000 m north-south (eastings 410000-475000 m and northings 5827500-58875 m as described in § 6.1). Vertical cell thickness starts increasing by a factor of 1.1 after a depth of 2000 m. A negative multiplier for on-diagonal impedance elements was included. All 403 sites which lie inside the area of interest were used in this inversion run. The majority of those sites are concentrated in the 4 profiles which were used for the 2D inversions (Spratt and Craven, 2011). As a result some cell columns have more than one site on top so that these cells are preferred in the modelling process and get more of the structure because of far greater emphasis in the data-fitting portion of the inversion than a cell with one site. Also, any disagreement between sites lying on the same cell face is almost impossible for the inversion to reproduce. This proved, however, to be an obvious issue at the surface of only one cell column. The inversion model was produced in 45 iterations with a step factor in β of 0.5, starting at 1000 and ending at 2.84×10^{-11} (β is the trade-off parameter which controls amount of model structure listed as λ in eq. 4.18). 8 nodes on the ACEnet cluster at 7 Gb memory each were used and each iteration took less than 250 hours computation time (on each node) for a total run time of under 11 250 hours. This inversion was chosen (model 7 in Table 7.1) to be presented in the body of this thesis

because it had undergone the most iterations and therefore had the largest drop in ϕ_d. Examples of impedances synthesized from this model (predicted data maps) at 33 Hz can be seen in Fig. 7.1 and 7.3. Maps (of both observed and predicted data) for all other frequencies can be found in Appendix C. These impedance maps were the primary tool for checking data fit. Numerical values of misfit were used only for checking model convergence as these values can over simplify 3D model misfit, it is necessary to know where/how the model is deviating from the Earth.

As seen in Fig. C.1-C.12, MT wavelengths are already penetrating 20 km into the model in some areas by 0.59 Hz, whereas in other areas EM waves have already died out within the uppermost kilometre at this frequency.

In Fig. 7.5, several features are immediately apparent. At the meeting point of lines A, B, C, and D a strong conductor is present, which is interpreted as a sedimentary deposit, perhaps the most promising hydrocarbon exploration target. This area is supposed to be overlain with resistive basalt, but likely the thickness is not enough for MT to detect it here but this is visible adjacent to the west. Conductors to either side of line B are probably faults running alongside a basement resistor. In general, more resistive areas have been interpreted as volcanic deposits, while less resistive features have been interpreted as sedimentary deposits. Conductivity features are examined more thoroughly in comparison with other data in § 7.2.2, 7.2.3, and 7.2.4.

Maps of frequency based observed and predicted data show poor data fit at frequencies above 900 Hz (see Fig. C.13 and C.14). At 900 Hz model response begins to fit the data well with mostly a 2D response (on diagonal tensor elements are mostly constant, similar to observed impedances) as seen in Fig. C.15. Predicted data con-

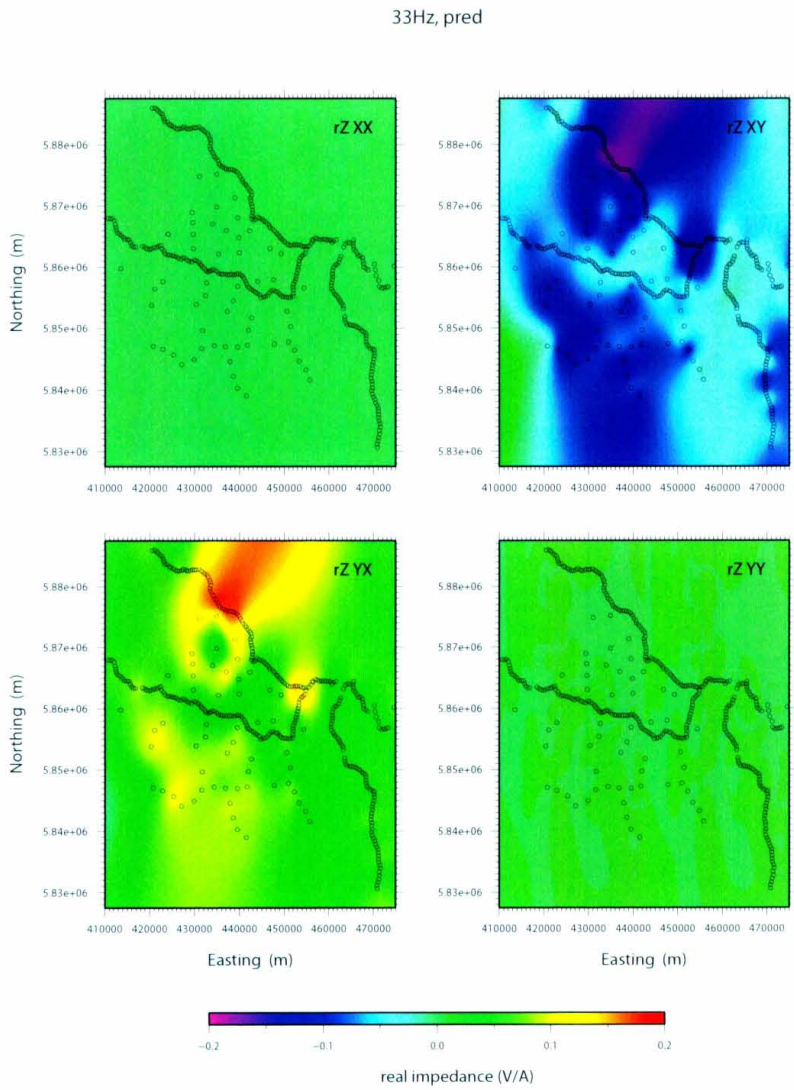

Figure 7.1: Real part of impedances for 33 Hz for data computed for the final model of the inversion discussed in § 7.2. Real observed data are in Fig. 7.3. See Appendix C for maps of data for all other frequencies included in the inversion.

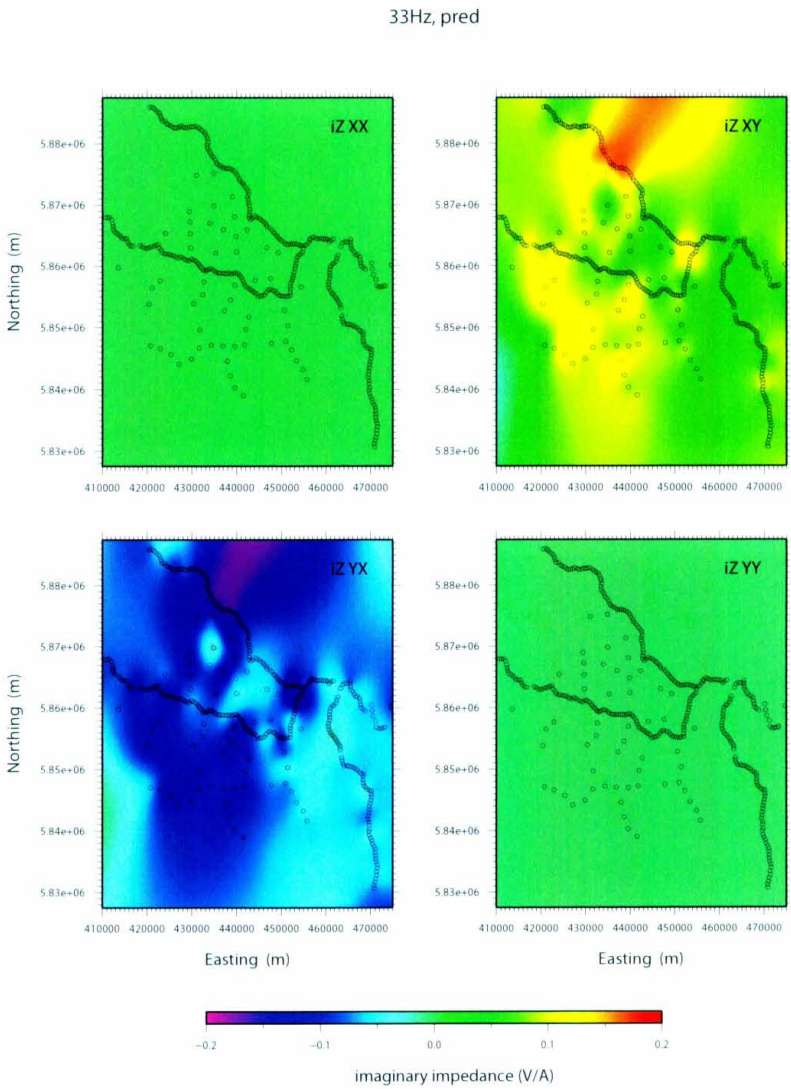

Figure 7.2: Imaginary part of impedances for 33 Hz for data computed for the final model of the inversion discussed in § 7.2. Imaginary observed data are in Fig. 7.4. See Appendix C for maps of data for all other frequencies included in the inversion.

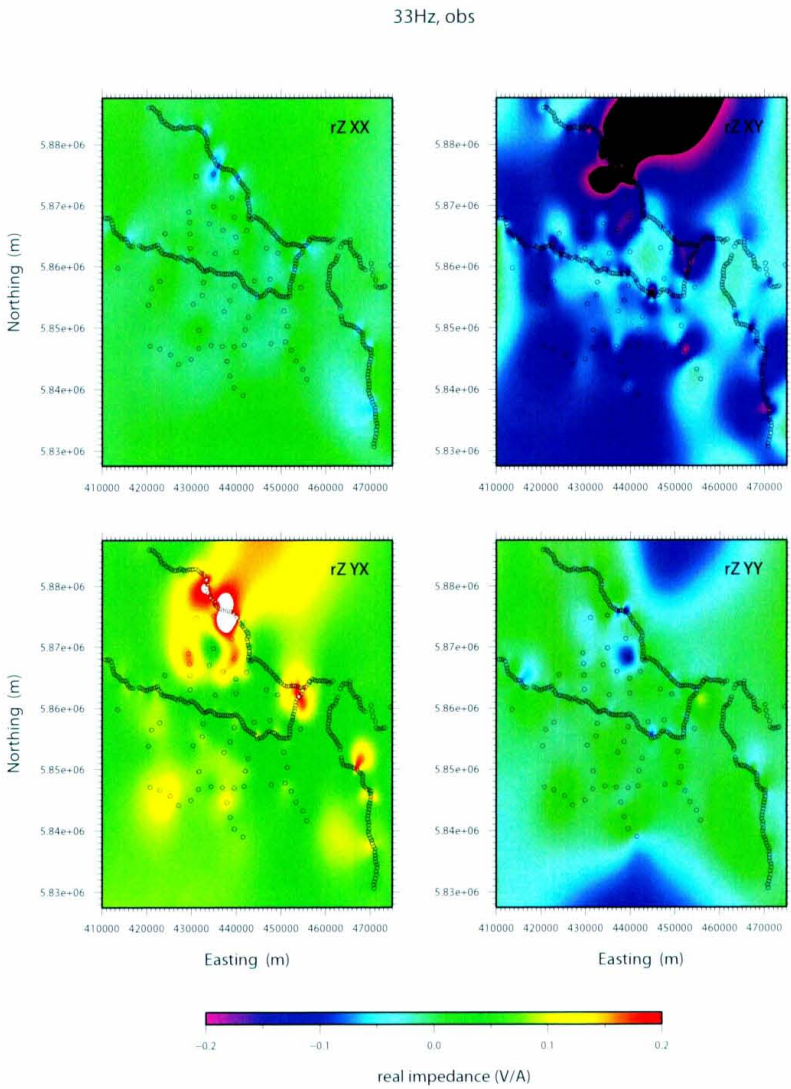

Figure 7.3: Real part of impedances for 33 Hz from acquired data, real predicted impedances are in Fig. 7.1. See Appendix C for maps of data for all other frequencies included in the inversion.

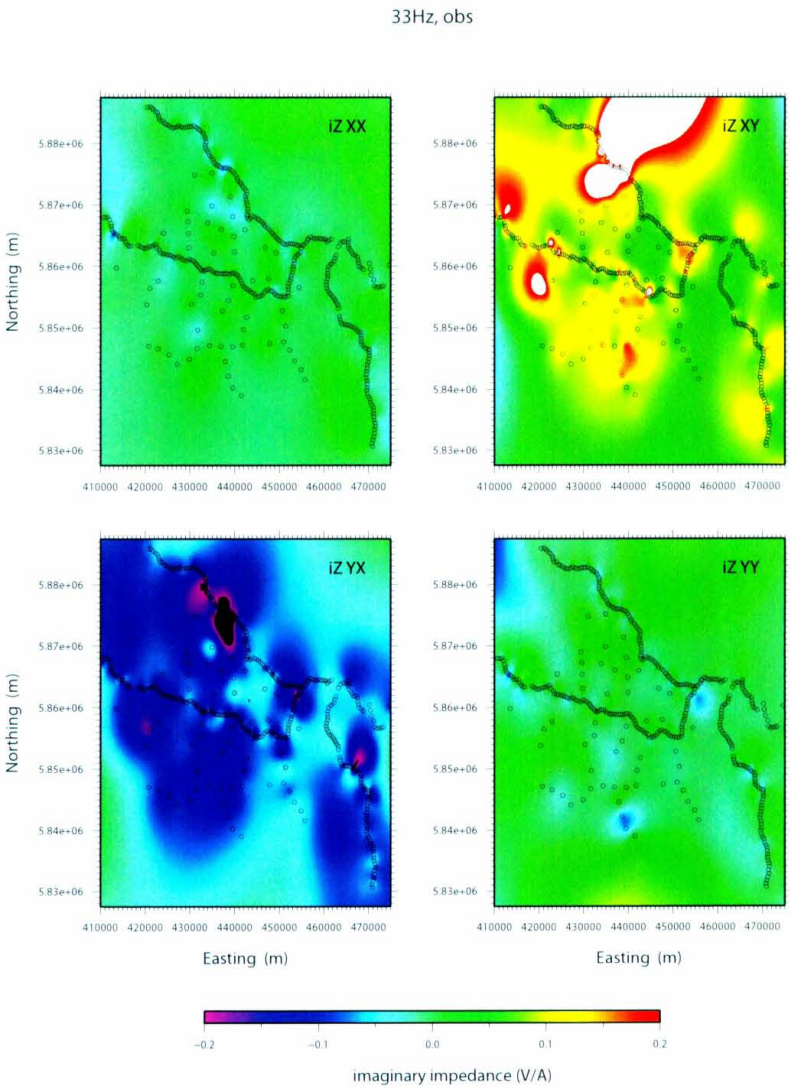

Figure 7.4: Imaginary part of impedances for 33 Hz from acquired data. imaginary predicted impedances are in Fig. 7.2. See Appendix C for maps of data for all other frequencies included in the inversion.

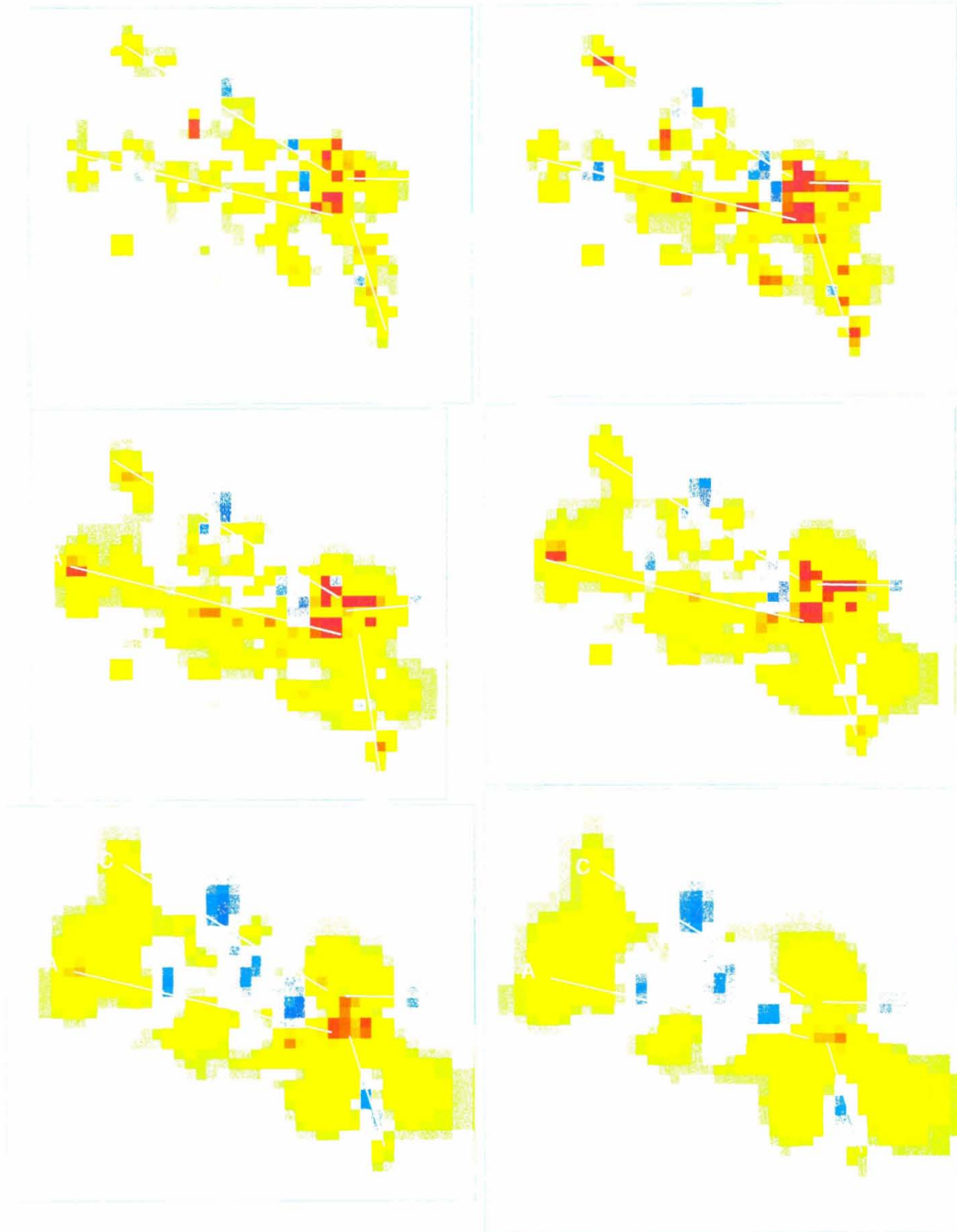
C
A
C
A

tinue to match the observed data better throughout the rest of the frequency range. Data fit is very tight along the 2D lines, but is good at infill sites as well. At 0.59 Hz (Fig. ??) The on diagonal impedance elements of the observed data begin to exhibit stronger amplitudes and predicted data start to exhibit similar change, showing increasing dimensionality of the model at lower frequencies. Skin depth maps show sites around Nazko are predominantly measuring the upper most 10 km of the Earth at frequencies above 0.215 (Fig. C.10 and C.11) meaning that the dimensionality increase here is fairly shallow and that strong conductivity is well fitted in the data.

Frequencies below 0.59 Hz show sensitivity to a mid crustal conductor identified in § 7.2.2. This mid-crustal conductor is well fitted below 0.59 Hz in the data between lines A and C in the off-diagonal impedances, however on-diagonal elements of the observed data show low amplitude in comparison and are not exhibited in predicted data. Slight on-diagonal fit can be seen at 0.073 Hz in Fig. ??. This mid-crustal conductor is also seen in several other models which have not pregressed through as many iterations (e.g. Fig D.31 or D.19)

Overall, observed and predicted data maps qualitatively show a good fit at all sites in the data, with a natural emphasis on 2D lines due to increased site concentration. The 3D inversion has allowed for more accurate lateral placement of conductive features, some of which lie off the 2D measurement lines. As well these features have been shown to be laterally limited (such as the mid-crustal conductor) or extensive (such as the crustal scale faulting seen in Fig. 7.10).

7.2.2 Comparison with 2D MT Inversion Results

The 2D inversions performed by Spratt and Craven (2010) provide a high resolution image of the subsurface. Since the 3D models are limited by computer memory, they have a much lower resolution than the 2D models. However, they do have a strong suit: a three-dimensional and hence truer representation of the actual dimensionality of the Earth. In this section the 2D inversion results will be compared with the portions of the 3D model which coincide with the 2D models.

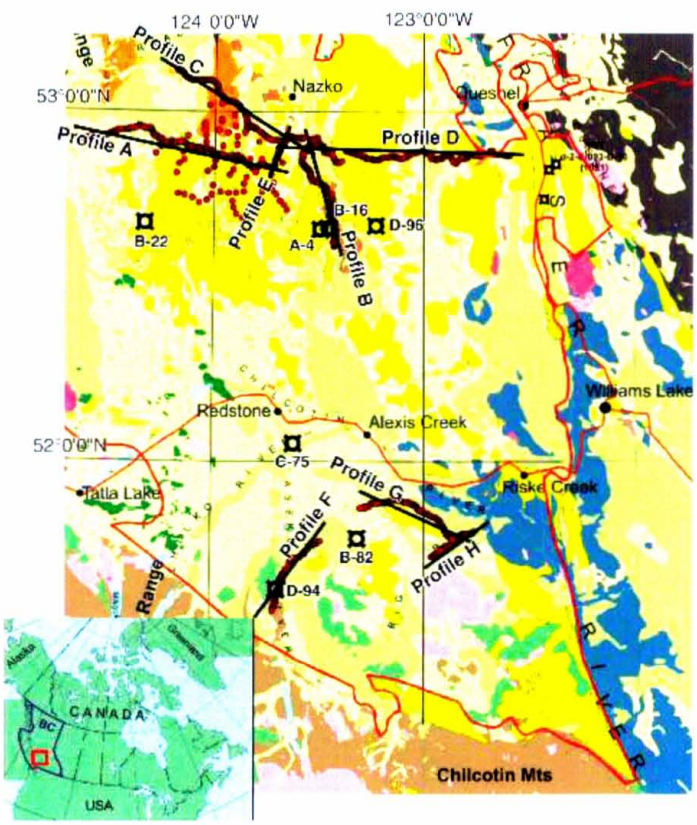

Figure 7.6: Relative positioning of MT measurement lines and the town of Nazko overlying local geology, after Spratt and Craven (2010).

2D inversions were performed by Spratt and Craven (2010) over 200 iterations

at frequencies between 10000-0.001 Hz. These data were inverted with apparent resistivity and phase (as opposed to full impedance tensor values used in the 3D inversion). Error floors for data were 7% for apparent resistivity and 2^o for phase.

Fig. 7.7 juxtaposes the profile A 2D inversion by Spratt and Craven (2010) with a slice through this author's 3D model from inversion 7 (see Table 7.1). This line runs roughly east-west through the middle of the area of interest (see Fig. 6.1). Immediately a great drop in resolution from the 2D to the 3D model is evident and features which are sharp in the 2D section are smeared out in the 3D model and even appear away from the location of the feature in the 2D section. The resistive Chilcotin basalt in the east of the section, labelled "A", is more apparent to the north of this line in the 3D volume. The mid-crustal conductor (E) is dimmer and deeper in the 3D model on this line than in 2D, but becomes brighter to the northeast of this section at depth. The surface conductor in the west (I) may be an aggregate of conductivity seen extending past the data cut off in the bottom section. This bright spot, i.e. higher conductivity, is interpreted as Eocene volcanic and sedimentary rock by Spratt and Craven (2011). The Hazelton basement (D+G) appears to be robust between both models, but slightly more resistive in 2D. Structure underlying the Eocene volcanic and sedimentary rock to the east of the dark Hazelton basement resistor may not be resolved in 3D because of low model sensitivity below the bright spot in the upper west portion of the model section, it is uncertain how the 2D inversion algorithm is handling the drop in sensitivity. Cretaceous sedimentary rock (F) is clear in both 2D and 3D models. Broad surficial elements agree decently (F, H, I), as well specific elements are similar but so a lesser degree (A and C).

Profile B (see Fig. 7.8) runs south from the town of Nazko along the Nazko river.

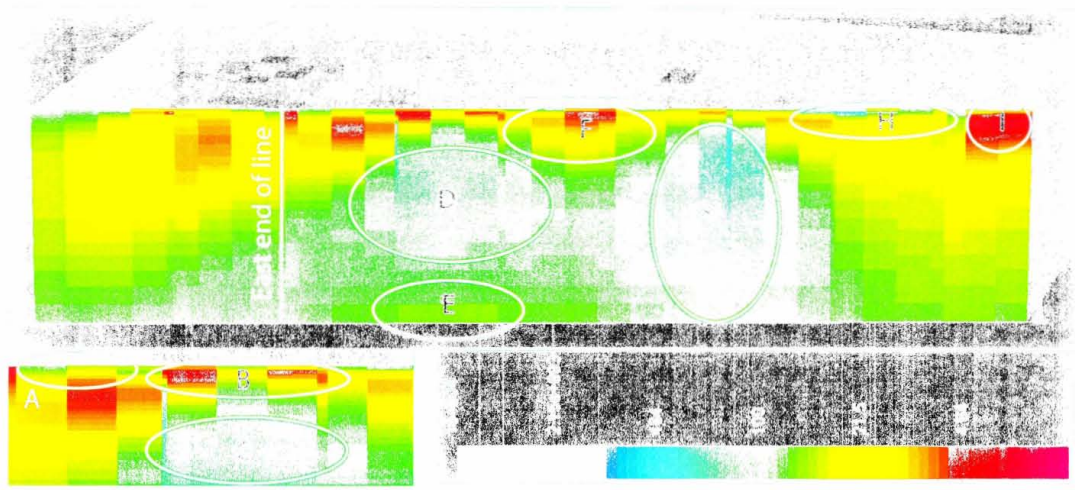
East end of line
A
B
D
E
F
RMS = 2.2

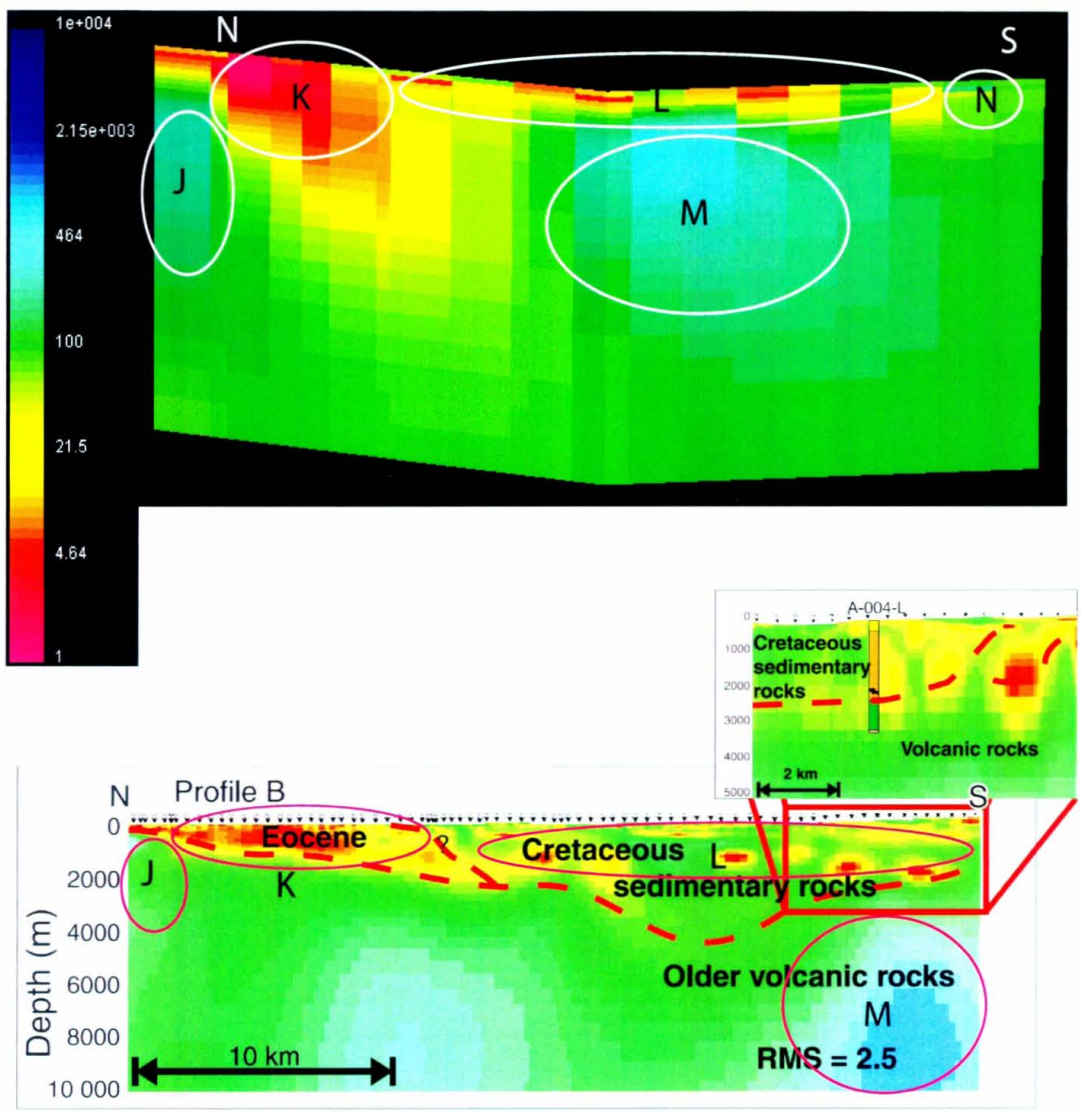

Figure 7.8: A comparison of a slice through 3D model (top) along the same orientation as profile B and the 2D section from Spratt and Craven (2010) (bottom). Description in main text. Colour bar shows units in Ωm for both models.

A fault runs through this area (Spratt and Craven, 2011) which could contribute to the dipping strong conductor (weak resistor at 5-50Ω m) K in the north portion of this section. This Eocene conductor (K) is evident in both the 2D and 3D sections. Structure off the sides is supported by the impedance maps for 320 Hz to 0.215 Hz in Appendix C. It is also possible that high conductance at the surface is lowering sensitivity to the resistor in the 3D volume. Minimum-structure inversion draws out the drop in conductivity for this body into the region where it has little sensitivity, perhaps the higher resolution (and increased structure) of the 2D model has allowed conductivities to vary more in this zone. This conductor is sensed by frequencies in the range 4.7 Hz - 0.073 Hz, and observed and model response impedance maps (see Fig. C.20-C.24) for these frequencies show good agreement in that area. Skin depth trends give a good idea of sensitivity in this area (see Fig. C.8-C.12), being that they stay shallow (less than 1 km for frequencies above 10 Hz) for most of the range, then quickly reach the bottom of the model in a few frequencies. This indicates a lack of emphasis in the calculation of data misfit at the bottom of the conductor. Globular conductors interpreted as Cretaceous sedimentary rock (L) by Spratt and Craven (2010) are collected thinly toward the surface in the upper image and are more laterally continuous. The localization of these conductors around points is noteworthy in the 2D section. The D^+ method states that MT responses stemming from a finite set of frequencies are reproduceable using finite sets of δ functions (Parker and Booker, 1996; Miensopust, 2010). This means that spikes in conductivities can satisfy MT responses during modelling of data, which would occur if the 2D inversion is unable to sufficiently lower the misfit using sensible models. This spikiness in 2D may be an artifact from essentially over-fitting the data (although the D^+ method has not

been shown to apply for full 2-D inversion), or, potentially arising from anisotropy. An example of anisotropic response from conductors can be seen in Boerner et al. (2000). Also rising to shallower depths, the resistor labeled "Older volcanic rocks" (M) is closer to the surface in the 3D model, perhaps because of a lack of sensitivity. This feature also appears to move northward in the 3D volume, although this could be an artifact of the perspective of the 3D model image in Fig. 7.8. At N, the top of the section gets more resistive in 3D than 2D. There is little difference between the model presented here and its cousin without the sign change in Fig. D.2 implying a 2D behaviour in the Earth.

Profile C (see Fig. 7.9) covers the northern-most portion of the study area, running north-west to south-east. The eastern-most portion approaches Nazko, and runs into the same area as the western portion of profile D. One difference which is readily observable in Fig. 7.9 is the deviation of the mid-crustal conductor (P) to the east in the upper image. As mentioned previously, this conductor lies out of profile and, in addition to the difference of the full impedance tensor being used to derive the upper image in comparison to just the off-diagonal elements used in the lower image, could also be emphasized here as a result of structure minimization by the inversion (placing the conductor in the center of the two resistors as opposed to closer to either which would effectively increase the measure of structure). The 2D inversion may also image the conductor better beneath the Hazelton unit and places it on section beneath that resistive feature. The 2D inversion is therefore likely laterally misplacing the mid-crustal conductor because of a geometric limitation. As well, it is not apparent from the 2D inversion whether this conductor seen in both lines A and C is laterally continuous past the study area but 3D results show that it is not

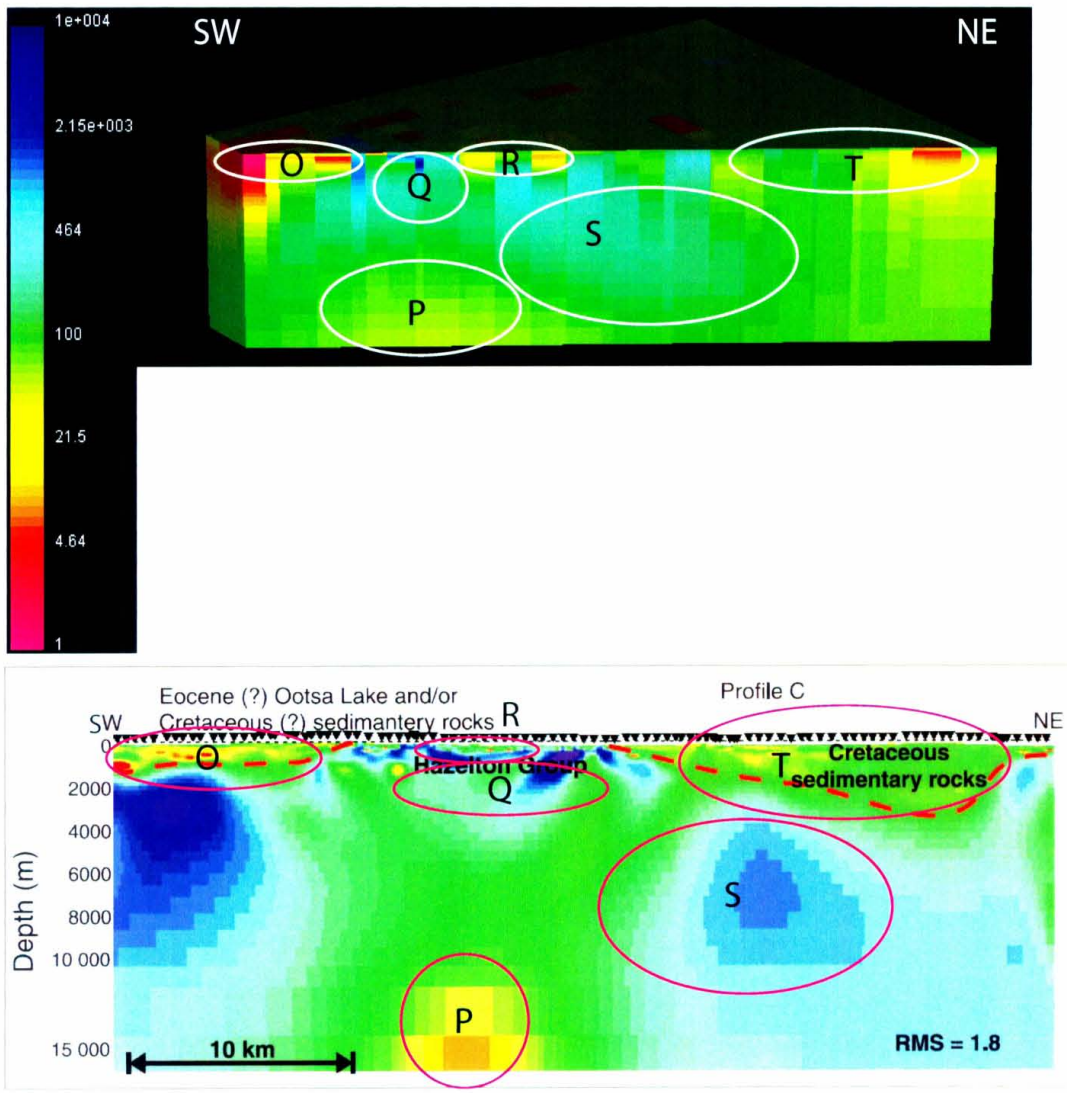

Figure 7.9: A comparison of a slice through 3D model (top) along same orientation as profile C and the 2D section from Spratt and Craven (2010) (bottom). Description in main text. Colour bar shows units in Ωm for both models.

an extensive striked trending conductor, but a limited feature not seen to the south of line A.

A large amount of conductance is also imaged out of section at O, in addition to that which lies in the scope of the cross section of the 3D model. The Hazelton group (Q) also appears more drawn out in the 3D inversion, overlain in both images by a thin conductor at R. The upper northwest sedimentary rock conductor (T) is closer to the surface, for which poor resolution could be held responsible. Again the underlying resistor may be present in the 2D section (or absent in the 3D section) because of a lack of model sensitivity at that depth, below the east end of the T conductor. There is no major difference between this model and its cousin without sign change shown in Fig. D.3 (implying 2D conductivity structure) , except for far lower conductivity in the mid-crustal conductor which should be present at P.

Profile D (see Fig 7.10) extends mostly out of the area of interest and most of the data has been omitted from the 3D inversion. However, some interesting structure is evident in the 3D results. Cretaceous sedimentary rock at Y is underlain by a resistor, which is potentially volcanic. The most prominent structure in Fig. 7.10 is a potential pair of faults extending deep into the crust (U). These faults appear to run parallel to a resistor (W), whose lateral extent in the area of interest is shown in panel III. In Fig. 7.10 panel III the two ovals (W) indicate the resistor which dives under a conductor (V) and runs between two conductors (U) approximately north-south. That image extends from 3000 m to 15000 m depth. The near vertical nature of this fault is evident in both 3D (in panel I) and in the 2D inversion results. The overlying conductor (V) is stronger in 3D on this line, also a bit thicker but more limited in lateral extent. An adjacent conductor (Cretaceous sediment) and resistor in the west

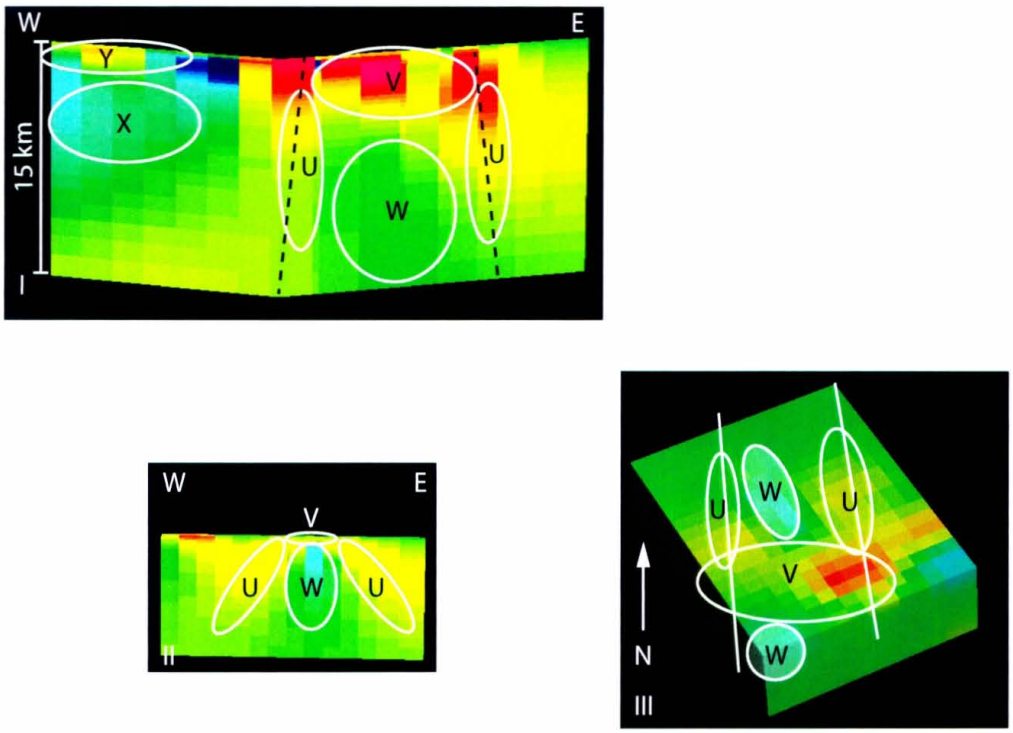

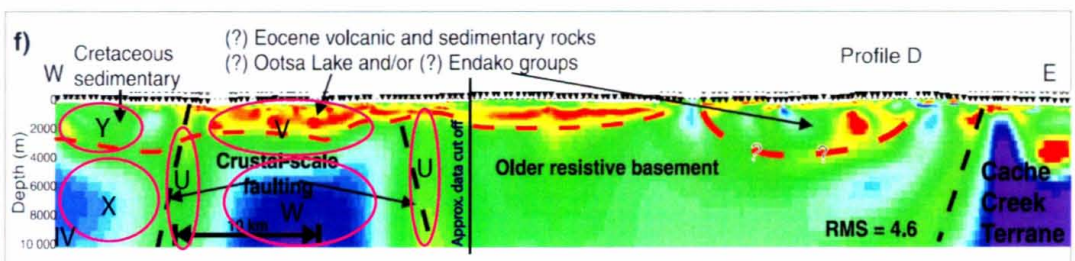

Figure 7.10: A comparison of a slice through 3D model (top) along same orientation as profile D and the 2D section from Spratt and Craven (2010) (bottom). Panel I shows main section of model for comparison, panel II shows cross-section of fault bounded conductor underlain by resistor, and panel III shows a depth slice at 3000 m through the fault bounded resistor under the conductor. Description in main text. Colour bar shows units in Ωm for both models.

are robust across both models but appear brighter and closer to the surface in 3D. The start of an underlying resistor (W) are also evident in both sections. In Fig. 7.10 II the continuance of the conductors is imaged. The fault-like nature persists as well as the conductor-over-resistor structure between the two faults. Here the surface conductor is spatially correlated with mapped conglomerate and sandstone (Bordet et al., 2011). It is important to note that data coverage here lies in a line above the resistor with a few sites on the right hand portion of that feature. Minimum-structure inversion would not include this extra structure unless it were required by the data, and the full impedance tensor gives information about what is happening to the sides of the measurement line as well as directly underneath. The model lacking a sign change in Fig. D.4 shows less surface conductivity at V, and a stronger resistor at W implying a more 3D response to conductivity structure in the data. The sign-changeless model also is more conductive at X and Y.

7.2.3 Comparison with Recent Geological Information

Results from recent geological mapping by Bordet et al. (2011) are shown in Fig. 1.10, compared with inversion results in Fig. 7.11. Chilcotin Basalt interpreted in the two and three dimensional sections in § 7.2.2 is very thin (100 m) at the east end of profile A as well as about two thirds to the western side. This is also mapped by Bordet et al. (2011) in Fig. 1.10. In close proximity to Chilcotin Basalt mapped at the west end of profile A, samples classified as basalt and scoria were mapped in the moderate surface resistor to the south. Moving eastward along profile A, moderately resistive areas coincide with areas mapped as dacite and rhyolite (DAC+RHY,

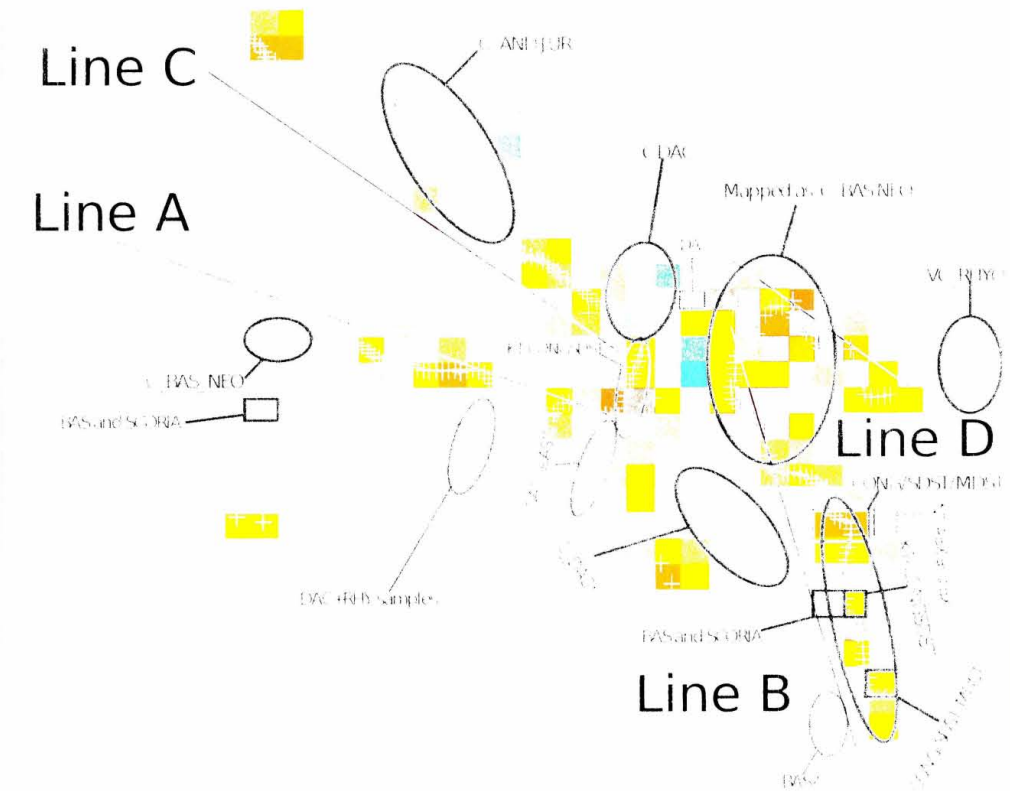
Line C
Line A
Line D
Line B

C_DAC GLASSY, C_DAC). Much of the area around profile B has been mapped as conglomerate, sandstone, and mudstone, which shows up as a surface conductor running the full length of that profile. To the sides of this profile basalt samples have been found in areas which increase in resistivity. In the middle of profile C an area mapped as Jurassic andesite agrees with an interpretation of the Hazelton group in both 2D and 3D sections, with another resistor further south-east corresponding to dacite. A large area mapped as Neogene basalt (C_BAS_NEO) corresponds to a large surface conductor. This area should be resistive at the surface, but a resistor is not seen by either the 3D or 2D inversion. Likely this package is either smaller than the resolution of the models (although this is probably not the case, 2D resolution is quite good), or thinner than distances which can be measured by MT (skin depth around 400 m for a resistive $5000\Omega m$ body at $7200Hz$).

7.2.4 Comparison With Gravity Data

The 3D conductivity model discussed in the preceding sections is compared with a gravity map from a Canadian Hunter Exploration Ltd. expedition in Fig. 7.12 (Spratt and Craven, 2010). In general, gravity troughs align with high conductivities and gravity highs coincide with conductivity lows. Typically, sedimentary rocks can be conductive with low density, while igneous rocks are resistive with high density. The sites of the mid-crustal conductors seen in Spratt and Craven (2010) are marked on the slices in Fig. 7.12 and shown in Fig. 7.13.

The gravity data along line B shows a broad low amplitude high, supporting interpretation of a resistor at depth in the 3D model as having an igneous nature.

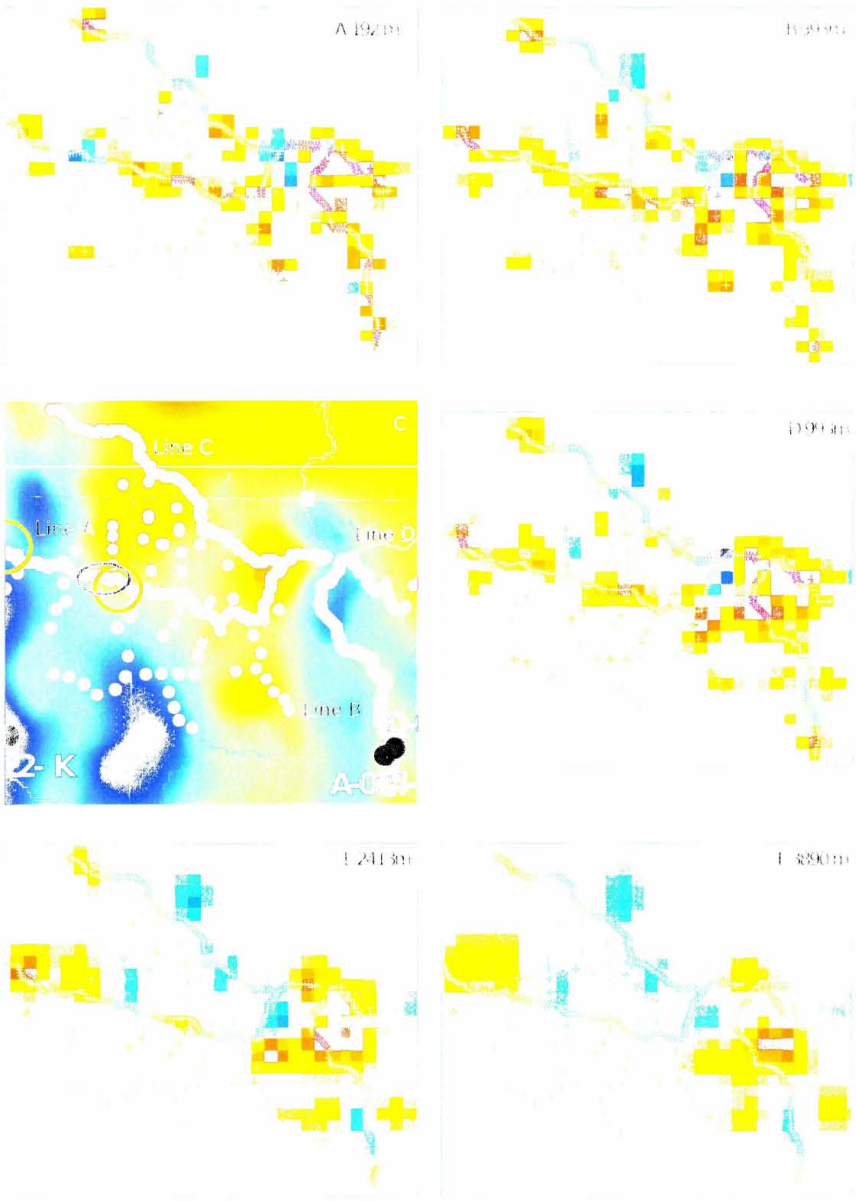
A 192m
B 819m
Line C
C
Line A
Line D
Line B
2- K
D 990m
E 241.8m
F 889.0m

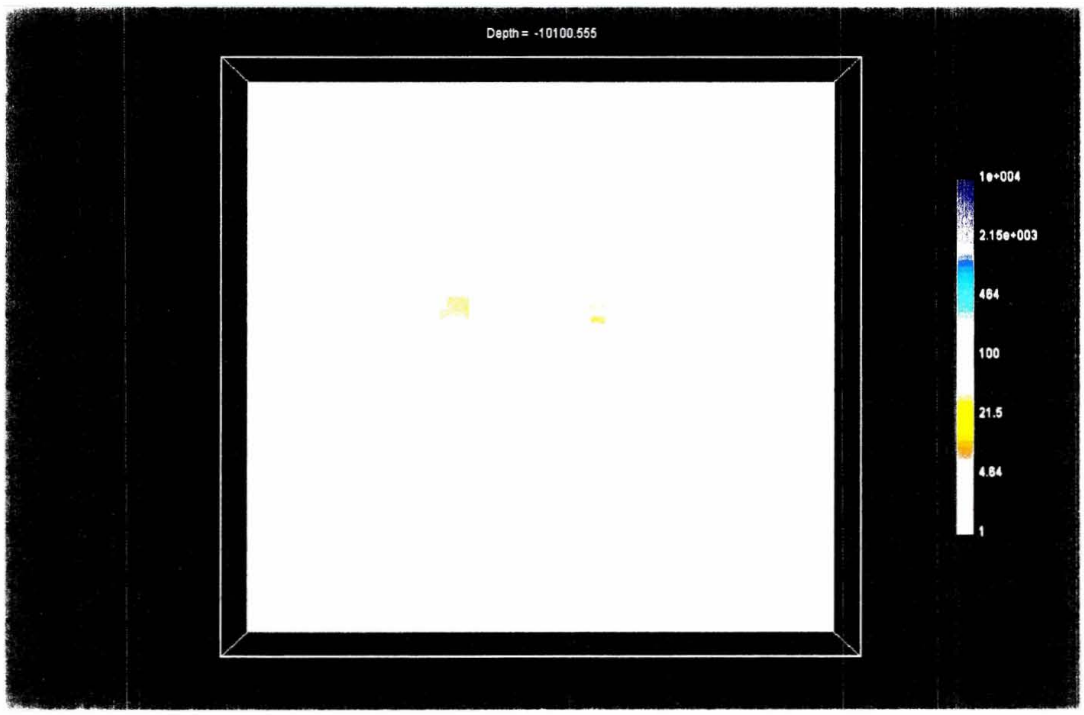
Depth = -10100.555
1e+004
2.15e+003
464
100
21.5
4.64
1

Along line C, gravity has sharpened, high amplitude peaks limited in extent to the position of surficial resistors seen in the conductivity slices at less than 600 m depth. Longer wavelength low gravity regions broaden to the lateral extent of deeper resistors at 2000 to 4000 m. These are likely surface volcanics and deeper volcanics. The deeper volcanics appear channelized in nature suggesting flow was directed in the paleo-physiography along rivers and valleys (Hayward and Calvert, 2009). A large conductor around Nazko is probably a sedimentary package as supported by low gravity, the presence of fluids in faults can also contribute to conductivity. This conductor changes abruptly to a resistor to the west coinciding with a change from low to high gravity.

Chapter 8

Conclusion

The 3D inversion model presented in the main body of this thesis portrays the general progression of conductive to resistive and back to a moderately conductive basement with increasing depth. The accuracy of this 3D inversion is limited mostly by resolution. This resolution limitation is a direct result of the heavy computational requirements for this type of modelling.

Models in this thesis range from 125 000 cells to 421 875. The 2D conductivity models of Spratt and Craven (2011) referenced in the preceding chapter is 74 rows by 313 columns for a total of 23162 cells (from personal communication with J. Spratt) showing the relative ease of 2D modelling vs 3D.

As a first examination of this model, it was checked against recent geological mapping done in Bordet et al. (2011). The model displayed conductivities characteristic of rocks mapped, except in situations where those rocks were too thin and resistive for MT to be sensitive to them anyway, e.g. mapped Chilcotin basalt around Nazko.

When various shallow layers of the main model were juxtaposed with gravity data,

interpretation of rock type of various conductors and resistors was strengthened. The low density areas roughly aligned with the conductivity maxima, while high density locations coincided with decreases in conductivity. In general these two forms of data indicate that units which are most likely igneous, because of high density and low conductivity, are limited in lateral extent, where they were previously believed ubiquitous.

Perhaps the most illustrative test of the 3D model is the comparison against the 2D inversion results presented in Spratt and Craven (2011). This test demonstrated some of the limitations of 3D inversion and 2D inversion. 3D inversion, limited by computation time (many months versus a few weeks), showed a significant decrease in resolution from the 2D results. 2D has the strong limitation of misplacing conductivity structures due to sensitivity to off-profile features. 2D is unable to capitalize on additional gradient information present in a full impedance tensor. Overall features in 3D are dimmer than in the 2D models. This could be an effect of either the larger number of iterations required to complete a 3D inversion vs. a 2D inversion (making it more difficult to get a tighter fit) or, an attempt to model anisotropy and off-line features with larger fluctuations in conductivity. Hazelton group basement is present across both sets of models, as is the Cretaceous sedimentary group – showing that these features may produce a 2D response in the data. The large midcrustal conductor in the middle of the 3D model is consistent with what 2D inversion would see if it were between profiles A and C – 2D being still sensitive to the edges of the offline conductor, requiring 3D inversion. A set of faults imaged in the 2D models can also be traced in the 3D inversion for a better understanding of the subsurface.

The 3D MT inversions are able to distinguish between resistive volcanic lithologies

and sandy packages, which are the target of oil exploration in the basin. Although the bottoms of these packages are difficult to image their lateral limits are evident. The 3D inversion has less vertical variation in conductivity while the 2D inversion changes quickly so that the bottoms of conductors are more smeared in 3D this could be a consequence of difference in resolution or a difference in weighting for vertical vs. horizontal structure in either algorithm. Smaller scale features, such as folds and thrusts are not imaged as well in 3D as in 2D as a result of the resolution limit. Larger features such as crustal scale faulting are imaged well, and their lateral continuity can even be estimated in the 3D volume. The model's main feature of interest for hydrocarbon exploration is the large bowl-like conductor situated at the meeting point of lines A, B, C, and D (at Nazko). This conductor could be a porous sandstone ideal for a reservoir (supported by gravity data in the area) with the overlying volcanic rocks mapped in the area by Bordet et al. (2011) providing a hydrocarbon seal. Any sedimentary rocks here are likely Cretaceous or Eocene in age which are suspected by Hannigan et al. (1994) to have both source rock potential with moderate (8%) porosity in the Eocene sedimentary rock and some secondary porosity from fracturing in the Cretaceous rock. Crustal scale faulting in the area augments the conductivity of this feature and could provide a fracture migration mechanism from any shales in the area providing hydrocarbon source potential.

Another interesting feature is the domed mid-crustal conductor in the basement. Seen in both the 2D and 3D models, this conductor is interpreted by Spratt and Craven (2010) to be a potential partial melt zone. In 3D this feature is present much deeper and has a much broader form. It is also shifted from its position in 2D, a display of the freedom 3D inversion has for placing anomalies more accurately.

A second tectonic feature imaged by the survey is the pair of crustal scale faults descending from the sides of profile B, which can be traced through the conductivity body.

The work compiled in this thesis had the end goal of taking a 3D MT survey and producing a conductivity model from it. This involved writing processing scripts and automating job iteration on computer clusters in an organized and controlled way. The 3D MT data were inverted and compared against other forms of data for interpretation and testing of the models, as well as qualitative assessments of the misfits resulting from the inversion trials. A whole suite of inversions were run in order to check the robustness of different conductivity features against an array of formats and parameters.

In addition to the 3D inversions, PSO was examined for the MT case and the results of those trials were examined against 1D results from commercial software. 1D conductivity structure from the PSO modelling displayed behaviour expected from the nechako basin: conductive overburden underlain by resistivity surface volcanics, followed by deeper conductivity. 1D results produced in Spratt and Craven (2008) display similar conductivity values at vary shallow depths. The PSO algorithm was not, however, able to reproduce deeper structure due to a limitation on number of layers in the model and a preference for thin, shallow conductors.

These models helped to provide additional information about the subsurface of the Nechako Basin. The inversions were able to model specific volcanic resistors at the surface such as portions of areas mapped as Chilcotin basalt. Prominent clastic units were well imaged at the suface coinciding with geological mapping. MT successfully imaged areas of interest to hydrocarbon exploration for further examination and

delineation.

Bibliography

D. A. Aruliah, U. M. Ascher, E. Haber, and D. Oldenburg. A method for the forward modelling of 3d electromagnetic quasi-static problems. *Math. Models Methods Appl Sci.*, 11:1–21, 2001.

D. B. Avdeev. Three-dimensional electromagnetic modelling and inversion from theory to application. *Surveys in Geophysics*, 26:767–799, 2005.

BC Government. *British Columbia's Pine Beetle Action Plan*. Ministry of Forests and Range of British Columbia, 2006. `http://www.for.gov.bc.ca/hfp/mountain_pine_beetle/`.

M. N. Berdichevsky and V. I. Dmitriev. Magnetotellurics in the context of the theory of ill-posed problems. In G. V. Keller, editor, *Inversitgations in Geophysics*, volume 11. Society of Exploration Geophysicists, 2002.

M. E. Best. *Qualitative Interpretation of Potential Field Profiles Southern Nechako Basin*, pages 73–78. British Columbia Ministry of Energy of Mines, Bemex Consulting International, 5288 Cordova Bay Road, Victoria, BC, V8Y2L4, 2004.

D. E. Boener, R. D. Kurtz, J. A. Craven, G. M. Ross, and F. W. Jones. A synthesis of electromagnetic studies in the lithoprobe alberta basement transect: Constraints

on paleoproterozoic indentation tectonics. *Canadian Journal of Earth Sciences*, 37: 1509–1534, November 2000.

E. Bordet, C. Hart, and D. Mitchinson. Preliminary lithological and structural framework of eocene volcanic rocks in the nechako region, central British Columbia. *Report 2011*, 13:870–896, 2011.

R. L. Burden and J. D. Faires. *Numerical Analysis*. Thomson Brooks/Cole, 8e edition, 2005.

C. Hickson and J. Cassidy. *Summary of Earthquake Activity, Nazko Cone Area*. Natural Resource Canada, Earth Sciences Sector, 2007. `http://earthquakescanada.nrcan.gc.ca/nazko/nazko_summary-eng.php`.

L. Cagniard. *Basic Theory of the Magneto-Telluric Method of Geophysical Prospecting*, volume 5 of *4*, chapter 1, pages 4–34. Society of Exploration Geophysicists, 1952.

A. J. Calvert, N. Hayward, B. R. Smithyman, and E. M. T. Takaougang. *Vibroseis Survey Acquisition in the Central Nechako Basin, South-Central British Columbia*, pages 145–150. Geoscience BC, 2008.

K. R. Christopherson. Applications of mangetotellurics to petroleum exploration in papua new guinea: A model for frontier areas. *Geophysics: The Leading Edge of Exploration*, pages 21–27, 1991.

S. C. Constable, A. S. Orange, G. M. Hoversten, and H. F. Morrison. Marine mag-

netotellurics for petroleum exploration part i: A sea-floor equipment system. *Geophysics*, 63, No. 3:816–825, 1998.

S. W. H. Cowley. Magnetosphere of the earth. In D. Gubbins and E. H. Bervera, editors, *Encyclopedia of Geomagnetism and Paleomagnetism*, pages 656–665. Spring, 2007.

L. Diakow and M. Mihalynuk. Geology of whitesail reach and troitsa lake map areas. *Canada/British Columbia Mineral Development Agreement*, 1987-1, 1986.

J. Dostal, K. Breitsprecher, B. N. Church, D. Thorkelson, and T. S. Hamilton. Eocene melting of precambrian lithospheric mantle: Analcime-bearing volcanic rocks from the challis-kamloops belt of south central British Columbia. *Journal of Volcanology and Geothermal Research*, 126:303–326, 2003.

D. C. Engebretson, A. Cox, and R. G. Gordon. Relative motions between oceanic and continental plates in the pacific basin. *Geological Society of Canada Special Papers*, 206, 1985.

C. A. Evenchick and D. J. Thorkelson. *Geology of the Spatsizi River map area, north-central British Columbia*, volume Bulletin 577. Geological Survey of Canada, Geological Survey of Canada Bookstore, 601 Booth Street, Ottawa, Ontario, K1A 0E8, 2005.

C. A. Evenchick, M. E. McMechan, V. J. McNicoll, and S. D. Carr. A synthesis of the jurassic-cretceous tectonic evolution of the central and southeastern canadian cordilleran: Exploration links across the orogen. In J. W. Sears, T. A. Harms, and

C. A. Evenchick, editors. *Whence the Mountains? Inquiries into the Evolution of Orogenic Systems*. Geological Society of America, Inc., 2007.

C. G. Farquharson. Numerical modelling for geophysical electromagnetic methods. Department of Earth Sciences, Memorial University of Newfoundland, St John's, NL, Canada, July 2009. Dublin Insitute for Advanced Studies, A short course given at the Dublin Institute of Advanced Studies 6th-14th July 2009.

C. G. Farquharson, D. W. Oldenburg, and E. Haber. An algorithm for the three-dimensional inversion of magnetotelluric data. In *SEG Int'l Exposition and 72nd Annual Meeting, Salt Lake City, Utah*. Society of Exploration Geophysicists, 2002.

R. E. Farrell, G. D. M. Andrews, J. K. Russell, and R. G. Anderson. Chasm and dog creek lithofacies, chilcotin group basalt, bonaparte lake map area, British Columbia. *Current Research*, M44-2007, 2007.

F. Ferri and J. Riddell. *The Nechako basin project: new insights from the southern Nechako Basin*, pages 89–124. BC Ministry of Energy, Mines and Petroleum Resource, PO Box 9323, Stn Prov Gov, Victoria, BC, V8W 9N3, 2008.

A. T. Filho, A. M. P. Mizusaki, and L. Antonioli. Magmatism and petroleum exploration in the brazilian paleozoic basins. *Marine and Petroleum Geology*, 25: 143–151, 2008.

Geosystem-Canada. Final report: Audio-magnetotelluric and magnetotelluric survey, Nechako Basin, British Columbia. Technical report, Publicworks and Government Services, Canada, 927 Raftsman Lane, Ottawa, Ontario, Canada, K1C 2V3, December 2007.

P. E. Gill, W. Murray, and M. H. Wright. *Practical Optimization*. Academic Press, 1981.

D. J. Griffiths. *Introduction to Electrodynamics*. Prentice Hall, 3rd edition, 1999.

E. Haber, U. M. Ascher, D. A. Aruliah, and D. Oldenburg. fast simulation of 3d electromagnetic problems using potentials. *Journal of Computational Physics*, 163: 153–171, 2000a.

E. Haber, U. M. Ascher, and D. Oldenburg. *On optimization techniques for solving nonlinear inverse problems*, pages 1263–1280. 2000b.

P. T. C. Hammer and R. M. Clowes. Lithosperic-scale structures and evolution of the north american cordillera: Comparisons between transects crossing southern and northern British Columbia and alaska. In J. W. Sears, T. A. Harms, and C. A. Evenchick, editors, *Whence the Mountains? Inquiries into the Evolution of Orogenic Systems*. Geological Society of America, Inc., 2007.

P. Hannigan, P. J. Lee, K. G. Osadetz, J. R. Dietrich, and K. Olsen-Heise. Oil and gas resource potential of the nechako-chilcotin area of British Columbia. Technical report, Institute of Sedmentary and Petroleum Geology, Geological Survey of Canada, 3303-33rd Street N.W., Calgary,AB, Canada, T2L 2A7, 1994.

N. Hayward and A. J. Calvert. Near-surface volcanic rocks in the se Nechako Basin, bc: Results of interpretation of seismic reflection data using first-arrival tomographic inversion. In *Frontiers + Innovation*, volume 3, pages 433–436. CSPG, CSEG, and CWLS, 2009.

R. B. Ickert, D. J. Thorkelson, D. D. Marshall, and T. D. Ullrich. Eocene adakitic volcanism in sourthern British Columbia: Remelting of arc basalt above a slab window. *Journal of Tectonophysics*, 464:164–185, 2009.

A. G. Jones, R. D. Kurtz, D. E. Boerner, J. A. Craven, and G. W. McNeice. Electromagnetic constraints on strike-slip fault geometry — the fraser river fault system. *Geology*, 20:561–564, June 1992.

J. Kennedy and J. Eberhart. Partile swarm optimization. In *Proceedings of IEEE International Conference on Neural Networks*, pages 1942–1948. IEEE, 1995.

K. Labitzke. The global signal of the 11-year sunspot cycle in the stratosphere: Differences between solar maxima and minima. *Meteorologische Zeitschrift*, 10(2): 83–90, 2001.

J. Ledo and A. G. Jones. Regional electrical resistivity structure or the southern Canadian Cordillera and its physical interpretation. *Journal of Geophysical Research*, 106:30755–30769, December 2001.

C. Lowe, J. Baker, and C. Evenchick. Constraints on the nature and thickness of sedimentary fill and underlying basement rocks in bowser and sustut basins, north-central British Columbia from analysis of potential field data. *Bulletin of Canadian Petroleum Geology*, 54 No. 1:62–84, March 2006.

A. Marti, P. Queralt, and J. Ledo. Waldim: A code for the dimensionality analysis of magnetotelluric data using the rotational invariants of the magnetotelluric tensor. *Computers & and Geosciences*, 35:2295–2303, 2009.

B. Mathews and J. Monger. *Roadside Geology of Southern British Columbia*. Mountain Press Publishing Company, 1st edition, 2005.

P. T. L. Menezes and J. M. Travassos. Magnetotellurics as a modeling tool in the extensive magmatic context of parana basin, brazil. *The Leading Edge*, pages 832–840, 2010.

M. P. Miensopust. *Multidimensional Magnetotelluics: A 2D Case Study and a 3D Approach to Simultaneously Invert for Resistivity Structure and Distortion*. National University of Ireland, 2010.

A. S. Orange. Magnetotelluric exploration for hydrocarbons. In *Proceedings of IEEE*, volume 77, pages 287–317. IEEE, 1989.

R. J. Palsgrove and R. M. Bustin. Stratigraphy and sedimentology of the lower skeena group, telkwa coalfield, central British Columbia (93l/11). *Geological Fieldwork 1989*, Paper 1990-1:449–454, 1990.

R. L. Parker and J. R. Booker. Optimal one-dimensional inversion and bounding of magnetotelluric apparent resistibity and phase measurements. *Physics of the Earth and Planetary Interiors*, 98:269–282, April 1996.

M. E. H. Pedersen and A. J. Chipperfield. Simplifying particle swarm optimization. *Applied Soft Computing*, 1987-1, 2009.

Phoenix-Geophysics. Sensors: Magnetic and electric field sensors for geophysical receivers. `http://www.phoenix-geophysics.com/products/sensors/`. 3781 Victoria Park Avenue, Unit 3, Toronto, Ontario, Canada, M1W3K5, August 2008.

J. Riddell. Lithostratigraphic and tectonic framework of Jurassic and Cretaceous intermontane sedimentary basins of south-central British Columbia. *Canadian Journal of Earth Sciences*, 48:870–896, June 2011.

J. Riddell and F. Ferri. Nechako project update. In *Geoscience Reports 2008*, pages 67–77. Ministry of Energy, Mines, and Petroleum Resources, 2008.

J. Riddell, F. Ferri, A. Sweet, and P. O'Sullivan. *New Geoscience Data from the Nechako Basin Project*, pages 59–87. Ministry of Energy, Mines an Petroleum Resources, British Columbia, 2007.

E. J. Rothwell and M. J. Cloud. *Electromagnetics*. CRC Press, 2nd edition, 2009.

R. Shaw and S. Srivastava. Particle swarm optimization: A new tool to invert geophysical data. *Geophysics*, 72(2):75–78, February 2007.

D. Siingh, R. P. Singh, A. K. Kamra, P. N. Gupta, R. Singh, V. Gopalakrishnan, and A. K. Singh. Review of electromagnetic coupling between the earth's atmosphere and the space environment. *Journal of Atmospheric and Solar-Terrestrial Physics*, 67:637–658, 2004.

F. Simpson and K. Bahr. *Practical Magnetotellurics*. Cambridge, 2005.

W. Siripunvaraporn.

B. R. Spies. Recent developments in the use of surface electrical methods for oil and gas exploration in the soviet union. *Geophysics*, 48, No. 8:1102–1112, 1983.

J. Spratt and J. Craven. A first look at the electrical resisvity structure in the Nechako

Basin from magnetotelluric studies west of nazko, bc. In *Geoscience Reports 2008*, pages 119–127. Ministry of Energy, Mines, and Petroleum Resources, 2008.

J. Spratt and J. Craven. Magentotelluric imaging of the Nechako Basin, British Columbia. *Geological Survey of Canada Current Research*, 3:1–9, 2010.

J. Spratt and J. Craven. Near-surface and crustal-scale images of the Nechako Basin, British Columbia, canada, from magnetotelluric investigations. *Canadian Journal of Earth Sciences*, 48:987–999, May 2011.

UBC-GIF. *MT3Dinv: A Program Library for Inversion of Magnetotelluric Data over 3D Structures*. UBC-Geophysical Inversion Facility, Department of Earth and Ocean Sciences, University of British Columbia, Vancouver, British Columbia, March 2003.

P. J. Umhoefer and K. L. Kleinspehn. Mesoscale and regional kinematics of the northwestern yalakom fault system: Major paleogene dextral faulting in British Columbia, canada. *Tectonics*, 14:78–94, 1995.

M. Unsworth. New dvelopments in conventional hydrocarbon exploration with electromagnetic methods. *CSEG Recoder*, 2005.

K. Vozoff. The magnetotelluric method. In M. N. Nabighian, editor, *Electromagnetic Methods In Applied Geophysics*, volume 2, Application, part B. Society of Exploration Geophysicists, 1987.

S. H. Ward and G. W. Hohmann. Electromagnetic theory for geophysical applica-

tions. In M. N. Nabighian, editor, *Electromagnetic Methods In Applied Geophysics*, volume 1, Theory. Society of Exploration Geophysicists, 1987.

P. Wessel and W. H. F. Smith. The generic mapping tools technical reference and cookbook. Technical report, University of Hawaii, July 2011. `http://gmt.soest.hawaii.edu/gmt/pdf/GMT_Doc.pdf`.

D. E. Wight. Society of exploration geophysicists mt/emap data interchange standard. Technical report, Society of Exploration Geophysicists, WSE Associates, 5808 Balcones Drive, Suite 202, Austin, Texas 78731, December 1987.

Appendix A

Impedance Rotation

The rotation is performed through left and multiplication by rotation matrices and their transposes:

$$\mathbf{Z}' = \mathbf{R}_x \mathbf{R}_z \mathbf{Z} \mathbf{R}_z^T \mathbf{R}_x^T \tag{A.1}$$

where $\mathbf{R}_z$ is a rotation about the z-axis and $\mathbf{R}_x$ is a rotation about the x-axis. In this way, the original impedance tensor is first rotated counter-clockwise about the the z-axis, then rotated counter-clockwise about the x-axis.

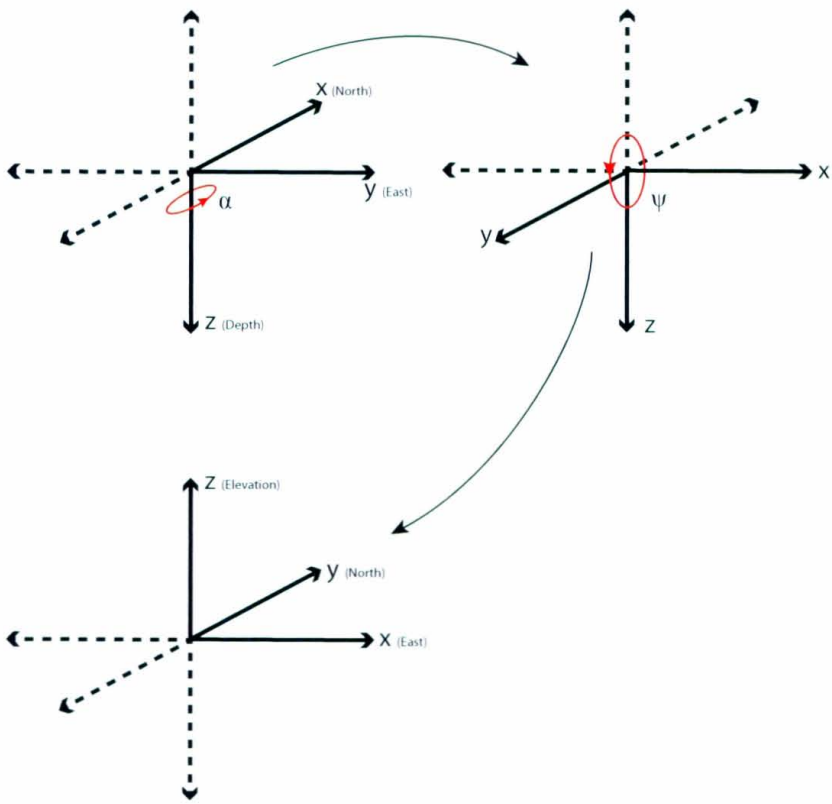

Figure A.1: Graphic demonstrating rotation of the coordinate axes carried out to reconcile differences between edi and MT3Dinv orientations.

$$\mathbf{Z}' = \begin{pmatrix} 1 & 0 & 0 \\ 0 & \cos\psi & \sin\psi \\ 0 & -\sin\psi & \cos\psi \end{pmatrix} \begin{pmatrix} \cos\alpha & \sin\alpha & 0 \\ -\sin\alpha & \cos\alpha & 0 \\ 0 & 0 & 1 \end{pmatrix} \begin{pmatrix} Z_{xx} & Z_{xy} & 0 \\ Z_{yx} & Z_{yy} & 0 \\ 0 & 0 & 0 \end{pmatrix} \begin{pmatrix} \cos\alpha & -\sin\alpha & \\ \sin\alpha & \cos\alpha & \\ 0 & 0 & 1 \end{pmatrix} \begin{pmatrix} 1 & 0 & 0 \\ 0 & \cos\psi & -\sin\psi \\ 0 & \sin\psi & \cos\psi \end{pmatrix} \tag{A.2}$$

For the rotation from EDI/measurement axes to the orientation used by MT3Dinv, set $\psi = \pi$ and $\alpha = \pi/2$.

$$\mathbf{Z}' = \begin{pmatrix} 1 & 0 & 0 \\ 0 & -1 & 0 \\ 0 & 0 & -1 \end{pmatrix} \begin{pmatrix} 0 & 1 & 0 \\ -1 & 0 & 0 \\ 0 & 0 & 1 \end{pmatrix} \begin{pmatrix} Z_{xx} & Z_{xy} & 0 \\ Z_{yx} & Z_{yy} & 0 \\ 0 & 0 & 0 \end{pmatrix} \begin{pmatrix} 0 & -1 & 0 \\ 1 & 0 & 0 \\ 0 & 0 & 1 \end{pmatrix} \begin{pmatrix} 1 & 0 & 0 \\ 0 & -1 & 0 \\ 0 & 0 & -1 \end{pmatrix} \tag{A.3}$$

$$\mathbf{Z}' = \begin{pmatrix} 0 & -1 & 0 \\ -1 & 0 & 0 \\ 0 & 0 & 1 \end{pmatrix} \begin{pmatrix} Z_{xx} & Z_{xy} & 0 \\ Z_{yx} & Z_{yy} & 0 \\ 0 & 0 & 0 \end{pmatrix} \begin{pmatrix} 0 & 1 & 0 \\ 1 & 0 & 0 \\ 0 & 0 & 1 \end{pmatrix} \tag{A.4}$$

$$\mathbf{Z}' = \begin{pmatrix} 0 & -1 & 0 \\ -1 & 0 & 0 \\ 0 & 0 & 1 \end{pmatrix} \begin{pmatrix} Z_{xy} & Z_{xx} & 0 \\ Z_{yy} & Z_{yx} & 0 \\ 0 & 0 & 0 \end{pmatrix} \tag{A.5}$$

$$\mathbf{Z}' = \begin{pmatrix} -Z_{yy} & -Z_{yx} & 0 \\ -Z_{xy} & -Z_{xx} & 0 \\ 0 & 0 & 0 \end{pmatrix} \tag{A.6}$$

Due to sign conventions in MT3Dinv (i.e. Fourier transform convention), it is also not only necessary to apply the impedance rotation but a conversion to SI units (multiplication factor $4\pi \times 10^{-4}$ and a complex conjugate). It was unclear whether it was also necessary to apply a -1 multiplier to on-diagonal elements (some lacking documentation) and so inversions were run with, A.7 and without A.8 it:

$$\mathbf{Z}' = -4\pi \times 10^{-4} \begin{pmatrix} -Z_{yy}{}^{*} & Z_{yx}{}^{*} & 0 \\ Z_{xy}{}^{*} & -Z_{xx}{}^{*} & 0 \\ 0 & 0 & 0 \end{pmatrix} \tag{A.7}$$

$$\mathbf{Z}' = 4\pi \times 10^{-4} \begin{pmatrix} Z_{yy}{}^{*} & Z_{yx}{}^{*} & 0 \\ Z_{xy}{}^{*} & Z_{xx}{}^{*} & 0 \\ 0 & 0 & 0 \end{pmatrix} \tag{A.8}$$

Appendix B

Code

This appendix is a collection of the code written during the undertaking of this thesis. These programs and shell scripts are explained in chapter 6. See Fig. 6.9 for summary flowchart of all operations. These are located on attached cd-rom.

Appendix C

Data Assessment

Skin depth was calculated with c-code for each column in the model. This was done by summing the theoretical amplitude drop (using eq. 2.15 in each cell in a column of the model until the amplitude reached $1/e$ of its original value. Effectively, the algorithm calculated how much skin depth (proportionately) was achieved in each cell based on thickness and conductivity.

C.1 16 frequencies, 50x50x50x, with sign change

C.1.1 Skin Depth Maps

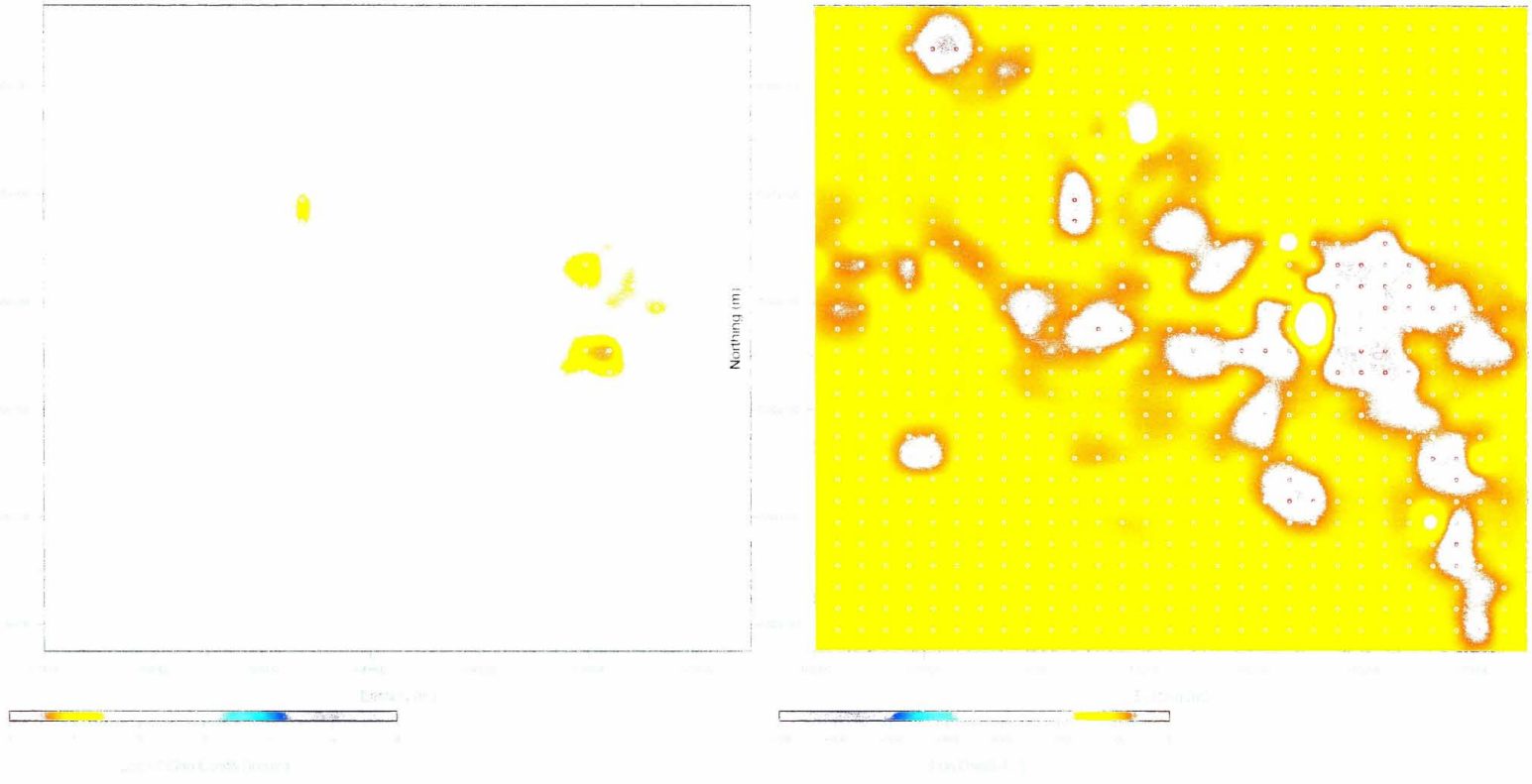
Northing (m)

Nothing in

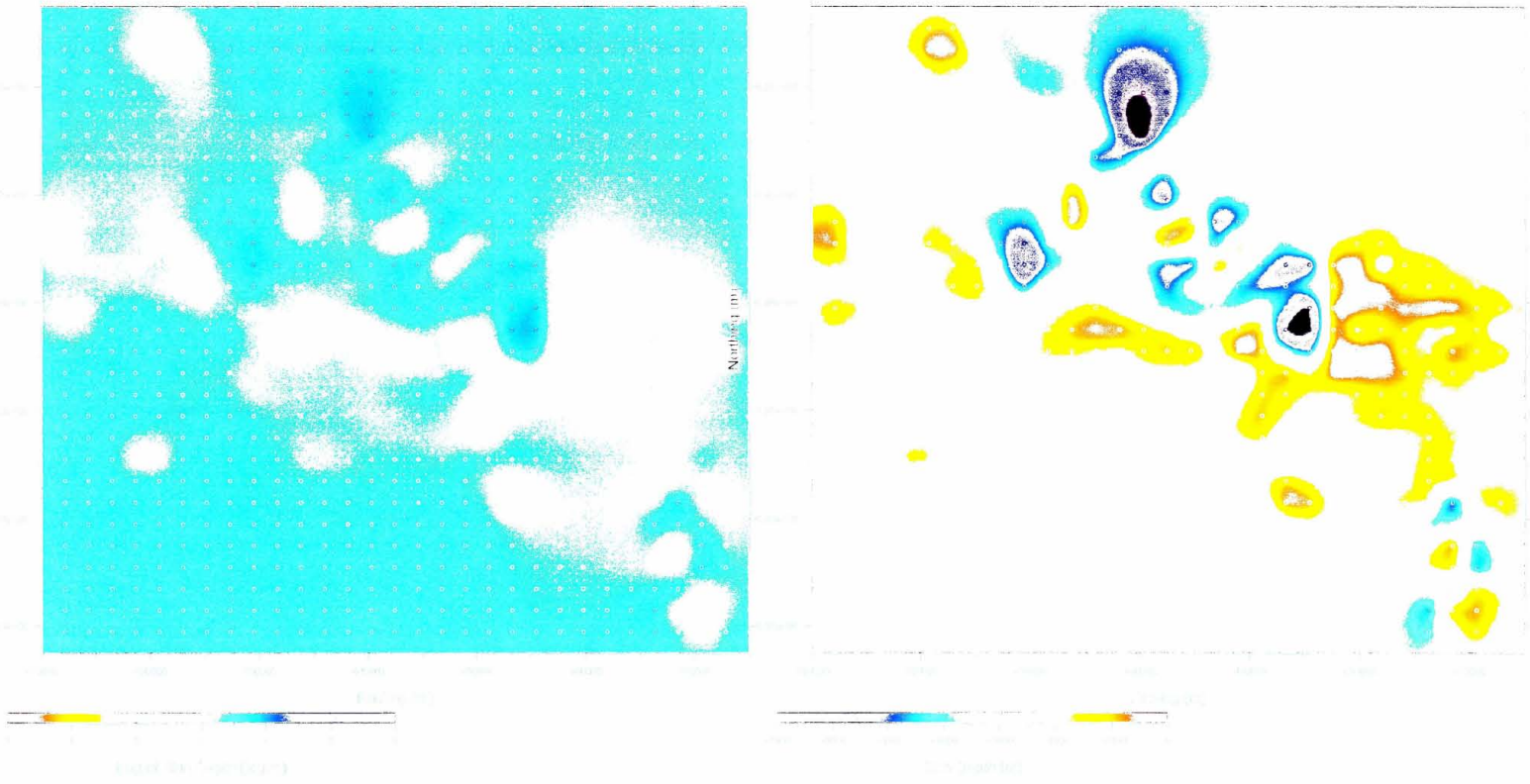

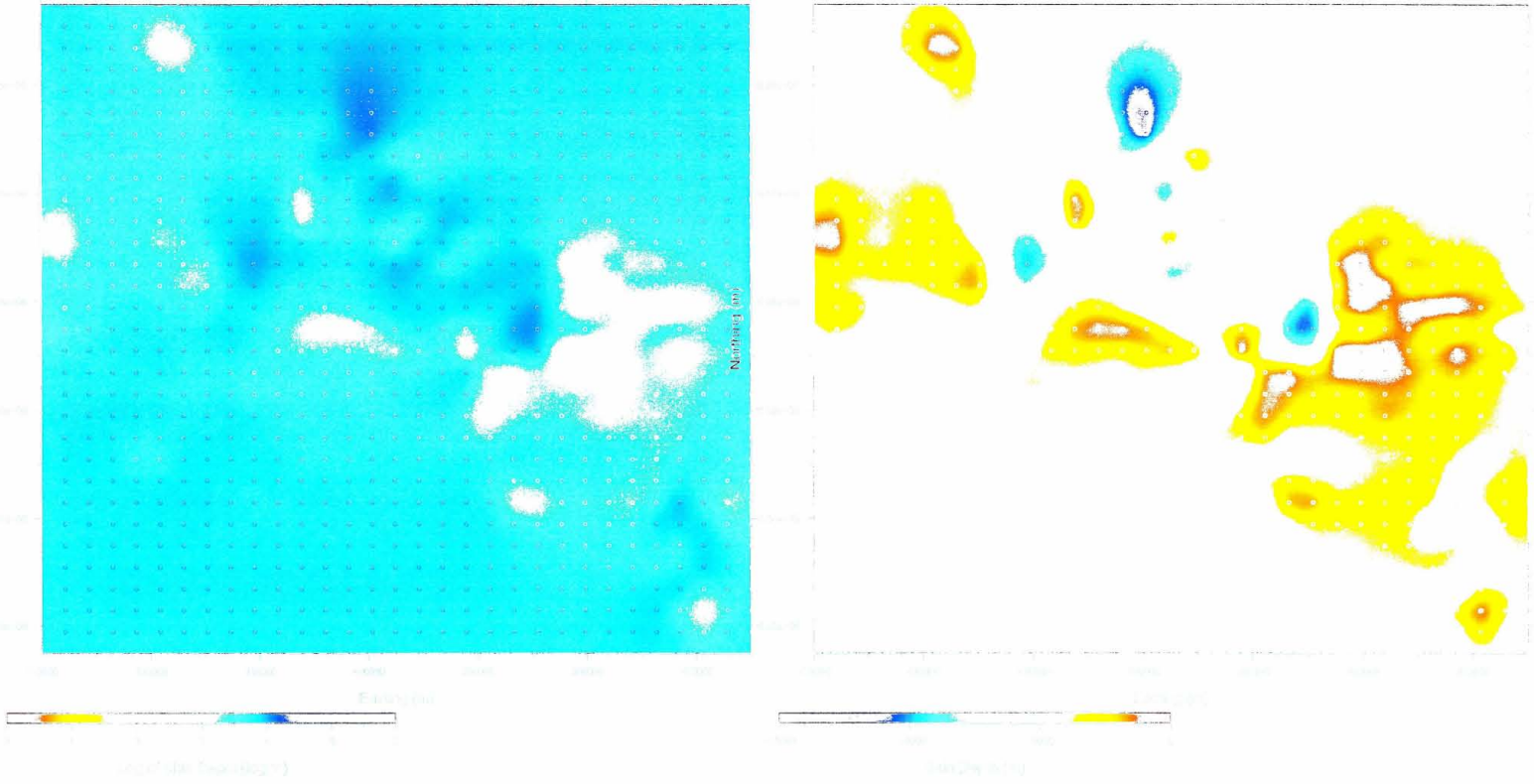

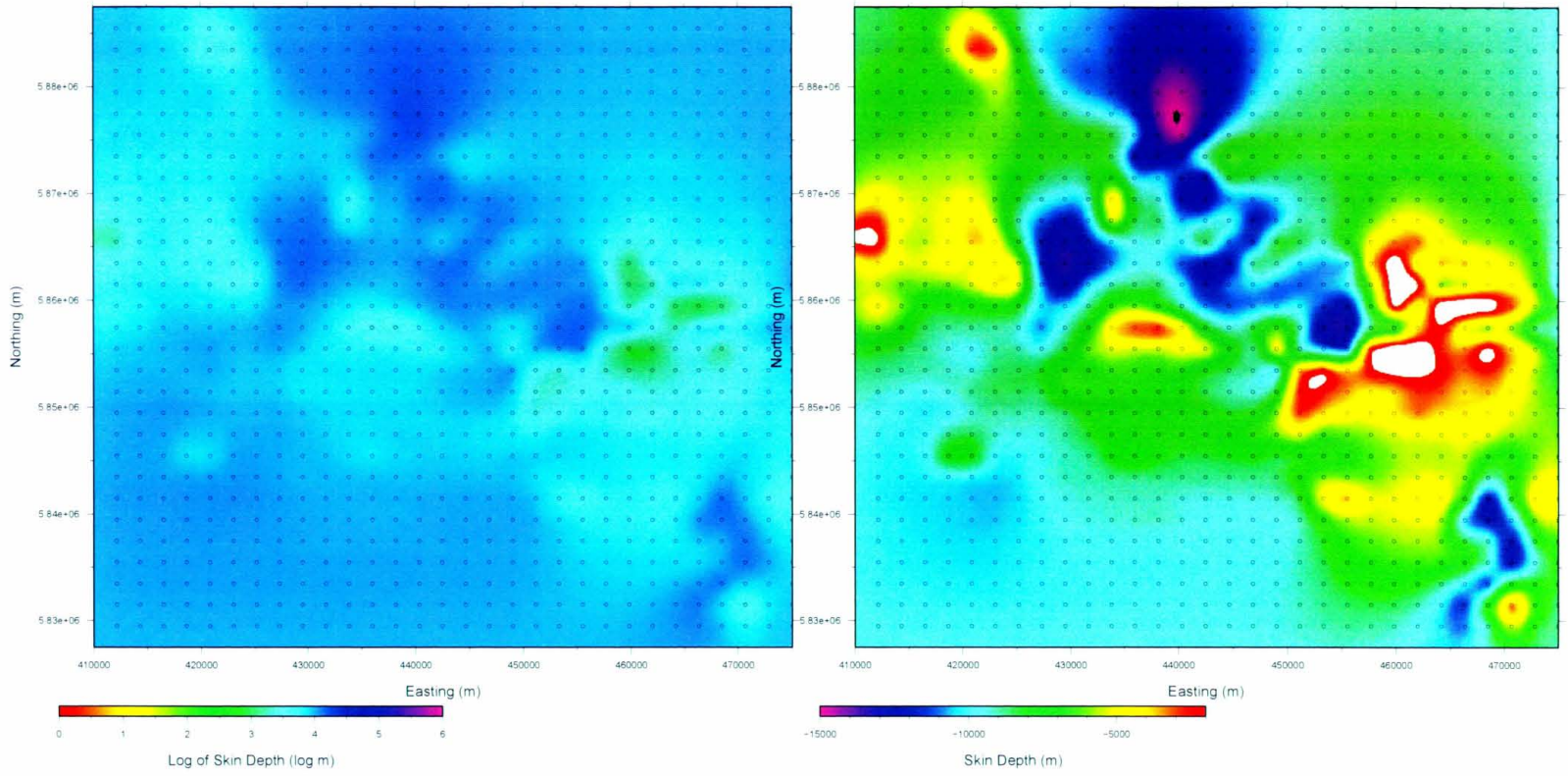

a) logarithmic skin depth

b) linear skin depth

Figure C.9: Map of skin depth for 1.72 Hz. Logarithmic scaling at left, linear scaling at right.

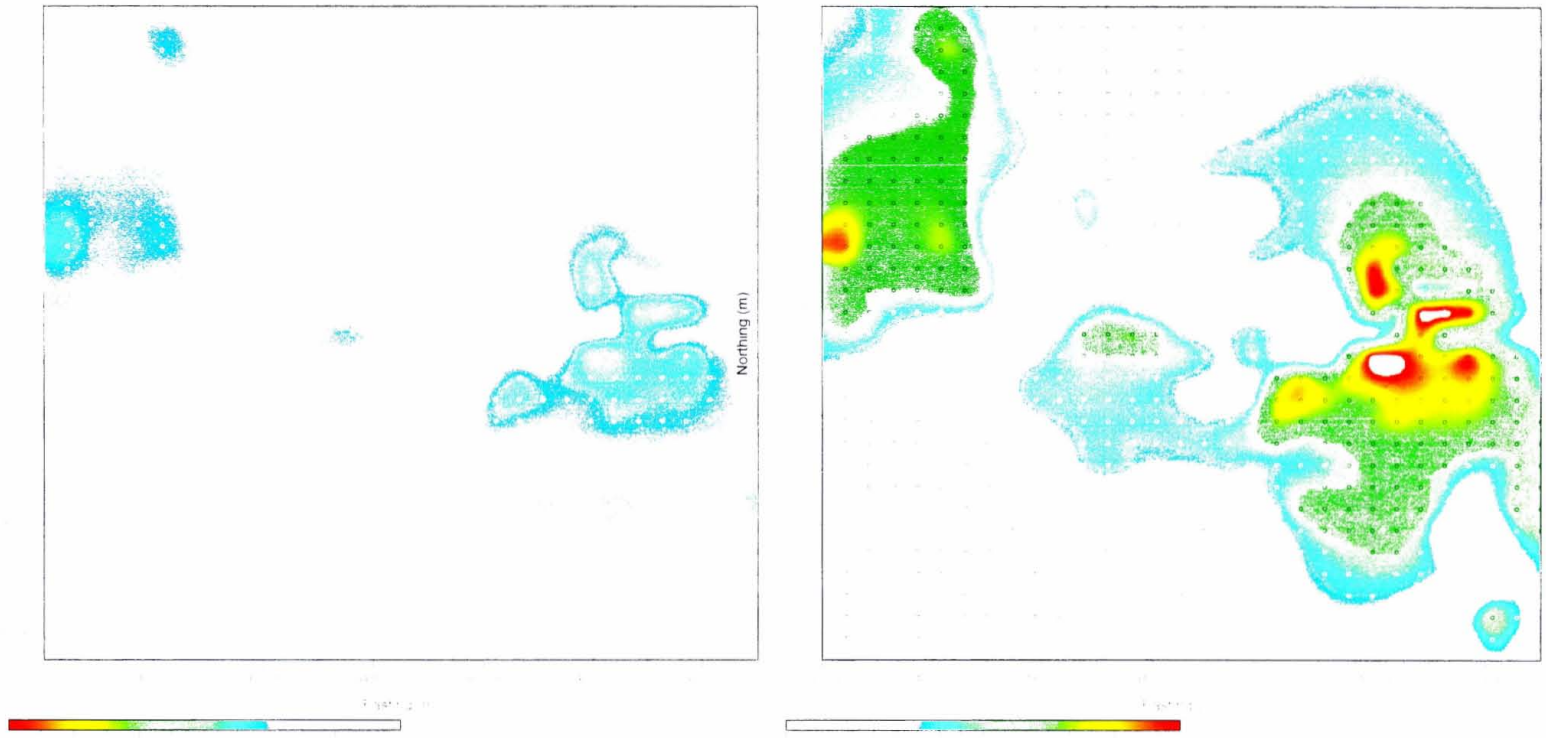

Figure C.10: Magnetic skin depth for 0.59 Hz. Log-attribute scaling at left, linear scaling at right.

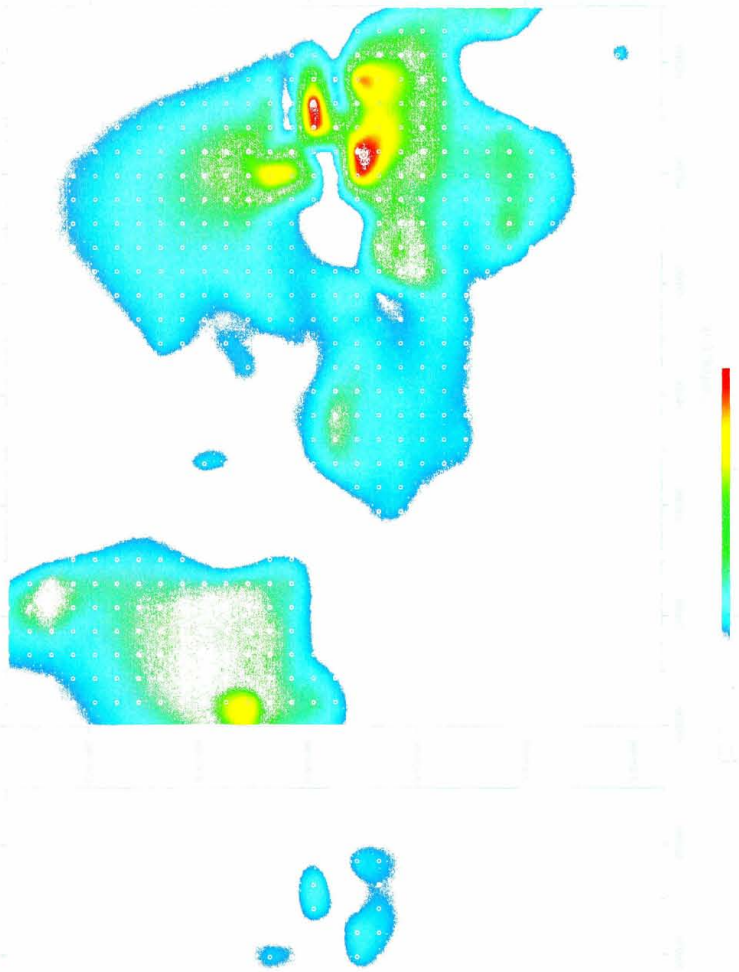

C.1.2 Observed and Predicted Data Maps

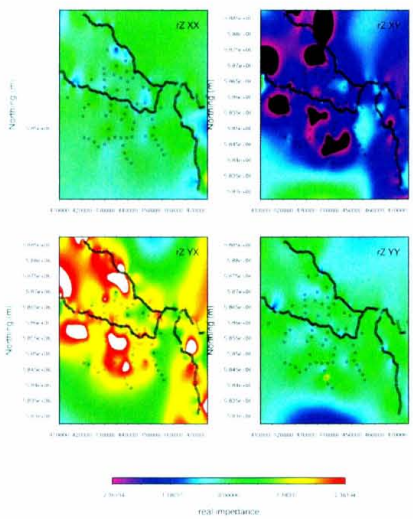

a) observed real impedance

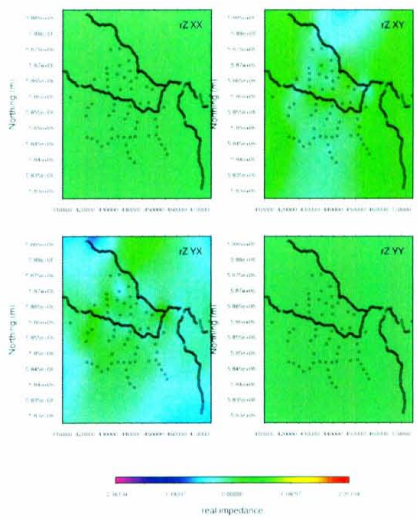

b) predicted real impedance

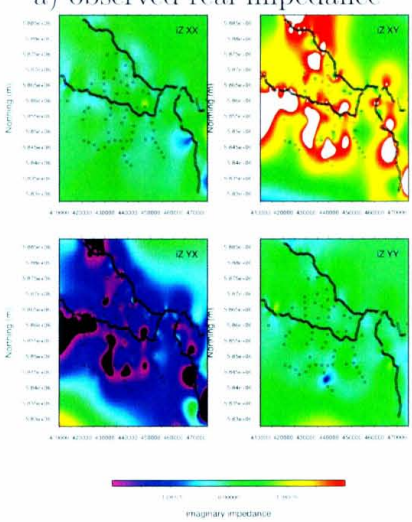

c) observed imaginary impedance

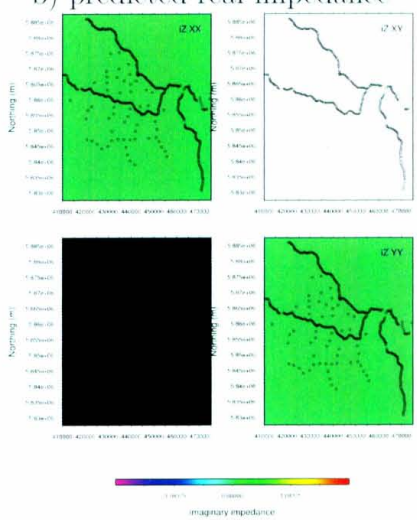

d) predicted imaginary impedance

Figure C.13: Observed (left) and predicted (right) impedances, both real and imaginary. Skin depth at frequency 7200 Hz shown in Fig. C.1

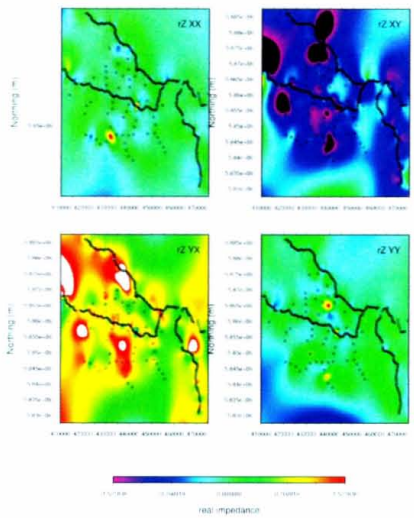

a) observed real impedance

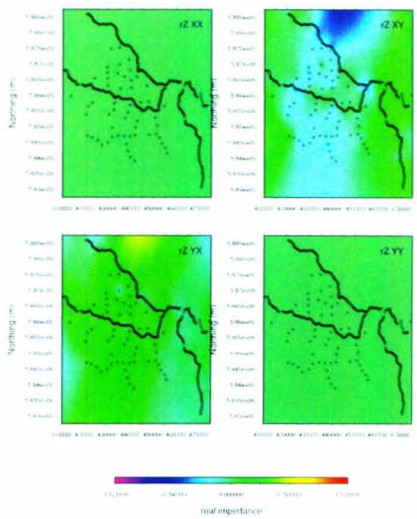

b) predicted real impedance

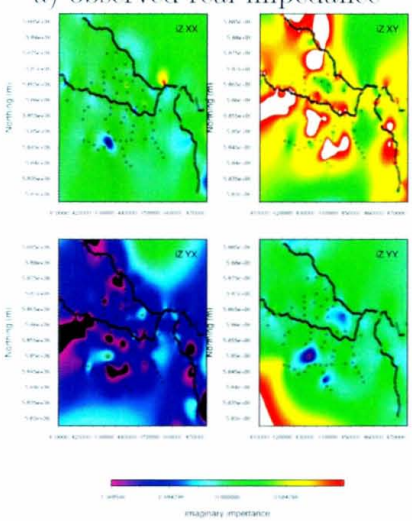

c) observed imaginary impedance

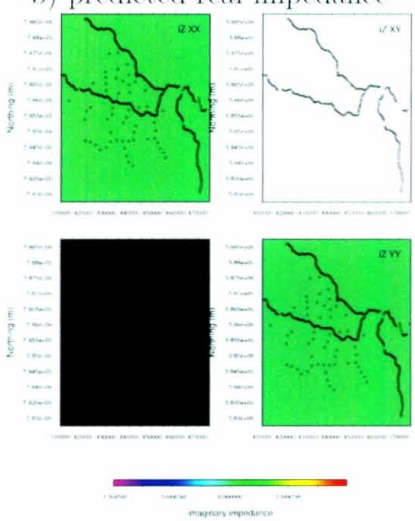

d) predicted imaginary impedance

Figure C.14: Observed (left) and predicted (right) impedances, both real and imaginary. Skin depth at frequency 2600 Hz shown in Fig. C.2

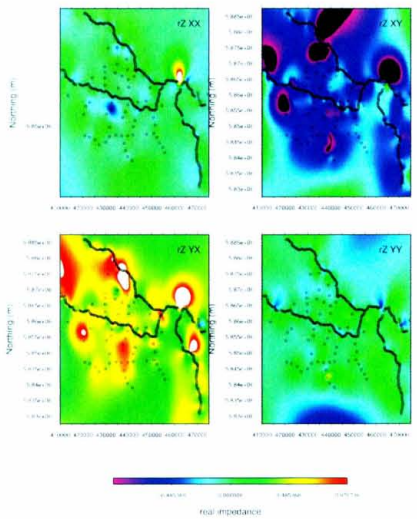

a) observed real impedance

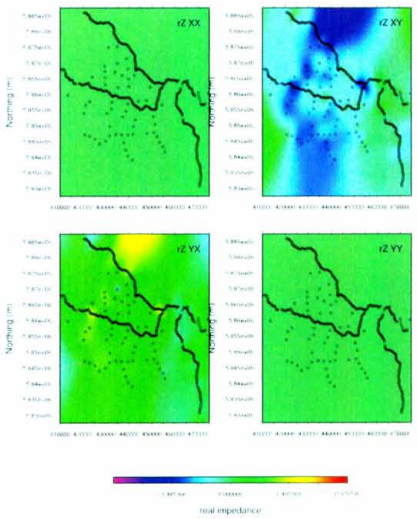

b) predicted real impedance

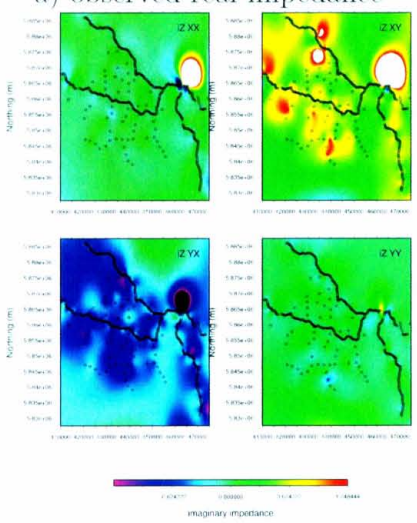

c) observed imaginary impedance

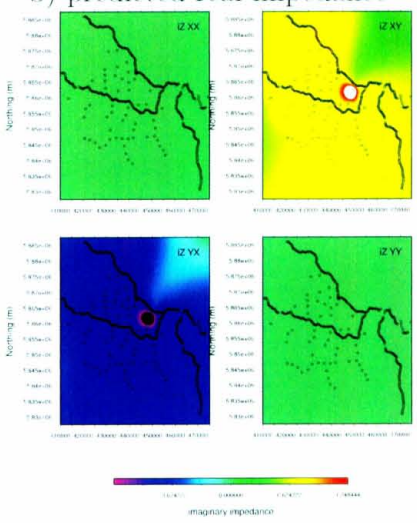

d) predicted imaginary impedance

Figure C.15: Observed (left) and predicted (right) impedances, both real and imaginary. Skin depth at frequency 900 Hz shown in Fig. C.3

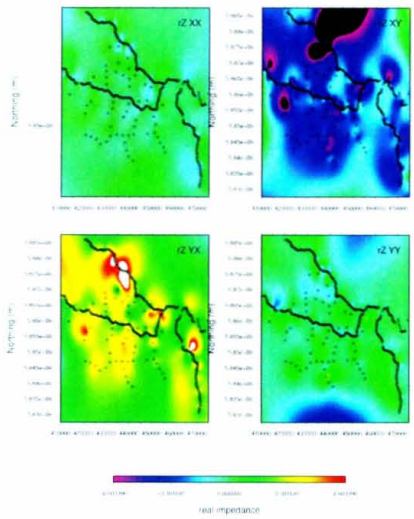

a) observed real impedance

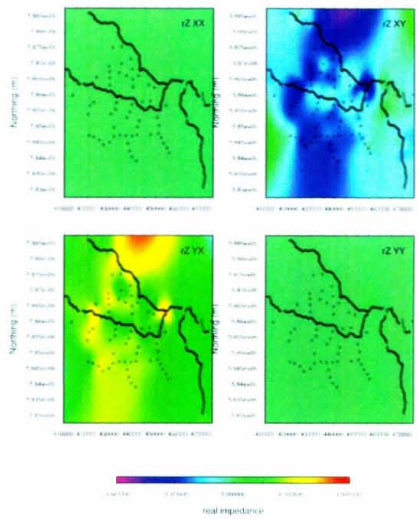

b) predicted real impedance

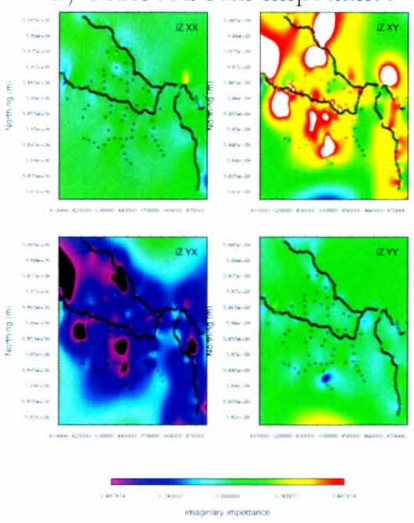

c)

observed imaginary impedance

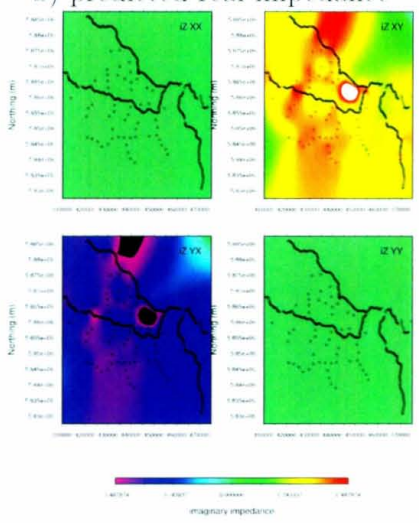

d) predicted imaginary impedance

Figure C.16: Observed (left) and predicted (right) impedances, both real and imaginary. Skin depth at frequency 320 Hz shown in Fig. C.4

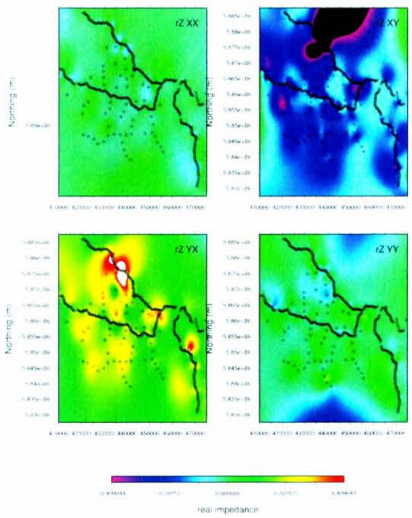

a) observed real impedance

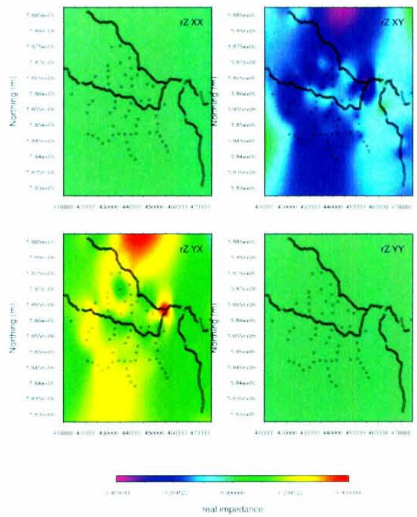

b) predicted real impedance

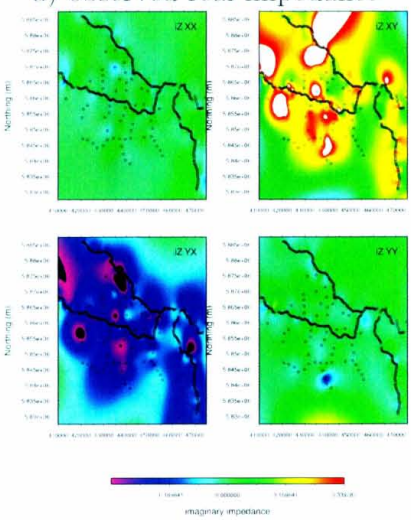

c) observed imaginary impedance

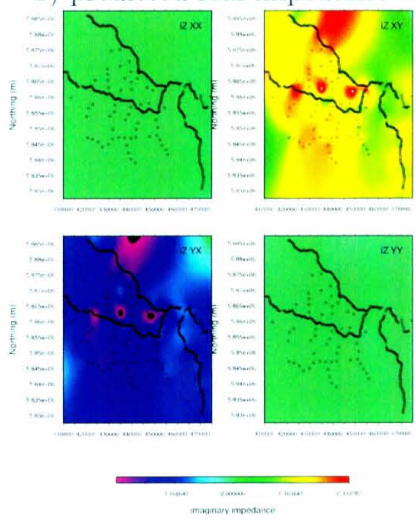

d) predicted imaginary impedance

Figure C.17: Observed (left) and predicted (right) impedances, both real and imaginary. Skin depth at frequency 150 Hz shown in Fig. C.5

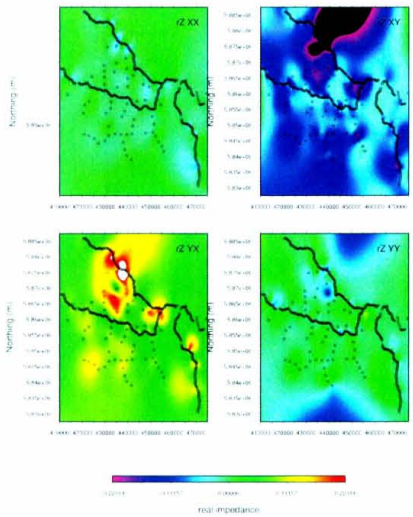

a) observed real impedance

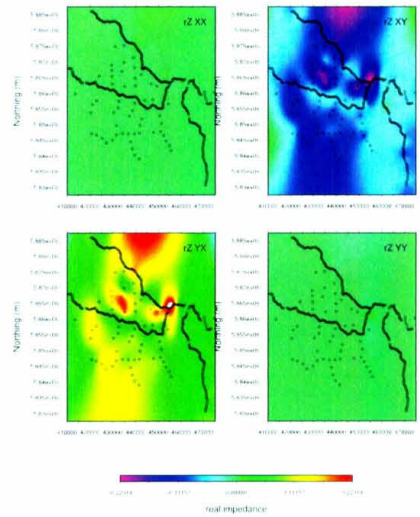

b) predicted real impedance

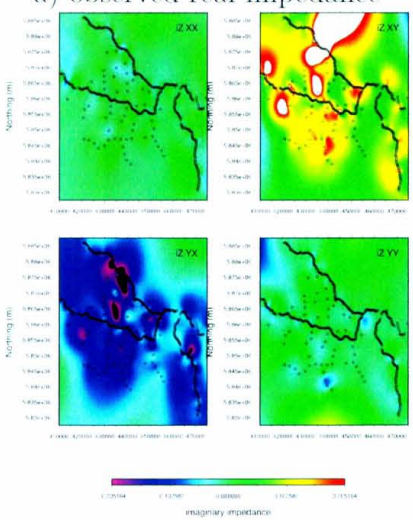

c) observed imaginary impedance

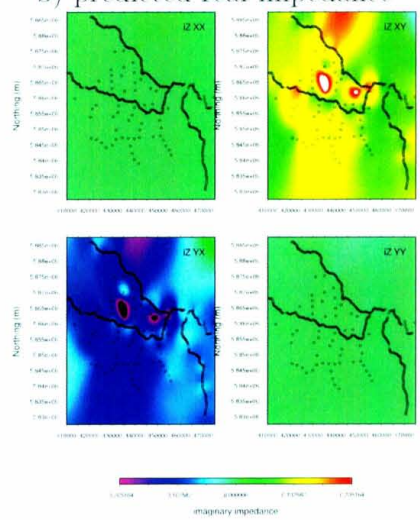

d) predicted imaginary impedance

Figure C.18: Observed (left) and predicted (right) impedances, both real and imaginary. Skin depth at frequency 40 Hz shown in Fig. C.6

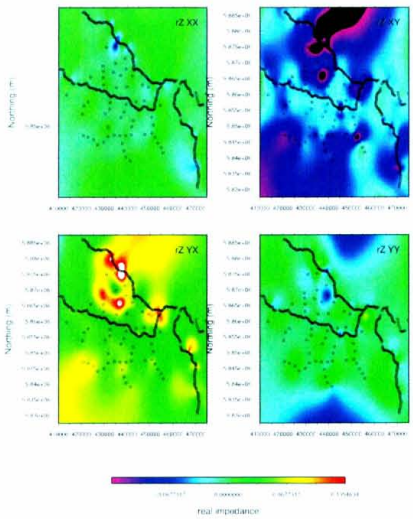

a) observed real impedance

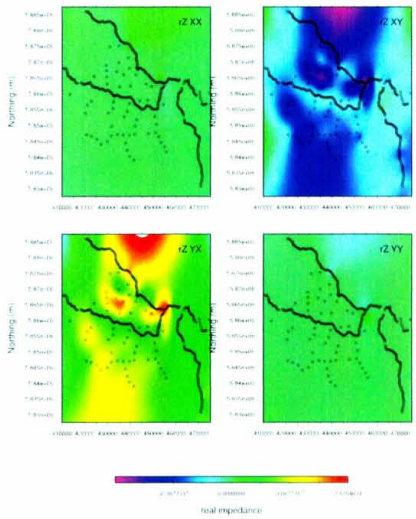

b) predicted real impedance

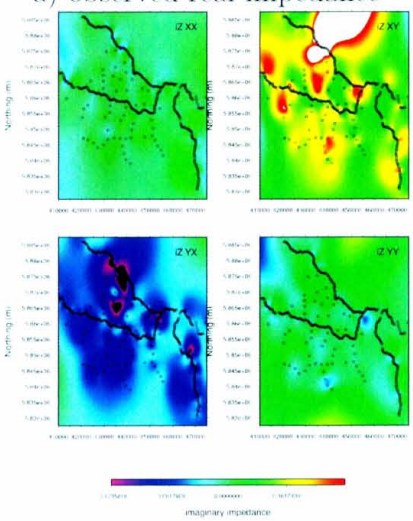

c) observed imaginary impedance

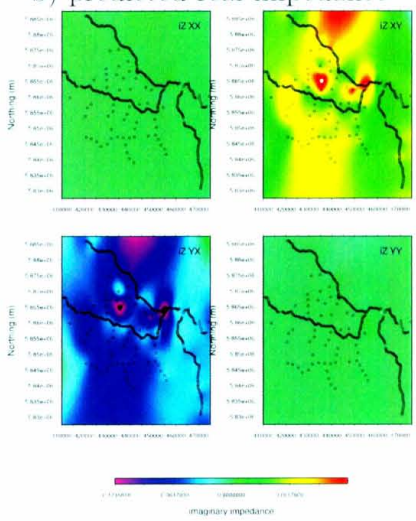

d) predicted imaginary impedance

Figure C.19: Observed (left) and predicted (right) impedances, both real and imaginary. Skin depth at frequency 13.7 Hz shown in Fig. C.7

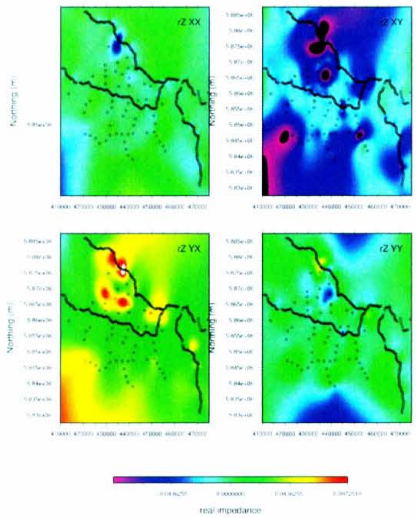

a) observed real impedance

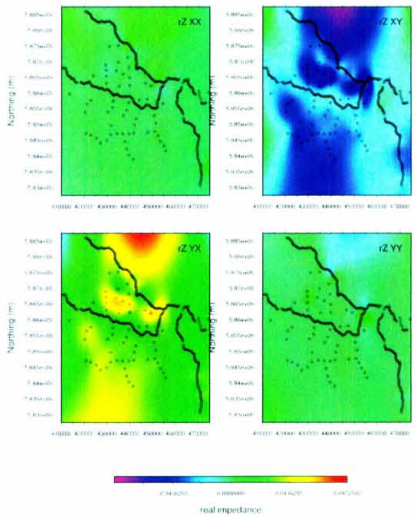

b) predicted real impedance

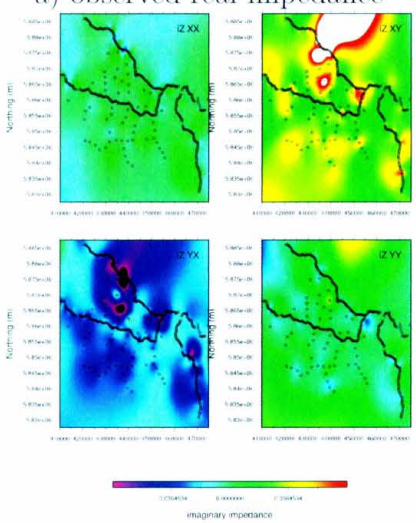

c) observed imaginary impedance

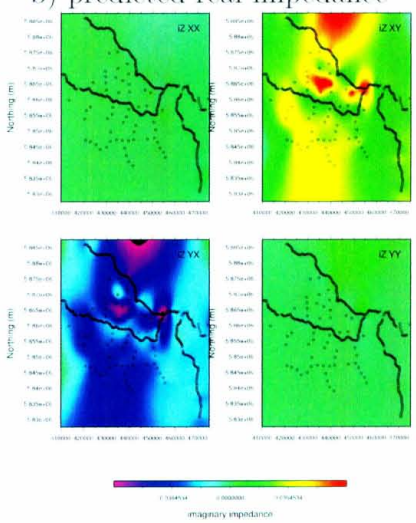

d) predicted imaginary impedance

Figure C.20: Observed (left) and predicted (right) impedances, both real and imaginary. Skin depth at frequency 4.7 Hz shown in Fig. C.8

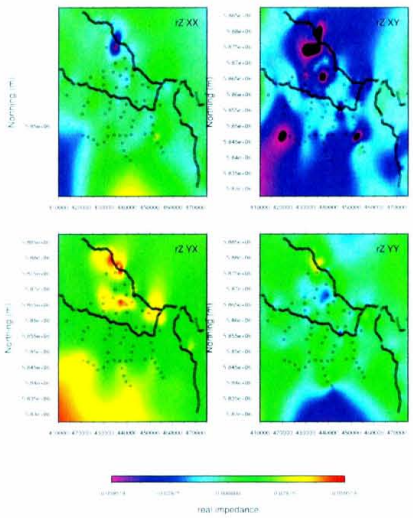

a) observed real impedance

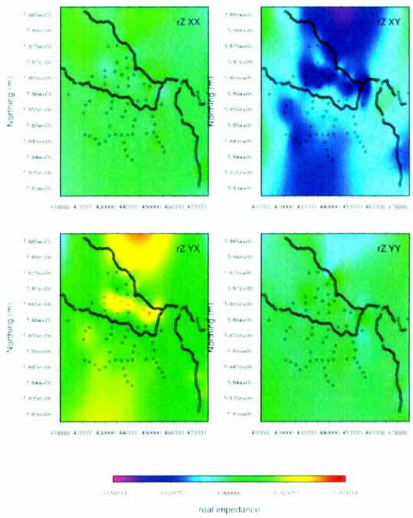

b) predicted real impedance

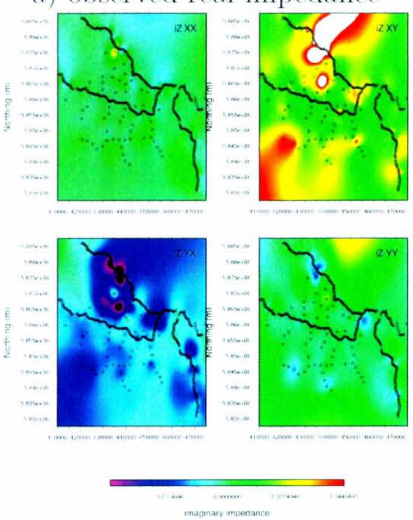

c) observed imaginary impedance

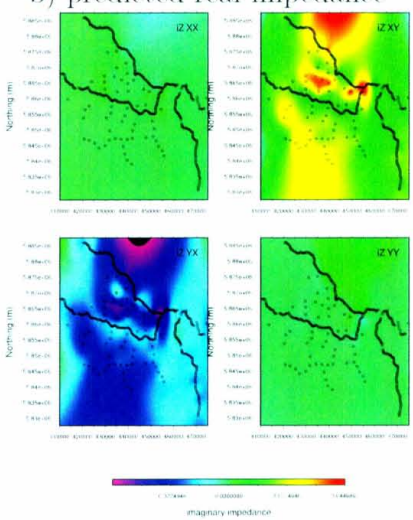

d) predicted imaginary impedance

Figure C.21: Observed (left) and predicted (right) impedances, both real and imaginary. Skin depth at frequency 1.72 Hz shown in Fig. C.9

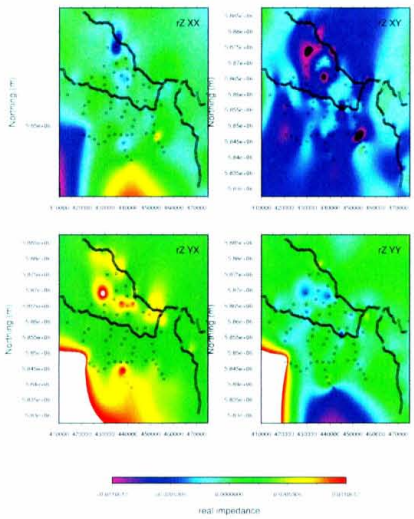

a) observed real impedance

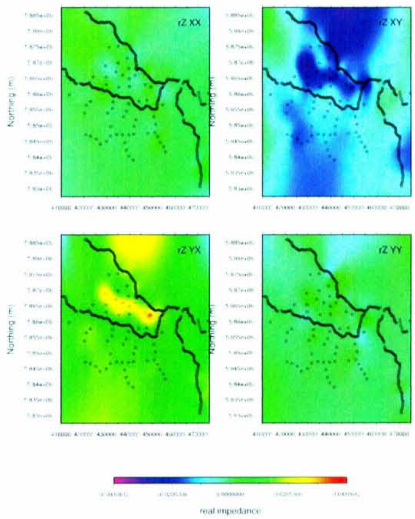

b) predicted real impedance

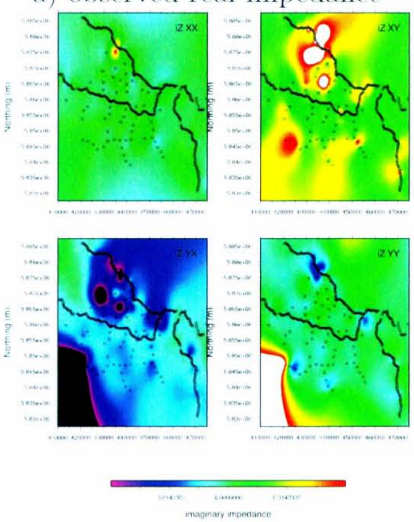

c) observed imaginary impedance

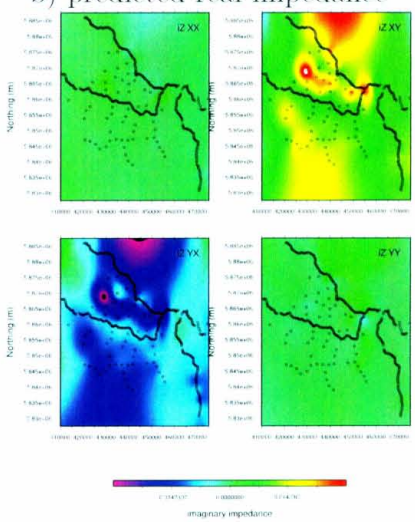

d) predicted imaginary impedance

Figure C.22: Observed (left) and predicted (right) impedances, both real and imaginary. Skin depth at frequency 0.59 Hz shown in Fig. C.10

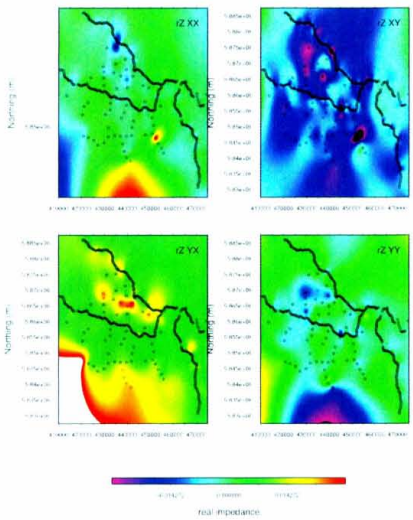

a) observed real impedance

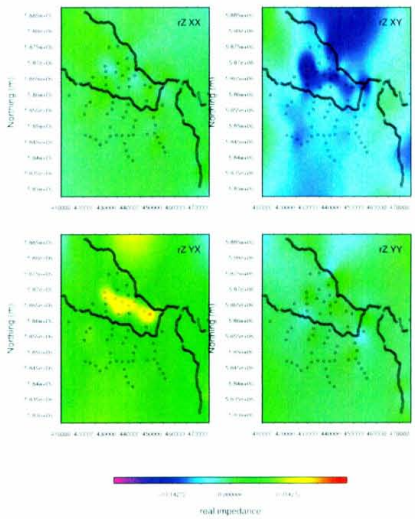

b) predicted real impedance

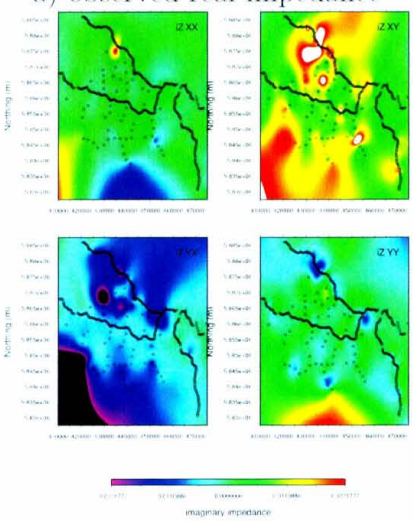

c) observed imaginary impedance

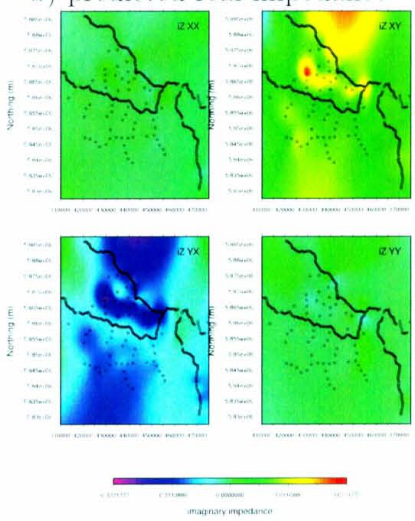

d) predicted imaginary impedance

Figure C.23: Observed (left) and predicted (right) impedances, both real and imaginary. Skin depth at frequency 0.215 Hz shown in Fig. C.11

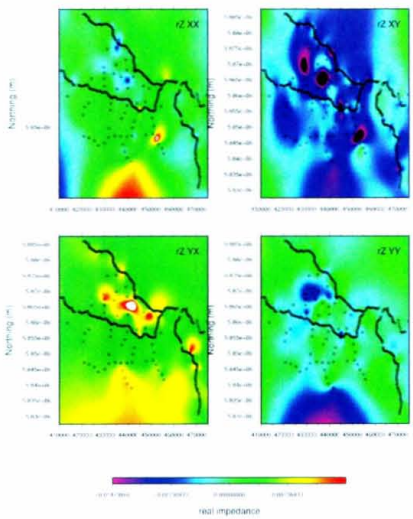

a) observed real impedance

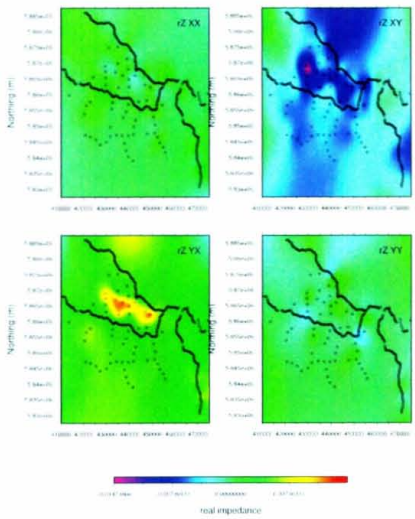

b) predicted real impedance

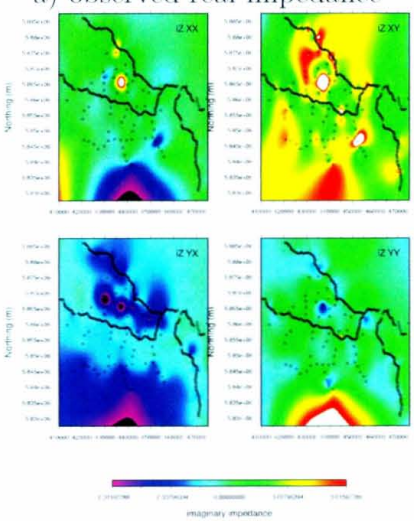

c) observed imaginary impedance

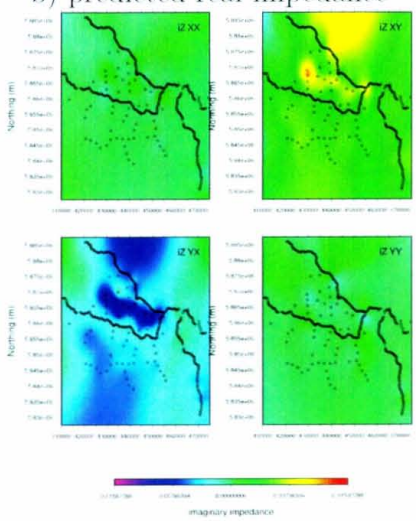

d) predicted imaginary impedance

Figure C.24: Observed (left) and predicted (right) impedances, both real and imaginary. Skin depth at frequency 0.073 Hz shown in Fig. C.12

C.2 16 frequencies, 62x62x62, no sign change

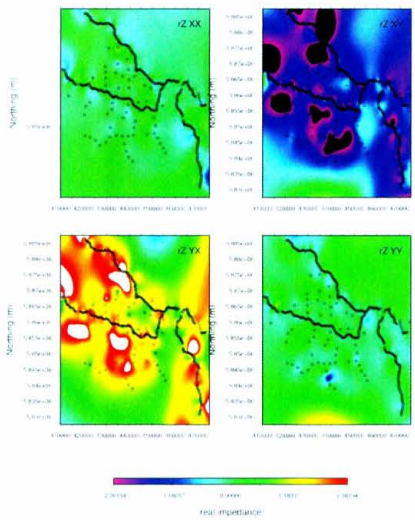

a) observed real impedance

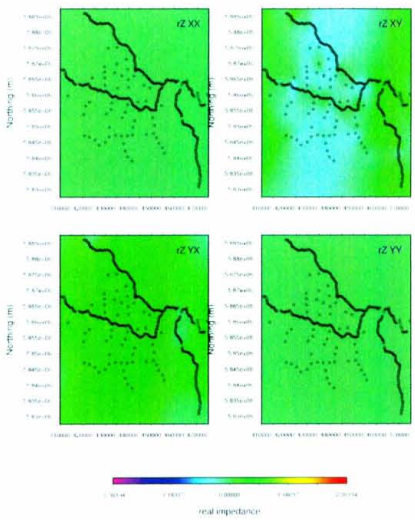

b) predicted real impedance

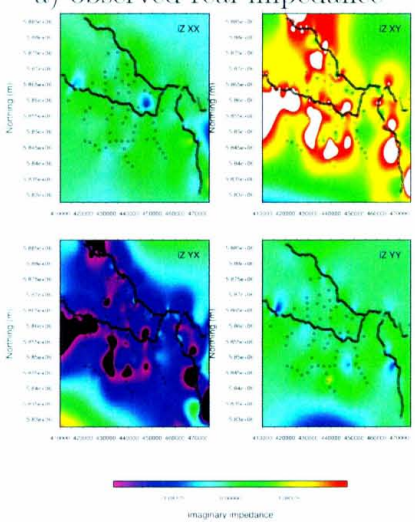

c) observed imaginary impedance

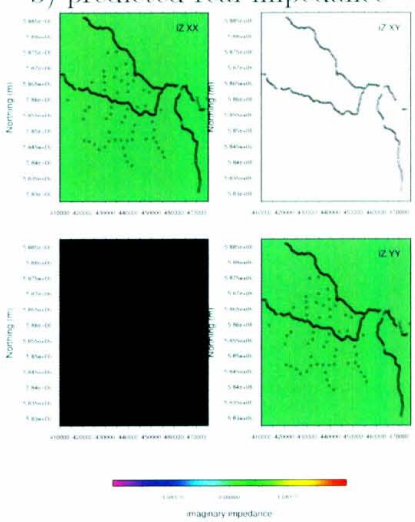

d) predicted imaginary impedance

Figure C.25: Observed (left) and predicted (right) impedances, both real and imaginary.

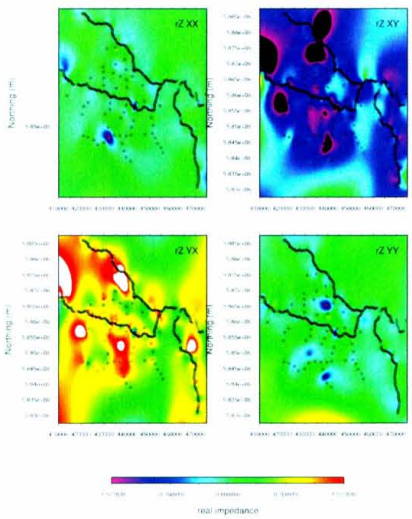

a) observed real impedance

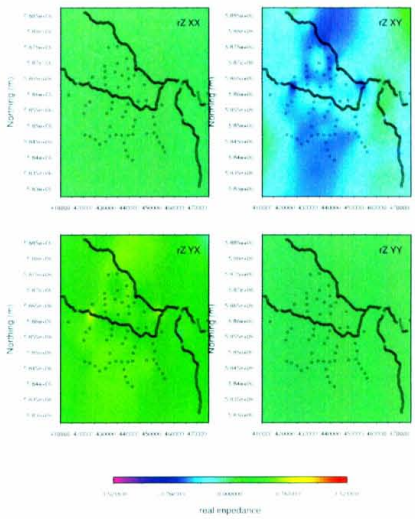

b) predicted real impedance

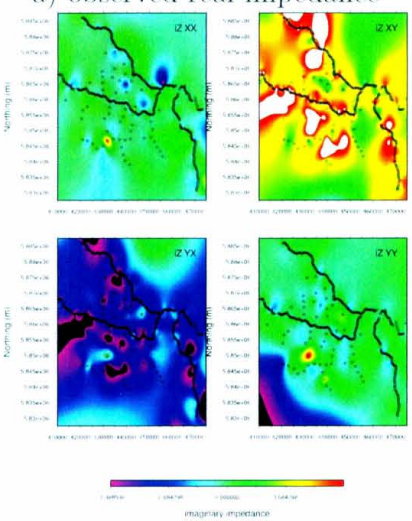

c) observed imaginary impedance

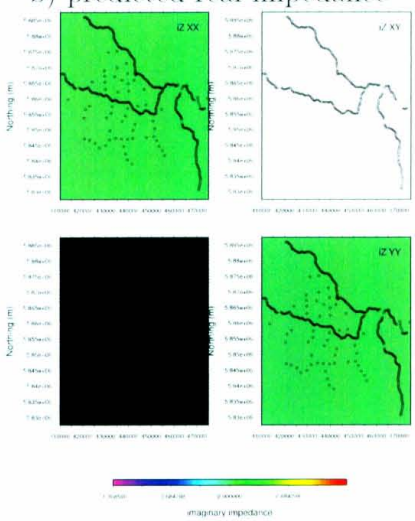

d) predicted imaginary impedance

Figure C.26: Observed (left) and predicted (right) impedances, both real and imaginary.

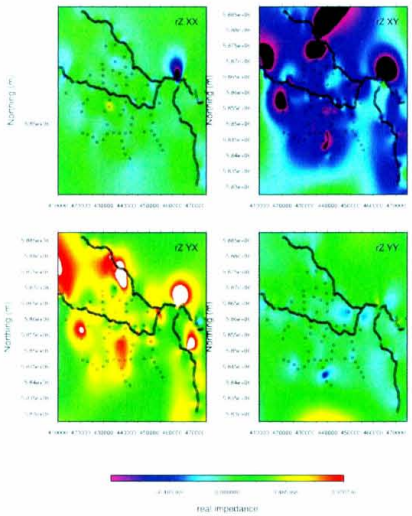

a) observed real impedance

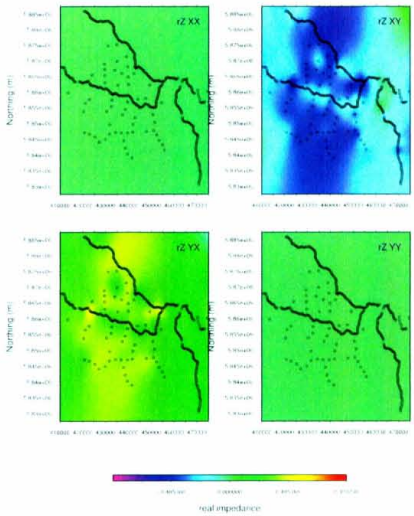

b) predicted real impedance

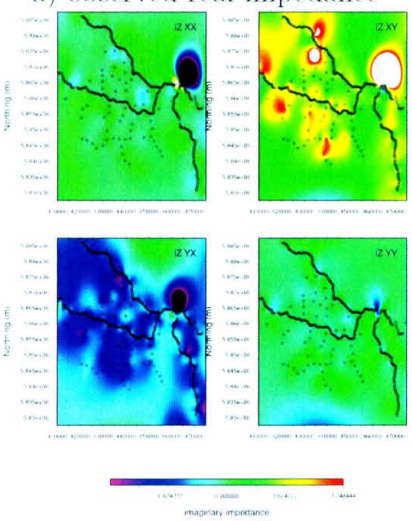

c) observed imaginary impedance

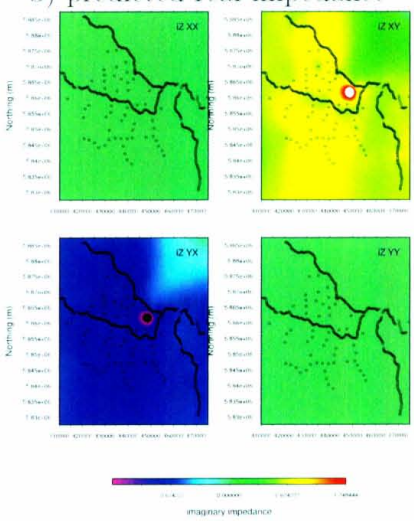

d) predicted imaginary impedance

Figure C.27: Observed (left) and predicted (right) impedances, both real and imaginary.

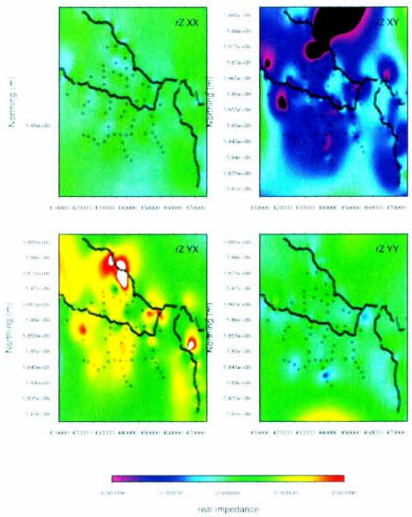

a) observed real impedance

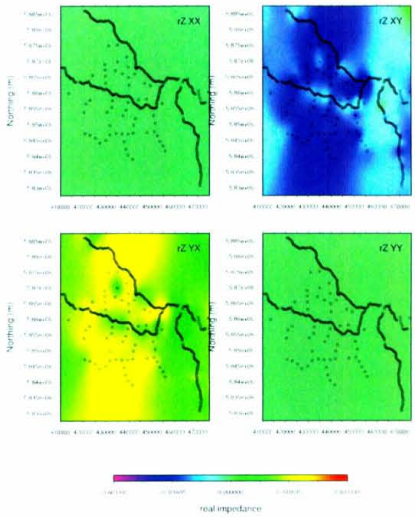

b) predicted real impedance

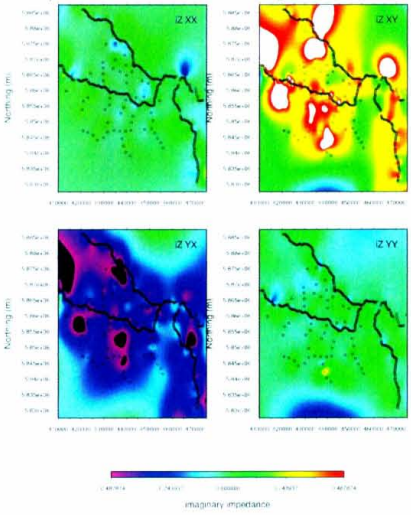

c) observed imaginary impedance

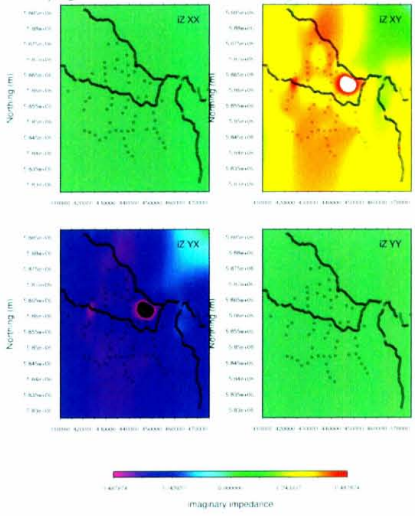

d) predicted imaginary impedance

Figure C.28: Observed (left) and predicted (right) impedances, both real and imaginary.

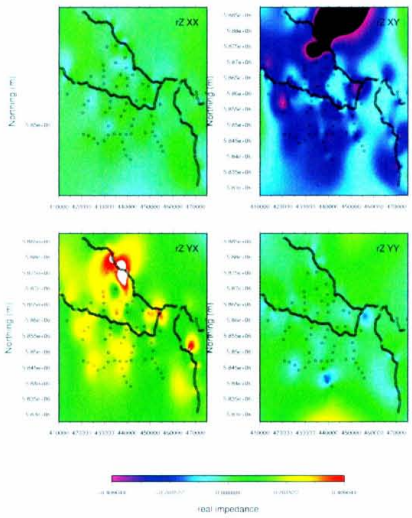

a) observed real impedance

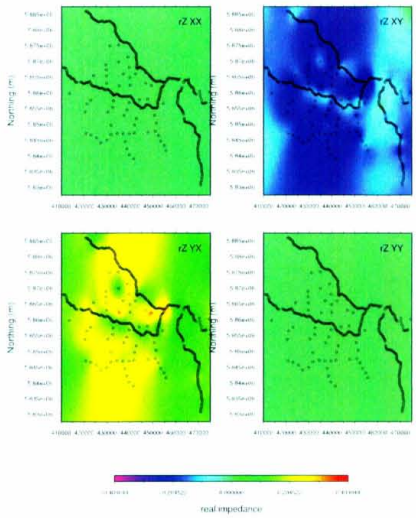

b) predicted real impedance

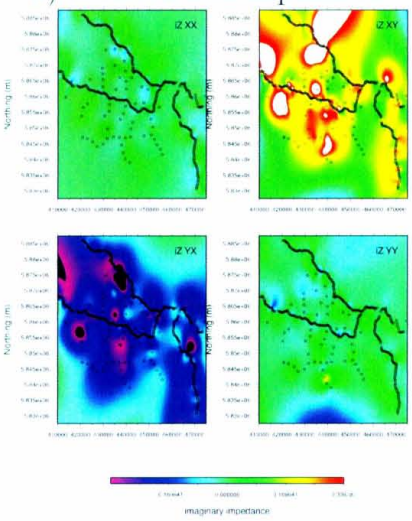

c) observed imaginary impedance

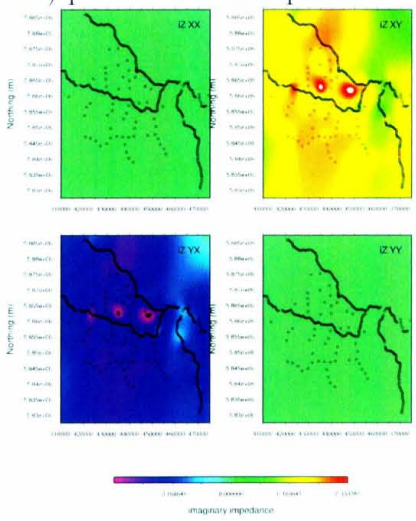

d) predicted imaginary impedance

Figure C.29: Observed (left) and predicted (right) impedances, both real and imaginary.

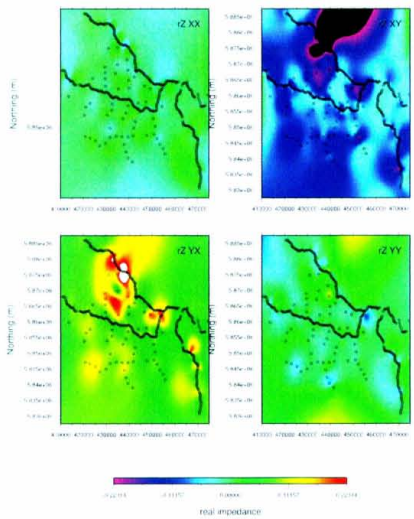

a) observed real impedance

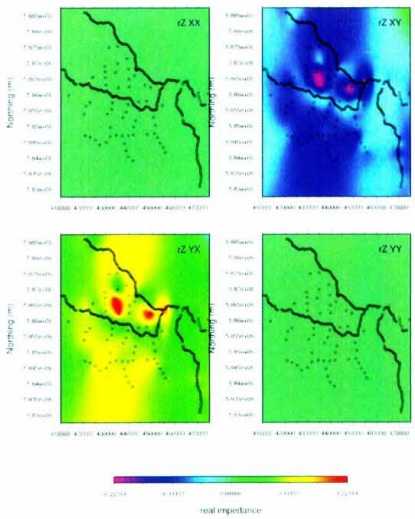

b) predicted real impedance

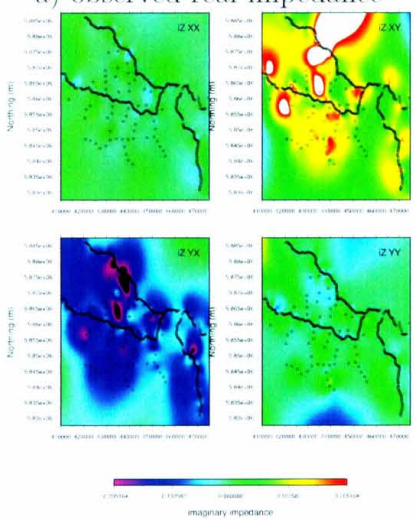

c) observed imaginary impedance

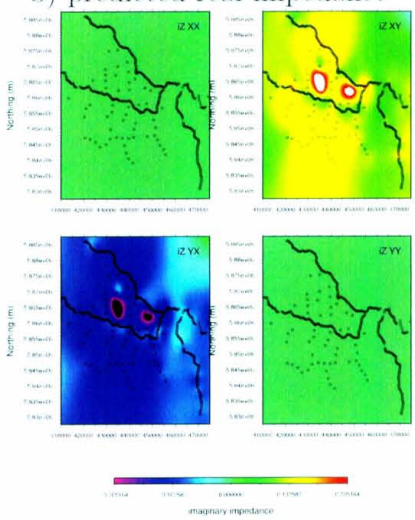

d) predicted imaginary impedance

Figure C.30: Observed (left) and predicted (right) impedances, both real and imaginary.

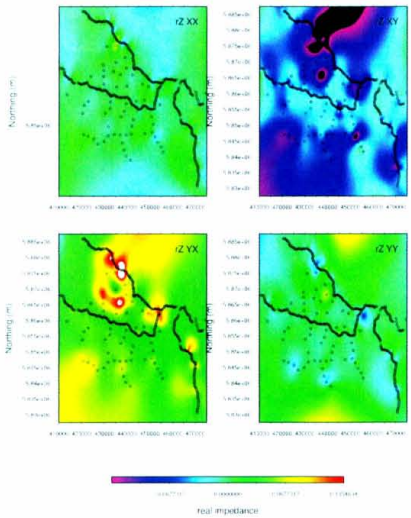

a) observed real impedance

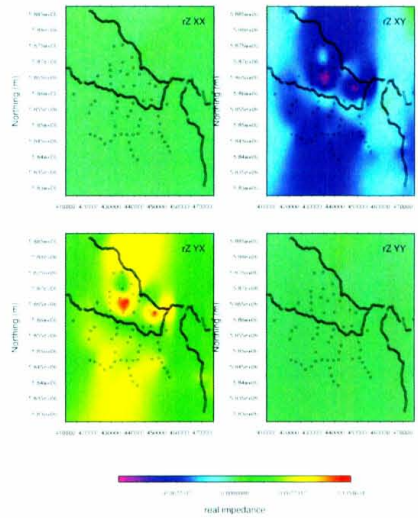

b) predicted real impedance

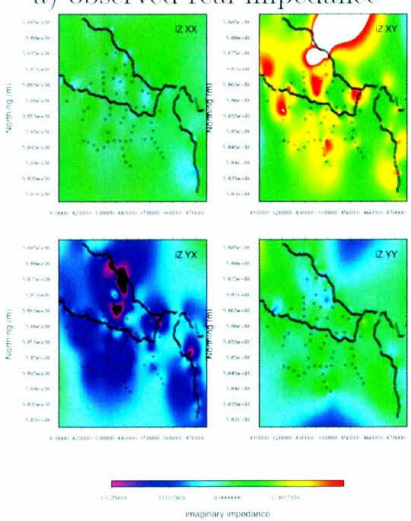

c) observed imaginary impedance

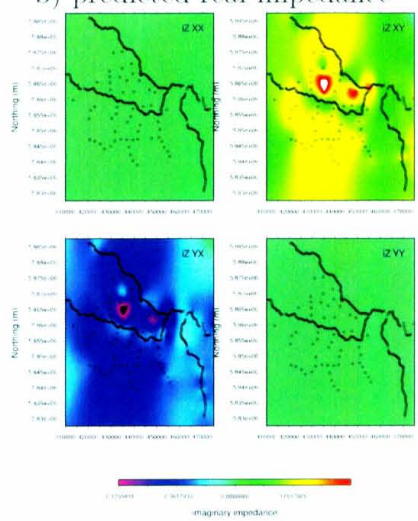

d) predicted imaginary impedance

Figure C.31: Observed (left) and predicted (right) impedances, both real and imaginary.

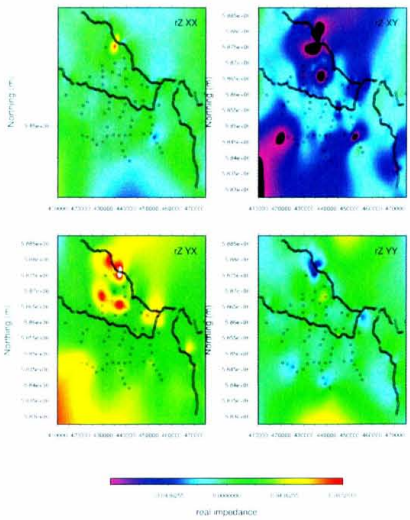

a) observed real impedance

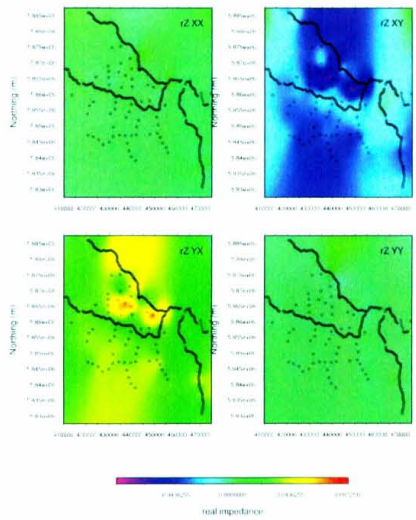

b) predicted real impedance

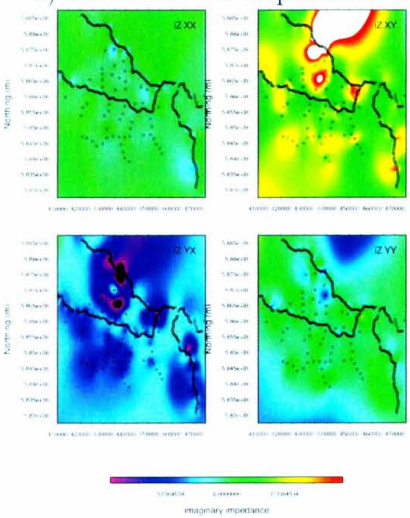

c) observed imaginary impedance

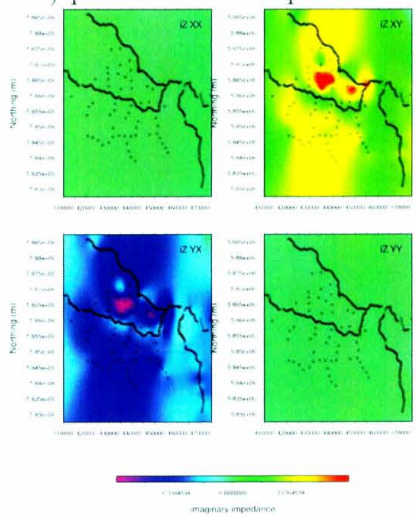

d) predicted imaginary impedance

Figure C.32: Observed (left) and predicted (right) impedances, both real and imaginary.

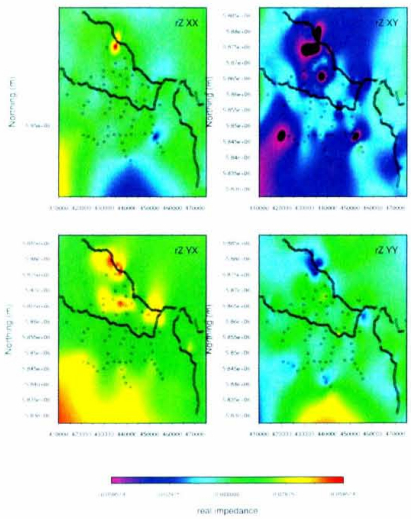

a) observed real impedance

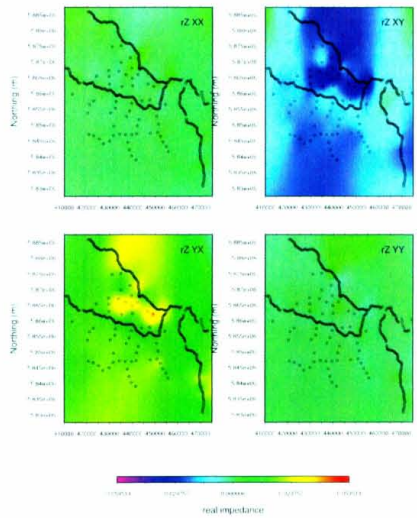

b) predicted real impedance

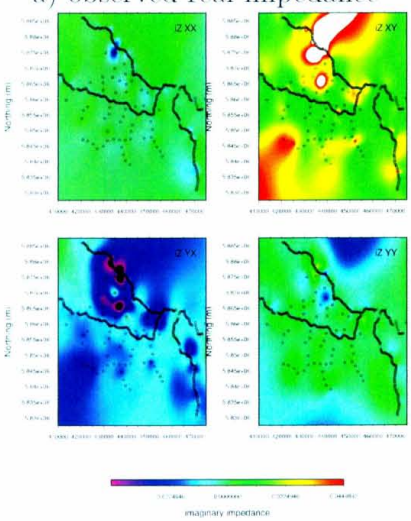

c) observed imaginary impedance

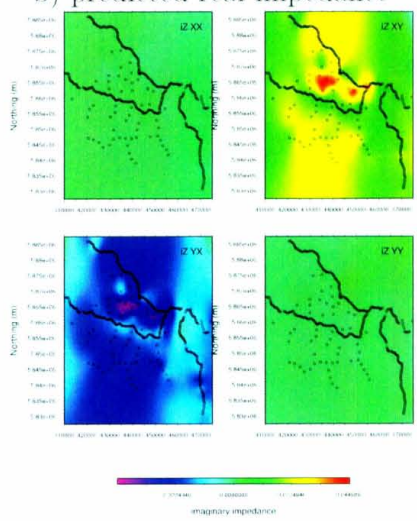

d) predicted imaginary impedance

Figure C.33: Observed (left) and predicted (right) impedances, both real and imaginary.

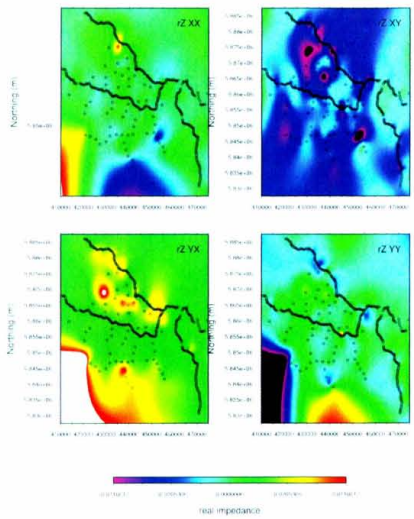

a) observed real impedance

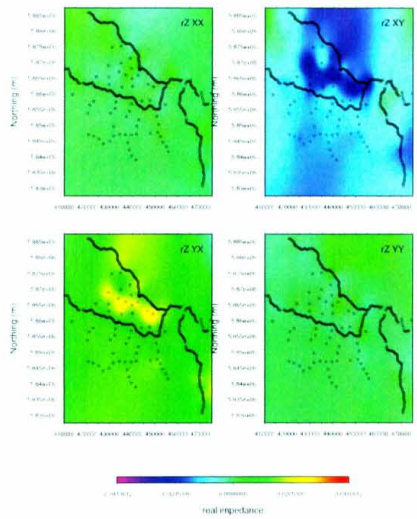

b) predicted real impedance

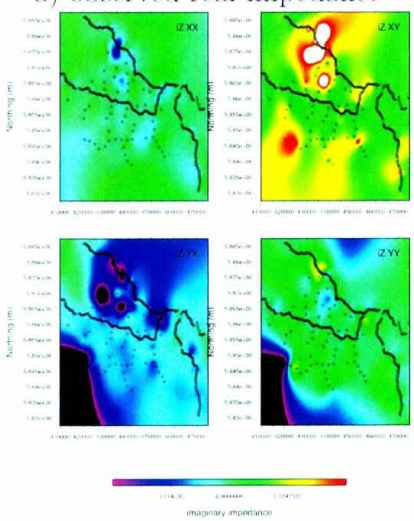

c) observed imaginary impedance

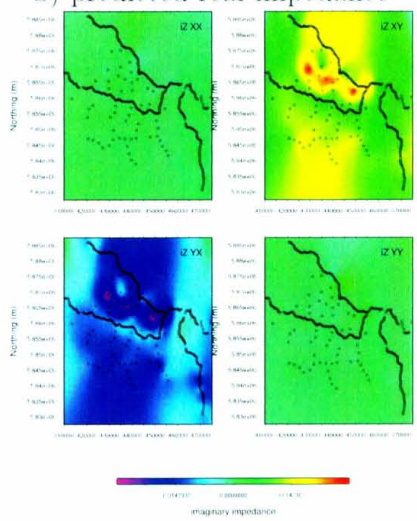

d) predicted imaginary impedance

Figure C.34: Observed (left) and predicted (right) impedances, both real and imaginary.

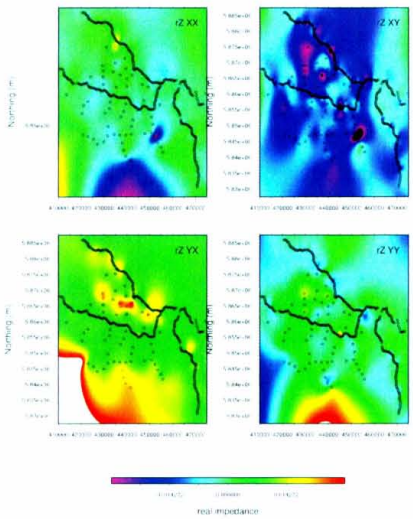

a) observed real impedance

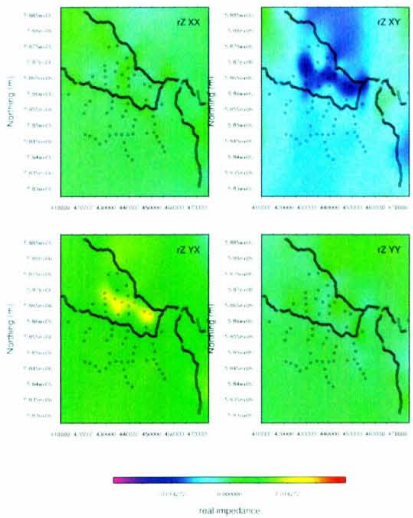

b) predicted real impedance

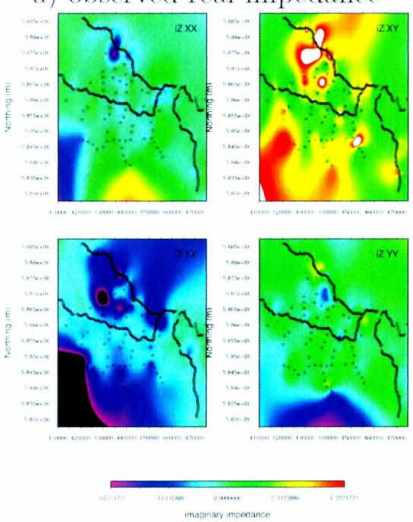

c) observed imaginary impedance

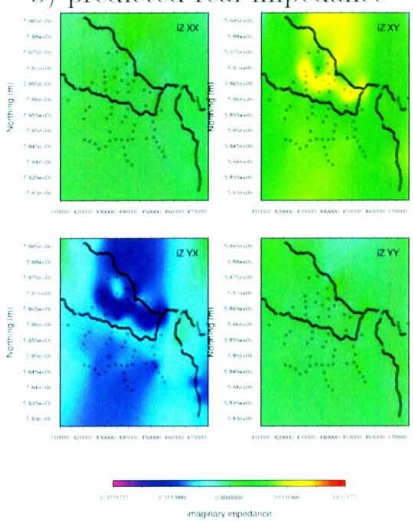

d) predicted imaginary impedance

Figure C.35: Observed (left) and predicted (right) impedances, both real and imaginary.

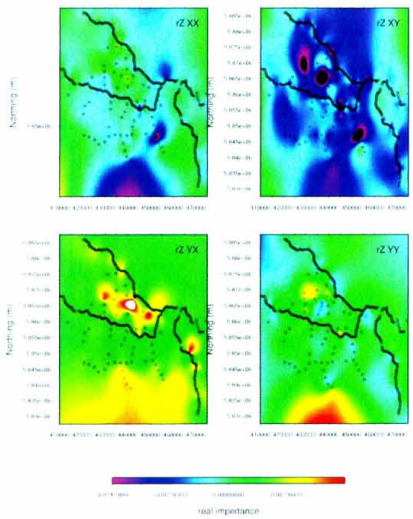

a) observed real impedance

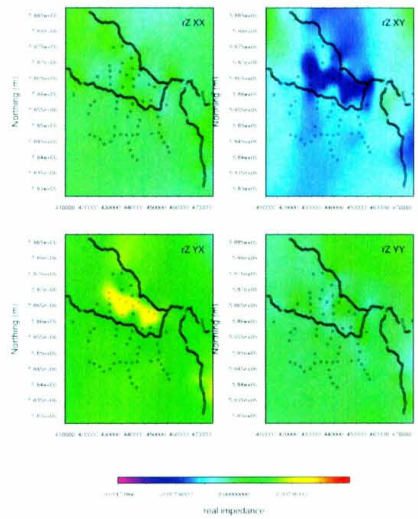

b) predicted real impedance

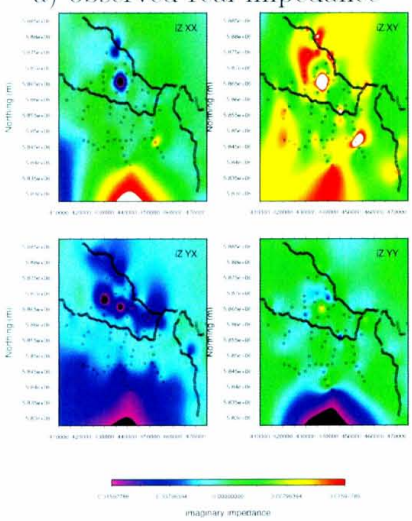

c) observed imaginary impedance

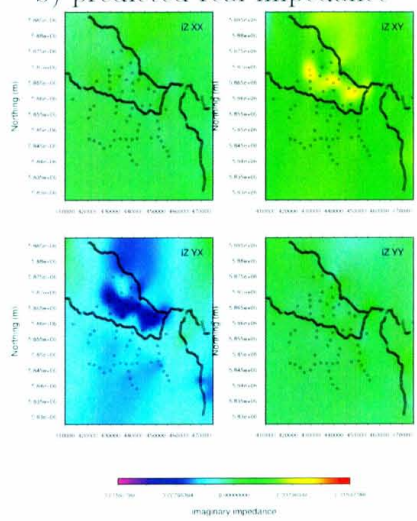

d) predicted imaginary impedance

Figure C.36: Observed (left) and predicted (right) impedances, both real and imaginary.

Appendix D

Comparison With Other Models

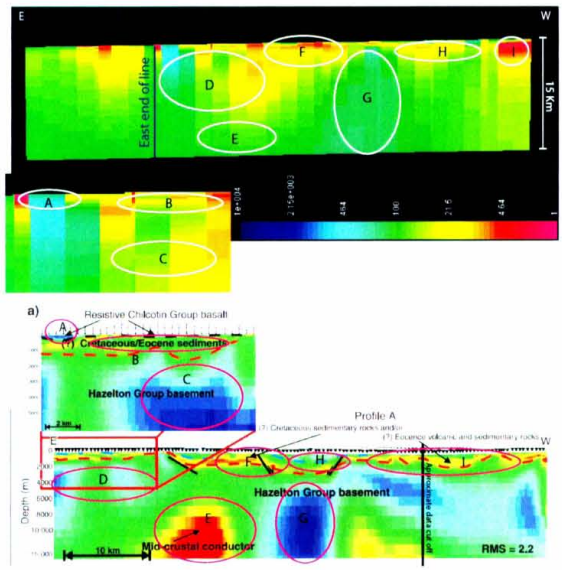

Figure D.1: Comparison with 2D for profile A, East to West. 16 frequencies, 50x50x50, without sign change.

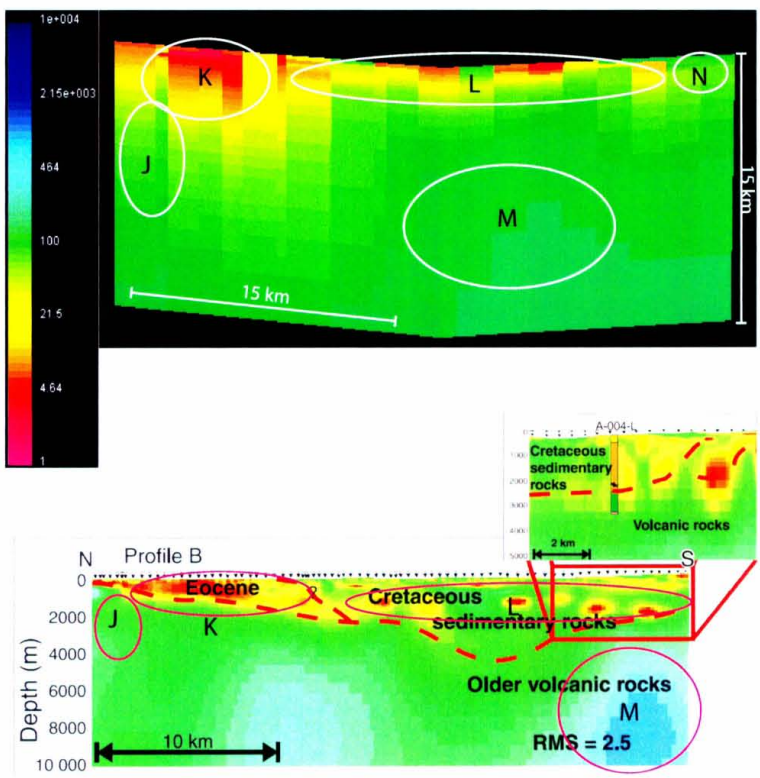

Figure D.2: Comparison with 2D for profile B, North to South. 16 frequencies, 50x50x50, without sign change.

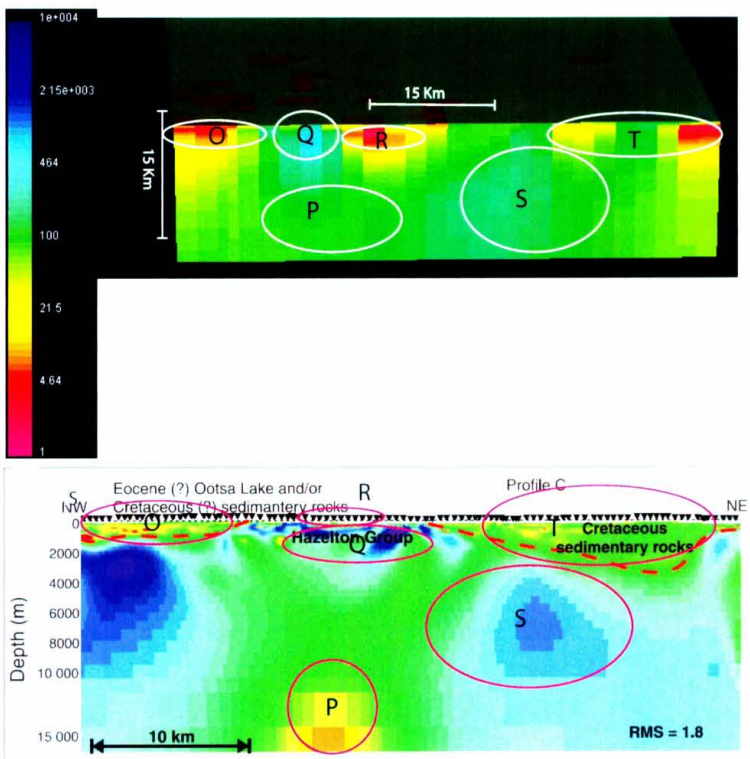

Figure D.3: Comparison with 2D for profile C, Southwest to Northeast. 16 frequencies, 50x50x50, without sign change.

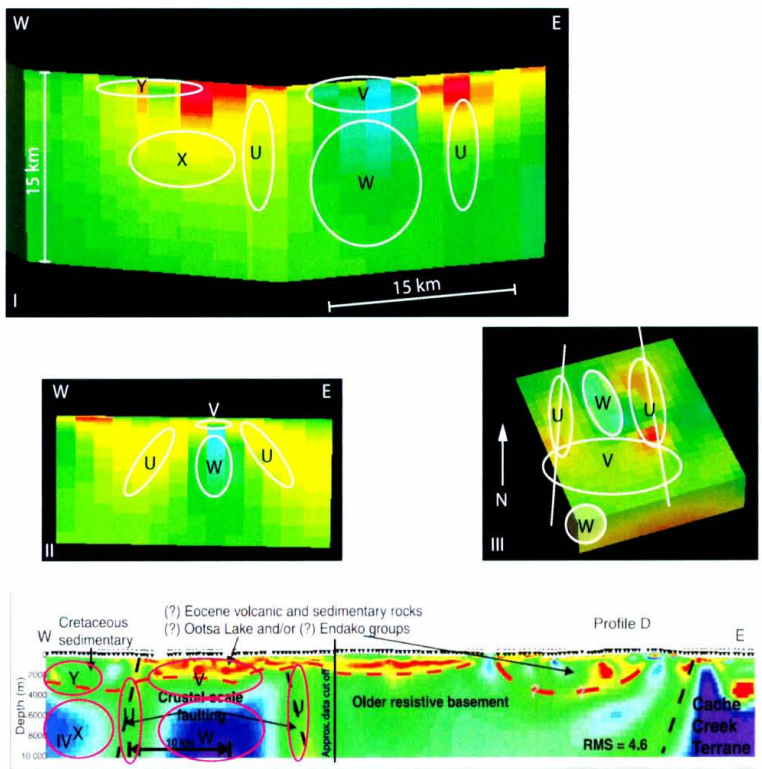

Figure D.4: Comparison with 2D for profile D, West to East. 16 frequencies, 50x50x50, without sign change.

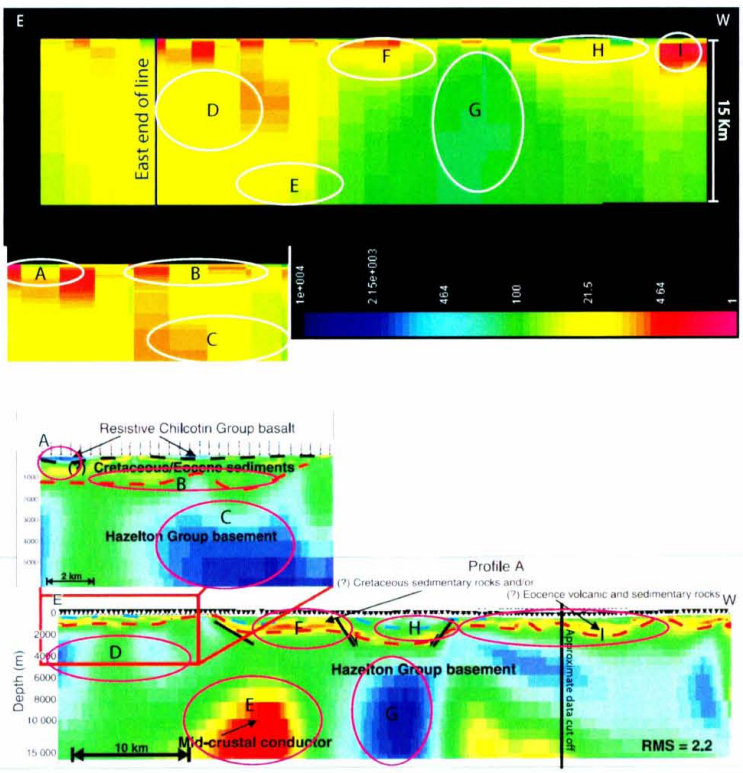

Figure D.5: Comparison with 2D for profile A, East to West. 8 frequencies, 50x50x50, with sign change.

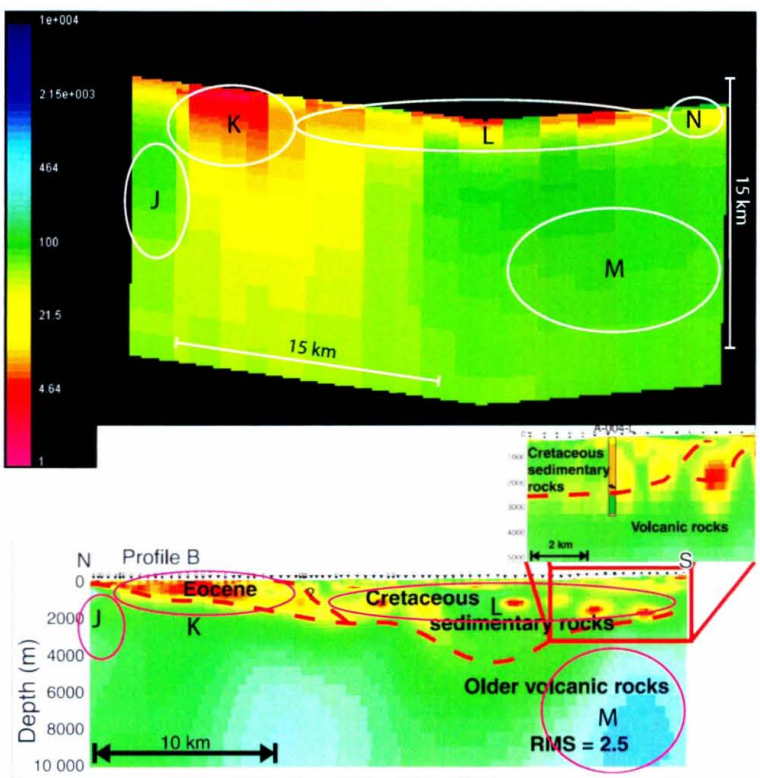

Figure D.6: Comparison with 2D for profile B, North to South. 8 frequencies, 50x50x50, with sign change.

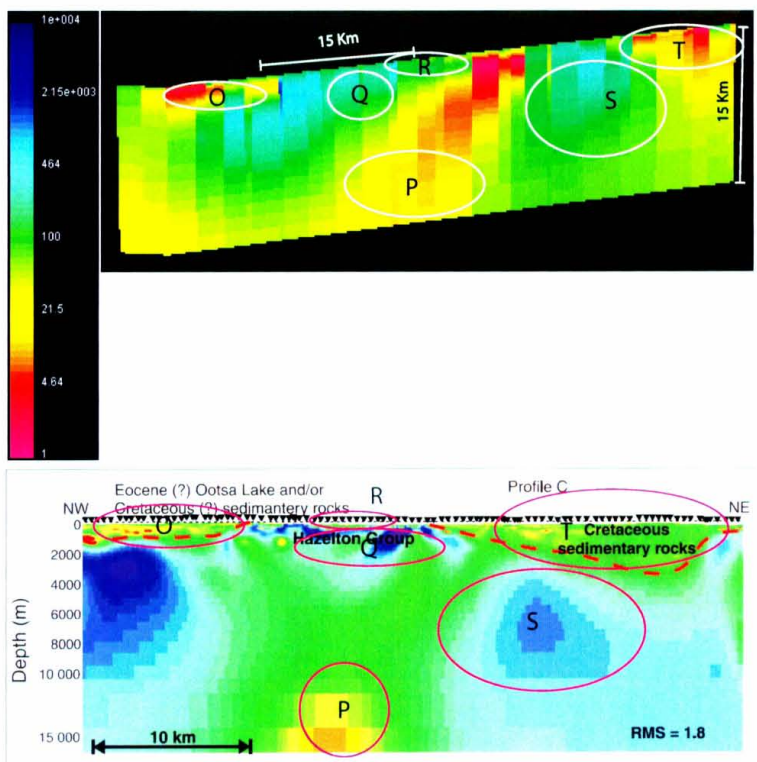

Figure D.7: Comparison with 2D for profile C. Southwest to Northeast. 8 frequencies, 50x50x50, with sign change.

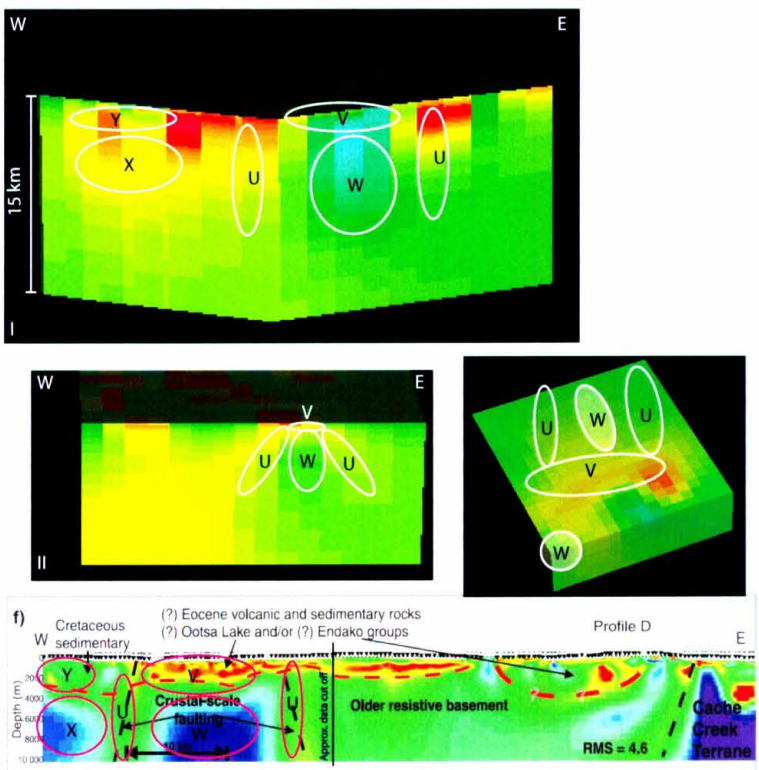

Figure D.8: Comparison with 2D for profile D, West to East. 8 frequencies, 50x50x50, with sign change.

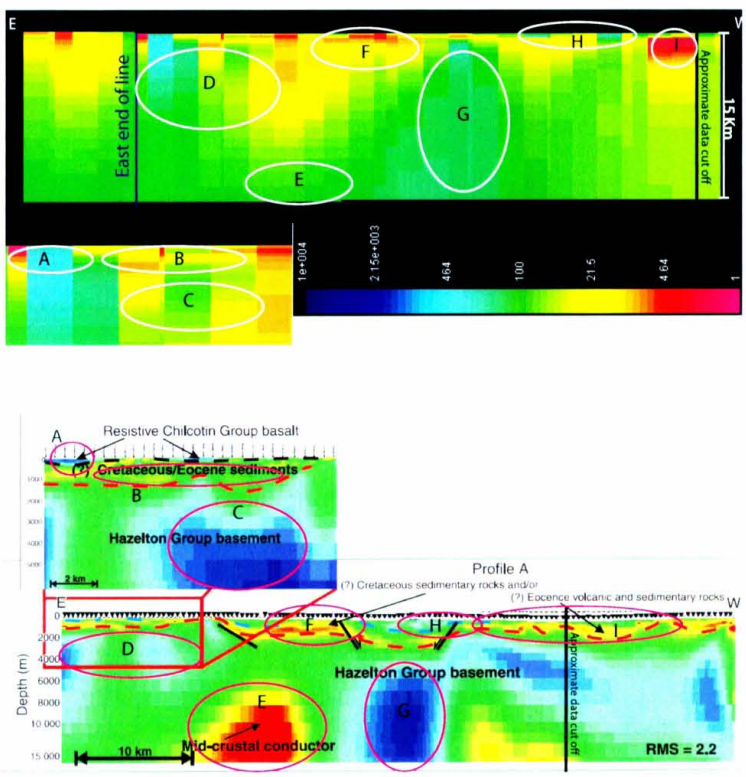

Figure D.9: Comparison with 2D for profile A, East to West. 8 frequencies, 50x50x50, without sign change.

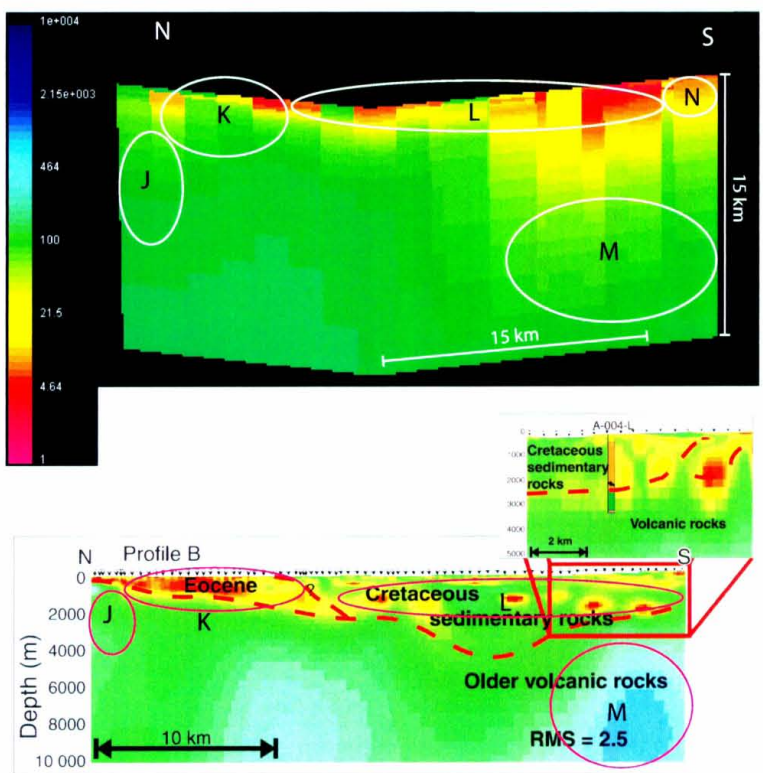

Figure D.10: Comparison with 2D for profile B, North to South. 8 frequencies, 50x50x50, without sign change.

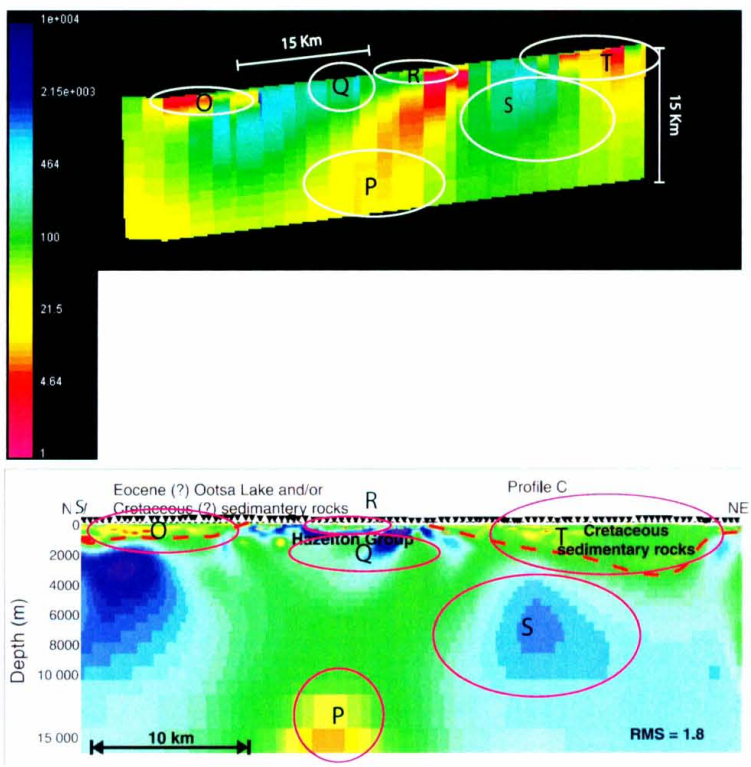

Figure D.11: Comparison with 2D for profile C, Southwest to Northeast. 8 frequencies, 50x50x50, without sign change.

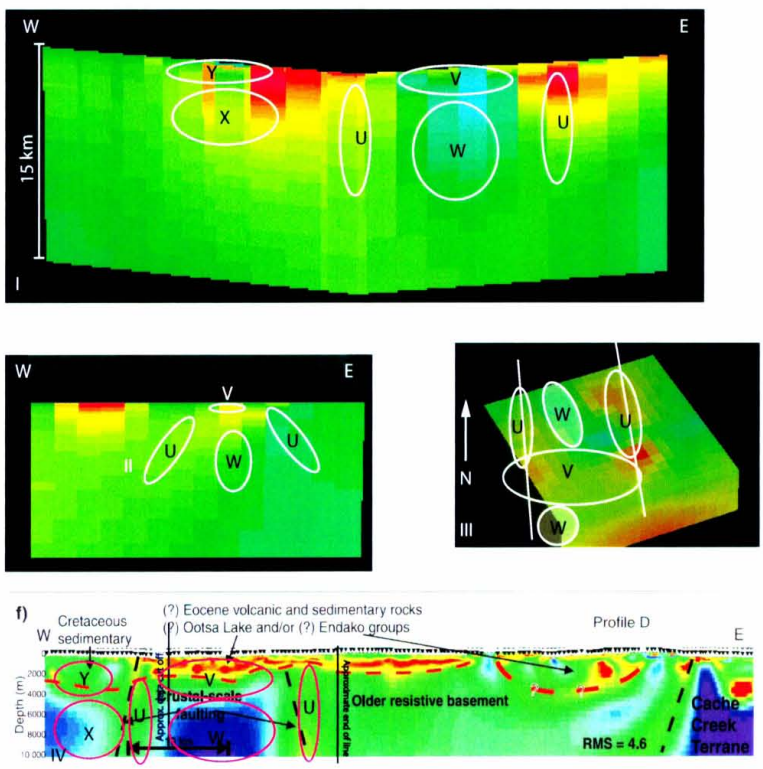

Figure D.12: Comparison with 2D for profile D, West to East. 8 frequencies, 50x50x50, without sign change.

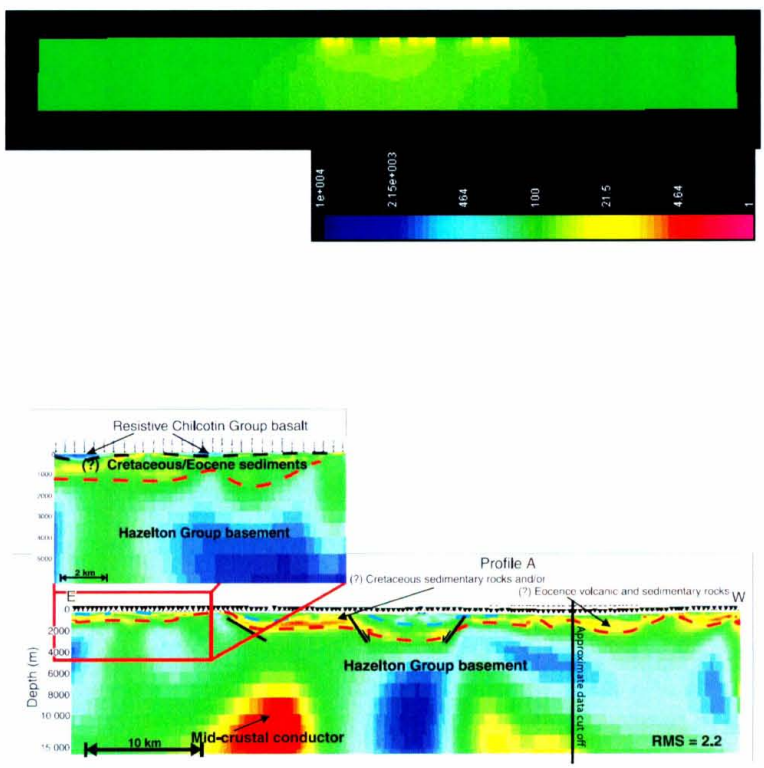

Figure D.13: Comparison with 2D for profile A, East to West. 18 frequencies, 75x69x70, with sign change and site thinning.

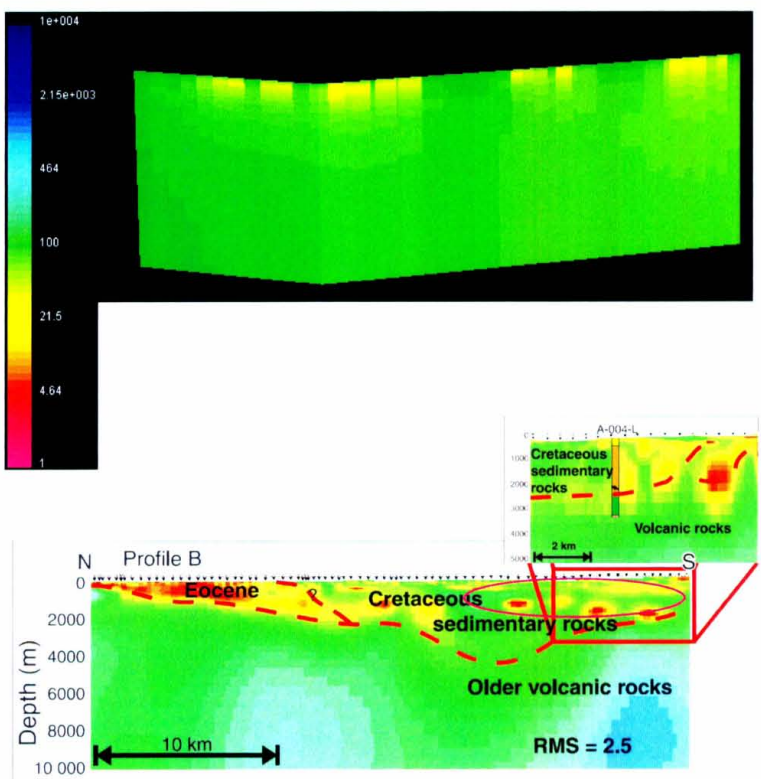

Figure D.14: Comparison with 2D for profile B, North to South. 18 frequencies, 75x69x70, with sign change and site thinning.

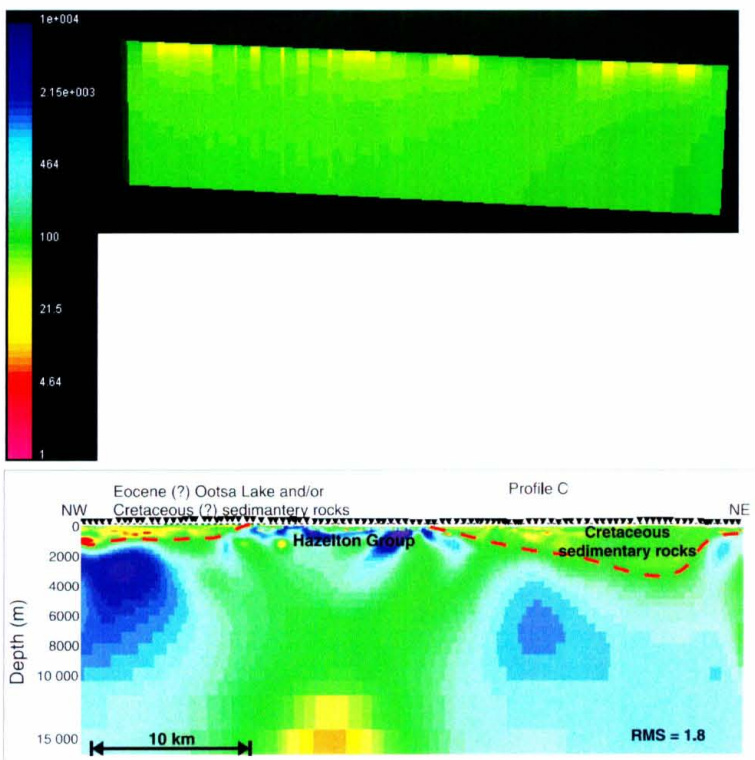

Figure D.15: Comparison with 2D for profile C, Southwest to Northeast. 18 frequencies, 75x69x70, with sign change and site thinning.

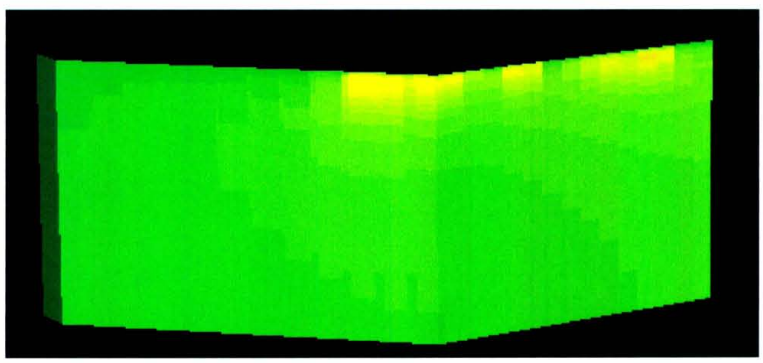

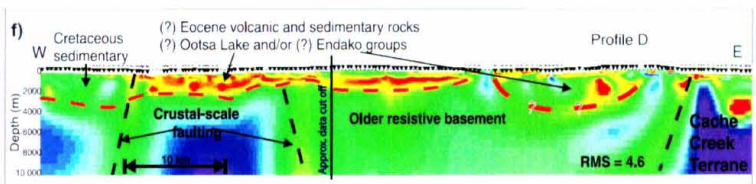

Figure D.16: Comparison with 2D for profile D. West to East. 18 frequencies, 75x69x70, with sign change and site thinning.

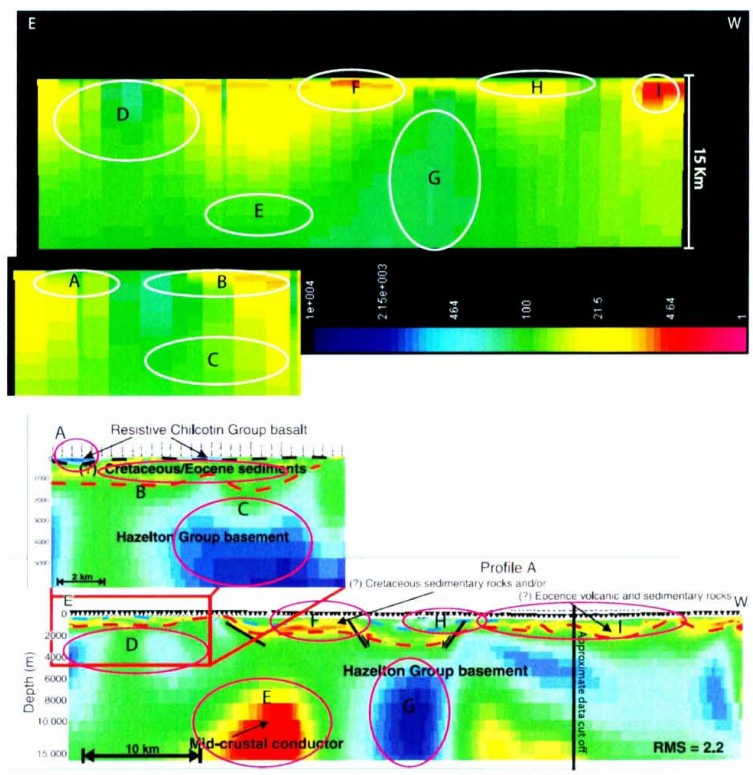

Figure D.17: Comparison with 2D for profile A, East to West. 8 frequencies, 62x62x62, without sign change.

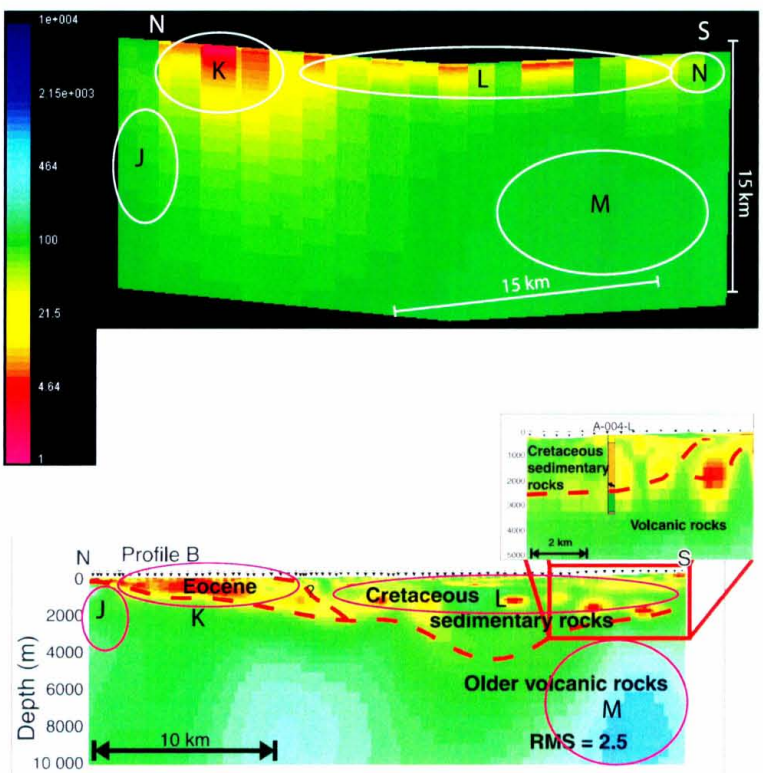

Figure D.18: Comparison with 2D for profile B, North to South. 8 frequencies, 62x62x62, without sign change.

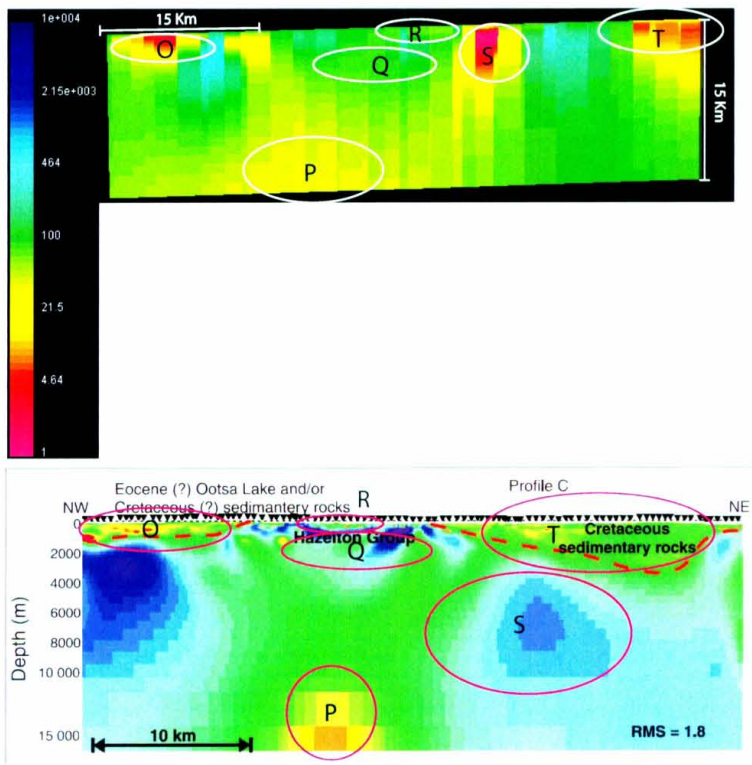

Figure D.19: Comparison with 2D for profile C, Southwest to Northeast. 8 frequencies, 62x62x62, without sign change.

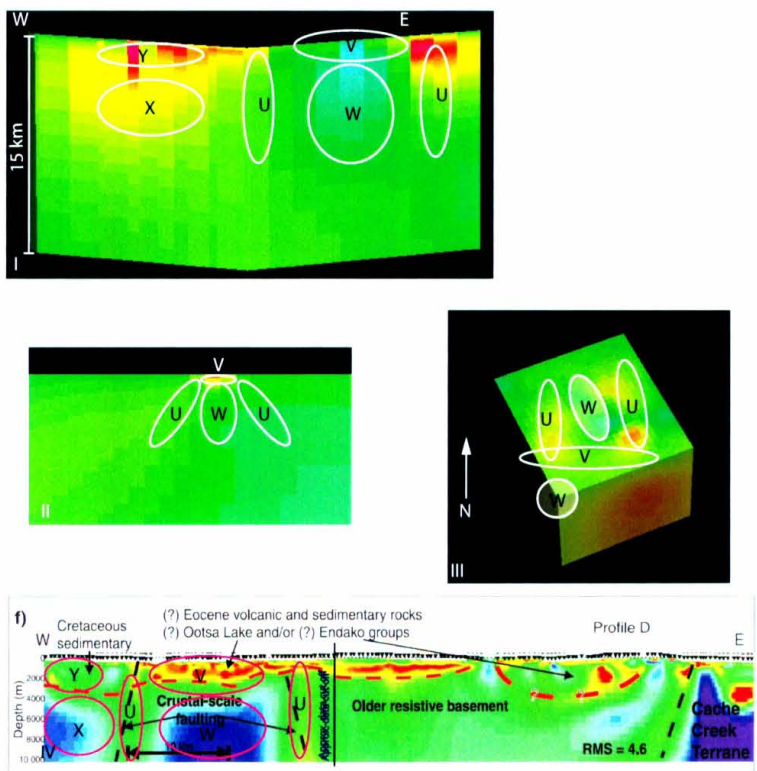

Figure D.20: Comparison with 2D for profile D, West to East. 8 frequencies, 62x62x62, without sign change.

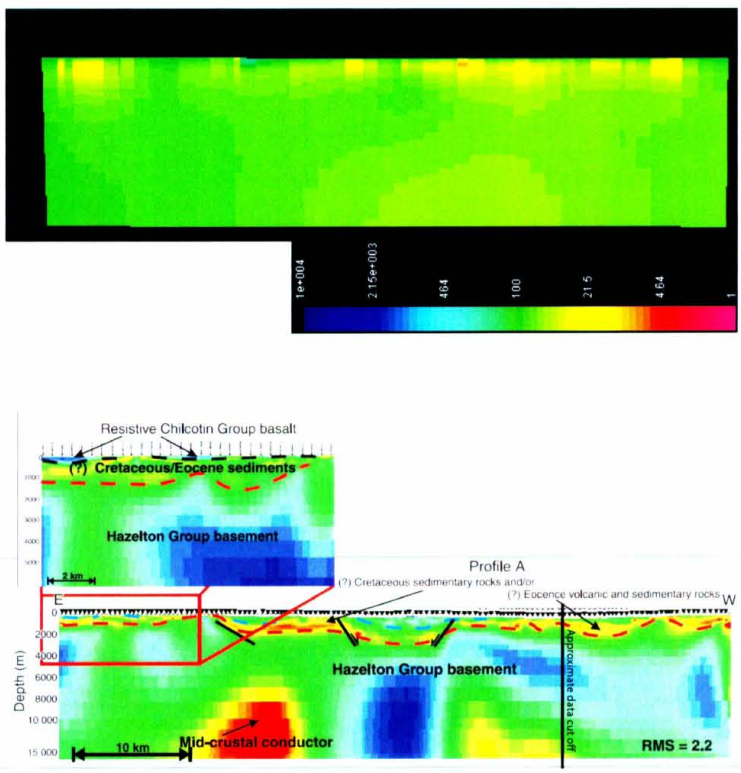

Figure D.21: Comparison with 2D for profile A, East to West. 18 frequencies, 75x69x70, without sign change.

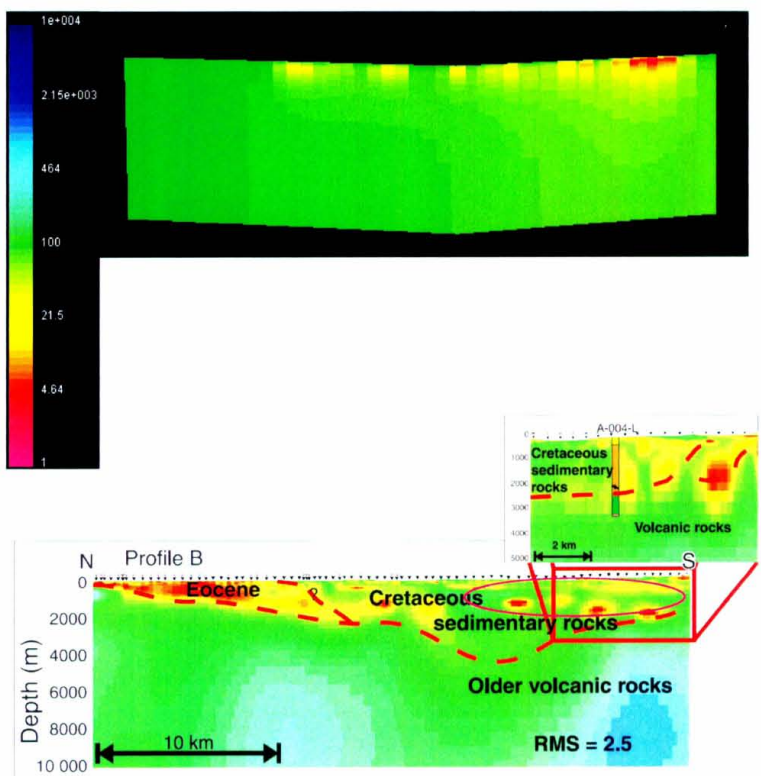

Figure D.22: Comparison with 2D for profile B, North to South. 18 frequencies, 75x69x70, without sign change.

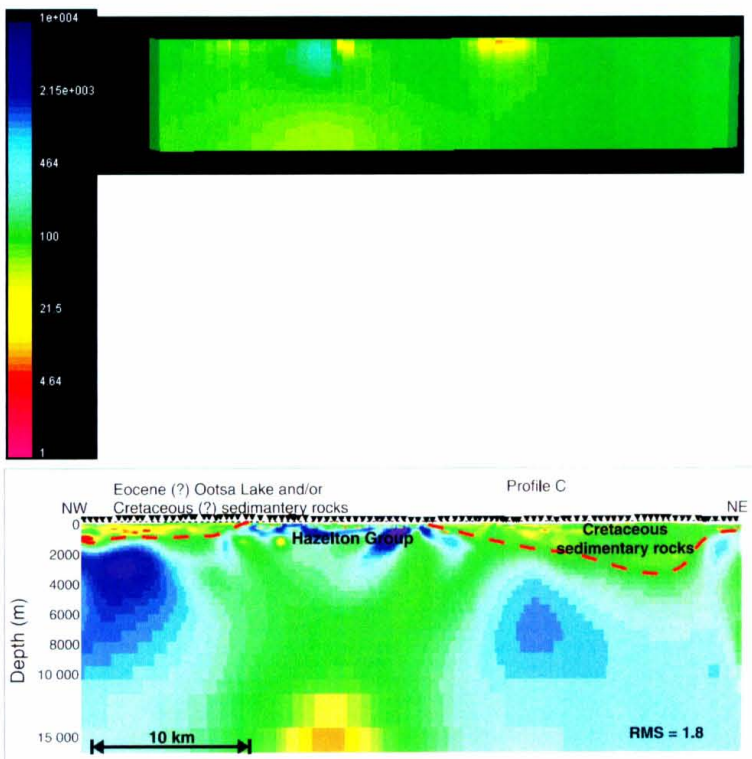

Figure D.23: Comparison with 2D for profile C, Southwest to Northeast. 18 frequencies, 75x69x70, without sign change.

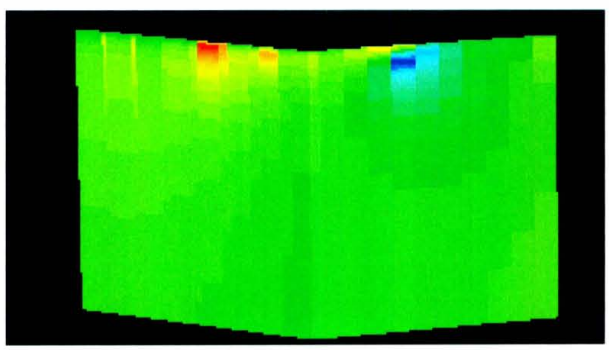

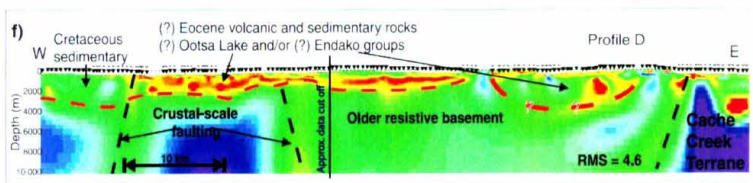

Figure D.24: Comparison with 2D for profile D, West to East. 18 frequencies, 75x69x70, without sign change.

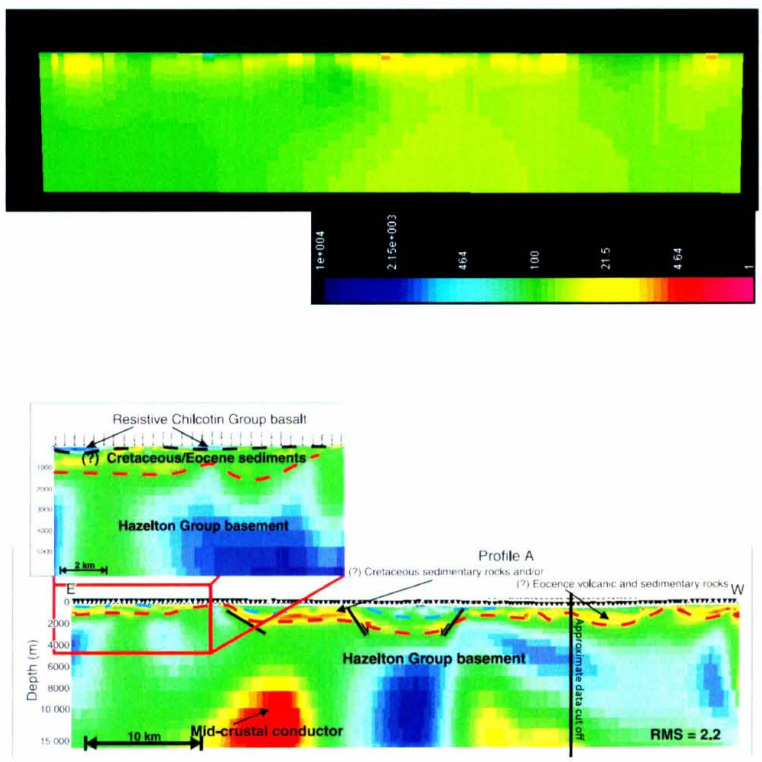

Figure D.25: Comparison with 2D for profile A, East to West. 18 frequencies, 75x69x70, with sign change.

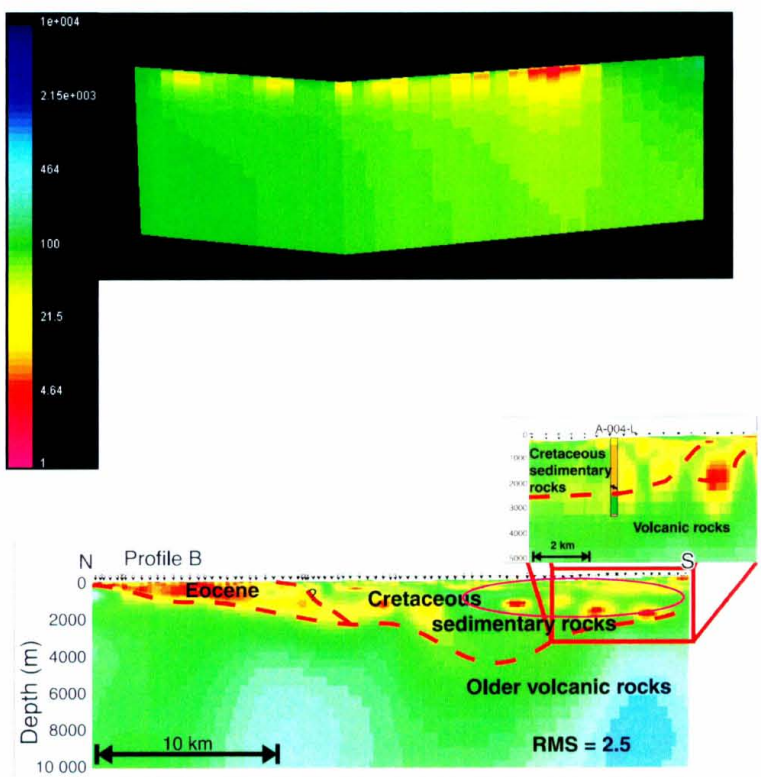

Figure D.26: Comparison with 2D for profile B, North to South. 18 frequencies, 75x69x70, with sign change.

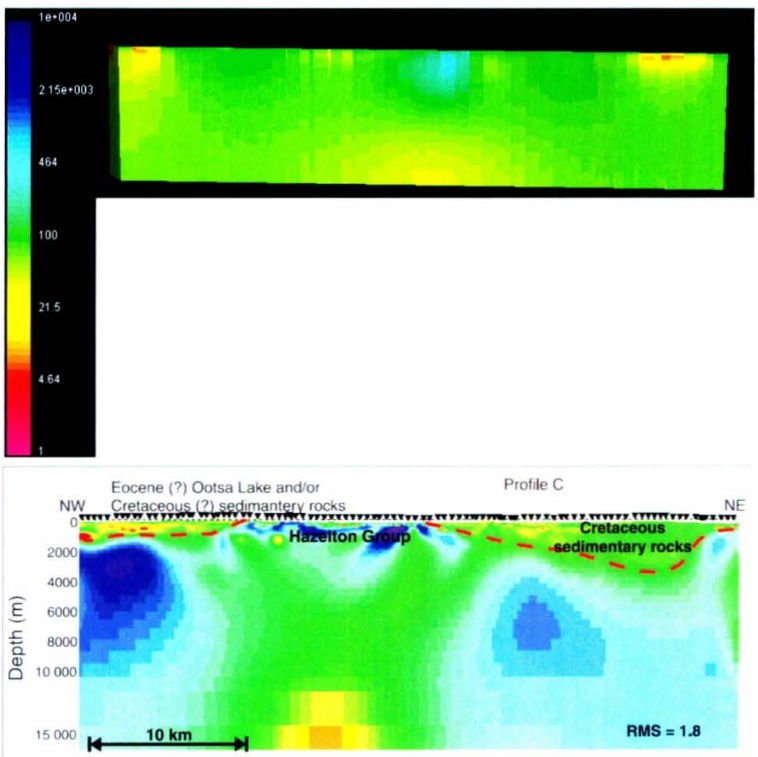

Figure D.27: Comparison with 2D for profile C, Southwest to Northeast. 18 frequencies, 75x69x70, with sign change.

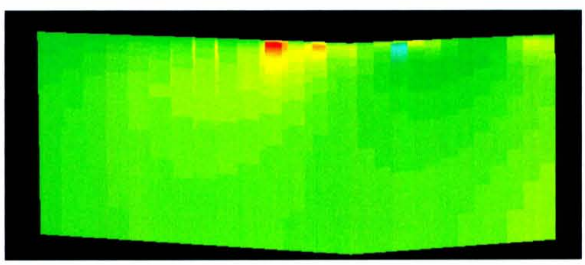

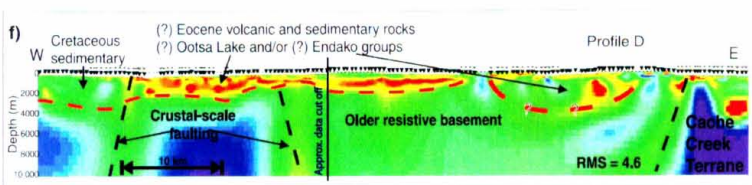

Figure D.28: Comparison with 2D for profile D, West to East. 18 frequencies, 75x69x70, with sign change.

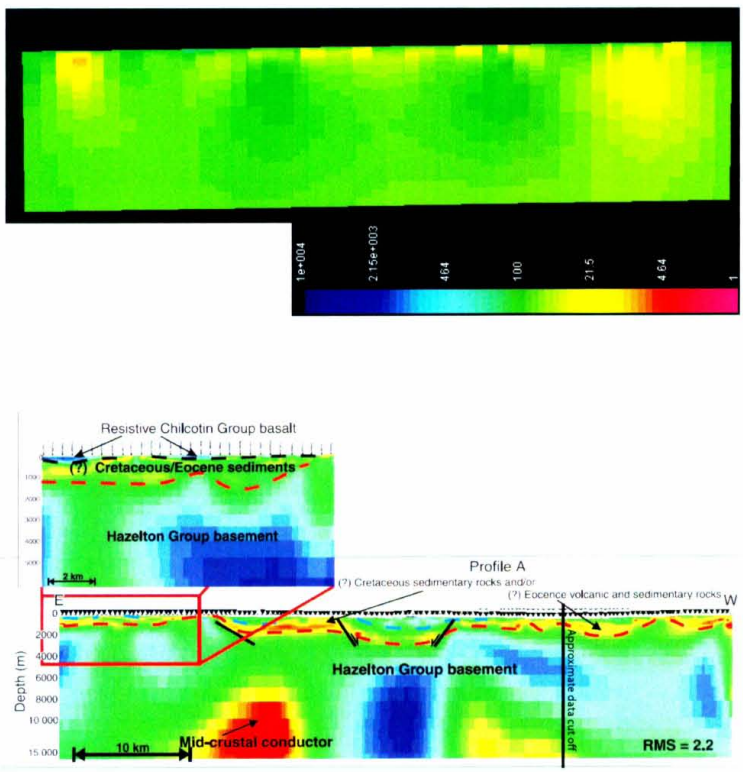

Figure D.29: Comparison with 2D for profile A, East to West. 16 frequencies, 75x75x75, with sign change.

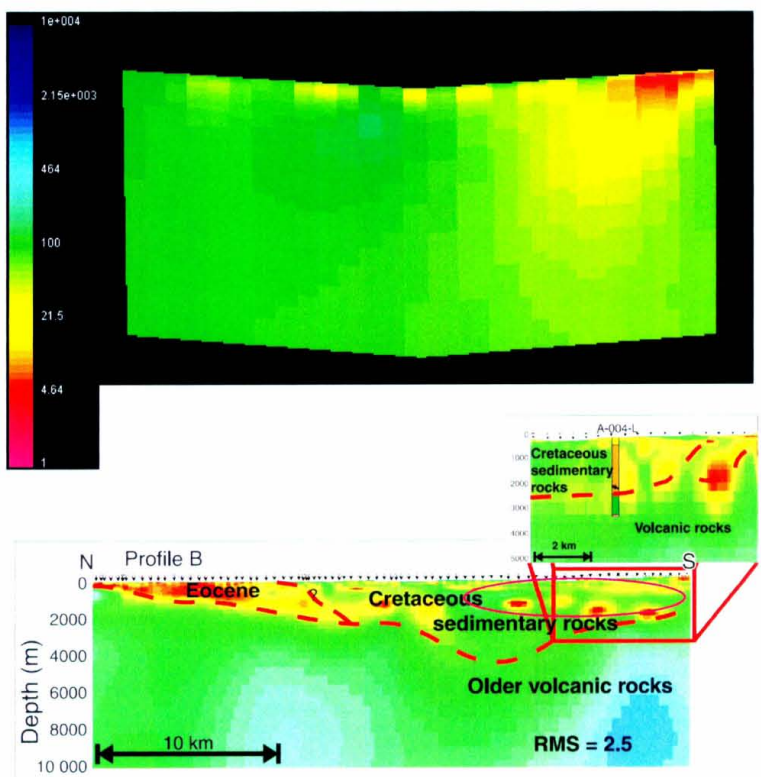

Figure D.30: Comparison with 2D for profile B, North to South. 16 frequencies, 75x75x75, with sign change.

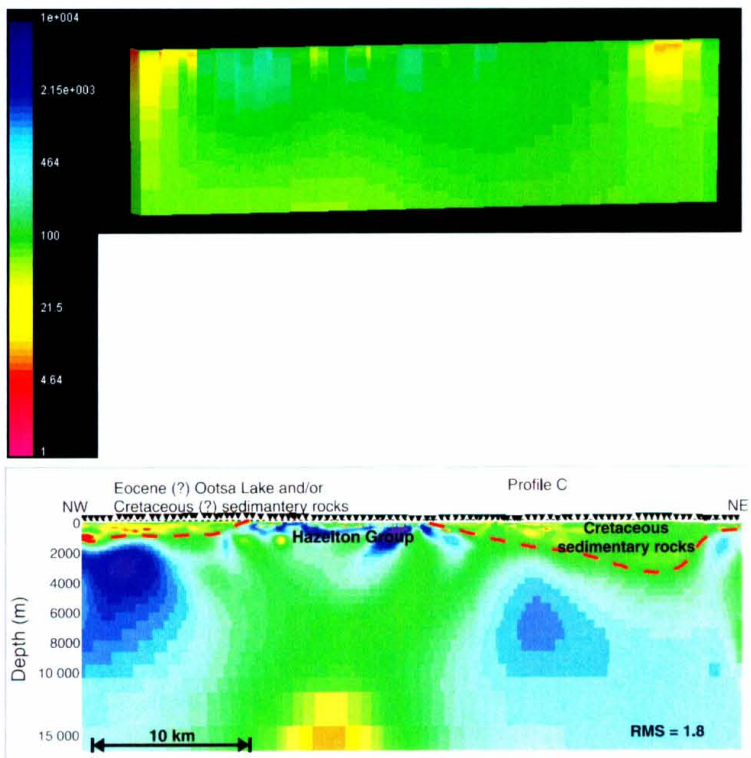

Figure D.31: Comparison with 2D for profile C, Southwest to Northeast. 16 frequencies, 75x75x75, with sign change.

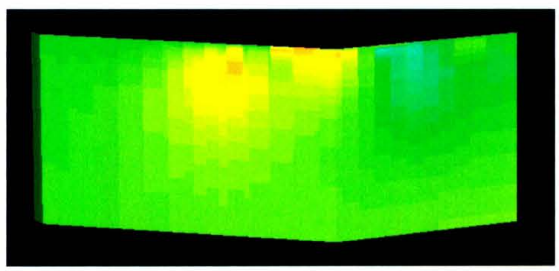

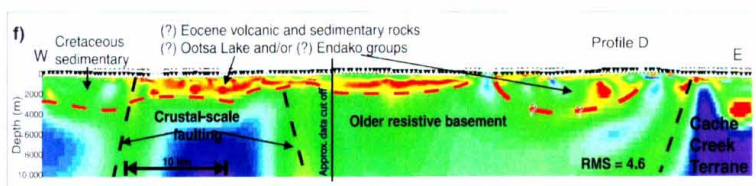

Figure D.32: Comparison with 2D for profile D, West to East. 16 frequencies, 75x75x75, with sign change.

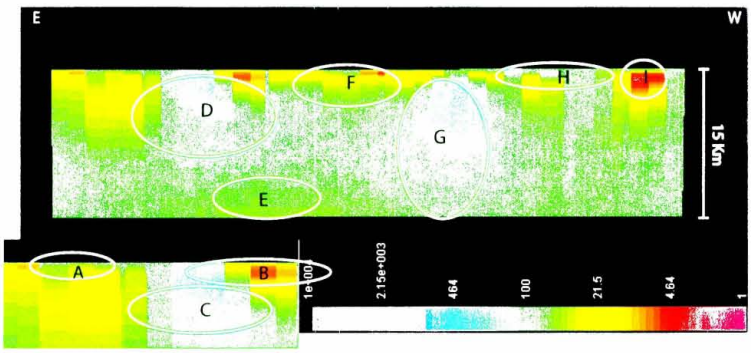

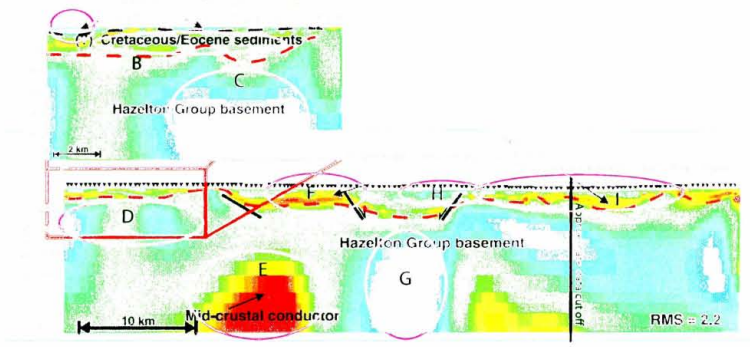

Figure [illegible] Comparison with 2D for profile A, East to West [illegible]
[illegible]

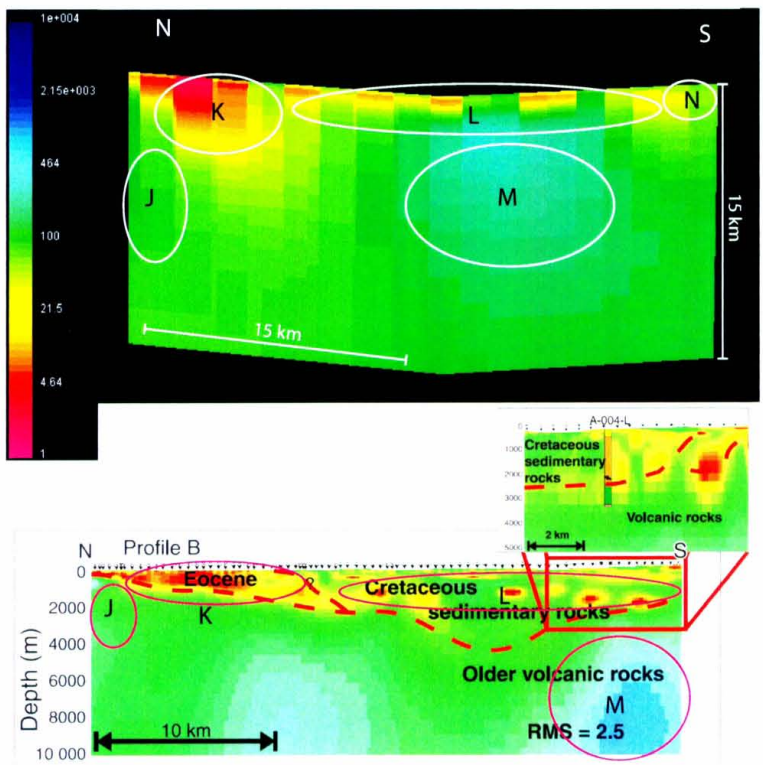

Figure D.34: Comparison with 2D for profile B, North to South. 16 frequencies, 62x62x62, without sign change.

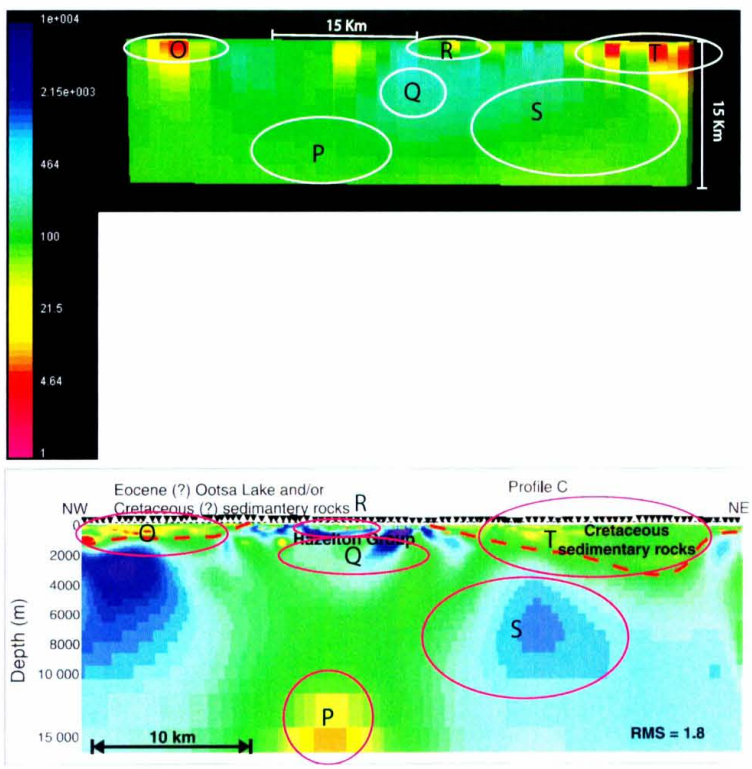

Figure D.35: Comparison with 2D for profile C, Southwest to Northeast. 16 frequencies, 62x62x62, without sign change.

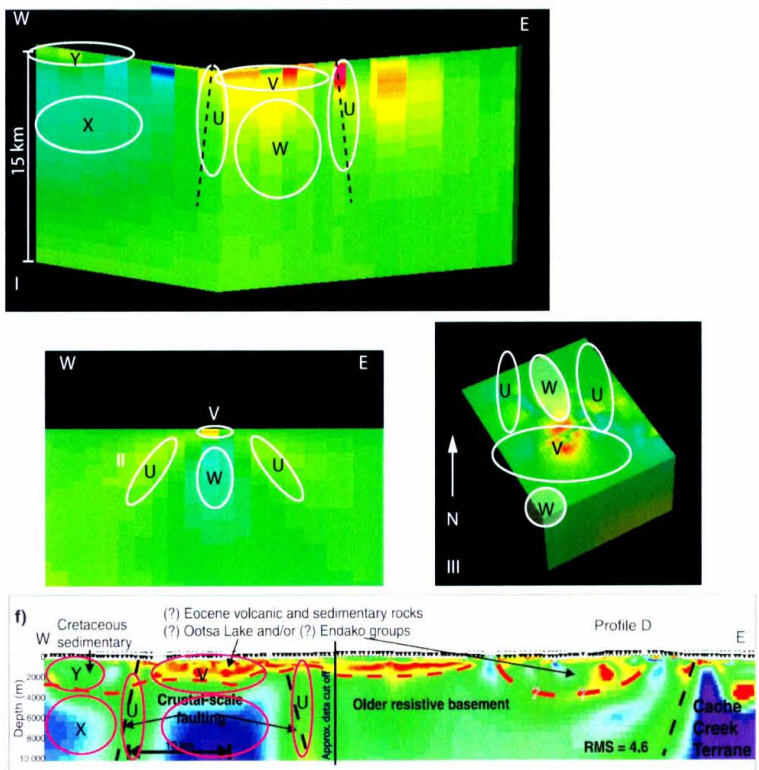

Figure D.36: Comparison with 2D for profile D, West to East. 16 frequencies, 62x62x62, without sign change.

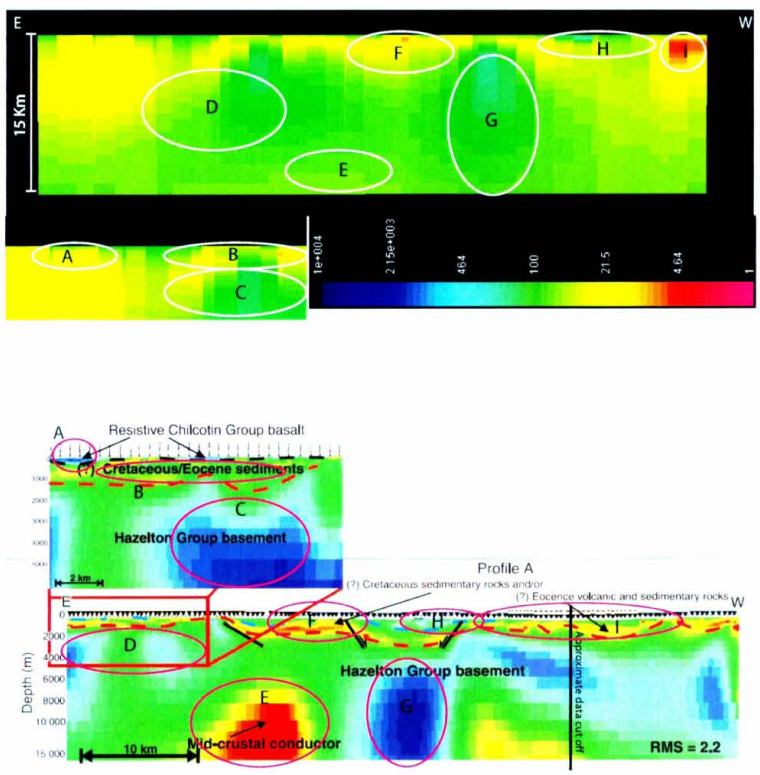

Figure D.37: Comparison with 2D for profile A, East to West. 16 frequencies, 62x62x62, with sign change.

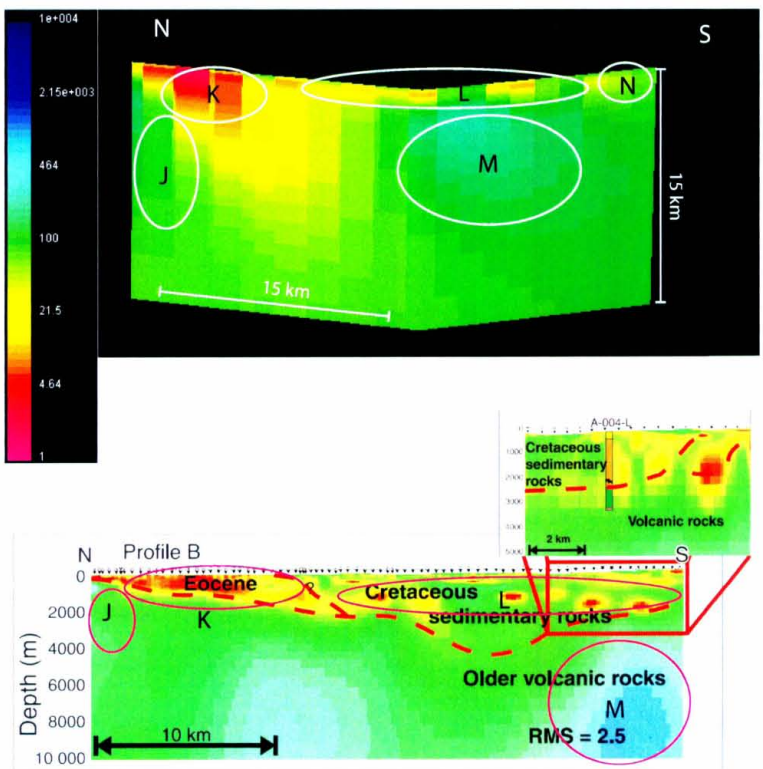

Figure D.38: Comparison with 2D for profile B, North to South. 16 frequencies, 62x62x62, with sign change.

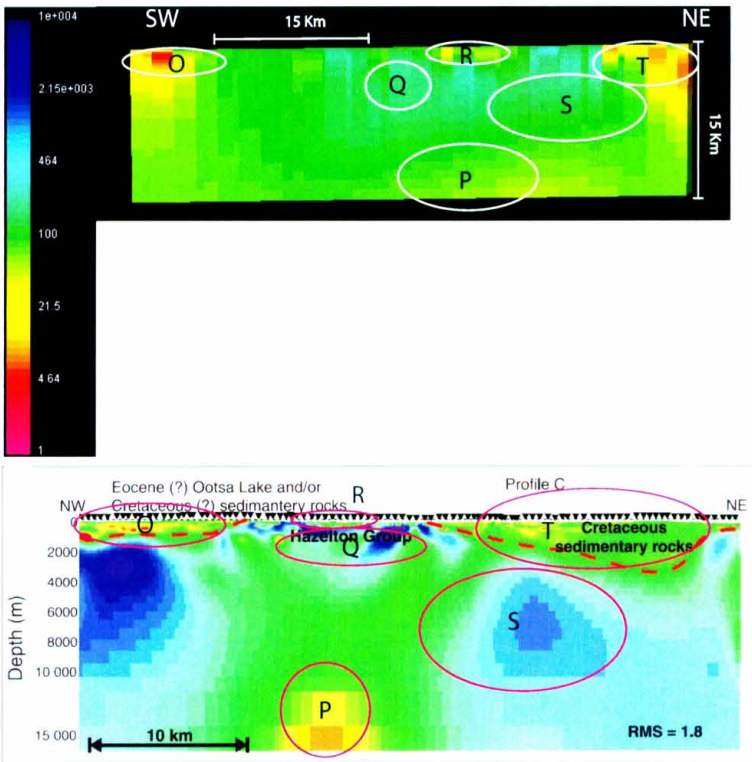

Figure D.39: Comparison with 2D for profile C, Southwest to Northeast. 16 frequencies, 62x62x62, with sign change.

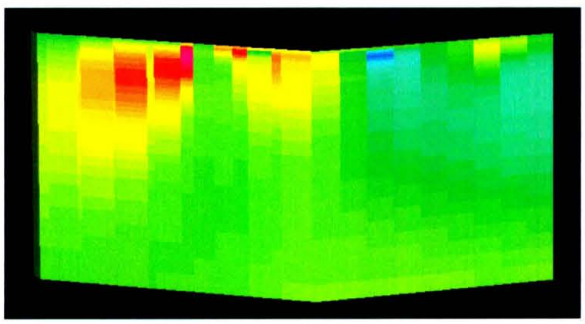

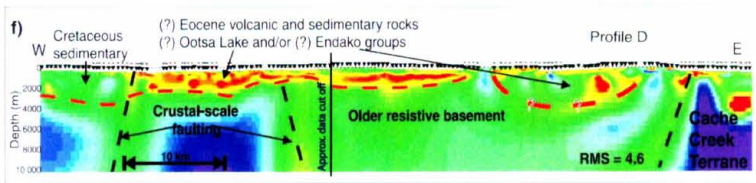

Figure D.40: Comparison with 2D for profile D, West to East. 16 frequencies, 62x62x62, with sign change.

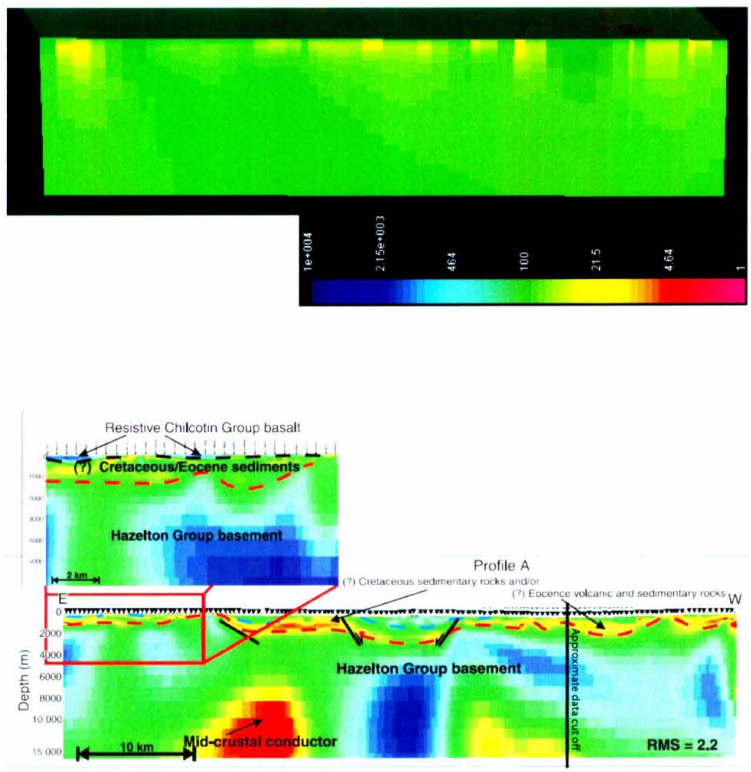

Figure D.41: Comparison with 2D for profile A, East to West. 8 frequencies, 75x75x75, with sign change.

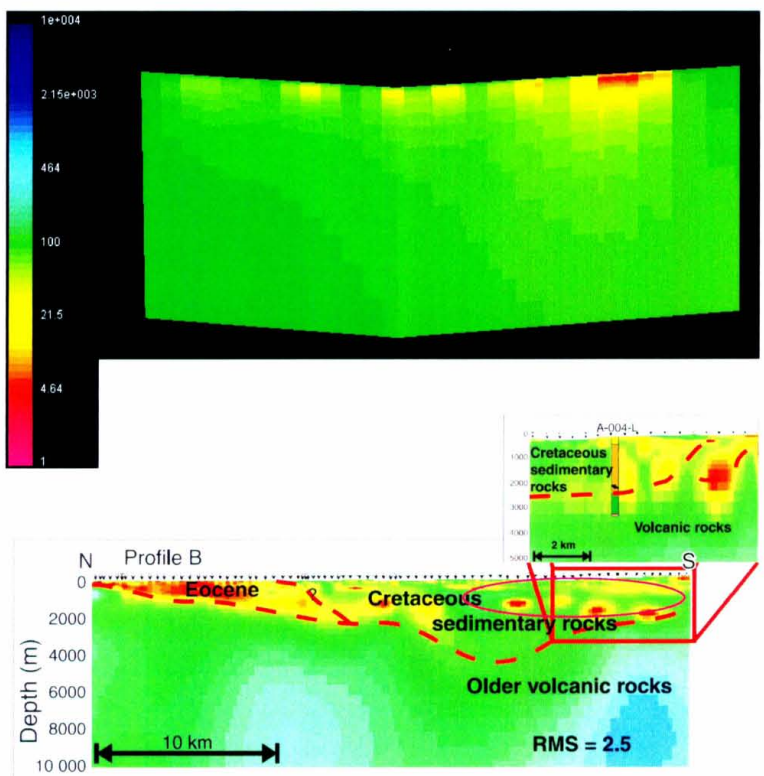

Figure D.42: Comparison with 2D for profile B, North to South. 8 frequencies, 75x75x75, with sign change.

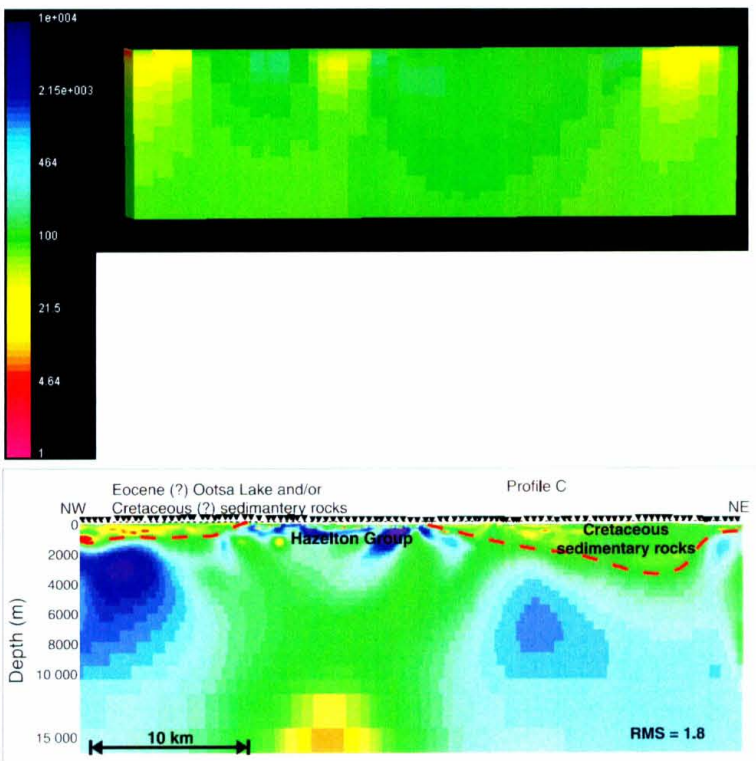

Figure D.43: Comparison with 2D for profile C, Southwest to Northeast. 8 frequencies, 75x75x75, with sign change.

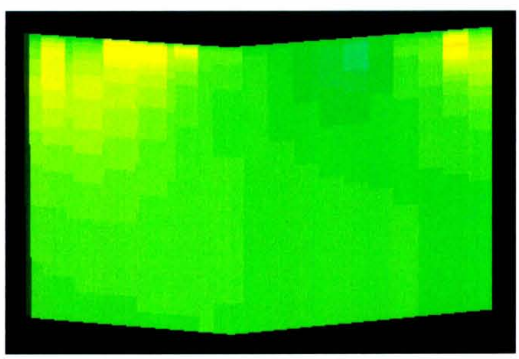

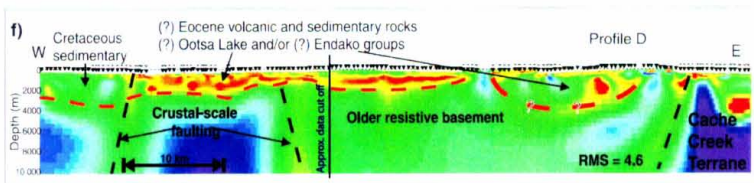

Figure D.44: Comparison with 2D for profile D, West to East. 8 frequencies, 75x75x75, with sign change.

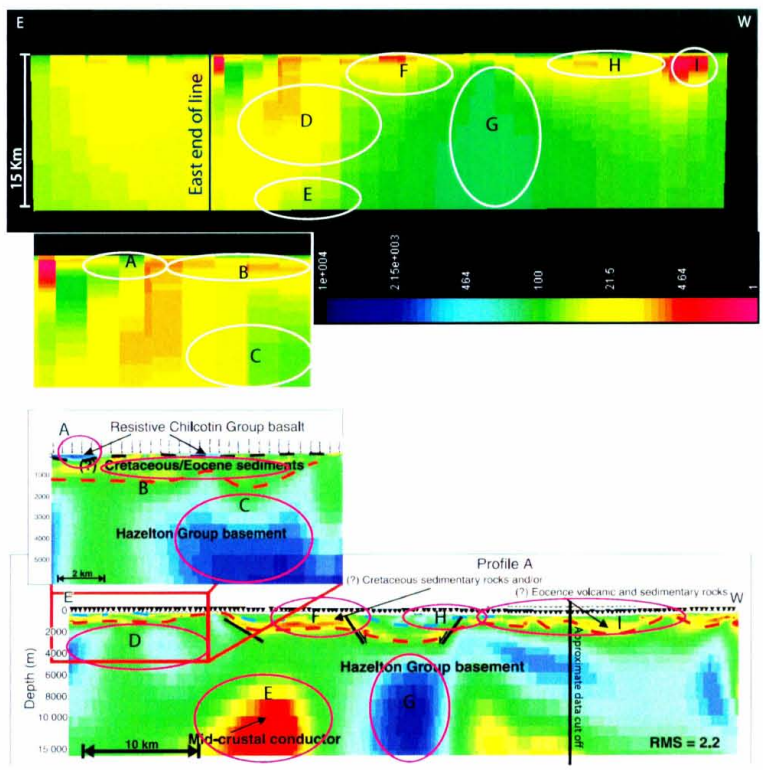

Figure D.45: Comparison with 2D for profile A, East to West. 8 frequencies, 62x62x62, with sign change.

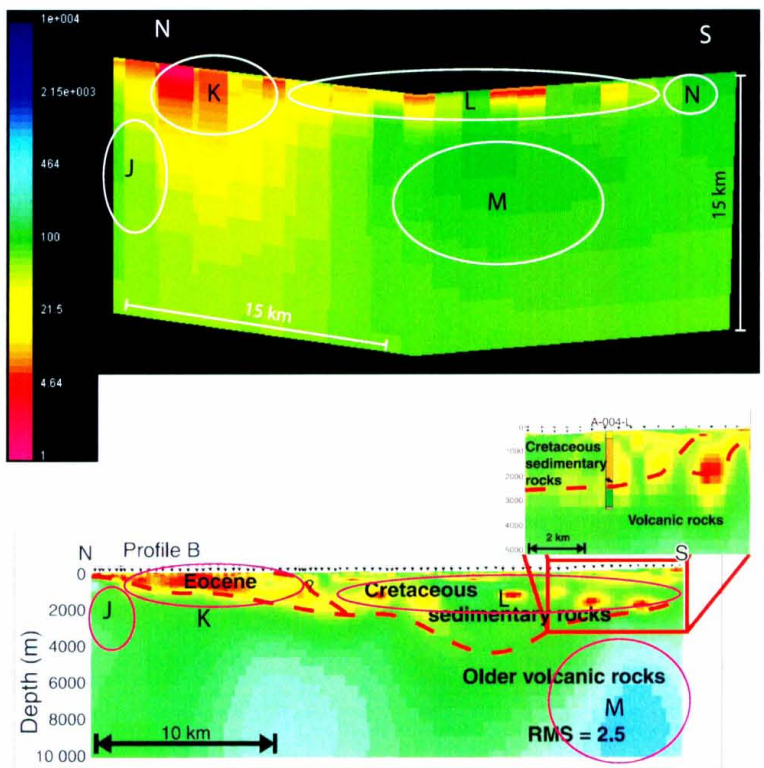

Figure D.46: Comparison with 2D for profile B, North to South. 8 frequencies, 62x62x62, with sign change.

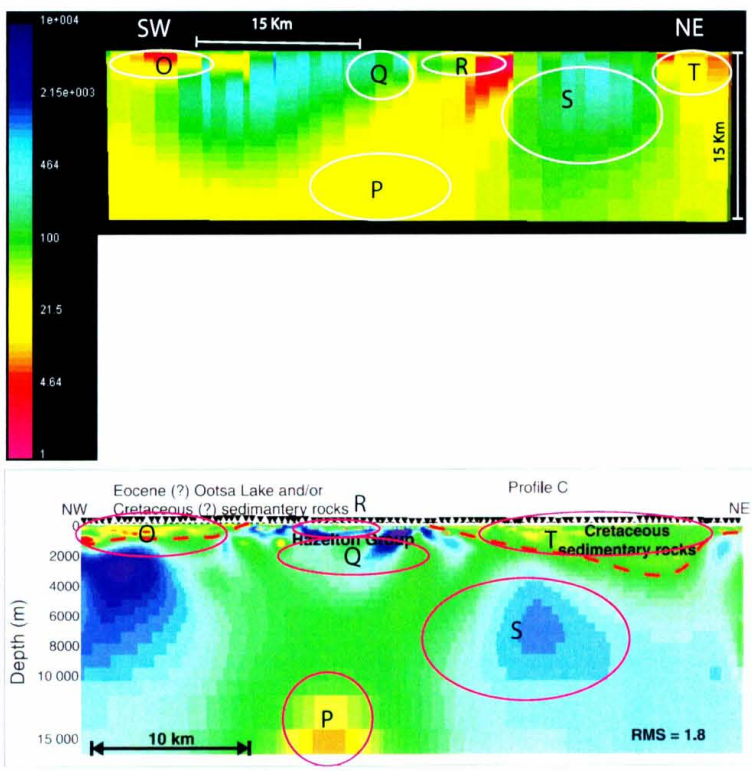

Figure D.47: Comparison with 2D for profile C, Southwest to Northeast. 8 frequencies, 62x62x62, with sign change.

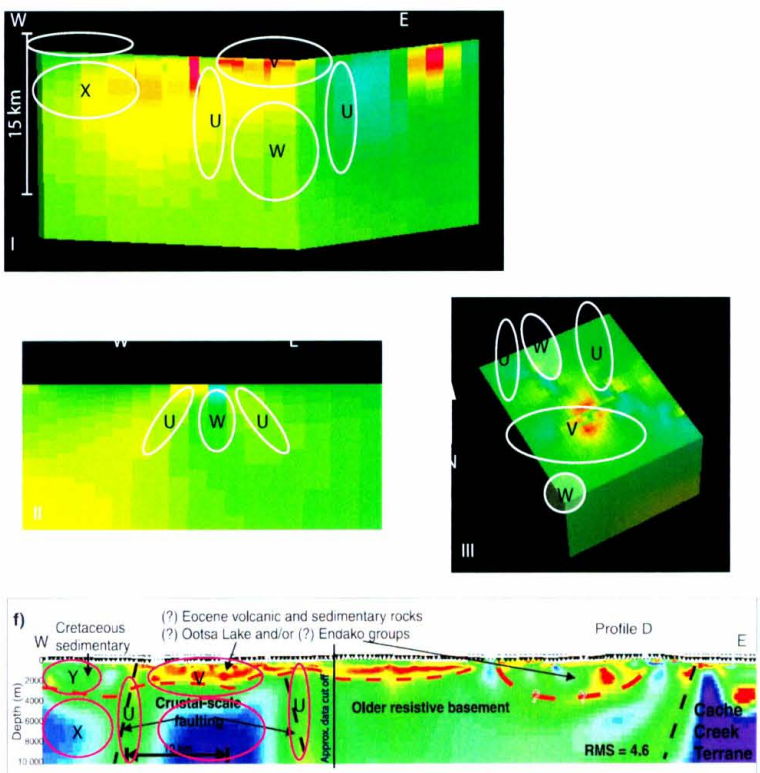

Figure D.48: Comparison with 2D for profile D, West to East. 8 frequencies, 62x62x62, with sign change.